NATIONAL TECHNICAL UNIVERSITY OF ATHENS

SCHOOL OF CIVIL ENGINEERING
Institute of Structural Analysis and Antiseismic Research

Nonlinear finite element modeling of shells for multiscale analysis applications

By

Sotiropoulos Gerasimos

Supervisor: Professor Vissarion Papadopoulos

A thesis submitted for the degree of
Doctor of Philosophy

May, 2021

APPROVAL

PhD THESIS EXAMINATION COMMITTEE

Professor Vissarion Papadopoulos

(Supervisor and Principal Advisor of the Committee)

National Technical University of Athens

School of Civil Engineering

Emeritus Professor Vlasis Koumousis

(Member Advisor of the Committee)

National Technical University of Athens

School of Civil Engineering

Professor Konstantinos Spiliopoulos

(Member Advisor of the Committee)

National Technical University of Athens

School of Civil Engineering

Professor Charalampos Gantes

(Member of the Examination Committee)

National Technical University of Athens

School of Civil Engineering

Associate Professor Maria Nerantzaki

(Member of the Examination Committee)

National Technical University of Athens

School of Civil Engineering

Assistant Professor Savvas Triantafyllou

(Member of the Examination Committee)

National Technical University of Athens

School of Civil Engineering

Associate Professor Michalis Fragiadakis

(Member of the Examination Committee)

National Technical University of Athens

School of Civil Engineering

TO MY GRANDPARENTS.

Acknowledgments

First of all, I would like to thank my family for their support throughout my studies. Because of their sacrifices, I was able to pursue my education.

I would also like to thank my supervisor Professor Vissarion Papadopoulos for his guidance and encouragement throughout my doctoral research.

I would like to thank the other members of the committee, Emeritus Professor Vlasis Koumousis and Professor Konstantinos V. Spiliopoulos, for their scientific advice. I would also like to thank the other members of the examination committee for their valuable comments and suggestions.

I also thank my esteemed colleagues for our cooperation. I would like also to acknowledge the administrative staff members of the Secretariat of the School of Civil Engineering Ms. Papailiou, Ms. Theofanidou, Ms. Andritsou and Ms. Boni that have always been very helpful.

Nonlinear finite element modeling of shells for multiscale analysis applications

ABSTRACT

In this thesis a formulation for multi-scale analysis of thin shells is presented. It is based on the first order homogenization theory and it allows for modeling, in a FE^2 method's context, of thin shells that meet the Kirchhoff Love hypothesis. The shells exhibit a heterogeneous micro-structure consisting of nonlinear materials and cohesive interfaces that periodically repeats itself in the in plane and out of plane direction of the shell with respect to its mid-surface.

The proposed methodology is then extended to shell structures that may undergo large deformations and strains and the same hypotheses are exploited for the periodicity of their heterogeneities and their size scale. Appropriate use of an attached coordinate system for the transformation of the utilized strain measures enables the neutralization of the moderately large rotations' effect on the implementation of constraints at the RVE level, simplifying this way the boundary value problem to be solved at the micro-structural level. Emanating from Hill's averaging theorem, which is satisfied by use of appropriated averaging relations for thin shells, the principle of virtual work for thin Kirchhoff Love shells is formulated to account for those transformations and the expression of a consistent Stiffness Matrix is analytically derived. The proposed methodology is assessed against popular benchmarks for thin shells and its applicability is demonstrated in virtual testing of thin nanocomposite structures.

Next the mechanical behavior of graphene reinforced nanocomposite structures is studied in a first order homogenization context. A simplified thin shell homogenization approach is followed for the modeling of graphene sheets with equivalent shell elements and a cohesive zone finite element model is utilized for modeling of the polymer graphene interaction. The effect of various characteristics of the micro structure such as the strength of the cohesive zone and geometry defects of the graphene sheets on the overall properties of the nanocomposite are under study.

ΠΕΡΙΛΗΨΗ ΤΗΣ ΔΙΔΑΚΤΟΡΙΚΗΣ ΔΙΑΤΡΙΒΗΣ

με τίτλο

'Μη γραμμική ανάλυση κελυφών με εφαρμογές στην ανάλυση πολλαπλών κλιμάκων'

●Τα δομικά υλικά, είτε είναι φυσικής προέλευσης είτε έχουν σχεδιασθεί από τον άνθρωπο και αφορούν βιομηχανικές ή εφαρμογές μηχανικού, είναι σε συγκεκριμένη κλίμακα ετερογενή. Τυπικά παραδείγματα περιλαμβάνουν κράματα μετάλλων, πολυκρυσταλλικά υλικά, νανοσύνθετα υλικά, μίγματα πολυμερών, πορώδη και ραγισμένα μέσα, βιολογικά υλικά, υλικά ξυλείας και κονιάματα. Αυτή η ετερογενής φύση έχει σημαντικό αντίκτυπο στην παρατηρούμενη μακροσκοπική συμπεριφορά των πολυφασικών υλικών. Διάφορα φαινόμενα που εμφανίζονται στο μακροσκοπικό επίπεδο προέρχονται από τις φυσικές ιδιότητες και τη μηχανική της υποκείμενης μικροδομής. Η συνολική συμπεριφορά των υλικών, που είναι ετερογενή σε μικροσκοπικό επίπεδο, εξαρτάται σε μεγάλο βαθμό από το μέγεθος, το σχήμα, τη χωρική κατανομή και τις ιδιότητες των μικροδομικών στοιχείων καθώς και των διεπιφανειών τους. Αντίστοιχα η εντατική κατάσταση και κατά συνέπεια η μηχανική απόκριση της μικροδομής επηρεάζεται από τα μακροσκοπικά θερμομηχανικά φορτία. Κατά συνέπεια, η μελέτη των μακροσκοπικών μηχανικών ιδιοτήτων δεν μπορεί να διαχωρισθεί από τη επιρροή των μικροσκοπικά παρατηρούμενων ετερογενειών.

Η μελέτη της σχέσης μεταξύ μικροδομικών φαινομένων και της μακροσκοπικής συμπεριφοράς όχι μόνο επιτρέπει την πρόβλεψη της συμπεριφοράς των υπαρχόντων πολυφασικών υλικών, αλλά συνιστά πολύτιμο εργαλείο για το σχεδιασμό νέων υλικών με μικροδομή κατάλληλη ώστε η προκύπτουσα μακροσκοπική συμπεριφορά να χαρακτηρίζεται από συγκεκριμένα στοιχεία. Ο προσδιορισμός των μακροσκοπικών χαρακτηριστικών των ετερογενών μέσων είναι ένα θεμελιώδες πρόβλημα σε πολλές εφαρμογές μηχανικής. Είναι ιδιαίτερα επίκαιρο καθότι, οι τρέχουσες τεχνολογικές εξελίξεις επιτρέπουν την επιβολή λεπτομερώς καθοριζόμενων ακολουθιών φόρτισης και αλλαγών φάσης στις χρησιμοποιούμενες πρώτες ύλες κατά τη διαδικασία παραγωγής πολυλειτουργικών έξυπνων υλικών. Αντίθετα, η πραγματοποίηση τυπικών πειραματικών μετρήσεων σε διάφορα δείγματα υλικών, για διάφορες φάσεις σωμάτων, κλάσματα όγκου και ιστορικά φόρτωσης είναι δύσκολα εφικτή, από πλευράς χρόνου και κόστους. Επιπρόσθετα είναι πρακτικώς αδύνατη η δημιουργία και η επίλυση σε λογικά χρονικά πλαίσια ενός λεπτομερούς μοντέλου πεπερασμένων στοιχείων σε πλήρη κλίμακα λόγω της συνήθως τεράστιας διαφοράς στην κλίμακα μήκους, της μικροδομής και του συνολικού φορέα. Το πρόβλημα αυτό προσεγγίζεται με κατάλληλες μεθοδολογίες που επιτρέπουν την ανάλυση των φορέων σε πολλαπλές κλίμακες (ΑΠΚ).

Για τους τρισδιάστατους φορείς, οι μεθοδολογίες ΑΠΚ είναι καλά θεμελιωμένες, και η εξέλιξη τους εκκινεί από τις προηγούμενες δεκαετίες. Μία πρώτη προσέγγιση για τον υπολογισμό μιας καταστατικής σχέσης για ένα ομογενή φορέα αντίστοιχο του μικροσκοπικά ετερογενούς προκύπτει από τη εφαρμογή, ενός κανόνα της ποσόστωσης με βάση τον όγκο κάθε πρόσμειξης του υλικού, στη συμμετοχή των μηχανικών της ιδιοτήτων στην συνολική έκφραση ενός σταθμισμένου καταστατικού μητρώου. Αυτή η προσέγγιση λαμβάνει υπόψη μόνο ένα χαρακτηριστικό, την κατ' όγκο αναλογία των εγκλεισμάτων στο συνολικό ετερογενές υλικό και για την ακρίβεια δικαιολογείται η χρήση της μόνο στην περίπτωση γραμμικά ελαστικών υλικών.

Μία πιο εξελιγμένη μέθοδος, του "ενεργού μέσου" εισήχθη από τον Eshelby [1] και αναπτύχθηκε περαιτέρω από ένα αριθμό ερευνητών (βλ. Hashin [2] Hashin and Shtrikman [3], Budiansky [4], Hill [5], Christensen and Lo [6]). Οι ιδιότητες ενός ισοδύναμου υλικού προκύπτουν ως αποτέλεσμα της αναλυτικής ή ημι-αναλυτικής λύσης ενός προβλήματος συνοριακών τιμών (BVP) για ένα σφαιρικό ή ελλειψοειδές έγκλεισμα ενός υλικού σε άπειρη μήτρα άλλου υλικού. Σε μια επέκταση αυτής της μεθόδου, ένα σωματίδιο μιας φάσης είναι ενσωματωμένο σε ένα ενεργό υλικό, του οποίου οι ιδιότητες δεν είναι γνωστές εκ των προτέρων [5,6]. Αυτές οι στρατηγικές δίνουν μια ικανοποιητική προσέγγιση για κατασκευές που έχουν κάποιο είδος γεωμετρικής κανονικότητας, αλλά δεν μπορούν να χρησιμοποιηθούν

για να στον υπολογισμό των ιδιοτήτων κατασκευών με συστάδες εγκλεισμάτων. Επιπλέον, έντονες αντιθέσεις μεταξύ των ιδιοτήτων των φάσεων δεν μπορούν να αναπαρασταθούν με ακρίβεια.

Παρόλο που έχουν γίνει κάποιες εργασίες για την επέκταση της ανωτέρω προσέγγισης σε μη γραμμικές περιπτώσεις, από τον Hill[5] ο οποίος πρότεινε μια προσαυξητική διατύπωση της μεθόδου , σημαντικά μεγαλύτερη πρόοδος στην εκτίμηση των μη γραμμικών ιδιοτήτων σύνθετων υλικών έχει επιτευχθεί με μεταβολικές διατυπώσεις (π.χ. ελάχιστη ενέργεια) που παρέχουν ανώτερα και κατώτατα όρια για την απόκριση του συνολικού σύνθετου υλικού.

Μια άλλη προσέγγιση υπολογιστικής ομογενοποίησης (computational homogenization) βασίζεται στη μαθηματική θεωρία ασυμπτωτικής ανάλυσης [7,8]. Σε αυτή τη μέθοδο διατυπώνεται ένα ασυμπτωτικό ανάπτυγμα των πεδίων μετατόπισης και τάσης συναρτήσει του λόγου του χαρακτηριστικού μήκους των ετερογενειών και του μεγέθους της μακροδομής [9-13]. Με αυτές τις μεθοδολογίες μπορούν να υπολογισθούν οι συνολικές ιδιότητες του σύνθετου υλικού καθώς και τοπικά μεγέθη όπως οι παραμορφώσεις και οι τάσεις, αλλά μπορούν να παρέχουν εκτιμήσεις μόνο για μικροδομές απλής γεωμετρίας και απλά μοντέλα υλικών με την παραδοχή μικρών παραμορφώσεων. Μια ολοκληρωμένη επισκόπηση των διαφορετικών μεθόδων ομογενοποίησης μπορεί να βρεθεί στην εργασία των Nemat-Nasser και Hori [14].

Ιδιαίτερο ενδιαφέρον παρουσιάζουν οι μέθοδοι "unit cell" οι οποίες επιτρέπουν την άντληση πληροφοριών από τη μικροδομή για τις ενεργές ιδιότητες των συνθετικών μερών του ετερογενούς υλικού, μέσω μιας διαδικασίας "εκ των προτέρων" επιβολής συγκεκριμένης ακολουθίας φόρτισης, και στη συνέχεια την αποτύπωση αυτής της πληροφορίας σε ένα επιλεγμένο φαινομενολογικό νόμο υλικού. Αυτή η προσέγγιση έχει χρησιμοποιηθεί σε μεγάλο αριθμό διαφορετικών εφαρμογών [15-22] Μια επιλογή παραδειγμάτων στο πεδίο των σύνθετων υλικών με μεταλλική μήτρα έχει συλλεχθεί στην εργασία των Suresh et al.[23]. Με τη μεθοδολογία αποτυπώνονται στη μακροσκοπική συμπεριφορά της κατασκευής και χαρακτηριστικά της μικροδομής που αναφέρονται στην μη γραμμική περιοχή, όμως είναι αδύνατο στη γενική περίπτωση να γίνει διατύπωση φαινομενολογικών νόμων που στους οποίους να μπορεί να αποτυπωθεί η σύνθετη συμπεριφορά διαφορετικών φάσεων. Ως εκ τούτου, οι τεχνικές αυτές δεν είναι κατάλληλες για μεγάλες παραμορφώσεις ούτε περίπλοκες ακολουθίες φόρτισης, ούτε λαμβάνουν υπόψη τις γεωμετρικές και φυσικές αλλαγές φάσης της μικροδομής.

oΤα τελευταία χρόνια, έχει αναπτυχθεί μια πολλά υποσχόμενη εναλλακτική προσέγγιση για την μοντελοποίηση των μικροσκοπικά ετερογενών υλικών η υπολογιστική ομογενοποίηση σε πολλαπλές κλίμακες "multiscale computational homogenization", που ονομάζεται επίσης εμφωλευμένη ανάλυση φορέων με πεπερασμένα στοιχεία "FE2". Πρόκειται για μία τεχνική η οποία για τον υπολογισμό της απόκριση της μικροδομής βασίζεται σε ένα πρόβλημα συνοριακών τιμών που επιβάλλεται με βάση την τρέχουσα μακροσκοπική παραμόρφωση.

Οι βασικές αρχές της κλασικής υπολογιστικής ομογενοποίησης έχουν σταδιακά εξελιχθεί από έννοιες που χρησιμοποιούνται σε άλλες μεθόδους ομογενοποίησης και περιγράφονται στο σχήμα ομογενοποίησης τεσσάρων βημάτων του Suquet[24]: (i) ορισμός ενός αντιπροσωπευτικού στοιχείου όγκου της μικροδομής(RVE), του οποίου η καταστατική συμπεριφορά των μεμονωμένων συστατικών θεωρείται γνωστή. (ii) διατύπωση συνοριακών συνθηκών για το μοντέλο του RVE με βάση μακροσκοπικές μεταβλητές (παραμορφώσεις) (macro to micro transition) (iii) επίλυση του προβλήματος συνοριακών τιμών του RVE και υπολογισμός των μακροσκοπικών μεταβλητών (τάσεις) (micro to macro transition) (iv) αριθμητικός υπολογισμός της σχέσης μεταξύ των μακροσκοπικών μεταβλητών εισόδου και εξόδου. Οι βασικές αρχές της υπολογιστικής ομογενοποίησης εισήχθησαν από τον

Suquet[24] και τους Guedes και Kikuchi[11] και βελτιώθηκαν περαιτέρω σε πιο πρόσφατες εργασίες.

Τα βασικότερα πλεονεκτήματα αυτής της μεθοδολογίας είναι τα εξής:

- Δεν απαιτεί μία εκ των προτέρων ρητή υπόθεση για το είδος της καταστατικής σχέσης που θα εξαχθεί από την μικροκλίμακα, αλλά η καταστατική συμπεριφορά της μικροδομής.

-Επιτρέπει την υπόθεση μεγάλων μετακινήσεων και στροφών για τη μικροκλίμακα και τη μακροκλίμακα.

-Δεν βασίζεται σε κάποια παραδοχή σχετική με το είδος της μη γραμμικότητας στη συμπεριφορά του υλικού.

-παρέχει τη δυνατότητα άντλησης λεπτομερών μικροδομικών πληροφοριών, συμπεριλαμβανομένης της φυσικής και γεωμετρικής εξέλιξης της μικροδομής και την αξιοποίηση τους στη μακροσκοπική ανάλυση.

-Επιτρέπει τη χρήση οποιασδήποτε τεχνικής μοντελοποίησης στο επίπεδο της μικροκλίμακας, π.χ. τη μέθοδο των πεπερασμένων στοιχείων (FEM), τη μέθοδο των συνοριακών στοιχείων (BEM), τη μέθοδο Voronoi Cell, αριθμητικές μεθόδους βασισμένες σε Fast Fourier Transforms, Transformation Field Analysis κ.α.

Ένα βασικό μειονέκτημα της μεθόδου FE^2 το υψηλό υπολογιστικό της κόστος, μπορεί πλέον να αρθεί με τη χρήση τεχνικών προγραμματισμού σε περιβάλλοντα υψηλών επιδόσεων (HPC), [25,26, 27], με την επιλεκτική προσομοίωση σε πολλαπλές κλίμακες μόνο των κρισιμότερων περιοχών του φορέα αλλά και με τη χρήση μεθόδων υποκατάστατης μοντελοποίησης και τεχνικών μηχανικής μάθησης τόσο για το μοντέλο της μικροκλίμακας αλλά και για την συνολική εξαγόμενη μικροδομική συμπεριφορά. Συγκεκριμένα στην εργασία [28] χρησιμοποιήθηκαν προσεγγιστικά σχήματα παρεμβολής, radial basis functions στην [29] και νευρωνικά δίκτυα στην [30,31].

○Στη συνέχεια διατυπώνονται οι παραδοχές της υπολογιστικής ομογενοποίησης πολλαπλών κλιμάκων. Οι μελετώμενοι φορείς θεωρούνται μακροσκοπικά επαρκώς ομοιογενείς, αλλά χαρακτηρίζονται από μία ετερογενή μικροδομή η οποία αποτελείται από διακριτές φάσεις, περιέχει εγκλείσματα, κόκκους, διεπαφές, κοιλότητες κλπ.. Το μήκος κλίμακας της μικροδομής θεωρείται αρκετά μεγαλύτερο από το χαρακτηριστικό μήκος της μοριακής δομής της, ώστε να δικαιολογείται για το RVE η θεώρηση συνεχούς μέσου. Ταυτόχρονα όμως ισχύει η υπόθεση του διαχωρισμού των κλιμάκων και συγκεκριμένα ότι το μήκος κλίμακας της μικροδομής θεωρείται πολύ μικρότερο από το τυπικό μήκος κύματος της φόρτισης της μακροσκοπικής δομής. Ως προς την περιοδικότητα της μικροδομής, γίνεται η ρεαλιστική παραδοχή της τοπικής περιοδικότητας. Θεωρείται ότι η κάθε συγκεκριμένη μορφολογία επαναλαμβάνεται σε μικρό τμήμα του φορέα και όχι σε ολόκληρο το φορέα. Οπότε διαφορετικές μικροδομές συνδέονται με κάθε μακροσκοπικό σημείο. Η παραδοχή της τοπικής περιοδικότητας επιτρέπει την μοντελοποίηση φορέων με μη ομοιόμορφα κατανεμημένα μικροδομικά χαρακτηριστικά, με στρωσιγενή και διαβαθμισμένη σύσταση.

●Το θεωρητικό πλαίσιο των μεθοδολογιών υπολογιστικής ομογενοποίησης στην μηχανική του συνεχούς μέσου, είναι καλά θεμελιωμένο και καλύπτει μεγάλο εύρος των προβλημάτων μηχανικής από τη θεωρία μικρών μετακινήσεων και τροπών [32,33] έως και τις θεωρίες πεπερασμένων τροπών [34] και τις θεωρίες ανώτερης τάξης. Είναι δυνατόν να συμπεριληφθούν αδρανειακά φαινόμενα ή φαινόμενα μεταφοράς θερμότητας στην ανάλυση πολλαπλών κλιμάκων [35,36]. Οι θεωρίες αυτές έχουν επεκταθεί και στο πεδίο της ηλεκτροελαστικότητας [37] και στη μοντελοποίηση συζευγμένων φαινομένων μαγνητισμού ελαστικότητας[38].

Αντιθέτως, τα ανωτέρω πλεονεκτήματα της ανάλυσης πολλαπλών κλιμάκων δεν έχουν αξιοποιηθεί στην ανάλυση λεπτών επιφανειακών φορέων με την παραδοχή μικρών ή μεγάλων μετακινήσεων. Σε αυτό το πεδίο, βάρος δίνεται κυρίως στην κατάλληλη επαναδιατύπωση κλασικών θεωριών ανάλυσης κελυφών ώστε να συμπεριληφθούν στην ανάλυση μη γραμμικοί φαινομενολογικοί νόμοι υλικού: πλαστικότητας[39-46], υπερελαστικότητας [47,48] η γενικότερες εκφράσεις τρισδιάστατων νόμων υλικού, ενώ βήματα προς την ανάπτυξη μίας θεωρίας ανάλυσης επιφανειακών φορέων σε πολλαπλές κλίμακες, με υψηλή ακρίβεια, είναι ιδιαίτερα περιορισμένα. Προς αυτήν την κατεύθυνση, μία διατύπωση επτά παραμέτρων για την ανάλυση κελυφών, παρουσιάσθηκε στο [49], είναι κατάλληλη για ανάλυση μεγάλων μετακινήσεων, αλλά δεν επιτρέπει την ταυτόχρονη ανάλυση σε δυο κλίμακες (FE^2) διότι χρησιμοποιεί εκ των προτέρων ολοκλήρωση για τον υπολογισμό της καταστατικής σχέσης που θα χρησιμοποιηθεί στη μακροκλίμακα. Ένα συζευγμένο μοντέλο μοριακής προσομοίωσης και μοντελοποίησης συνεχούς μέσου διατυπώνεται στην [50] για την προσομοίωση φαινομένων ρηγμάτωσης στερεών κελυφών. Η θερμομηχανική απόκριση επιφανειακών φορέων με ορθογωνική μικροδομή μελετήθηκε στην εργασία [51] στα πλαίσια ενός αλγορίθμου δεύτερης τάξης δύο κλιμάκων "SOTS". Ιδιαίτερης σημασίας είναι οι συνεισφορές [52,53] στις οποίες προτείνεται μία μεθοδολογία δεύτερης τάξης για την ανάλυση κελυφών σε πολλαπλές κλίμακες, στις οποίες εσωτερικά μεγέθη διατομής της Θεωρίας Κελυφών υπολογίζονται από το μικροδομικό πρόβλημα συνοριακών τιμών για ένα μοντέλο αντιπροσωπευτικού όγκου που περιγράφει ολόκληρη τη διατομή του κελύφους, περιορίζοντας όμως έτσι τη δυνατότητα προσομοίωσης πολύ συγκεκριμένων φορέων, ως προς το πάχος τους και μόνο την εντός επιπέδου περιοδικότητα της μικροδομικής μορφολογίας.

Στην παρούσα διατριβή προτείνεται μία μεθοδολογία για την ταυτόχρονη ανάλυση σε πολλαπλές κλίμακες λεπτών επιφανειακών φορέων που εμπίπτουν στη θεωρία Kirchhoff Love. Ανήκει στις θεωρίες πρώτης τάξης και βασίζεται στη συνθήκη μακροσκοπικής ομοιογένειας του Hill[54]. Γίνεται ολοκληρωμένη διατύπωση των μακροσκοπικών εξισώσεων ισορροπίας, του προβλήματος συνοριακών τιμών της μικροκλίμακας, και των σχέσεων μετάβασης κλίμακας για τα χρησιμοποιούμενα μέτρα τάσεων και παραμορφώσεων ξεχωριστά για τις περιπτώσεις μικρών και μεγάλων παραμορφώσεων και την αντίστοιχη έκφραση της συνθήκης μακροσκοπικής ομοιογένειας.

Στις επακόλουθες εξισώσεις οι γραφικοί συμβολισμοί χρησιμοποιούνται ως εξής: Έντονα γράμματα χρησιμοποιούνται για διανύσματα ή τανυστές δευτέρας τάξης, απλοί χαρακτήρες χρησιμοποιούνται για τις πράξεις μεταξύ πινάκων και διανυσμάτων ή για συνιστώσες τανυστών σε δεδομένη βάση, λατινικά ψηφία κατά τη σημειογραφία Einstein σημαίνουν ότι ο αντίστοιχος χαρακτήρας παίρνει τις τιμές 1,2 έως 3 ενώ η χρήση Ελληνικών χαρακτήρων χρησιμοποιείται για τις τιμές 1 έως 2.

○Αρχικά παρουσιάζεται η ανάλυση κελυφών σε πολλαπλές κλίμακες με την υπόθεση των μικρών μετακινήσεων. Η θεωρία Kirchhoff Love για την ανάλυση κελυφών αποτελεί επέκταση της θεωρίας Euler-Bernoulli για τις δοκούς, και σύμφωνα με αυτή η περιγραφή της θέσης ενός υλικού σημείου του κελύφους προκύπτει από την θέση της μέσης επιφάνειας και μία απόσταση ζ προς το κάθετο διάνυσμα σε αυτήν, το οποίο θεωρείται ότι και στην παραμορφωμένη κατάσταση παραμένει επίσης κάθετο.

Θεωρείται ότι η μέση επιφάνεια του κελύφους είναι μία συνάρτηση ψ(ξ) του παραμετρικού χώρου ξ=[ξ,η] στον τρισδιάστατο Ευκλείδιο Χώρο ψ: ξ→$\mathbf{R}^3$. Στο πλαίσιο μιας διακριτοποίησης των εξισώσεων, μια παραμετροποίηση του διανύσματος θέσης της επιφάνειας προκύπτει από τον γραμμικό συνδυασμό συναρτήσεων σχήματος και επικόμβιων ποσοτήτων

$$x_m = \psi\{\xi,\eta\} = \sum N^i(\xi,\eta)x^i \qquad \textbf{(1)}$$

Θεωρώντας και μία τρίτη παράμετρο ζ κατά τη διεύθυνση του πάχους ο πλήρης όγκος του κελύφους είναι ορισμένος και η θέση ενός υλικού σημείου σε απόσταση ζ από την μέση επιφάνεια δίνεται ως εξής

$$\mathbf{x}_\theta = \mathbf{x}_{mid} + \zeta \mathbf{a}_3, \quad -t/2 \leq \zeta \leq t/2 \tag{2}$$

Το μοναδιαίο κάθετο διάνυσμα θεωρείται σταθερό κατά τη διεύθυνση του πάχους του κελύφους και δίνεται ως

$$\mathbf{a}_3 = \frac{\mathbf{a}_1 \times \mathbf{a}_2}{|\mathbf{a}_1 \times \mathbf{a}_2|} \tag{3}$$

Οι συνιστώσες του μετρικού τανυστή και της καμπυλότητας του κελύφους ορίζονται ως εξής

$$\alpha_{\alpha\beta} = \mathbf{a}_\alpha \cdot \mathbf{a}_\beta \tag{4}$$

$$b_{\alpha\beta} = -\boldsymbol{\alpha}_\alpha \cdot \boldsymbol{\alpha}_{3,\beta} = -\boldsymbol{\alpha}_\beta \cdot \boldsymbol{\alpha}_{3,\alpha} = \boldsymbol{\alpha}_{\alpha,\beta} \cdot \boldsymbol{\alpha}_\alpha \tag{5}$$

Τα συν-διακυμαινόμενα διανύσματα βάσης στη θέση ζ από τη μέση επιφάνεια του κελύφους ορίζονται ως εξής

$$\mathbf{g}_\alpha = \mathbf{a}_\alpha + \zeta \mathbf{a}_{3,\alpha} \tag{6}$$

$$\mathbf{g}_3 = \mathbf{a}_3$$

συναρτήσει αυτών στη μέση επιφάνεια του κελύφους

$$\boldsymbol{\alpha}_\alpha = x_{m,a} \tag{7}$$

Η μετακίνηση ενός υλικού σημείου στη μέση επιφάνεια του κελύφους προκύπτει από τη διαφορά της τελικής με την αρχική κατάσταση.

$$\mathbf{u} = \mathbf{x}_{mid} - \mathbf{x}_{mid}^0 \tag{8}$$

Αγνοώντας τους όρους ανώτερης τάξης στις παραγώγους των μετακινήσεων λαμβάνεται η τελική έκφραση του μεμβρανικού και καμπτικού μέρους του τανυστή παραμόρφωσης

$$\varepsilon_{\alpha\beta} = \frac{1}{2}\left(a_\alpha^0 \cdot u_{,\beta} + a_\beta^0 \cdot u_{,\alpha}\right) \tag{9}$$

$$\kappa_{\alpha\beta} = \frac{1}{2}\left(a_\alpha^0 \cdot \Delta a_{3,\beta} + a_\beta^0 \cdot \Delta a_{3,\alpha} + u_{,\alpha} \cdot a_{3,\beta}^0 + u_{,\beta} \cdot a_{3,\alpha}^0\right) \tag{10}$$

όπου με a_α^0 συμβολίζονται τα εφαπτόμενα διανύσματα βάσης στην απαραμόρφωτη κατάσταση του κελύφους, ενώ οι παράγωγοι του κάθετου διανύσματος δίνονται χρησιμοποιώντας την Ιακωβιανή ορίζουσα j^0 ως

$$a_{3,\alpha}^0 = \left(j^0\right)^{-1}\left(a_{1,\alpha}^0 \times a_2^0 + a_1^0 \times a_{2,a}^0\right) \tag{11}$$

$$\Delta a_{3,\alpha} = \left(j^0\right)^{-1}\left(u_{,1a} \times a_2^0 + u_{,1}^0 \times a_{2,a}^0 + a_{1,a}^0 \times u_{,2} + a_1^0 \times u_{,2a}\right) \tag{12}$$

Και τελικά οι συνολικές συνιστώσες της εντός επιπέδου μακροσκοπικής παραμόρφωσης σε ένα σημείο σε απόσταση ζ από τη μέση επιφάνεια δίνεται ως

$$\varepsilon_{\alpha\beta}^{M} = \varepsilon_{\alpha\beta} + \zeta \kappa_{\alpha\beta} \tag{13}$$

◦Στη συνέχεια, για τη δεδομένη μακροσκοπική παραμόρφωση μορφώνεται το μικροδομικό πρόβλημα συνοριακών τιμών.
Αγνοώντας τη συνεισφορά των αδρανειακών δυνάμεων υποθέτουμε ότι το RVE παραμορφώνεται, υπό συνθήκες στατικής ισορροπίας [55]:

$$\nabla \cdot \sigma = 0 \quad \text{in} \quad \Omega_{RVE} \tag{14}$$

Μία από τις βασικές παραδοχές της προτεινόμενης μεθοδολογίας είναι η εξίσωση της συνολικής μακροσκοπικής παραμόρφωσης με την μέση τιμή της μικροδομικής παραμόρφωσης του αντίστοιχου RVE

$$\mathbf{\varepsilon}_{M} = \frac{1}{V_{RVE}} \int_{\Omega_{RVE}} \mathbf{\varepsilon}_{m} dV \tag{15}$$

Για την περίπτωση των λεπτών κελυφών, η κλασσική σχέση μεσοστάθμισης των παραμορφώσεων μετατρέπεται σε έναν εντός επιπέδου περιορισμό. Αντίστοιχα, στην παρακάτω εξίσωση, ο συμβολισμός 'hat' σημαίνει περιορισμό του τανυστή παραμορφώσεων στις εντός του εφαπτόμενου επιπέδου συνιστώσες του, οι οποίες δίνονται από τη σχέση (13) και αναφέρονται στη βάση που ορίζουν τα διακυμαινόμενα διανύσματα βάσης της απαραμόρφωτης κατάστασης.

$$\hat{\mathbf{\varepsilon}}_{M} = \frac{1}{V_{RVE}} \int_{\Omega_{RVE}} \hat{\mathbf{\varepsilon}}_{m} dV \tag{16}$$

Αυτή η συνθήκη πληρούται με την επιβολή κατάλληλων περιορισμών στο τρισδιάστατο μικροδομικό πρόβλημα συνοριακών τιμών. Συγκεκριμένα, ένα επίπεδο νοητό υπερστοιχείο επίπεδης έντασης που θεωρείται περιγεγραμμένο στο RVE στην μέση επιφάνεια του (στοιχείο ABCD στο σχήμα), υποβάλλεται σε επιβαλλόμενες εντός επιπέδου μετακινήσεις ανάλογες της μακροσκοπικής παραμόρφωσης σύμφωνα με την παρακάτω σχέση

$$\hat{u}_{m} = \hat{\mathbf{\varepsilon}}_{M} \hat{X}_{m} \tag{17}$$

Συγκεκριμένα αυτή η σχέση υλοποιείται σε όλα τα σημεία του στοιχείου ABCD, ενώ κάθε ένα από τα περιφερειακά σημεία ολόκληρου του RVE υποβάλλεται στην ίδια μετακίνηση με αυτή του σημείου που αντιστοιχεί στην προβολή του στο στοιχείο ABCD. Όπως εξηγείται στην Εικόνα 1, σε ένα περιφερειακό σημείο L_{in} του RVE με συντεταγμένες X_1, X_2 και X_3 επιβάλλονται οι ίδιες μετακινήσεις u_1 και u_2 που προκύπτουν από την εξίσωση (17) για τον αντίστοιχο κόμβο V_i του περιγεγραμμένου υπερστοιχείου με τις ίδιες συντεταγμένες X_1 και X_2 :

$$u_1^{edge}\left(X_1, X_2, X_3\right) = \hat{u}_1^{vertex}\left(X_1, X_2\right) \tag{18}$$
$$u_2^{edge}\left(X_1, X_2, X_3\right) = \hat{u}_2^{vertex}\left(X_1, X_2\right)$$

Με αυτόν τον τρόπο, οι εντός επιπέδου επιβαλλόμενες μετακινήσεις του υπερστοιχείου (ABCD), προκαλούν στο συνολικό RVE εντατική κατάσταση αντίστοιχη της επίπεδης έντασης. Οι βασικές μορφές παραμόρφωσης $\varepsilon_{11}^{M}, \varepsilon_{22}^{M}, \varepsilon_{12}^{M}$ που συνάδουν με αυτή την εντατική κατάσταση φαίνονται στο σχήμα Εικόνα 2. Η εκτός επιπέδου αξονική παραμόρφωση ε_{33}^{M} δεν επιβάλλεται σα περιορισμός αλλά η τιμή της προκύπτει από την ανάλυση, από την εκτός επιπέδου παραμόρφωση του RVE. Οι μετακινήσεις του τύπου (18) επιβάλλονται ομοιόμορφα καθ' ύψος της διατομής, οπότε οι εκτός επιπέδου διατμητικές παραμορφώσεις $\varepsilon_{3\alpha}^{M}$ είναι εκ των προτέρων 0. Περιορισμοί θέτονται επίσης για τις εκτός

επιπέδου κινήσεις ελευθέρου στερεού. Δεσμεύονται οι μετακινήσεις κατά X_3 τριών ακραίων σημείων του 3, 4 και 8 στο παρακάτω σχήμα.
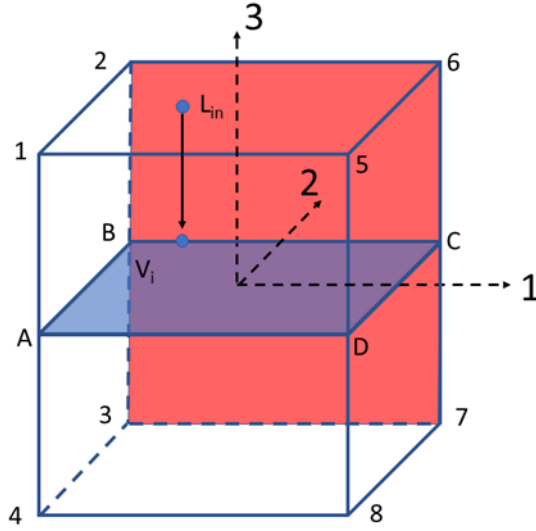
Εικόνα 1: RVE και επιβαλλόμενες συνοριακές συνθήκες

(b) Virtual element deformation modes

(c) Corresponding RVE deformation modes
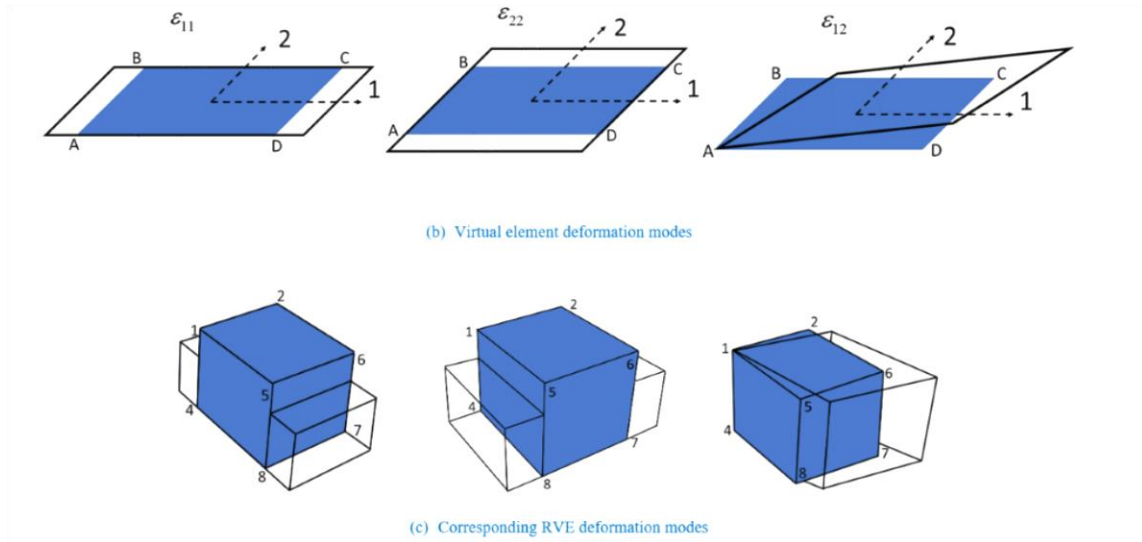
Εικόνα 2: Εντός επιπέδου μορφές παραμόρφωσης του υπερστοιχείου ABCD και ολόκληρου του RVE

Μία μεσοσταθμική σχέση ισχύει και για τον τανυστή των τάσεων:

$$\widehat{\boldsymbol{\sigma}}_M = \frac{1}{V_{RVE}} \int_{\Omega_{RVE}} \widehat{\boldsymbol{\sigma}}_m \; dV = \frac{1}{V_{RVE}} \int_{\partial\Omega_{RVE}} sym[\hat{t} \otimes x] \, dA \tag{19}$$

όπου $\hat{t} = \sigma \cdot n$ είναι το πεδίο των ανεπτυγμένων στο σύνορο έλξεων και στην οποία έχει χρησιμοποιηθεί το θεώρημα απόκλισης. Οι εκτός επιπέδου έλξεις t είναι ταυτοτικά ίσες με μηδέν, διότι κανένας περιορισμός δεν εφαρμόζεται προς την κατεύθυνση 3 και οι συνθήκες επίπεδης έντασης ισχύουν $\sigma_{33}^{M} = 0$. Με συνδυασμό των εξισώσεων (15)(19) και λαμβάνοντας χρησιμοποιώντας την (17), το μακροσκοπικά παραγόμενο έργο ισούται με το μεσοσταθμικό παραγόμενο έργο στη μικροδομή.

$$\boldsymbol{\sigma}_M : \dot{\boldsymbol{\varepsilon}} = \frac{1}{V_{RVE}} \int_{\Omega_{RVE}} \boldsymbol{\sigma}_m : \dot{\boldsymbol{\varepsilon}}_m dV \tag{20}$$

Αυτή η σχέση πληροί την συνθήκη μακροσκοπικής ομοιογένειας Hill Mandel [56]. Με αυτόν τον τρόπο, τα μακροσκοπικά ενεργειακά συζυγή μεγέθη παραμόρφωσης και τάσης μπορούν να αντικατασταθούν από τα αντίστοιχα μεσοσταθμισμένα μικροδομικά μεγέθη στην έκφραση της Αρχής των Δυνατών Έργων στο μακροσκοπικό επίπεδο.

○Στη συνέχεια εστιάζουμε στο μικροδομικό πρόβλημα συνοριακών τιμών (14) το οποίο μαζί με τις απαραίτητες συνοριακές τιμές (17) μπορεί να επιλυθεί με τη μέθοδο των πεπερασμένων στοιχείων. Θεωρώντας μία διακριτοποίηση του πεδίου των μετακινήσεων u_m και μηδενίζοντας τους κατάλληλους β.ε. των αντίστοιχων κινήσεων ελευθέρου στερεού, οι εναπομείναντες β.ε. του προβλήματος χωρίζονται σε δύο κατηγορίες, σε αυτούς που συμμετέχουν στον περιορισμό της εξίσωσης (17) και σε β.ε. που είναι τελείως ελεύθεροι. Οι δεσμευμένοι β.ε. που συμβολίζονται στη συνέχεια με 'e' περιλαμβάνουν τους εντός επιπέδου μετακινησιακούς β.ε. των περιφερειακών κόμβων του rve, ενώ οι ελεύθεροι β.ε. που συμβολίζονται με 'p' περιλαμβάνουν τους εκτός επιπέδου μετακινησιακούς των περιφερειακών κόμβων και όλους τους β.ε. των υπόλοιπων εσωτερικών κόμβων.

$$u = \begin{bmatrix} u_e \\ u_p \end{bmatrix} \tag{21}$$

Ο ίδιος διαμερισμός εφαρμόζεται και στο διάνυσμα των επικόμβιων δράσεων και στο μητρώο στιβαρότητας

$$f = \begin{bmatrix} f_e \\ f_p \end{bmatrix} \qquad K = \begin{bmatrix} K_{ee} & K_{ep} \\ K_{pe} & K_{pp} \end{bmatrix} \tag{22}$$

Για κάθε περιφερειακό σημείο «q» του RVE, διάνυσμα u_q των εντός επιπέδου μετακινήσεων προκύπτει με βάση την από την αντίστοιχη προβολή του σημείου στο επίπεδο (ABCD) και τη σχέση (17)

$$u_q = \begin{bmatrix} u_1 & u_2 \end{bmatrix}^T = D_q^T \hat{\varepsilon} \tag{23}$$

όπου το μητρώο D_q και το διάνυσμα $\hat{\varepsilon}$ συγκεντρώνουν τις μικροσκοπικές συντεταγμένες και τις μακροσκοπικές επιβαλλόμενες παραμορφώσεις

$$D_q := \frac{1}{2} \begin{bmatrix} 2x_1 & 0 \\ 0 & 2x_2 \\ x_2 & x_1 \end{bmatrix}, \hat{\varepsilon}^T := [\varepsilon_{11}^M \quad \varepsilon_{22}^M \quad 2\varepsilon_{12}^M] \tag{24}$$

Συλλέγοντας σε ένα καθολικό πίνακα D τις επιμέρους συνεισφορές D_q για κάθε περιφερειακό σημείο του RVE η διακριτοποιημένη μορφή της εξίσωσης (17) γίνεται

$$u_e = D^T \hat{\varepsilon}, \qquad D = \begin{bmatrix} D_1, D_2, ..., D_p \end{bmatrix} \tag{25}$$

Ο περιορισμός (25) εφαρμόζεται στους εξωτερικούς β.ε. 'e' μέσω κατάλληλων πολλαπλασιαστών Lagrange δ που εξισορροπούν της αντίστοιχες επικόμβιες δράσεις. Τότε η διακριτοποιημένη μορφή του μικροδομικού προβλήματος συνοριακών τιμών δίνεται ως εξής

$$f_e = \delta \tag{26}$$
$$f_p = 0$$
$$u_e - D^T \hat{\varepsilon} = 0$$

Μετά τη λύση του προβλήματος αυτού, ο μακροκοπικός τανυστής τάσης μπορεί να υπολογισθεί μέσω της σχέσης (19) η οποία λαμβάνει την εξής διακριτοποιημένη μορφή

$$\hat{\sigma} := \frac{1}{|V|} D\delta \tag{27}$$

Θεωρώντας μία απειροστή προσαύξηση $\Delta\hat{e}$ του μακροσκοπικού τανυστή παραμορφώσεων γύρω από μία γνωστή θέση ισορροπίας οι συνεπακόλουθες επαυξήσεις στις μετακινήσεις Δu_e, Δu_p, στους πολλαπλασιαστές Lagrange και τη συνολική μακροσκοπική τάση επαύξηση $\Delta\hat{\sigma}$ δίνονται διαδοχικά

$$\Delta u_e = D^T \Delta\hat{e} \tag{28}$$

$$\Delta u_p = -K_{pp}^{-1} K_{pe} \Delta u_e$$

$$\Delta d = \tilde{K}_{ee} D^T \Delta\hat{e}$$

$$\Delta\hat{\sigma} = \frac{1}{V} D \Delta\delta$$

όπου $\tilde{K}_{ee} = K_{ee} - K_{ep} K_{pp}^{-1} K_{pe}$. Οπότε το μακροσκοπικό καταστατικό μητρώο δίνεται από τη σχέση

$$C = \frac{1}{|V|} D \tilde{K}_{ee} D^T \tag{29}$$

○Η μακροσκοπική ισορροπία διέπεται από την αρχή των Δυνατών Έργων

$$\delta W^{internal} + \delta W^{ext} = 0 \tag{30}$$

όπου

$$\delta W^{internal} = -\int \sigma_M : \delta\varepsilon_M dV \tag{31}$$

$$\delta W^{ext} = \int f \cdot \delta u_M dV \tag{32}$$

είναι οι εκφράσεις του εσωτερικού και του εξωτερικού Δυνατού Έργου για μεταβολή δu$_M$ η οποία αναφέρεται στο πεδίο των μετατοπίσεων στη μακροκλίμακα. Το δυνατό έργο των εσωτερικών δυνάμεων γράφεται ως εξής

$$\int \sigma_M : \delta\varepsilon_M dV = \int n : \delta\varepsilon_M + m : \delta\kappa_M dA \tag{33}$$

συναρτήσει των εντατικών μεγεθών διατομής

$$n^{\alpha\beta} = \int_{-h/2}^{h/2} \sigma_M^{\alpha\beta} d\zeta \tag{34}$$

$$m^{\alpha\beta} = \int_{-h/2}^{h/2} \sigma_M^{\alpha\beta} \zeta d\zeta$$

τα οποία υπολογίζονται με τη χρήση αριθμητικής ολοκλήρωσης, συναρτήσει της απόκρισης $\sigma_M^{\alpha\beta}$ RVE που λαμβάνεται στα καθ' ύψος σημεία ολοκλήρωσης. Με όμοιο τρόπο υπολογίζονται και τα κατά τη διατομή ολοκληρούμενα καταστατικά μητρώα συναρτήσει

$$C_A = \int_{-h/2}^{h/2} C d\zeta, \qquad C_B = \int_{-h/2}^{h/2} C \zeta d\zeta, \qquad C_D = \int_{-h/2}^{h/2} C \zeta^2 d\zeta \tag{35}$$

συναρτήσει τον οποίων εκφράζονται τα διαφορικά των μεβρανικών δυνάμεων και των καμπτικών ροπών ως εξής

$$dn^{\alpha\beta} = C_{M_A}^{\alpha\beta\gamma\delta} d\varepsilon_{\gamma\delta} + C_{M_B}^{\alpha\beta\gamma\delta} d\kappa_{\gamma\delta} \tag{36}$$

$$dm^{\alpha\beta} = C_{M_B}^{\alpha\beta\gamma\delta} d\varepsilon_{\gamma\delta} + C_{M_D}^{\alpha\beta\gamma\delta} d\kappa_{\gamma\delta}$$

Η σχέση (30) πρέπει να ισχύει για δυνατή μετακίνηση κατά οποιονδήποτε β.ε. και μπορεί να γραφεί ως εξής

$$\delta W = \frac{\partial W}{\partial u_r} \delta u_r = 0 \tag{37}$$

και με αυτόν τον τρόπο προκύπτει η ισορροπία εσωτερικών και εξωτερικών δυνάμεων

$$F_r^{internal} = \int \boldsymbol{n} : \frac{\partial \boldsymbol{\varepsilon_M}}{\partial u_r} + \boldsymbol{m} : \frac{\partial \boldsymbol{k_M}}{\partial u_r} dA \qquad (38)$$

$$F_r^{ext} = \int f \cdot \frac{\partial u}{\partial u_r} dA$$

Επακολούθως, το εφαπτομενικό μητρώο στιβαρότητας δίνεται ως εξής

$$K_{rs}^{internal} = \int \frac{\partial \boldsymbol{n}}{\partial u_s} : \frac{\partial \boldsymbol{\varepsilon_M}}{\partial u_r} + \frac{\partial \boldsymbol{m}}{\partial u_s} : \frac{\partial \boldsymbol{k_M}}{\partial u_r} dA. \qquad (39)$$

όπου αντικαθιστώντας την σχέση (36) λαμβάνεται η τελική του μορφή

$$K_{rs}^{internal} = \int \left(\boldsymbol{C}_{M_A} : \frac{\partial \boldsymbol{\varepsilon_M}}{\partial u_s} + \boldsymbol{C}_{M_B} : \frac{\partial \boldsymbol{k_M}}{\partial u_s} \right) : \frac{\partial \boldsymbol{\varepsilon_M}}{\partial u_r} + \left(\boldsymbol{C}_{M_B} : \frac{\partial \boldsymbol{\varepsilon_M}}{\partial u_s} + \boldsymbol{C}_{M_D} : \frac{\partial \boldsymbol{k_M}}{\partial u_s} \right) : \frac{\partial \boldsymbol{k_M}}{\partial u_r} dA \qquad (40)$$

●Στη συνέχεια επεκτείνεται η παραπάνω θεωρία ώστε να περιλαμβάνει την παραδοχή μεγάλων μετακινήσεων και στροφών καθώς και πεπερασμένων τροπών. Ξεκινώντας από την μακροσκοπική περιγραφή του φορέα, με αυτές τις παραδοχές πλέον υπάρχει σαφής διάκριση της απαραμόρφωτης γεωμετρίας (αναφοράς) από την τρέχουσα γεωμετρία του φορέα. Η κατάσταση αναφοράς περιγράφεται πλέον από μια σχέση αντίστοιχη της (2) ως εξής

$$\boldsymbol{X} = \boldsymbol{X_m} + \zeta \boldsymbol{A_3} \qquad (41)$$

ενώ η σχέση (2) εξακολουθεί να ισχύει καθώς, προκύπτει από την παραδοχή της θεωρίας Kirchhoff Love ότι το αρχικά κάθετο στη μέση επιφάνεια του κελύφους διάνυσμα παραμένει κάθετο στην παραμορφωμένη γεωμετρία.

Με αντίστοιχο τρόπο ορίζονται και τα συν-διακυμαινόμενα διανύσματα βάσης στην γεωμετρία αναφοράς.

$$\boldsymbol{G_1} = \boldsymbol{X_{m,\xi}} + \zeta \boldsymbol{A_{3,\xi}} \qquad (42)$$

$$\boldsymbol{G_2} = \boldsymbol{X_{m,\eta}} + \zeta \boldsymbol{A_{3,\eta}}$$

$$\boldsymbol{G_3} = \boldsymbol{A_3}$$

Με κεφαλαίο γράμμα συμβολίζονται ποσότητες που αναφέρονται στην κατάσταση αναφοράς. Οι μετρικές συνιστώσες προκύπτουν από τη σχέση $G_{ij} = \boldsymbol{G_i} \cdot \boldsymbol{G_j}$ σαν $G_{\alpha\beta} = \boldsymbol{G_\alpha} \cdot \boldsymbol{G_\beta}$, $G_{\alpha 3} = G_{3\alpha} = 0$ και $G_{33} = 1$. Τα αντι-διακυμαινόμενα διανύσματα βάσης ορίζονται από την εξής ιδιότητα $\boldsymbol{G^i} \cdot \boldsymbol{G_j} = \delta^i{}_j$. Μπορούν να υπολογισθούν συναρτήσει των αντι-διακυμαινόμενων μετρικών συνιστωσών $G^{\alpha\beta}$ από τη σχέση $\boldsymbol{G^\alpha} = G^{\alpha\beta} \boldsymbol{G_\beta}$ και $\boldsymbol{G^3} = \boldsymbol{G_3}$ όπου οι συνιστώσες $[G^{\alpha\beta}] = [G_{\alpha\beta}]^{-1}$ δίνονται από μία αντιστροφή μητρώου.

Στη συνέχεια ορίζεται μία βοηθητική καρτεσιανή βάση, για την κατάσταση αναφοράς, η οποία είναι στατική και δεν ακολουθεί την παραμόρφωση του φορέα.

$$\boldsymbol{E_1} = \frac{\boldsymbol{G_1}}{|\boldsymbol{G_1}|} \qquad \boldsymbol{E_2} = \frac{\boldsymbol{G_1} - (\boldsymbol{G_2} \cdot \boldsymbol{E_1})\boldsymbol{E_1}}{|\boldsymbol{G_1} - (\boldsymbol{G_2} \cdot \boldsymbol{E_1})\boldsymbol{E_1}|} \qquad \boldsymbol{E_3} = \boldsymbol{A_3} \qquad (43)$$

Ορίζεται επίσης μία τοπική καρτεσιανή βάση για την παραμορφωμένη κατάσταση η οποία ακολουθεί πλήρως την μέση επιφάνεια του κελύφους στην οποία τα δύο της διανύσματα είναι εφαπτόμενα.

$$\boldsymbol{e_1} = \frac{\boldsymbol{g_1}}{|\boldsymbol{g_1}|} \qquad \boldsymbol{e_2} = \frac{\boldsymbol{g_1} - (\boldsymbol{g_2} \cdot \boldsymbol{e_1})\boldsymbol{e_1}}{|\boldsymbol{g_1} - (\boldsymbol{g_2} \cdot \boldsymbol{e_1})\boldsymbol{e_1}|} \qquad \boldsymbol{e_3} = \boldsymbol{a_3} \qquad (44)$$

Η βαθμίδα της παραμόρφωσης (deformation gradient) DG ορίζεται ως εξής

$$F_N = g_i \otimes G^i \tag{45}$$

και μπορεί να αναλυθεί σε δυο συνεισφορές μία μεμβρανική και μία καμπτική

$$F = F_S + F_N \tag{46}$$

όπου $F_S = g_a \otimes G^a$ και όπου $F_N = g_3 \otimes G^3$. Είναι ένας τανυστής δύο σημείων και μπορεί να εκφρασθεί με χρήση των δύο προηγούμενων βάσεων ως εξής

$$F = F^{ij} e_i \otimes E_j \tag{47}$$

Η έκφραση αυτή επιλέγεται διότι συγκεντρώνει τη συνεισφορά του μεμβρανικού μέρους σε ένα μητρώο 2x2 $[F^{\alpha\beta}]$ ενώ όπως φαίνεται με αντικατάσταση των σχέσεων (42)(43) και (44) οι συνιστώσες $F^{\alpha 3} = F^{3a} = 0$. Τέλος, προκύπτει $F^{33} = 1$ καθώς προς το παρόν έχει αμεληθεί η εκτός επιπέδου αξονική παραμόρφωση λ_N η τελική τιμή της οποίας προκύπτει από την απόκριση του υλικού.

○Για την έκφραση των εξισώσεων ισορροπίας τόσο στη μικροκλίμακα όσο και στη μακροκλίμακα, με τη θεώρηση μεγάλων μετακινήσεων και στροφών, χρησιμοποιούνται οι κατάλληλοι τανυστές παραμόρφωσης και τάσης, και γίνεται επαναδιατύπωση της Αρχής των Δυνατών Έργων, των σχέσεων μεσοστάθμισης των εντατικών μεγεθών και της συνθήκης μακροομοιογένειας.

Αγνοώντας, τις αδρανειακές δυνάμεις, θεωρούμε ότι το RVE, βρίσκεται σε στατική ισορροπία:

$$\nabla \cdot P_m = 0 \tag{48}$$

Η παραμόρφωση του συνδέεται με τη μακροσκοπική παραμόρφωση μέσω μίας σχέσης μεσοστάθμισης του τανυστή παραμορφώσεων

$$\tag{49}$$
$$F = F_M := \frac{1}{V_{RVE}} \int_{V_{RVE}} F_m \, dV$$

όπου ο δείκτης m χαρακτηρίζει μικροδομικές ποσότητες και ο δείκτης M συμβολίζει μικροσκοπικές σταθμισμένες ποσότητες. Αυτή η παραδοχή ισοδυναμεί με περιορισμό για όλες τις συνιστώσες της βαθμίδας της παραμόρφωσης (DG) εκτός από την F^{33}. Για αυτήν την συνιστώσα, η σχέση μεσοστάθμισης αξιοποιείται, για τον υπολογισμό της τιμής της, μετά τη λύση του μικροδομικού προβλήματος συνοριακών τιμών. Για να ικανοποιηθούν αυτοί οι περιορισμοί κατάλληλες συνοριακές συνθήκες επιβάλλονται στο RVE. Συγκεκριμένα, επιλέγοντας επιβαλλόμενες μετακινήσεις ('linear displacements'), για να επιβληθεί ή σχέση $F^{\alpha\beta} = F_M^{\alpha\beta}$ απαιτείται για τους περιφερειακούς κόμβους του RVE να ισχύει

$$\hat{x}_m = \hat{F} \cdot \hat{X}_m \tag{50}$$

όπου η $\hat{F} = F^{\alpha\beta} e_a \otimes E_\beta$ είναι το εντός επιπέδου μέρος του DG και $\hat{x}_m = x_1 e_1 + x_2 e_2$ και $\hat{X}_m = X_1 E_1 + X_2 E_2$ τα εφαπτόμενα στη μέση επιφάνεια μέρη των διανυσμάτων κατεύθυνσης στην τρέχουσα κατάσταση και την κατάσταση αναφοράς του φορέα. Εναλλακτικά περιοδικές συνοριακές συνθήκες ('Periodic boundary conditions') μπορούν να επιλεγούν. Συγκεκριμένα μπορεί να εφαρμοσθεί η σχέση $\hat{x}_m^+ - \hat{x}_m^- = \hat{F}(\hat{X}_m^+ - \hat{X}_m^-)$ για τη σχετική μετακίνηση αντίστοιχων κόμβων σε απέναντι περιφερειακά μέτωπα του RVE.

Για τις εκτός επιπέδου διατμητικές συνιστώσες $F_M^{3\alpha}$, αρκεί να επιβληθεί για κάθε περιφερειακό κόμβο του RVE η εκτός επιπέδου μετακίνηση του να ισούται με αυτήν του αντίστοιχου κόμβου στο απέναντι μέτωπο το RVE

$$\tilde{x}^+ - \tilde{x}^- = 0 \tag{51}$$

Αντίστοιχες συνοριακές συνθήκες χρησιμοποιούνται και για την επιβολή του περιορισμού $F_M^{\alpha 3} = 0$. Αντικαθιστώντας τις σχέσεις (51) και (50) στην (49) γίνεται φανερό ότι αυτή πληρείται.

Η δεύτερη σχέση μεσοστάθμισης αφορά τον τανυστή τάσεων 'First Piola Kirchhoff' (FPK) και διατυπώνεται ως εξής

$$\boldsymbol{P} = \boldsymbol{P_M} := \frac{1}{V_{RVE}} \int_{V_{RVE}} \boldsymbol{P_m}\, dV \;=\; \frac{1}{V_{RVE}} \int_{\Gamma_{RVE}} \boldsymbol{p} \otimes \boldsymbol{X_m}\, d\Gamma \tag{52}$$

όπου $\boldsymbol{p} = \boldsymbol{N} \cdot \boldsymbol{P_m}$ είναι το κάθετο στο σύνορο διάνυσμα έλξεων. Για τα το τελευταίο μέρος της εξίσωσης (52) έχει χρησιμοποιηθεί το θεώρημα απόκλισης, η σχέση (48) και το γεγονός ότι $\nabla \cdot \boldsymbol{X_m} = \boldsymbol{I}$. Αυτή η σχέση, αξιοποιείται για την μετάβαση από τη μικροκλίμακα στη μακροκλίμακα. Ο ομογενής περιορισμός (51) προκαλεί αντιπεριοδικές έλξεις μεταξύ απέναντι μετώπων του RVE [57,58] στα οποία εφαρμόζεται. Οι συνεισφορές αυτών των έλξεων αλληλοαναιρούνται και συνολικά δεν προκύπτει συνεισφορά στο μακροσκοπικό έργο για τις συνιστώσες $P^{\alpha 3}$ και $P^{3\alpha}$.

Κανένας περιορισμός σχετικός με την εκτός επιπέδου εφελκυστική παραμόρφωση του RVE δεν έχει επιβληθεί στο RVE, βάσει της παραδοχής επίπεδης έντασης για τη μικροδομή και γι' αυτό η συνιστώσα $P_M^{33} = 0$. Περισσότερες λεπτομέρειες για τον υπολογισμό των εντός επιπέδου συνιστωσών P_M^{33} του μακροσκοπικού τανυστή FPK, στο πλαίσιο μιας διακριτοποίησης του μικροδομικού προβλήματος δίνονται στη συνέχεια.

Αντικαθιστώντας τις σχέσεις για (49)(52) για τα μεσοσταθμικά μεγέθη και τις συνοριακές συνθήκες (50) γίνεται φανερό ότι η συνθήκη μακρομοιογένειας (53) ισχύει

$$\frac{1}{V_{RVE}} \int_{V_{RVE}} \boldsymbol{P_m} : \delta \boldsymbol{F_m^T}\, dV_0 = \boldsymbol{P_M} : \delta \boldsymbol{F_M^T} \quad \forall \delta \boldsymbol{x} \tag{53}$$

και η μεταβολή του μακροσκοπικού δυνατού έργου ισούται με τη μέση τιμή του δυνατού έργου της μικροδομής.

○Στη συνέχεια στα πλαίσια της επίλυσης του μικροδομικού προβλήματος με πεπερασμένα στοιχεία, χωρίζουμε τους β.ε. που προκύπτουν από τη διακριτοποίηση του προβλήματος, σε αυτούς που είναι ελεύθεροι και συμβολίζονται με 'a', σε αυτούς που συμμετέχουν σε περιορισμούς επιβολής μετακίνησης και προέρχονται από την εξίσωση (51) και συμβολίζονται με 'b' και σε αυτούς που εμπλέκονται σε περιορισμούς που προέρχονται από την εξίσωση (51) και συμβολίζονται με 'c'. Αυτή η ομαδοποίηση αφορά τους εναπομείναντες β.ε. μετά τη δέσμευση των κινήσεων ελευθέρου στερεού του RVE. Χρησιμοποιώντας πολλαπλασιαστές Lagrange για την επιβολή των ανωτέρω περιορισμών, η λύση πεπερασμένων στοιχείων του μικροδομικού προβλήματος συνοριακών τιμών περιγράφεται από τις εξής μη γραμμικές αλγεβρικές εξισώσεις

$$f_a(x) = 0 \tag{a}$$
$$f_b(x) = \delta \tag{b}$$
$$x_b - D^T F = 0 \tag{c}$$

(54)

$$f_c(x) - P^T \pi = 0 \qquad \text{(d)}$$
$$P x_c = 0 \qquad \text{(e)}$$

όπου η εξίσωση (54)-c είναι η διακριτοποιημένη μορφή της (50) και το μητρώο D προκύπτει από επιμέρους μητρώα D_q που δίνονται για κάθε node p από τη σχέση

$$[x_b] = \begin{bmatrix} x_1 \\ x_2 \end{bmatrix} = [D_p^T][F] = [\begin{bmatrix} X_1 & 0 & X_2 & 0 \\ 0 & X_2 & 0 & X_1 \end{bmatrix} \begin{bmatrix} F^{11} \\ F^{22} \\ F^{12} \\ F^{21} \end{bmatrix} \qquad \textbf{(55)}$$

όπου οι συντεταγμένες x_1, x_2 και X_1, X_2 αναφέρονται στο τοπικό καρτεσιανό σύστημα του RVE το οποίο ταυτίζεται με το σύστημα συντεταγμένων που ακολουθεί πλήρως τη μέση επιφάνεια του κελύφους (44). Η αρχή αυτού του τοπικού συστήματος συντεταγμένων τοποθετείται για την απλοποίηση των υπολογισμών στο γεωμετρικό κέντρο του RVE. Το μητρώο B, ομοίως συγκεντρώνει επιμέρους συνεισφορές προσημασμένων 'Boolean' μητρώων B_P που αναφέρονται σε ζεύγη σημείων τα οποία αντιστοιχούν στον περιορισμό (51)

$$B_b = [0 \quad \cdots \quad 1 \quad \cdots \quad 0 \quad | \quad 0 \quad \cdots \quad -1 \quad \cdots \quad 0] \qquad \textbf{(56)}$$

Παίρνουν την τιμή $\neq 0$ για τους αντίστοιχους β.ε. που εξισώνονται κατά τον περιορισμό (51). Η πρώτη διάσταση του συνολικού μητρώου B ισούται με το συνολικό αριθμό των περιορισμών αυτού του είδους. Για την απλούστευση των υπολογισμών στο μητρώο K_{cc}, αριθμούνται πρώτα οι βαθμοί ελευθερίας 'c' που συμμετέχουν με θετικό πρόσημο σε αυτούς τους περιορισμούς.

Σε μία επαναληπτική διαδικασία Newton Raphson, η οποία ξεκινά από μία γνωστή θέση ισορροπίας όπου οι εξισώσεις (54) ισχύουν, εφαρμόζεται μία προσαύξηση ΔF στην μακροσκοπική παραμόρφωση η οποία ισοδυναμεί σε μία προσαύξηση Δx_b στο διάνυσμα x_b της τελικής θέσης των β.ε. 'b' και ακολούθως στα διανύσματα x_a, x_c, δ και π, οι τελικές τιμές των οποίων διορθώνονται επαναληπτικά, χρησιμοποιώντας την παρακάτω γραμμικοποίηση των σχέσεων (54), εώς ότου αυτές πληρούνται ξανά και έχει βρεθεί η νέα θέση ισορροπίας.

$$f_a(x) + K_{aa}\Delta x_a + K_{ab}\Delta x_b + K_{ac}\Delta x_c = 0 \qquad \text{(a)} \qquad \textbf{(57)}$$
$$f_b(x) - \delta + K_{ba}\Delta x_a + K_{bb}\Delta x_b + K_{bc}\Delta x_c - \Delta\delta = 0 \qquad \text{(b)}$$
$$x_b - D^T F + \Delta x_b - D^T \Delta F = 0 \qquad \text{(c)}$$
$$f_c(x) - P^T \pi + K_{ca}\Delta x_a + K_{cb}\Delta x_b + K_{cc}\Delta x_c - P^T \Delta\pi = 0 \qquad \text{(d)}$$
$$P x_c + P \Delta x_c = 0 \qquad \text{(e)}$$

Στη συνέχεια υιοθετείται ένας μετασχηματισμός βάσης για κάθε ζεύγος β.ε. από τους 'c' ώστε να αποφευχθεί ο υπολογισμός των πολλαπλασιαστών Lagrange π.

$$[\hat{u}_c] = \begin{bmatrix} \hat{u}_{c1}^p \\ \hat{u}_{c2}^p \end{bmatrix} = [T_p^T]\begin{bmatrix} u_c^+ \\ u_c^- \end{bmatrix} \qquad \text{(a)} \qquad \textbf{(58)}$$

$$[T_p^T] = \begin{bmatrix} T_1^p \\ T_2^p \end{bmatrix} = \begin{bmatrix} \frac{\sqrt{2}}{2} & -\frac{\sqrt{2}}{2} \\ \frac{\sqrt{2}}{2} & \frac{\sqrt{2}}{2} \end{bmatrix} \qquad \text{(b)}$$

Κάθε ένας από τους περιορισμούς (57)-e μπορεί ισοδύναμα να εφαρμοσθεί θέτοντας τον αντίστοιχο βαθμό β.ε. $\hat{u}_{c1}^p = 0$. Η δεύτερη γραμμή του πίνακα προκύπτει από μία διαδικασία ορθογωνιοποίησης Gram-Schmidt. Επίσης πρέπει να παρατηρηθεί ότι

$$T_1^p B_p^T \neq 0 \tag{59}$$
$$T_2^p B_p^T = 0$$

Οι εξισώσεις (58) και (59) σε καθολικό επίπεδο ως εξής

$$[\hat{u}_c] = \begin{bmatrix} \hat{u}_{c1} \\ \hat{u}_{c2} \end{bmatrix} = \begin{bmatrix} T_1 \\ T_2 \end{bmatrix} [u_c] = [T^T][u_c] \tag{60} \quad \text{(a)}$$

$$T^T B^T = \begin{bmatrix} T_1 \\ T_2 \end{bmatrix} [B^T] = \begin{bmatrix} B'^T \\ 0 \end{bmatrix} \quad \text{(b)}$$

Με τη χρήση της (60)-b, η σχέση (57)-d μετασχηματίζεται ως εξής

$$T_1(f_c(x) + K_{ca}\Delta x_a + K_{cb}\Delta x_b) - T_1 K_{cc}(T_1^T \hat{u}_{c1} + T_2^T \hat{u}_{c2}) - T_1 B^T(\lambda + \Delta\lambda) = 0 \quad \text{(a)} \tag{61}$$
$$T_2(f_c(x) + K_{ca}\Delta x_a + K_{cb}\Delta x_b) - T_2 K_{cc}(T_1^T \hat{u}_{c1} + T_2^T \hat{u}_{c2}) = 0 \quad \text{(b)}$$

Η εξίσωση (57)-e αντικαθίσταται από την εξίσωση $\hat{u}_{c1} = 0$ η οποία αντικαθίσταται ευθέως στην μετασχηματισμένη μορφή των εξισώσεων (57)-a,b και (a) (61)-b δίνοντας την τελική μορφή των γραμμικοποιημένων εξισώσεων ως εξής

$$f_a(x) + K_{aa}\Delta x_a + K_{ab}\Delta x_b + K_{ac}T_2^T \hat{u}_{c2} = 0 \quad \text{(a)} \tag{62}$$
$$f_b(x) - \delta + K_{ba}\Delta x_a + K_{bb}\Delta x_b + K_{bc}T_2^T \hat{u}_{c2} - \Delta\delta = 0 \quad \text{(b)}$$
$$T_2(f_c(x) + K_{ca}\Delta x_a + K_{cb}\Delta x_b) - T_2 K_{cc}T_2^T \hat{u}_{c2} = 0 \quad \text{(c)}$$

Για δεδομένο προσαυξητικό βήμα ΔF στην μακροσκοπική παραμόρφωση αντίστοιχη προσαύξηση Δx_b που υπολογίζεται από την εξίσωση (57)-c οι τιμές των στα διανύσματα x_a, u_c πλέον διορθώνονται επαναληπτικά με χρήση των μετασχηματισμένων εξισώσεων (62)-a,c έως ότου $|\{f_a^T|(T_2 f_2)^T\}| < tol$. Τότε μπορεί να χρησιμοποιηθεί η διακριτοποιημένη μορφή της εξίσωσης (52) η οποία δίνεται ως εξής

$$[P] = \begin{bmatrix} P^{11} \\ P^{22} \\ P^{12} \\ P^{21} \end{bmatrix} = \frac{1}{V_{RVE}} D\delta = \frac{1}{V_{RVE}} Df_b \tag{63}$$

Τέλος για μία απειροστή προσαύξηση ΔF γύρω από μία γνωστή θέση ισορροπίας όπου εξισώσεις (54)a-e ισχύουν, χρησιμοποιώντας την (57)-c και συμπυκνώνοντας στατικά τις εξισώσεις (62)a και c στην εξίσωση (62)b λαμβάνεται η εξής σχέση

$$\Delta\delta = K'_{bb} D^T \Delta F \tag{64}$$

η οποία επακολούθως δίνει

$$\Delta P = \frac{1}{V_{RVE}} DK'_{bb} D^T \Delta F \tag{65}$$

συνεπώς οι συνιστώσες του τανυστή ελαστικότητας δίνονται σε μητρωική μορφή ως εξής

$$\mathcal{A} = \frac{1}{V_{RVE}} DK'_{bb} D^T \Delta F \tag{66}$$

Είναι σημαντικό να σημειωθεί για τους υπολογισμούς που ακολουθούν ότι οι απειροστές προσαυξήσεις ΔP και ΔF που χρησιμοποιούνται στις παραπάνω σχέσεις αναφέρονται σε συνιστώσες των τανυστών P και F σε συγκεκριμένες βάσεις που έχουν ορισθεί προηγουμένως και η σχέση (66) αναφέρεται συγκεκριμένα στις συνιστώσες αυτές και δεν αποτελεί μία γενική σχέση για την συνολική έκφραση των δύο τανυστών.

○Η ισορροπία στο μακροσκοπικό επίπεδο διέπεται από την Αρχή των Δυνατών Έργων η οποία με τη χρήση της συνθήκης μακροομοιογένειας (53) λαμβάνει την εξής μορφή

$$\delta W = \delta W_{int} - \delta W_{ext} \qquad \text{(a)} \qquad \textbf{(67)}$$

$$\delta W_{int} = \int_{V_0} \delta \boldsymbol{F}^T : \boldsymbol{P_M} \, dV_0 \qquad \text{(b)}$$

Μία λύση πεπερασμένων στοιχείων βασισμένη στην παραπάνω μεταβολική διατύπωση απαιτεί C^1 συνέχεια των για τις χρησιμοποιούμενες συναρτήσεις σχήματος [59]. Η σχέση αυτή πρέπει να ισχύει για μια μεταβολή σε οποιοδήποτε β.ε. που προκύπτει από τη διακριτοποίηση του πεδίου των μετακινήσεων, και έτσι προκύπτει η έκφραση της ισορροπίας εσωτερικών και εξωτερικών επικόμβιων δράσεων

$$R = F_{int} - F_{ext} \qquad \text{(a)} \qquad \textbf{(68)}$$

$$F_{int}^{u_r} = \int_{V_0} \frac{\partial \boldsymbol{F}^T}{\partial u_r} : \boldsymbol{P_M} \, d\Omega_0 \qquad \text{(b)}$$

Για να αξιοποιηθούν στην παραπάνω σχέση (68)-b, εξισώσεις οι οποίες έχουν εξαχθεί προηγουμένως αυτή ξαναγράφεται ως εξής

$$F_{int}^{u_r} = \int_{V_0} (\boldsymbol{G}^i \otimes \boldsymbol{g}_{i,u_r}) : (P^{jk} \boldsymbol{E}_j \otimes \boldsymbol{e}_k) \, d\Omega_0 \qquad \textbf{(69)}$$

όπου έχει χρησιμοποιηθεί ότι $\delta \boldsymbol{F} = (\boldsymbol{g}_{i,u_r} \otimes \boldsymbol{G}^i)\delta u_r$.

Η σχέση (68)-a αποτελεί ένα σύστημα μη γραμμικών εξισώσεων που γραμμικοποιούνται ώστε να επιλυθούν με μία επαναληπτική διαδικασία Newton Raphson. Το εφαπτομενικό μητρώο δυσκαμψίας των (των εσωτερικών δράσεων) δίνεται από την εξής σχέση

$$K_{rs}^{int} = \int_{V_0} \frac{\partial^2 \boldsymbol{F}^T}{\partial u_r \partial u_s} : \boldsymbol{P_M} + \frac{\partial \boldsymbol{F}^T}{\partial u_r} : \frac{\partial \boldsymbol{P_M}}{\partial u_s} \, d\Omega_0 = \int_{V_0} (\boldsymbol{G}^i \otimes \boldsymbol{g}_{i,rs}) : \boldsymbol{P_M} + (\boldsymbol{G}^i \otimes \boldsymbol{g}_{i,r}) : \boldsymbol{P}_{\boldsymbol{M},s} d\Omega_0 \qquad \textbf{(70)}$$

Όπου με τη χρήση της σχέσης

$$(P^{ij} \boldsymbol{E}_i \otimes \boldsymbol{e}_j)_{,s} = P_{,s}^{ij} \boldsymbol{E}_i \otimes \boldsymbol{e}_j + P^{ij} (\boldsymbol{E}_i \otimes \boldsymbol{e}_j)_{,s} = A_{ijkl}(F_{,s}^{kl}) \boldsymbol{E}_i \otimes \boldsymbol{e}_j + P^{ij}(\boldsymbol{E}_i \otimes \boldsymbol{e}_{j,s}) \qquad \textbf{(71)}$$

μπορούν να χρησιμοποιηθούν οι συνιστώσες του τανυστή ελαστικότητας A_{ijkl} που δίνονται από τη σχέση (66). Γι' αυτήν τη σχέση έχει ληφθεί υπόψη ότι μόνο η μεταβολή μιας βάσης που ακολουθεί την παραμόρφωση του φορέα είναι διάφορη του μηδέν $\delta \boldsymbol{e}_{i,u_r} \neq 0$. Περισσότερες λεπτομέρειες για τον υπολογισμό των μεταβολών $\boldsymbol{g}_{i,r}$, $\boldsymbol{g}_{i,rs}$, $F_{,s}^{kl}$ και $\boldsymbol{e}_{j,s}$ δίνονται στο παράρτημα.

●Μία από τις βασικότερες εφαρμογές της ανάλυσης φορέων σε πολλαπλές κλίμακες αποτελεί η μελέτη των ιδιοτήτων νανοσύνθετων υλικών μέσω της λεπτομερούς μοντελοποίησης της μικροδομής τους . Μία νέα γενιά νανοσύνθετων υλικών με εγκλείσματα που έχουν ως βάση τον άνθρακα, όπως το γραφένιο (Graphene) και οι νανοσωλήνες άνθρακα (Carbon Nano Tubes CNTs) παρουσιάζουν εξαιρετικές μηχανικές ιδιότητες ακόμη και όταν οι προσμείξεις αυτές χρησιμοποιούνται σε πολύ μικρές περιεκτικότητες.

Οι τεχνικές υπολογιστικής ομογενοποίησης χρησιμοποιούνται σε δύο στάδια στην προσομοίωση νανοσύνθετων πολυμερών υλικών με εγκλείσματα γραφενίου. Αφενός μία ιεραρχική προσέγγιση ομογενοποίησης ακολουθείται για τον προσδιορισμό των ιδιοτήτων ενός επιφανειακού φορέα με ιδιότητες ισοδύναμες με αυτές των φύλλων γραφενίου. Αφετέρου η πρώτης τάξης θεωρία υπολογιστικής ομογενοποίησης ακολουθείται για την ταυτόχρονη ανάλυση σε δύο κλίμακες του συνολικού νανοσύνθετου υλικού που περιλαμβάνει το γραφένιο μαζί με τη πολυμερική μήτρα και το θεωρούμενο νόμο διεπαφής.

Προτείνεται επίσης μία γενικευμένη μεθοδολογία προσομοίωσης νανοσύνθετων υλικών βασισμένη στο συνδυασμό της τεχνικής ενσωμάτωσης διαφορετικών τύπων στοιχείων και στα πεπερασμένα στοιχεία διεπαφής. Η μεθοδολογία αυτή επιτρέπει την δημιουργία μοντέλων RVE, για νανοσύνθετα υλικά με τους προαναφερθέντες τύπους

εγκλεισμάτων, και είναι ιδιαίτερα αποτελεσματική καθώς απαιτεί μειωμένο αριθμό β.ε. σε σχέση με τις συμβατικές μεθόδους διακριτοποίησης, χωρίς να υπεισέρχεται κάποια απλοποιητική παραδοχή στην ανάλυση.

○Το γραφένιο είναι ένα αναδυόμενο υλικό που έχει προσελκύσει τεράστιο επιστημονικό ενδιαφέρον λόγω των εξαιρετικών μηχανικών και ηλεκτρικών ιδιοτήτων του. Είναι ένα αλλότροπο άνθρακα, το οποίο σχηματίζει ένα εξαγωνικό κυψελωτό πλέγμα που μπορεί να έχει πάχος ενός ατόμου, γνωστό ως μονοστρωματικό φύλλο γραφενίου (SLGS) που συντίθεται με διάφορες μεθόδους [60-62]. Το γραφένιο έχει βρεθεί ότι είναι το ισχυρότερο υλικό που έχει δοκιμαστεί ποτέ [63-64] με συντελεστή Young 1 TPa και αντοχή σε εφελκυσμό 130 GPa, καθιστώντας το ένα πολλά υποσχόμενο υλικό για δομικές εφαρμογές. Τα φύλλα γραφενίου (GS) και τα παράγωγά του προϊόντα, οι νανοσωλήνες άνθρακα (CNT), έχουν χρησιμοποιηθεί επιτυχώς ως υλικά πλήρωσης σε νονανοσύνθετα υλικά [65, 66], ενισχύοντας σημαντικά τις μηχανικές ιδιότητες της μήτρας. Οι επιτυχημένες εφαρμογές περιλαμβάνουν σύνθετα υλικά τόσο μεταλλικής μήτρας [67, 68] όσο και πολυμερούς μήτρας [69, 70]. Στη συνέχεια παρουσιάζεται μία μεθοδολογία για τη μοντελοποίηση της μηχανικής συμπεριφοράς και των ιδιοτήτων των νανοσύνθετων γραφενίου σε πολλαπλές κλίμακες. Δύο ξεχωριστά σημεία στη διαδικασία μοντελοποίησης των νανοσύνθετων γραφενίου παρουσιάζονται λεπτομερώς, πρώτα η μέθοδος προσομοίωσης του γραφενίου και στη συνέχεια ο μηχανισμός μεταφοράς φορτίου μεταξύ της μήτρας και του εγκλείσματος.

Οι μέθοδοι μοντελοποίησης που διατίθενται σήμερα για την προσομοίωση της μηχανικής συμπεριφοράς του γραφενίου, λαμβάνουν υπόψη τις διατομικές αλληλεπιδράσεις μεταξύ των ατόμων άνθρακα στο εξαγωνικό πλέγμα. Οι υπολογιστικές μέθοδοι που χρησιμοποιούνται ευρέως, μπορούν γενικά να ταξινομηθούν σε δύο κατηγορίες: i) στην μοριακή μοντελοποίηση [71, 72] με κυριότερες υποκατηγορίες τις μεθόδους μοριακής μηχανικής και την προσομοίωση ab-initio και ii) τις προσεγγίσεις της μηχανικής συνεχούς μέσου [73-75] συμπεριλαμβανομένης της ανάλυσης με πεπερασμένα στοιχεία. Κάθε μία από τις παραπάνω μεθόδους, συνοδεύεται από διαφορετικές επιδόσεις ανάλογα με την κλίμακα του χρόνου και του μεγέθους της μοντελοποίησης. Οι τεχνικές Ab-initio και οι τεχνικές μοριακής μηχανικής παρέχουν γενικά υψηλή ακρίβεια, αλλά λόγω του υψηλού υπολογιστικού κόστους που τις χαρακτηρίζει, είναι κατάλληλες για μοντέλα μικρού μεγέθους και για μικρές χρονικές περιόδους [75, 76] Από την άλλη πλευρά, οι τεχνικές συνεχούς μέσου είναι ικανοποιητικά ακριβείς και υπολογιστικά αποδοτικές για μεγαλύτερα μοντέλα και προσομοιώσεις χρονικά μεγαλύτερες.

Η κύρια αρχή πίσω από τις προσεγγίσεις μηχανικής συνεχούς, που συνήθως αναφέρονται ως μέθοδοι Molecular Structural Mechanics (MSM), είναι η προσομοίωση των ομοιοπολικών δεσμών μεταξύ των ατόμων άνθρακα, με ισοδύναμα δομικά πεπερασμένα στοιχεία [76]. Οι ιδιότητες αυτών των πεπερασμένων στοιχείων μπορούν να υπολογιστούν αναλυτικά κάνοντας χρήση κριτηρίων ισοδύναμης ενέργειας παραμόρφωσης, για τη θεωρούμενη κάθε φορά διατύπωση του δυναμικού (force field) της διατομικής αλληλεπίδρασης. Κατά την πιο διαδεδομένη μέθοδο, οι ομοιοπολικοί δεσμοί άνθρακα αντικαθίστανται με πεπερασμένα στοιχεία δοκού, με τα οποία μπορεί να προσομοιωθεί κατάλληλα η απομάκρυνση των ατόμων και οι αλλαγές στη γωνία των μεταξύ τους δεσμών. Ενώ αυτή η προσέγγιση ενέχει μικρότερο υπολογιστικό κόστος και είναι αρκετά ακριβής σε σύγκριση με τις μοριακές προσομοιώσεις [76-79], και για αυτήν όμως το υπολογιστικό κόστος αυξάνεται δραματικά για μεγαλύτερες κλίμακες στο χρόνο και το μέγεθος της προσομοίωσης. Για το λόγο αυτό, η εσχάρα των πεπερασμένων στοιχείων δοκού μπορεί να αντικατασταθεί με ένα ισοδύναμο αραιό πλέγμα πεπερασμένων στοιχείων, με τελικό στόχο την δημιουργία ενός μοντέλου με σημαντικά λιγότερους βαθμούς ελευθερίας (dofs) αλλά με ικανοποιητική ακρίβεια. Ο τύπος των πεπερασμένων στοιχείων που χρησιμοποιούνται στο υποκατάστατο αυτό μοντέλο εξαρτώνται από τη συνολική γεωμετρία του νανο-σωματιδίου. Για παράδειγμα, για την προσομοίωση της μηχανικής συμπεριφοράς των CNT που έχουν γραμμική διαμόρφωση, το αντίστοιχο MSM μοντέλο τους υποκαθίσταται με ισοδύναμα στοιχεία δοκού (EBE) κάθε ένα από τα οποία αντιστοιχεί σε τμήμα του MSM πλέγματος πεπερασμένων στοιχείων[80-82]. Τα μοντέλα που προκύπτουν έχουν λιγότερα πεπερασμένα στοιχεία και επιτρέπουν προσομοιώσεις μεγαλύτερης κλίμακας μεγέθους ή χρόνου.

Στην παρούσα εργασία η ανωτέρω τεχνική εφαρμόζεται για τη μοντελοποίηση σε πολλαπλές κλίμακες φύλλων γραφενίου (Graphene Sheets) με αραιά μοντέλα συνεχούς μέσου. Τα μεγάλα σε μέγεθος GSs συμπεριφέρονται σαν κελύφη, σε αντίθεση με τα CNT που προσομοιάζουν δοκούς. Χρησιμοποιούνται λοιπόν ισοδύναμα στοιχεία κελύφους (ESE) που για τη δημιουργία ενός μοντέλου υποκατάστατου των αντίστοιχων λεπτομερών μοντέλων μοριακής μηχανικής MSM. Το ESE πρέπει να είναι σε θέση να αντιπροσωπεύει με ακρίβεια τόσο τη μεμβρανική όσο και την καμπτική συμπεριφορά της πλάκας του GS. Εάν πληρείται αυτή η απαίτηση, τότε αυτό το ESE μπορεί να ενσωματωθεί σε ένα τρισδιάστατο μοντέλο της πολυμερικής μήτρας πολυμερούς, διαμορφώνοντας έτσι ένα RVE κατάλληλο για τη μελέτη της συνολικής μηχανικής συμπεριφοράς του νανοσύνθετου. Ο μηχανισμός μεταφοράς φορτίου μεταξύ της μήτρας και του εγκλείσματος επηρεάζει σημαντικά τις μηχανικές ιδιότητες του συνολικού νανοσύνθετου υλικού. Οι αριθμητικές προσομοιώσεις υποδεικνύουν ότι η δυσκαμψία και η αντοχή της διεπιφάνειας, καθορίζουν το άνω όριο της επιτευκτής μηχανικής ενίσχυσης του νανοσύνθετου για το συγκεκριμένο έγκλεισμα και την ολίσθηση που εμφανίζεται όταν προκύπτει αστοχία [80,83]. Γι' αυτούς τους λόγους έχουν προταθεί διάφορες τεχνικές χημικής διεργασίας για ενίσχυση της συνοχής μεταξύ της μήτρας και του εγκλείσματος [84, 85]. Για προσομοίωση της απόκρισης της διεπιφάνειας, μοντέλα τριβής έχουν ήδη εφαρμοστεί με επιτυχία στη μοντελοποίηση νανοσύνθετων CNT [80, 86]. Στην παρούσα μελέτη, η διεπιφάνεια μοντελοποιείται σαν μία συνεκτική ζώνη (Cohesive zone model CZM) μεταξύ του ESE και της τρισδιάστατης μήτρας. Η συνεκτική συμπεριφορά ορίζεται μέσω ενός καταστατικού νόμου έλξης-ολίσθησης μεταξύ των δύο με μία εκ των προτέρων γνωστή μη γραμμική συμπεριφορά. Τα πεπερασμένα στοιχεία συνεκτικής ζώνης (Cohesive zone elements CZE) έχουν εφαρμοστεί με επιτυχία για τη προσομοίωση φαινομένων αποκόλλησης και διαχωρισμού σύνθετων ή νανοσύνθετων υλικών [87] καθώς και σε περιπτώσεις μοντελοποίησης ενισχυμένου χάλυβα [88], επιτυγχάνοντας επαρκή σύμπτωση με τα πειραματικά δεδομένα και ως εκ τούτου επιλέγονται σε αυτήν τη μελέτη για τη μοντελοποίηση αυτής της ενδιάμεσης ζώνης διεπαφής .

o Στη συνέχεια θα εστιάσουμε σε κάθε ένα από τα παραπάνω βήματα της μεθοδολογίας ξεκινώντας από τις προσομοιώσεις MSM των φύλλων γραφενίου και τον προσδιορισμό των ιδιοτήτων του ισοδύναμου αδρού μοντέλου κελύφους.

Τα φύλλα γραφενίου (GS) μπορούν να θεωρηθούν σαν μεγάλα μόρια που αποτελούνται από άτομα άνθρακα σε ένα εξαγωνικό κυψελωτό πλέγμα. Κατά την προσέγγιση MSM, η κίνηση των πυρήνων των ατόμων άνθρακα εξαρτάται από τις αλληλεπιδράσεις ηλεκτρονίου-πυρήνα και πυρήνα-πυρήνα [89]. Μια αναπαράσταση ενός εξαγωνικού δικτυωτού πλέγματος GS φαίνεται στην Εικόνα 3. Οι συνολικές δυνάμεις πεδίου που καθορίζουν την αλληλεπίδραση των ατόμων άνθρακα προκύπτουν από την θεωρούμενη δυναμική ενέργεια αλληλεπίδρασης (potential energy), η έκφραση της οποίας παρουσιάζει άμεση ομοιότητα με την διατύπωση της ελαστικής ενέργειας παραμόρφωσης των στοιχείων δοκού. Μια λεπτομερής περιγραφή της προσέγγισης MSM μπορεί να βρεθεί στο έργο των Li και Chou [76] που αρχικά πρότειναν το μοντέλο, υποθέτοντας ένα στοιχείο δοκού κυκλικής διατομής. Όμως η παραδοχή ότι οι εντός και εκτός επιπέδου καμπτικές δυσκαμψίες της δοκού είναι ίσες, είναι ακριβής, μόνο για την προσομοίωση της εντός επιπέδου συμπεριφοράς του γραφενίου. Οι Lu και Hu πρότειναν μία ελλειπτική διατομή για τα στοιχεία δοκου, καθώς η εκτός του επιπέδου δυσκαμψία υπερεκτιμάται σε μεγάλο βαθμό με την κλασσική μέθοδο MSM, όπως προκύπτει και από ατομικές προσομοιώσεις. Ως εκ τούτου, προτάθηκε μια τροποποιημένη έκφραση της MSM στην οποία η εκτός επιπέδου καμπτική δυσκαμψία των στοιχείων δοκού υπολογίζεται με βάση την ασθενή ενέργεια αναστροφής του ομοιοπολικού δεσμού. Μια λεπτομερής περιγραφή αυτής της λεγόμενης τροποποιημένης προσέγγισης (modified MSM mMSM) μπορεί να βρεθεί στο έργο του Chen [90] που πρότεινε μια ορθογώνια διατομή για τη μοντελοποίηση με στοιχεία δοκού των ομοιοπολικών δεσμών.

Μία κλασσική διάταξη προσομοίωσης mMSM, το πείραμα εφελκυσμού μπορεί να χρησιμοποιηθεί για τον προσδιορισμό των εντός επιπέδου μηχανικών ιδιοτήτων του γραφενίου. Μία τέτοια δοκιμή πραγματοποιήθηκε σε αυτήν την εργασία για ένα GS 22.1676x21.1676 nm, φορτιζόμενο στην κατεύθυνση 'zig-zag', (βλ. Εικόνα 3) . Για πάχος του φύλλου γραφενίου ίσο με την απόσταση $t = 0,34$nm μεταξύ δύο φύλλων GS, το μέτρο Ελαστικότητας και ο λόγος Poisson, για το εντός επιπέδου φαινόμενο Poisson,

υπολογίστηκε ως E = 1,04TPa και ν = 0,0607, αντίστοιχα. Πρακτικά τα ίδια αποτελέσματα ελήφθησαν για την κατεύθυνση 'armchair', επαληθεύοντας την υπόθεση ότι το GS μπορεί να θεωρηθεί ότι έχει συμπεριφορά ισοτροπικής μεμβράνης [74]. Παρόλο που το υπολογιζόμενο Young's Modulus του GS είναι συνεπές με άλλες μελέτες, οι τιμές του λόγου Poisson που αναφέρονται στις εργασίες [71,74,76,91,92] είναι διασκορπισμένες σε ένα ευρύ φάσμα από 0,06 έως 0,45. Όπως αναφέρεται στην εργασία [91], υπάρχει έλλειψη πειραματικών αποτελεσμάτων που θα επέτρεπαν την ορθή επικύρωση των θεωρητικών μοντέλων.
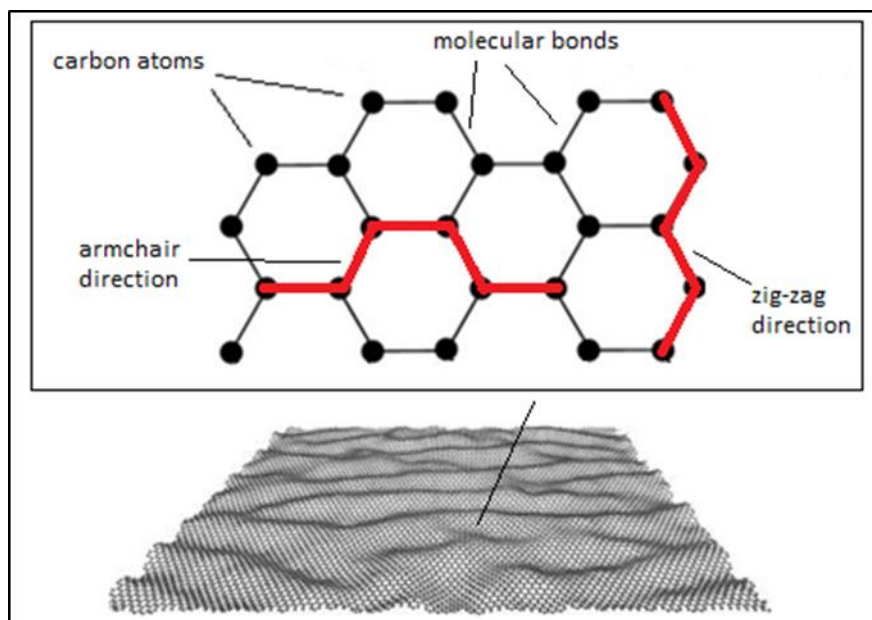
Εικόνα 3 Το εξαγωνικό πλέγμα των ατόμων άνθρακα στο μόριο του γραφενίου

○Παρά το γεγονός ότι η προσομοίωση mMSM είναι οικονομικότερη υπολογιστικά σε σύγκριση με ατομικές προσομοιώσεις [76-79], το κόστος της ανάλυσης εξακολουθεί να είναι υψηλό όταν προσομοιώνονται σχετικά μεγάλα μοντέλα GS. Για παράδειγμα, ένα μοντέλο mMSM ενός φύλλου γραφενίου μονής στρώσης (SLGS) 88,76x84,66 nm αποτελείται από περίπου 106 β.ε., καθιστώντας ακόμη και τις απλές στατικές περιπτώσεις φόρτισης βαριές υπολογιστικά. Είναι λοιπόν προφανές ότι οι προσομοιώσεις στην κλίμακα των μικρομέτρων με τα τρέχοντα μοντέλα mMSM είναι πολύ αναποτελεσματικές. Γι' αυτό το λόγο όπως προαναφέρθηκε, στην παρούσα εργασία προτείνεται ένα αδρό μοντέλο πεπερασμένων στοιχείων, αποτελούμενο από ισοδύναμα στοιχεία κελύφους (Equivalent Shell Element ESE), για να υποκαταστήσει το πλήρες μοντέλο mMSM ενός μεμονωμένου φύλλου γραφενίου SLGS. Κάθε στοιχείο κελύφους ESE αντιστοιχεί σε πλήθος στοιχείων δοκού της mMSM προσομοίωσης, μειώνοντας το υψηλό υπολογιστικό κόστος για την προσομοίωση μοντέλων μεγάλης κλίμακας και χρονικών περιόδων. Το φύλλο γραφενίου SLGS αναμένεται να έχει συπεριφορά τύπου πλάκας όταν υπόκειται σε φορτία εκτός επιπέδου και συμπεριφορά τύπου μεμβράνης όταν υπόκειται σε φορτία εντός επιπέδου. Επί του παρόντος σε ορισμένες εργασίες έχει προταθεί η προσομοίωση της καμπτικής συμπεριφοράς του SLGS με ισοδύναμα στοιχεία πλάκας [93-94] αλλά δεν έχει προταθεί κάποιο μοντέλο που να υποκαθιστά την καμπτική και την μεμβρανική συμπεριφορά του γραφενίου. Η δυσκολία εντοπίζεται στο γεγονός ότι για τις ίδιες ελαστικές παραμέτρους θα πρέπει ένα ισοδύναμο στοιχείο κελύφους να επιδεικνύει συγκεκριμένες ιδιότητες κατά την

κάμψη και την μεμβρανική καταπόνηση. Μία δοκιμή κάμψης δείχνει ότι η πραγματική δυσκαμψία του SLGS είναι πολύ μικρότερη από αυτήν που λαμβάνεται εάν χρησιμοποιηθούν οι τιμές των ελαστικών παραμέτρων που προέκυψαν για την μεβρανική ένταση E = 1TPa και v = 0,0607. Η απλούστερη λύση είναι να χρησιμοποιηθεί ένα στοιχείο κελύφους με αποσυζευγμένη δυσκαμψία για τις δύο αυτές μορφές παραμόρφωσης σύμφωνα με τη σχέση:

$$K = \begin{bmatrix} K_m & \\ & K_b \end{bmatrix}$$

(72)

όπου Km είναι το υπομητρώο που αντιστοιχεί στην μεμβρανική συμπεριφορά και Kb είναι το υπομητρώο που αναφέρεται στην καμπτική συμπεριφορά του κελύφους. Με αυτόν τον τρόπο είναι δυνατό να επιλεγούν ξεχωριστά ζεύγη παραμέτρων που θα καθορίζουν τις δυσκαμψίες Km και Kb ώστε αυτές να ταιριάζουν με την συμπεριφορά του SLGS όπως αυτή αποτυπώνεται στις mMSM προσομοιώσεις. Το πρόβλημα προσδιορισμού ένα ισοδύναμου στοιχείου κελύφους μετασχηματίζεται στο πρόβλημα αναζήτησης ενός ισοδύναμου μεμβρανικού στοιχείου και ενός ισοδύναμου στοιχείου πλάκας. Στην Εικόνα 4 απεικονίζονται οι β.ε. που αντιστοιχούν στους δύο αυτούς τύπους στοιχείων.
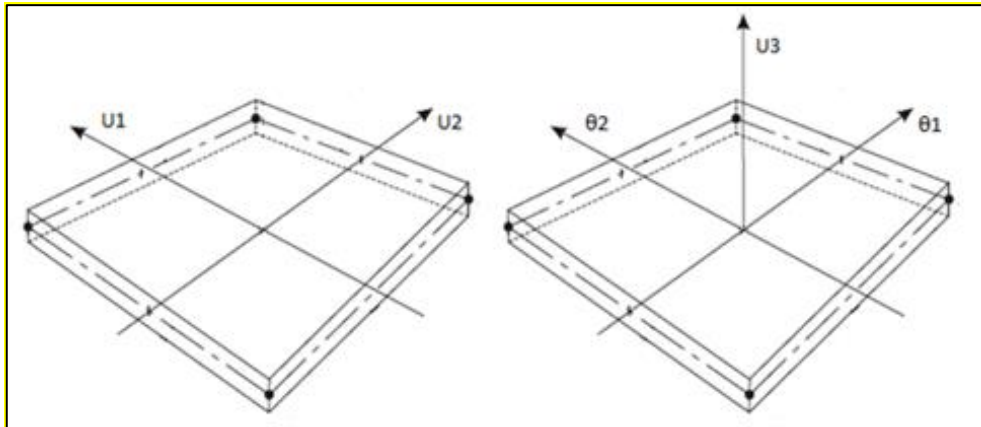
Εικόνα 4 Βαθμοί ελευθερίας ενός τετρεπαλευρικού τετρακομβικού μεμβρανικού στοιχείου και ενός στοιχείου πλάκας

Όπως προαναφέρθηκε, οι μεμβρανικές ιδιότητες του SLGS έχουν προσδιορισθεί από τις εντός επιπέδου δοκιμαστικές φορτίσεις ως E=1TPa, v=0.0607 για το πάχος t=0.34 nm και μπορούν να χρησιμοποιηθούν άμεσα στο υπομητρώο Km. Για να αποδοθεί με το ΕΡΕ σωστά η καμπτική συμπεριφορά που προκύπτει από το mMSM μοντέλο, μία αριθμητική διαδικασία ακολουθείται, με την οποία εξασφαλίζεται η τήρηση συγκεκριμένων κριτηρίων ίσης ενέργειας παραμόρφωσης και μετακινήσεων για το πλήρες μοντέλο mMSM και το υποκατάστατο του ΕΡΕ όταν αυτά υποβάλονται στην ίδια φόρτιση υπό τις ίδιες συνοριακές συνθήκες όπως περιγράφεται στη συνέχεια.

οΘεωρώντας τα αποτελέσματα της mMSM προσομοίωσης ως την ακριβή απόκριση του φύλλου γραφενίου, χρησιμοποιείται ένας αλγόριθμος βελτιστοποίησης με σκοπό την ελαχιστοποίηση του σφάλματος μεταξύ της απόκρισης του υποκατάστατου μοντέλου ΕΡΕ και της mMSM προσομοίωσης. Μία ορθογωνική πλάκα από ΕΡΕ θεωρείται πακτωμένη στις τέσσερις πλευρές όπως και η αντίστοιχη εσχάρα στοιχείων δοκών mMSM και φορτίζονται στο κέντρο από συγκεντρωμένη δύναμη 6pN. Η αντικειμενική συνάρτηση που θα ελαχιστοποιηθεί είναι η διαφορά μεταξύ της συνολικής ενέργειας παραμόρφωσης των

μοντέλων mMSM και EPE, ενώ ταυτόχρονα τίθεται ο περιορισμός τα φορτία να εμφανίζουν την ίδια μέγιστη μετακίνηση.
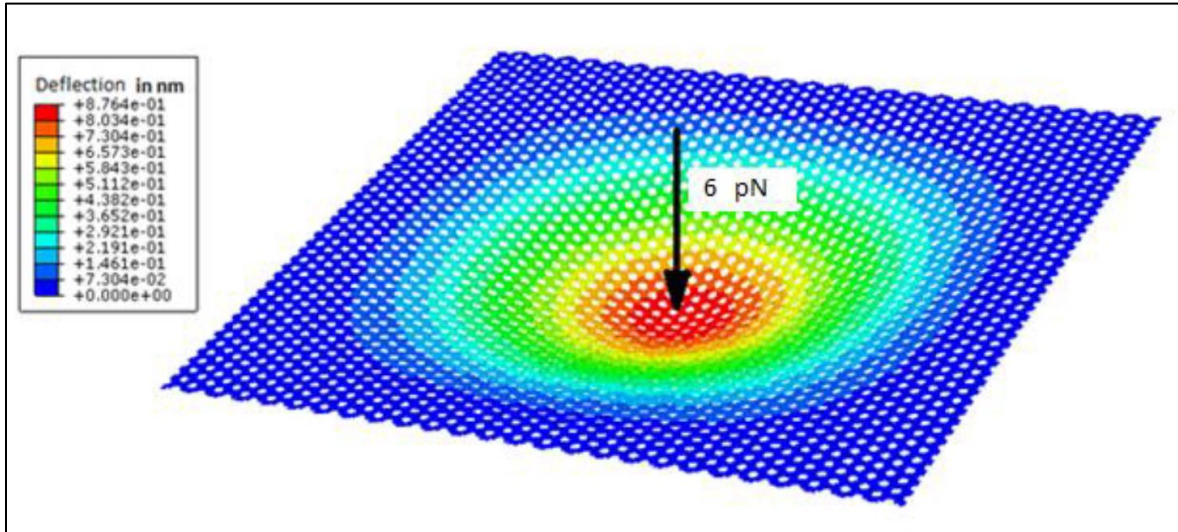
Εικόνα 5 Εσχάρα δοκών μοντέλου mMSM για ορθογωνικό φύλλο γραφενίου μονής στρώσης διαστάσεων 11.08nmx10.58nm πακτωμένο στις 4 πλευρές και συγκεντρωμένο φορτίο στο κέντρο

Η αντικειμενική συνάρτηση διατυπώνεται ως εξής:

$$f(X) = |Vfr - Vpl(X)| \qquad \text{(73)}$$

όπου Vfr είναι ή ενέργεια παραμόρφωσης του mMSM χωρικού πλαισίου και Vpl είναι η ενέργεια παραμόρφωσης του μοντέλου EPE, και εξαρτάται από τις τιμές των παραμέτρων $X = [E \ v \ t]^T$, δηλαδή το μέτρο ελαστικότητας, ο λόγος του Poisson, και το πάχος του κελύφους αντίστοιχα, ενώ επιβάλλεται και ο εξής περιορισμός

$$|\max Ufr - \max Upl(X)| \leq tol \qquad \text{(74)}$$

όπου $\max Ufr$ είναι η μέγιστη μετακίνηση του mMSM και $\max Upl$ είναι η μέγιστη μετακίνηση του μοντέλου EPE.

Η καμπτική συμπεριφορά μία ισότροπης πλάκας χαρακτηρίζεται πλήρως από την δυσκαμψία της D_e η οποία δίνεται ως εξής:

$$D_e = \frac{Et^3}{12(1 - v^2)} \qquad \text{(75)}$$

Είναι προφανές ότι η ίδια τιμή για τη δυσκαμψία D_e μπορεί να προκύψει για διαφορετικές τιμές του διανύσματος παραμέτρων X, δηλαδή για διαφορετικούς συνδυασμούς τιμών των παραμέτρων E, t και v. Οπότε το παραπάνω πρόβλημα βελτιστοποίησης μπορεί να απλοποιηθεί εάν επιλεγεί εκ των προτέρων η τιμή του λόγου Poisson $v=0.0607$, ίδια με αυτήν που προκύπτει για το μεμβρανικό πρόβλημα και μία τιμή για το πάχος $t=0.001nm$. Η βελτιστοποίηση τότε εκτελείται μόνο για την αναζήτηση της τιμής του μέτρου ελαστικότητας E. Εκ των υστέρων μπορεί να τεθεί και το πάχος t να συμπίπτει με το πάχος του ΕΜΕ και να επαναϋπολογισθεί το E ώστε να διατηρηθεί ίδια η δυσκαμψία της πλάκας από την εξίσωση (75). Αυτή η απλοποίηση δεν επηρεάζει την επίλυση του προβλήματος βελτιστοποίησης και επιτυγχάνεται λύση με σφάλμα μικρότερο του 0.3% για την μέγιστη μετακίνηση και μικρότερο του 0.8% για την αντικειμενική συνάρτηση. Για την παραπάνω διαδικασία δεν έγιναν κάποιες παραδοχές για το μέγεθος και το σχήμα του φύλλου του γραφενίου. Συνεπώς το υπολογιζόμενο στοιχείο EPE μπορεί να υποκαταστήσει τη καμπτική συμπεριφορά του μοντέλου mMSM ανεξαρτήτως του σχήματος της εσχάρας και των διαστάσεων της. Η πυκνότητα της διακριτοποίησης του μοντέλου EPE προκύπτει από μία ανάλυση σύγκλισης. Ένας κάναβος 40x40 πεπερασμένων στοιχείων δίνει μία επαρκώς

ακριβή λύση για την οποία επιτυγχάνεται σύγκλιση για τη τιμή του *E*=5.341e10 MPa. Επίσης έγινε μία διερεύνηση για το μέγεθος του φύλλου γραφενίου για το οποίο παρατηρείται ομογενής καμπτική συμπεριφορά. Από την ανάλυση αυτή λαμβάνεται, για ένα SLGS διαστάσεων 105x111 nm η τιμή στην οποία συγκλίνει το μέτρο ελαστικότητας *E*=5.316e10 MPa του ισοδύναμου στοιχείου κελύφους. Όμως όπως φαίνεται στην Εικόνα 6 και για μικρότερα μεγέθη της τάξεως των 44.3x42.3 nm του φύλλου γραφενίου το σφάλμα μεταξύ του μοντέλου mMSM και του αδρού υποκατάστατου μοντέλου είναι πολύ μικρό και κάτω από τις προαναφερθείσες τιμές για την ελαστική ενεργεια παραμόρφωσης και τη μέγιστη μετακίνηση.
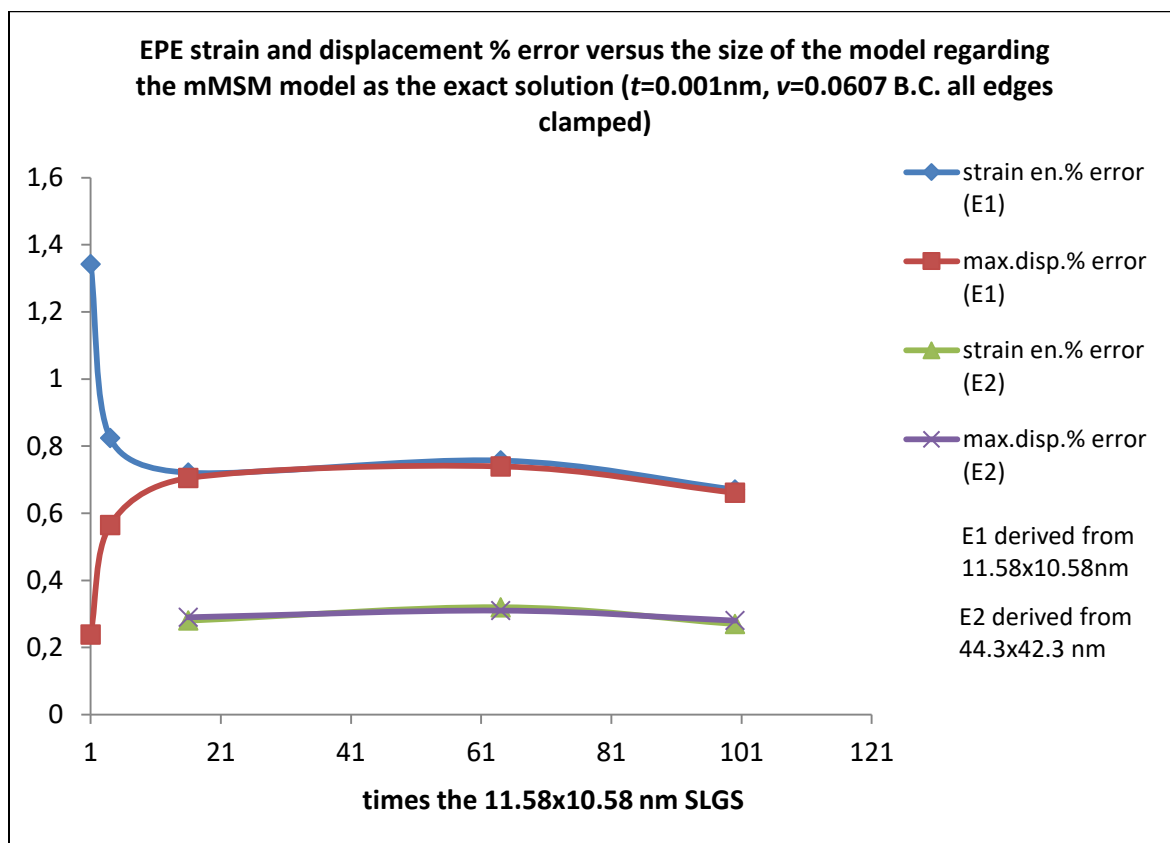
Εικόνα 6 Μέγιστο σφάλμα μοντέλου EBE για την ελαστική ενέργεια παραμόρφωσης και τη μεγιστη μετακίνηση

Μία πλάκα ορίζεται πλήρως από την δυσκαμψία της *D*$_e$ και αφού αυτή υπολογισθεί τότε μπορεί να χρησιμοποιηθεί σε προβλήματα με διαφορετικές συνοριακές συνθήκες ή περιπτώσεις φόρτισης. Παρόμοιες δοκιμές εκτελέστηκαν για προβλήματα κάμψης με διαφορετικές συνθήκες στήριξης και φόρτισης όπως το μη συμμετρικό πρόβλημα που φαίνεται στην Εικόνα 7 έδειξαν σφάλματα ίδιας τάξης μεγέθους, κάτω του 1% στην ενέργεια παραμόρφωσης και στη μέγιστη μετακίνηση για όλα τα μεγέθη των μοντέλων.

Για τις εφαρμογές που ακολουθούν οι τιμες t=0.001nm και *E*=5.316e10 MPa έχουν προσαρμοσθεί με βάση τη σχέση (75) ώστε το πάχος να συμπίπτει με αυτό του ισοδύναμου μεμβρανικού στοιχείου t=0.34nm, προκύπτει ως *E*=1.352 GPa και μπορεί να χρησιμοποιηθεί στην κλίμακα των μικρομέτρων με ακρίβεια μεγαλύτερη του 99%. Εν τέλει, το ESE ενός φύλλου γραφενίου μιας στρώσης μπορεί να διατυπωθεί σαν συνδυασμός των EME και EPE με χρήση της σχέσης (72).
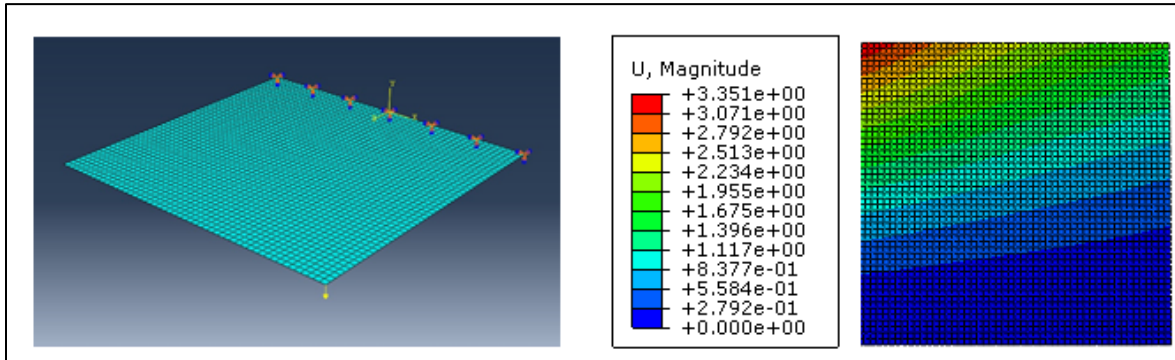
Εικόνα 7 Μη συμμετρική φόρτιση μονόπακτης πλάκας με συγκεντρωμένο φορτίο σε γωνιακό κόμβο. Διαστέσεις 44.3x42.3nm διακριτοποιημένη με 50x50 πεπερασμένα στοιχεία.

○Στη συνέχεια μελετάται ο μηχανισμός μεταφοράς φορτίου μεταξύ της μήτρας και του φύλλου γραφενίου Interfacial Load Transferring Mechanism (ILTM), ο οποίος έχει ιδιαίτερο ενδιαφέρον, διότι επηρεάζει άμεσα τις μηχανικές ιδιότητες του νανοσύνθετου υλικού και την συνολική του απόκριση. Σε ένα νανοσύνθετο υλικό πολυμερικής μήτρας τα άτομα άνθρακα του γραφενίου αλληλεπιδρούν μεταξύ τους με ισχυρούς ομοιοπολικούς δεσμούς, ενώ συνδέονται με την μήτρα με ασθενείς δυνάμεις Van der Waals[86,95]. Διάφορες χημικές διεργασίες 'functionalization' μπορούν να εφαρμοσθούν ώστε να συνδεθούν με ομοιοπολικούς δεσμούς τα άτομα άνθρακα με το πολυμερές βελτιώνοντας έτσι σε μεγάλο ποσοστό τη δυσκαμψία και την αντοχή του ILTM. Πειραματικές μελέτες της μηχανικής συμπεριφοράς νανονοσύνθετων υλικών με εγκλείσματα CNT [93] αποκαλύπτουν μία μη γραμμική σχέση δύναμης μετακίνησης μετά το όριο διαρροής της διεπιφάνεια κατά τη δοκιμή εξόλκευσης. Συνεπώς, για την ακριβή μοντελοποίηση των νανοσύνθετων υλικών με βάση τους νανοσωλήνες άνθρακ (CNT reinforced composites CNT-RC, GS reinforced composites GS-RC) πρέπει να ληφθεί κατάλληλα υπ όψιν και ο ILTM.

Τρεις προσεγγίσεις έχουν προταθεί για την μοντελοποίηση της αλληλεπίδρασης του εγκλείσματος με τη μήτρα: i) ένα μοντέλο τριβής 'shear lag' [80,86,94] ii)ένα μοντέλο μη γραμμικής ελαστικής σύνδεσης [95,93] και iii)ένα μοντέλο συνεκτικής ζώνης [87, 96]. Στην παρούσα εργασία, δε μπορεί να εφαρμοσθεί ένα μοντέλο τριβής λόγω της απουσίας διατμητικών τάσεων στην εξωτερική επιφάνεια του ESE. Επιπρόσθετα, ένα μοντέλο ελαστικών συνδέσεων απαιτεί την προσομοίωση του φύλλου γραφενίου με στοιχεία δοκού, καθώς με αυτήν την προσέγγιση η αλληλεπίδραση των ατόμων του γραφενίου και της μήτρας με βάση το δυναμικό Lenard Jones γίνεται με διακριτό τρόπο. Αντιθέτως, ένα μοτέλο συνεκτικής ζώνης ορίζει μια αλληλεπίδραση μεταξύ των επιφανειών του εγκλείσματος (ESE) και τη μήτρα με βάση έναν καταστατικό νόμο έλξης-ολίσθησης (traction separationTS), μία αναλυτική έκφραση για τον οποίο έχει προταθεί για την περίπτωση του γραφενίου με βάση το δυναμικό Lenard Jones[96]. Επίσης προσομοιώσεις μοριακής δυναμικής για GS-RC αναφέρουν αντίστοιχη συμπεριφορά[97] ενώ και στην εργασία [98] προτείνεται ένα μοντέλο συνεκτικής ζώνης σε ένα πλαίσιο ανάλυσης φορέων σε πολλαπλές κλίμακες. Συνεπώς στην παρούσα εργασία έχει υιοθετηθεί η θεώρηση μιας συνεκτικής ζώνης με συγκεκριμένο νόμο traction-separation για τη μοντελοποίηση του ILTM.

Ένας τυπικός νόμος TS ορίζει το διάνυσμα των αναπτυσόμενων έλξεων μεταξύ των δύο επιφανειών σα συνάρτηση της μεταξύ τους απόστασης διαχωρισμού δ. Στην απλούστερη μορφή του, θεωρείται μία αποσυζευγμένη απόκριση στις τρεις κατευθύνσεις: στην εγκάρσια διεύθυνση n, και τις διατμητικές s και t, στην επαφή των επιφανειών, οι οποίες ταυτίζονται και με τους τοπικούς άξονες u_3, u_2 and u_1 του ESE σύμφωνα με τη σχέση:

$$t = \begin{bmatrix} Kn & & \\ & Km & \\ & & Kt \end{bmatrix} \begin{bmatrix} \delta n \\ \delta s \\ \delta t \end{bmatrix} \tag{76}$$

όπου *Kn, Ks* και *Kt* είναι οι συνιστώσες της δυσκαμψίας της διεπιφάνειας στις αντίστοιχες διευθύνσεις. Θεωρείται στην αρχή μία γραμμική ελαστική απόκριση, και ένα κριτήριο έναρξης βλάβης (damage initiation) βασισμένο σε μία μέγιστη τιμή έλξης. Το κριτήριο αυτό διατυπώνεται ως εξής:

$$\max\left\{\frac{tn}{ISn} \quad \frac{ts}{ISs} \quad \frac{tt}{ISt}\right\}=1 \tag{77}$$

όπου *IS* είναι η τάση του κριτηρίου βλάβης (interfacial strength) αντίστοιχα για τις τρεις διευθύνσεις. Εάν αρχίσει ο σχηματισμός βλάβης τότε, η δυσκαμψία της διεπιφάνειας φθίνει με βάση το θεωρούμενο νόμο εξέλιξης της βλάβης. Εισάγεται μία μεταβλητή *D* που αναφέρεται στη συσωρευμένη βλάβη και λαμβάνει τη τιμή *D=0* για μηδενική βλάβη και την τιμή *D=1* για τη μέγιστη βλάβη όπου πλέον η αναπτυσσόμενη έλξη μηδενίζεται. Οι συνιστώσες της συνολικής έλξης των επιφανειών δίνονται συναρτήσει και της μεταβλητής *D* σύμφωνα με την εξής σχέση:

$$tn=(1-D)\overline{tn}, \quad ts=(1-D)\overline{ts}, \quad tt=(1-D)\overline{tt} \tag{78}$$

όπου $\overline{tn}$, $\overline{ts}$ and $\overline{tt}$ είναι οι έλξεις που υπολογίζονται θεωρώντας πλήρως ελαστική απόκριση χωρίς βλάβη.

Οι τιμές του *D* εξαρτώνται και από το επιλεγόμενο μοντέλο εξέλιξης της βλάβης. Τυπικά η εξέλιξη της βλάβης μπορεί να διατυπωθεί με βάση την ενέργεια θραύσης η την ενεργή μετατόπιση και να ακολουθεί ένα γραμμικό η εκθετικό νόμο. Επίσης μπορεί να εξαρτηθεί από μία συζευγμένη έκφραση που να περιλαμβάνει όλες τις συνιστώσες της ολίσθησης της διεπιφάνειας. Αυτή η γενικευμένη προσέγγιση μπορεί να χρησιμοποιηθεί σε κάθε τύπο ILTM για GS-RC είτε αναπτύσσονται ομοιοπολικοί δεσμοί είτε όχι. Στην παρούσα εργασία θεωρούμε για την εξέλιξη της βλάβης μία διατύπωση βασισμένη στην ενεργή μετακίνηση και μία γραμμική εξασθένιση της στιβαρότητας της διεπιφάνειας μετά την εκκίνηση του σχηματισμού βλάβης. Η ενεργή μετακίνηση δ_m εκφράζεται συναρτήσει των σχετικών μετακινήσεων των δύο επιφανειών στις τρεις διευθύνσεις:

$$\delta m=\sqrt{\delta n^2+\delta s^2+\delta t^2} \tag{79}$$

Όπως φαίνεται στην Εικόνα 8 η μεταβλητή *D* συσσώρευσης της βλάβης αναπτύσσεται γραμμικά με βάση την παρακάτω έκφραση:

$$D=\frac{\delta_m^f(\delta_m^{max}-\delta_m^0)}{\delta_m^{max}(\delta_m^f-\delta_m^0)} \tag{80}$$

όπου δ_m^f, δ_m^0 and δ_m^{max} είναι η ενεργή μετακίνηση κατά την πλήρη αστοχία, κατά την έναρξη της βλάβης και η μέγιστη τιμή που αυτή έχει λάβει κατά τη χρονοϊστορία φόρτισης αντίστοιχα.
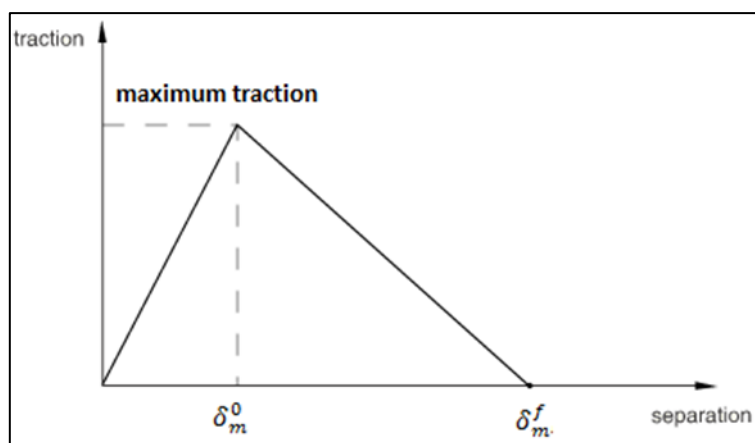
Εικόνα 8 Γραμμική σχέση έλξης ολίσθησης και εξέλιξη της βλάβης

       Προσεγγιστικές τιμες για τις παραμέτρους που ορίζουν πλήρως το θεωρούμενο νόμο TS για την κάθετη και την εφαπτομενική διεύθυνση μπορούν να ληφθούν από προσομοιώσεις μοριακής δυναμικής. Ενδεικτικές τιμές που προκύπτουν για το γραφένιο και κάποιο πολυμερές δίνονται στον Πίνακας 1.

Reported by	Loading conditions	Maximum Shear Traction observed	Maximum Normal Traction observed
Zhang [98]	Normal separation of Flat SLGS from polyethylene		503.4 MPa
	damage zone located in polymer		217.3MPa
Liu [99]	Pull-out of Flat SLGS in polyethylene	112 MPa	
Awasthi [100]	Normal and Shear Mode separation of SLGS in polyethylene	108.3 MPa	170.6 MPa

Πίνακας 1 Τιμές μέγιστης έλξης παρατηρούμενες σε προσομοιώσεις μοριακής δυναμικής GS-RC θεωρώντας αλληλεπίδραση VDW μεταξύ της μήτρας και του εγκλείσματος

Όπως συμπεραίνεται στην εργασία [100] πολλές παράμετροι της μοντελοποίησης όπως το μέγεθος του και το είδος των θεωρούμενων συνοριακών συνθηκών μπορεί να επηρεάσουν την ακρίβεια των προσομοιώσεων και κατ' επέκταση των δεδομένων που λαμβάνονται από αυτές για τη μηχανική συμπεριφορά της διεπιφάνειας κατά τον διαχωρισμό μήτρας εγκλείσματος. Όπως φαίνεται από τον Πίνακα 1 οι τιμές που λαμβάνονται για την IS ποικίλουν, και μάλιστα διαφέρουν σημαντικά από αυτές που παρατηρούνται πειραματικά. Οι μέγιστες τιμές για την έλξη κατά την εφαπτομενική διεύθυνση διαχωρισμού στις εργασίες [101-104] είναι 2.3MPa, 0.46-0.69MPa, 0.5MPa, and 0.5 MPa αντίστοιχα, αλλά και η τιμή του έργου διαχωρισμού που παρατηρείται στην [100] είναι πολύ διαφορετική από την πειραματικά μετρούμενη στις εργασίες [102] και [104].

       Ένας άλλος παράγοντας που επηρεάζει σημαντικά τις τιμές των παραπάνω παραμέτρων είναι η διαδικασία 'functionalization' που είναι μία χημική κατεργασία της διεπιφάνειας που βελτιώνει τις ιδιότητες συνοχής της. Όπως γίνεται προφανές στις εργασίες [105] και [106] με τη βελτίωση μέσω functionalization η τιμή της IS κατά την εφαπτομενική διεύθυνση (ολίσθηση) μπορεί να φθάσει τα 35 MPa που πρακτικά αντιστοιχούν σε μία κατάσταση πλήρους σύνδεσης της μήτρας με τα εγκλείσματα. Στην εργασία [105]

συμπεραίνεται ότι η αποτελεσματικότητα του functionalization για την βελτίωσης της αντοχής IS κατά την κάθετη διεύθυνση διαχωρισμού μειώνεται με την αύξηση της ποσότητας του υλικού που χρησιμοποιείται για το grafting όμως η αρχική τιμή που αντιστοιχεί σε functionalization καθαρού γραφενίου είναι 727.9Mpa που είναι πάρα πολύ υψηλή. Από αυτές τις εργασίες προκύπτει ότι παράμετροι όπως το μέγεθος του μοντέλου, η πυκνότητα του grafting, το μέγεθος της πολυμερικής αλυσίδας καθώς και οι διαστάσεις του φύλλου γραφενίου επηρεάζουν την παρατηρούμενη τιμή της αντοχής IS.

Όλες οι παραπάνω παρατηρήσεις είναι ενδεικτικές της σημαντικής αβεβαιότητας που προκύπτει για τον προσδιορισμό των παραμέτρων που χαρακτηρίζουν τον μηχανισμό ILTM η οποία οδηγεί σε μεγάλες διακυμάνσεις για τις παρατηρούμενες τιμές. Είναι προφανής λοιπόν η ανάγκη εκτέλεσης μίας παραμετρικής διερεύνησης για το εύρος των πιθανών τιμών που μπορούν να λάβουν οι παράμετροι του μοντέλου ILTM ώστε να αποτιμηθεί η επιρροή τους στις μακροσκοπικές ιδιότητες του νανοσύνθετου υλικού. Τα αποτελέσματα της διερεύνησης αυτής δίνονται αναλυτικά στο κύριο μέρος της διατριβής. Από αυτά προκύπτει ότι το υποκατάστατο μοντέλο που προτείνεται μπορεί να συνδυασθεί επιτυχώς με το μοντέλο συνεκτικής ζώνης για τη δημιουργία ενός συνολικού μοντέλου RVE που μπορεί να αποδώσει επιτυχώς την επιρροή του μηχανισμού μεταφοράς φορτίου μεταξύ μήτρας και εγκλείσματος στην συνολική συμπεριφορά του νανοσύνθετου υλικού.

ₒΣτη συνέχεια περιγράφεται το στοιχείο αντιπροσωπευτικού όγκου το οποίο ορίζεται για το πρόβλημα υπολογιστικής ομογενοποίησης 1^{ης} τάξης των νανοσύνθετων υλικών. Για τον υπολογισμό των συνολικών ιδιοτήτων CNT-RC έχουν χρησιμοποιηθεί διάφορες διατάξεις RVE [107]. Με τον ίδιο τρόπο, ένα ορθογωνικό RVE κατασκευάζεται στην παρούσα εργασία θεωρώντας ένα φύλλο γραφενίου, μοντελοποιημένο με ESE, εντός της πολυμερικής μήτρας που διακριτόποιείται με τρισδιάστατα πεπερασμένα στοιχεία. Για την περίπτωση, που το φύλλο γραφενίου θεωρείται πλήρως συνδεδεμένο με την μήτρα τότε μπορούν τα πεπερασμένα στοιχεία ESE να ενσωματωθούν στα τρισδιάστατα στοιχεία με μεθοδολογίες σύνδεσης διαφορετικών τύπων στοιχείων [80,86] Αυτή η μεθοδολογία είναι ιδιαίτερα απλή και επιτρέπει την αποφυγή πολύπλοκης διακριτοποίησης και μπορεί να χρησιμοποιηθεί για φύλλα γραφενίου επίπεδης και κυματοειδούς γεωμετρίας. Μία τυπική διάταξη ενός φύλλου γραφενίου στο κέντρο ενός RVE και η λεπτομέρεια σύνδεσης του με τα στοιχεία συνεχούς μέσου, με τη χρήση στοιχείων συνεκτικής ζώνης φαίνονται στην Εικόνα 9 .
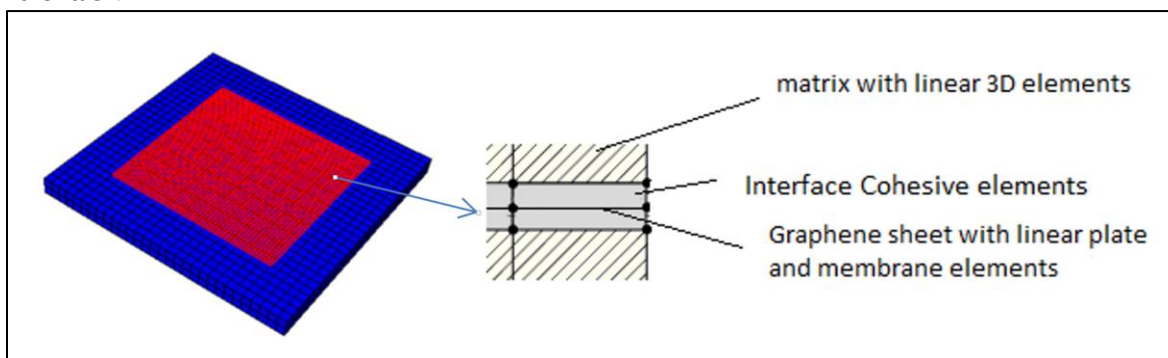
Εικόνα 9 Διακρίτοποίηση με πεπερασμένα στοιχεία ενός ορθογωνικού RVE με ένα ενσωματωμένο ένα φύλλο γραφενίου και μοντελοποίηση της συνεκτικής ζώνης με πεπερασμένα στοιχεία.

Για την υλοποίηση μίας συνεκτικής ζώνης για τον ILTM, όπως περιγράφηκε παραπάνω, θα χρησιμοποιηθούν συνεκτικά στοιχεία (cohesive elements), στα οποία ανατίθεται το μοντέλο εξέλιξης βλάβης που δίνεται στην Εικόνα 8. Πρόκειται για στοιχεία ειδικού τύπου μηδενικού αρχικού πάχους με καταστατική συμπεριφορά που ορίζεται συναρτήσει ενός

νόμου έλξης-ολίσθησης. Η απομάκρυνση των δύο επιφανειών SLGS και πολυμερούς δίνεται σε ένα σημείο της συνεκτικής ζώνης ως εξής:

$$\Delta = \begin{bmatrix} u \\ v \\ w \end{bmatrix}_{top} - \begin{bmatrix} u \\ v \\ w \end{bmatrix}_{bot} = BD_{coh} \qquad \textbf{(81)}$$

όπου *u, v, w* είναι η μετακίνηση σε αντίστοιχο σημείο της άνω και κάτω επιφάνειας που ορίζονται στο εγκλεισμα και την μήτρα, *B* είναι έναμητρώο που περιλαμβάνει τις συναρτήσεις σχήματος και D_{coh} είναι οι επικόμβιοι βαθμοί ελευθερίας των cohesive elements 1. Η αρχή των δυνατών έργων διατυπώνεται ως εξής:

$$\delta D_{coh}^{T} \int_{A} B^{T}(I-D)CBdA = \int_{A} \delta\Delta\tau dA \qquad \textbf{(82)}$$

D είναι ένα διαγώνιο μητρώο που αποτελείται από τις τιμές της μεταβλητής συσσωρευμένης βλάβης που ορίζεται από τηνσχέση (80), *C* είναι το καταστατικό μητρώο που αναφέρεται στην ελαστική απόκριση αναφοράς δίχως βλάβη κατά τη σχέση (76) και *τ* είναι ο τανυστής έλξεων. Και τελικά το μητρώο στιβαρότητας τους δίνεται από τη σχέση

$$K_{coh} = \int_{A} B^{T}(I-D)C BdA \qquad \textbf{(83)}$$

○Για να ληφθεί υπόψη η τυχαιότητα των γεωμετρικών χαρακτηριστικών των φύλλων γραφενίου, αυτά θεωρούνται σαν επίπεδα με εκτός επιπέδου γεωμετρικές ατέλειες. Οι ατέλειες αυτές μπορούν να περιγραφθούν στα πλαίσια μιας στοχαστικής ανάλυσης με τη χρήση ενός δισδιάστατου στοχαστικού πεδίου μηδενικής μέσης τιμής. Δείγματα ενός τέτοιου πεδίου μπορούν να παραχθούν με την μέθοδο της φασματικής αναπαράστασης [108]. Με αυτήν την προσέγγιση, μπορούν να δημιουργηθούν ατέλειες συμβατές με μία συνάρτηση φασματικής πυκνότητας (SDF). Στην παρούσα εργασία χρησιμοποιήθηκε μία SDF εκθετικού τύπου

$$S_{f_0 f_0} = \frac{\sigma_f^2}{4\pi} b_1 b_2 \exp\left[-\frac{1}{4}\left(b_1^2 \kappa_1^2 + b_2^2 \kappa_2^2 \right) \right] \qquad \textbf{(84)}$$

όπου σ_f η τυπική απόκλιση του στοχαστικού πεδίου και b_1, b_2 είναι τα μήκη συσχέτισης που επηρεάζουν το σχήμα του φάσματος. Στην Εικόνα 10 φαίνονται οι συναρτήσεις τυχαία παραγόμενων ατελειών.

Στο κύριο μέρος της παρούσας εργασίας παρουσιάζονται τα αποτελέσματα προσομοιώσεων της μηχανικής συμπεριφοράς πολυμερών υλικών GS-RC, με τη χρήση RVE για τη δημιουργία των οποίων εφαρμόζονται οι ανωτέρω μεθοδολογίες ενώ μελετάται η επιρροή σε αυτήν i)των χαρακτηριστικών του ILTM όπως η μέγιστη διεπιφανειακή τάση, η δυσκαμψία της συνεκτικής ζώνης και η μέγιστη ολίσθηση αστοχίας και ii)των γεωμετρικών χαρακτηριστικών των φύλλων γραφενίου όπως οι εκτός επιπέδου ατέλειες
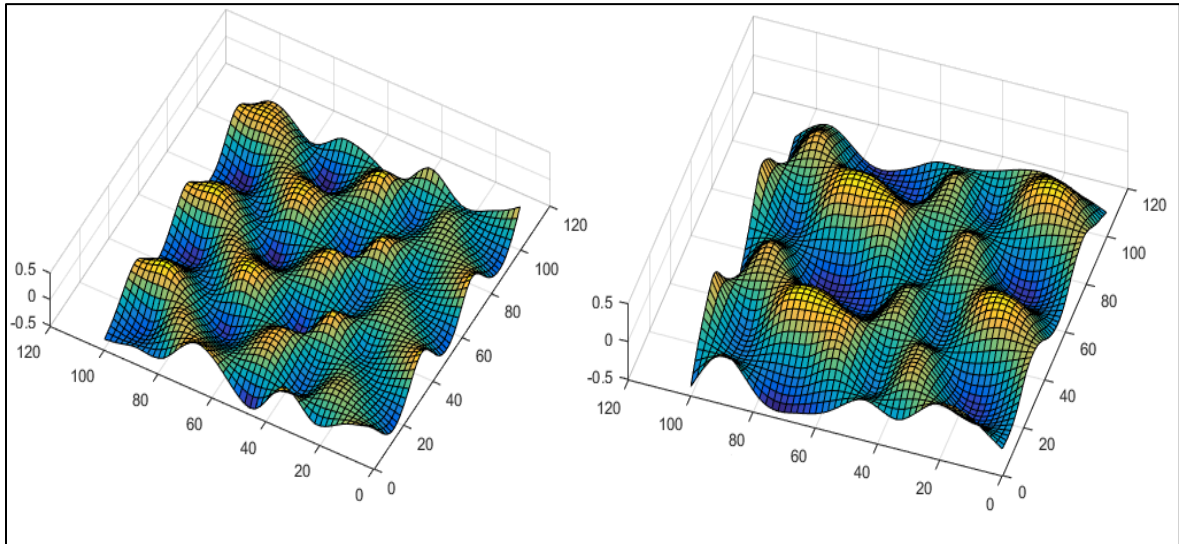
Εικόνα 10 Τυχαία παραγόμενες γεωμετρίες 100x100nm SLGS, για ένα α) κύμα σχετικής υψηλής συχνότητας (b₁=b₂=1) και β) χαμηλής συχνότητας κυματισμούς (b₁=b₂=20)

Πίνακας περιεχομένων

1 Introduction

1.1 Motivation

An essential part of the analysis and design of structures is the accurate description of the non-linear behavior of the material. Building materials, such as metal alloys, polymer mixtures, nanocomposites, porous media, mortars, are mostly heterogeneous on a certain scale. The complex mechanical response resulting from the heterogeneity in the microstructure of the material cannot be accurately described in an explicit formulation of a phenomenological law. The ability to predict, by means of numerical methods, the overall mechanical properties of composite materials, based on characteristics of the microstructure, such as the shape, content and mechanical behavior of inclusions and their interaction at the interface, is of great importance in engineering applications as it allows for savings in resources and time involved in painstaking experimental procedures, and it also allows for the precise modeling and optimal design of the whole structure. For this reason, the methodologies of modelling of structures at multiple scales are of particular research interest. The predominant methodology of "computational homogenization" is a family of algorithms based on a four-point scheme by Suquet and on the macro-homogeneity condition. It allows for the concurrent finite element modeling of structures in multiple scales, i.e. "FE^2 modeling ". They are considered more prevalent because they involve continuous exchange of data, between multiple analysis levels, relevant not only to the geometric and mechanical properties of the microstructure but to the stress state of the macroscopic structure and the microstructure as well. Steps taken for the application of this methodology in the case of thin shells described by the Kirchhoff Love theory are very limited. This thesis aims in the formulation a comprehensive methodology for the analysis in multiple scales of thin shells. It should involve an appropriate description of the macroscale equilibrium, the microscale boundary value problem and the scale transition equations between the two levels of the "FE^2" analysis.

Geometric non-linearity is a key factor that affects the mechanical behaviour of thin shell structures and should always be taken into account for the modelling and design of structures. By use of suitable strain and stress tensors and the corresponding expression of the used phenomenological law for the material, the Priciple of Virtual Work can be suitably employed for the solution of thin shell buckling problems with simultaneous consideration of material non-linearity. However, for these types of problems, the case of shells characterized by a heterogeneous microstructure has not been sufficiently studied. The formulation of a methodology for the multiscale analysis of thin shell structures along with the assumption of large displacements and rotations for both scales is a second research objective of the dissertation.

One of the main applications of multiscale analysis is the study of the properties of nanocomposite materials through the detailed modelling of their microstructure. Next generation nanocomposite materials reinforced with carbon-based inclusions, such as graphene (Graphene) and carbon nanotubes (Carbon Nano Tubes CNTs), exhibit excellent mechanical properties even when the inclusions are used in very low concentrations. This is due to the special characteristics of graphene that exhibits a Young's modulus of 1 TPa and a tensile strength of 130 GPa. Because these values are incomparably higher than those of

conventional polymeric materials, details in the description of the microstructure of the nanocomposite material such as the geometric characteristics of the graphene inclusions as well as the load transfer mechanism between the matrix and the inclusions greatly influence its overall macroscopic behavior. However, the computational cost involved in a detailed molecular simulations of a sufficiently large graphene sheet and the corresponding three-dimensional representative volume of the total nanocomposite material, is very high and it does not allow for a thorough study of the behavior of graphene sheet reinforced nanocomoposite materials (GS-RC). The third objective of the thesis is to utilize simplified computational homogenisation methodologies for the creation of a computationally efficient surrogate model for graphene. This should be used for modeling of the microstructure of GS-RC and the simulation of their mechanical behaviour.

1.2 Outline

This thesis is organized in 5 chapters, outlined as follows

Chapter 2 introduces the reader to the basic principles of computational homogenisation that can be used for multi-scale analysis of microscopically heterogeneous three-dimensional continua. The cases of small and finite deformation problems are presented separately but they are based on the same principles that will constitute the basis of the forthcoming derivations.

In Chapter 3, the existing theoretical framework for the incorporation of constitutive equations developed for three dimensional materials within the context of large deformation modelling of thin Kirchhoff Love shells is presented. The focus is on how the plane stress condition can be applied in the expression of existing constitutive laws. Exploitation of this condition in a multiscale finite element analysis setting is a key point of the proposed formulation.

In Chapter 4, an integrated theory for multiscale analysis of microscopically heterogeneous thin shells undergoing small deformations, is presented. The macroscopic and microscopic boundary value problems are formulated with account for the specific assumptions of Kirchhoff Love theory in a small deformation and strains analysis context. Averaging relations are also reworded in this framework and it is demonstrated that Hill's averaging theorem is indeed satisfied.

In Chapter 5, the proposed formulation is extended to large deflection analysis. The Principle of Virtual Work governing equilibrium at the microscopic and macroscopic level, the averaging theorem and the associated scale transition equations are formulated in terms of appropriate stress and strain measures that can accurately describe the state of a shell structure undergoing large displacements and rotations. Useful transformations of strain measures, which allow for simplification of the implementation of a finite element solution of the non-linear boundary value problem of the microstructure are provided.

Chapter 6, presents existing methodologies for modeling of graphene sheets and the proposed simplified methodology for the creation of an accurate surrogate model based on a computational homogenization concept for thin sheets. An integrated simulation technique is presented for the modeling of GS-RC including the matrix-inclusion interface and the stochastic properties of the geometry of the microstructure.

Lastly, Chapter 7 discusses the conclusions drawn from this research and presents a summary of the contributions

2 Multi-scale analysis of heterogeneous media

In this section, we present the existing theoretical framework of computational homogenisation that can be used for the multi-scale analysis of microscopically heterogeneous three-dimensional continua. It constitutes the theoretical basis of the forthcoming derivations. Starting from the basic hypotheses of the methodology, we then focus on the basic computational micro to macro transitions, the microstructural boundary value problem and the corresponding expression of the macro-homogeneity condition.

2.1 Basic Hypotheses

According to the basic assumption of computational homogenisation, the structures under study are macroscopically sufficiently homogeneous but they exhibit a heterogeneous microstructure consisting of multiple phases, cavities and interfaces. The length scale of the heterogeneities is larger than the molecular dimensions and the constituents of the microstructure can be modelled via a continuum mechanics approach. It is also assumed that the scale separation hypothesis holds, namely the microscopic length scale is much smaller than the characteristic size of macroscopic structure or the wave length of the macroscopic loading.

An assumption of local periodicity is made, namely the microstructure can have different morphologies corresponding to different macroscopic points, while it repeats itself in a small vicinity of each individual macroscopic point, but not in the whole macroscopic specimen (Figure 1). This way it is possible to model the effect of a non-uniform microstructure on the macroscopic response.
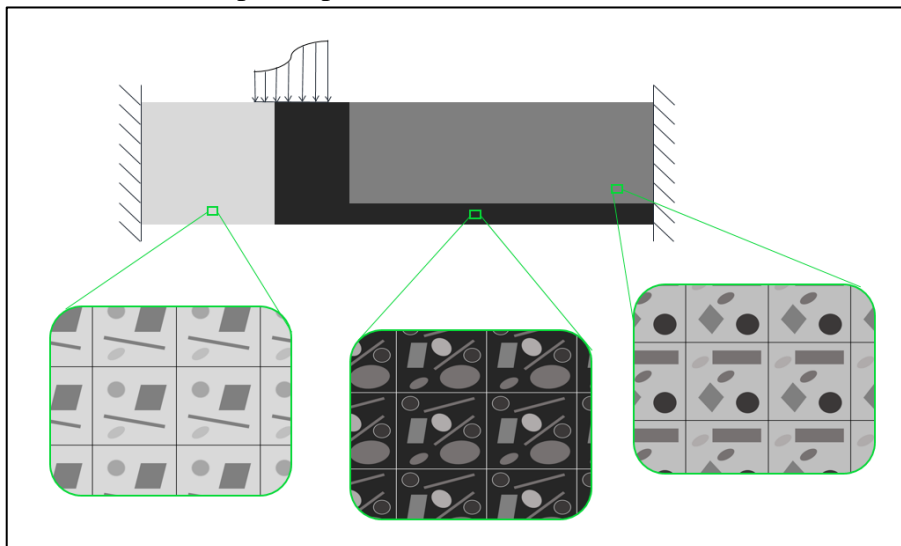

Figure 1 : The assumption of local periodicity. Different microstructure morphologies repeat themselves in different parts of the structure

In the classical computational homogenisation procedure, the macroscopic strain is calculated for every material point of the macrostructure (e.g. the integration points of the macroscopic mesh within a finite element (FE) environment). Its value for a macroscopic point is next used to formulate the boundary conditions to be imposed on the RVE that is assigned to this point. Upon the solution of the BVP for the RVE, the macroscopic stress tensor is obtained by averaging the resulting RVE stress field over the volume of the RVE. As a result, the (numerical) stress–deformation relationship at the macroscopic point is readily available. Additionally, the local macroscopic consistent tangent is derived from the microstructural stiffness. This computational homogenization technique is built entirely within a standard local continuum mechanics concept, where the response at a (macroscopic) material point depends only on the first gradient of the displacement field. Thus, this computational homogenisation framework is sometimes referred to as the "first-order".

In the subsequent sections, the essential steps of the first-order computational homogenisation process are discussed in more detail. First the problem on the microlevel is defined, then the aspects of the coupling between micro- and macrolevel are considered and finally the realization of the whole procedure within an FE context is explained.

2.2 Micro-to-macro-transitions at small strains

2.2.1 Deformation of a microstructure at small strains

Let $\{u: \mathbb{B} \times \mathbb{R} \to \mathbb{R}^3\}$ denote the displacement field at a material point $\{x \in \mathbb{B}\}$ and a time $\{t \in \mathbb{R}\}$ of the microstructure $\mathbb{B} \subset \mathbb{R}^3$, and $\boldsymbol{\varepsilon} := sym[\nabla u]$ be the microscopic strain. Furthermore, we introduce the velocity field $\dot{\boldsymbol{u}} := \partial_t u(x, t)$ and the acceleration field $\ddot{\boldsymbol{u}} := \partial_{tt}^2 u(x, t)$ of the microstructure.

2.2.2 Microscale boundary value problem

We assume that the RVE deforms in a state of dynamic equilibrium

$$div\boldsymbol{\sigma} - \rho_0 \ddot{\boldsymbol{u}} = 0 \quad \text{in } \mathbb{B} , \tag{85}$$

where the symmetric stress $\boldsymbol{\sigma}$ is assumed to be related to the strain $\boldsymbol{\varepsilon}$ by a constitutive equation

$$\boldsymbol{\sigma} := \partial_\varepsilon \, \hat{\psi}(\boldsymbol{\varepsilon}; \boldsymbol{x}) \text{ in } \mathbb{B} \tag{86}$$

governed by a strain energy function $\hat{\psi}$. Integrating equation (85) over the domain $\mathbb{B}$, and applying the Gauss theorem, yields the global expression of equilibrium conditions

$$\int_{\partial\mathbb{B}} \boldsymbol{\tau} \, dA - \int_{\mathbb{B}} \rho_0 \ddot{\boldsymbol{u}} \, dV = 0 \text{ and } \int_{\partial\mathbb{B}} \boldsymbol{x} \times \boldsymbol{\tau} \, dA - \int_{\mathbb{B}} \boldsymbol{x} \times \rho_0 \ddot{\boldsymbol{u}} \, dV = 0 \tag{87}$$

where

$$\boldsymbol{\tau} := \boldsymbol{\sigma}\boldsymbol{n} \text{ on } \partial\mathbb{B} \tag{88}$$

denotes the traction field on the surface with outward normal $\boldsymbol{n}$ at $\boldsymbol{x} \in \mathbb{B}$. The boundary value problem governing equilibrium of the microstructure B includes certain boundary conditions for the displacement $\boldsymbol{u}$, which relate the deformation of the microstructure to a prescribed

macroscopic strain mode $\bar{\boldsymbol{\varepsilon}}(t)$. These boundary conditions, that should be consistent with an averaging theorem, are presented in the next Section.

2.2.3 Averaging Relations and Hill's macro homogeneity condition

Let $\mathcal{V} \subset \mathbb{R}^3$ denote the RVE associated with the microstructure $\mathbb{B} \subset \mathbb{R}^3$. This volume is assumed to consist of the solid part $\mathbb{B}$ and the perforation part $\mathbb{H} \subset \mathbb{R}^3$ (Figure 2). Hence the decompositions of the RVE and the surface of the solid part are given as

$$\mathcal{V} = \mathbb{B} \cup \mathbb{H} \quad \text{and} \quad \partial\mathcal{V} = \partial\mathbb{B} \cup \partial\mathbb{H} \tag{89}$$

Accordingly, by use of this decomposition, the overall macrostress $\bar{\boldsymbol{\sigma}}(t)$ and the overall macro-strain $\bar{\boldsymbol{\varepsilon}}(t)$ of the microstructure $\mathbb{B}$ are defined as

$$\bar{\boldsymbol{\sigma}} := \frac{1}{|\mathcal{V}|}\int_{\partial\mathbb{B}} sym[\boldsymbol{\tau} \otimes \boldsymbol{x}]\, dA \quad , \qquad \bar{\boldsymbol{\varepsilon}} := \frac{1}{|\mathcal{V}|}\int_{\partial\mathbb{B}} sym[\boldsymbol{u} \otimes \boldsymbol{n}]\, dA \tag{90}$$

where $\boldsymbol{\tau}$ is the traction and u the displacement at $\boldsymbol{x} \in \partial\mathcal{V}$ on the surface of the representative volume. The averaging theorem, as formulated by Hill [5], requires the average of the microscopic stress power to be equal to the macroscopic stress power. We may write the macroscopic stress power in terms of the variables defined in (90)

$$\bar{\boldsymbol{\sigma}} : \dot{\bar{\boldsymbol{\varepsilon}}} = \frac{1}{|\mathcal{V}|}\int_{\partial\mathbb{B}} \boldsymbol{\tau} \cdot \dot{\boldsymbol{u}}\, dA \tag{91}$$

The sensitivity of the macroscopic stress $\bar{\boldsymbol{\sigma}}(t)$ with respect to the macroscopic strain $\bar{\boldsymbol{\varepsilon}}(t)$ is determined by the overall tangent moduli $\bar{\boldsymbol{C}}(t)$. In elasticity, we may write

$$\bar{\boldsymbol{\sigma}} = \bar{\boldsymbol{C}} : \dot{\bar{\boldsymbol{\varepsilon}}} \quad \text{with} \quad \bar{\boldsymbol{C}} := \partial_{\bar{\boldsymbol{\varepsilon}}}\, \bar{\boldsymbol{\sigma}}. \tag{92}$$
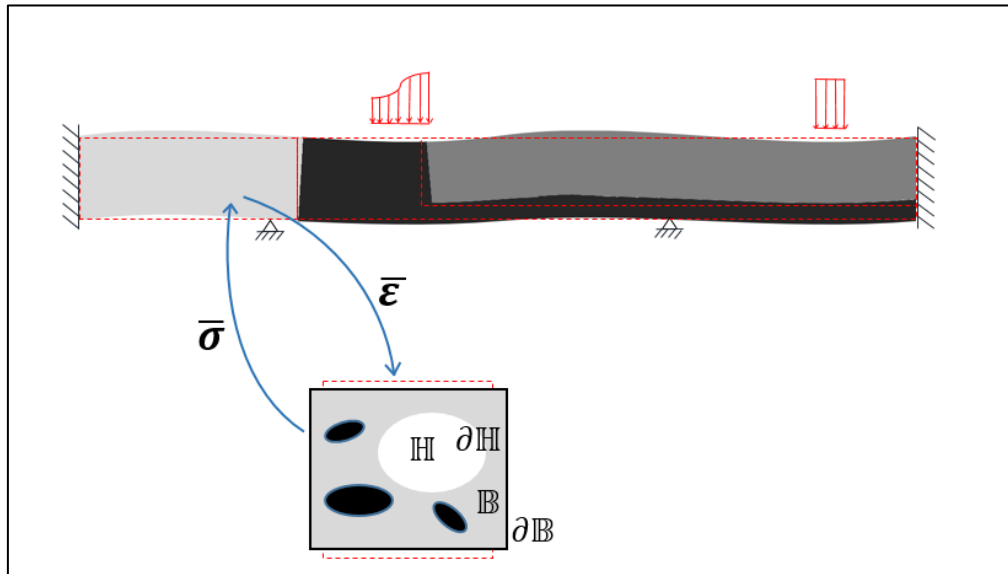

Figure 2 Scale transitions for small deformation multiscale problems. Red dashed lines denoted the undeformed configurtation of the structure.

2.2.4 Boundary conditions for the microstructure

Appropriate boundary conditions for the displacement **u** and the traction $\boldsymbol{\tau}$ are imposed on the microstructure in order to satisfy condition (91). It can be assumed that the tractions on the surface of the perforations in the interior of the RVE vanish, i.e.

$$\boldsymbol{\tau}(\boldsymbol{x},t) = 0 \quad \text{at} \quad \boldsymbol{x} \in \partial\mathbb{H} \tag{93}$$

The boundary conditions on the remaining part $\partial\mathcal{V}$, i.e. the surface of the RVE, must be related to given macroscopic overall variables. We investigate two classical cases: (i) linear displacements and (ii) periodicity conditions. A crucial aspect is the formulation in the deformation-driven context where the macroscopic strains $\bar{\boldsymbol{\varepsilon}}(t)$ are prescribed and the macroscopic overall stresses $\bar{\boldsymbol{\sigma}}(t)$ are computed. Thus, all boundary conditions mentioned above must be formulated in terms of the displacement field $\boldsymbol{u}$ and the given macroscopic strain mode $\bar{\boldsymbol{\varepsilon}}(t)$.

2.2.4.1 Linear displacements on the boundary

Prescribed displacement boundary conditions are expressed in terms of the macroscopic strain $\bar{\boldsymbol{\varepsilon}}$ as

$$\boldsymbol{u}(\boldsymbol{x},t) = \bar{\boldsymbol{\varepsilon}}(t)\boldsymbol{x} \quad \text{at} \quad \boldsymbol{x} \in \partial\mathcal{V} \tag{94}$$

This condition defines a linear mapping of the boundary ∂V of the RVE. Insertion of (94) into (91) confirms that the averaging theorem is a priori satisfied.

2.2.4.2 Periodic deformation and antiperiodic tractions on the boundary

Based on the assumption of microstructural periodicity presented in Section 2.1 a second possibility to a priori satisfy the averaging theorem (91) is to assume the periodicity conditions

$$\boldsymbol{u}(\boldsymbol{x}^+,t) - \boldsymbol{u}(\boldsymbol{x}^-,t) = \bar{\boldsymbol{\varepsilon}}(t)(\boldsymbol{x}^+ - \boldsymbol{x}^-) \qquad \text{(a)} \tag{95}$$
$$\boldsymbol{\tau}(\boldsymbol{x}^+,t) + \boldsymbol{\tau}(\boldsymbol{x}^-,t) = 0 \qquad \text{(b)}$$

representing periodic deformations and antiperiodic tractions on the boundary of the RVE Here, we consider opposite parts of the RVE boundary that compose the surface $\partial\mathcal{V} = \partial\mathcal{V}^+ \cup \partial\mathcal{V}^-$ with outward normal $n^+ = -n^-$ at associated points $\boldsymbol{x}^+ \in \partial\mathcal{V}^+$ and $\boldsymbol{x}^- \in \partial\mathcal{V}^-$, respectively. In order to show that (95) satisfies the averaging theorem, we at first take into account the antiperiodic traction condition (95)-b and recast the definitions (90) and (91) into the special forms

$$\bar{\boldsymbol{\sigma}} := \frac{1}{4|\mathcal{V}|} \int_{\partial\mathbb{B}} sym[[\![\boldsymbol{\tau}]\!] \otimes \boldsymbol{x}] \, dA \quad , \qquad \bar{\boldsymbol{\varepsilon}} := \frac{1}{4|\mathcal{V}|} \int_{\partial\mathbb{B}} sym[[\![\boldsymbol{u}]\!] \otimes \boldsymbol{n}] \, dA \tag{96}$$

and

$$\bar{\boldsymbol{\sigma}} : \dot{\bar{\boldsymbol{\varepsilon}}} = \frac{1}{4|\mathcal{V}|} \int_{\partial\mathbb{B}} [\![\boldsymbol{\tau}]\!] \cdot [\![\dot{\boldsymbol{u}}]\!] \, dA \tag{97}$$

respectively. Here, $[\![\bullet]\!](\boldsymbol{x},t) = (\bullet)^+ - (\bullet)^-$, and is defined at point $\boldsymbol{x} \in \partial\mathcal{V}$ on the surface of the microstructure; it denotes the jump of the field $(\bullet)$ with respect to the associated points

$x^+ \in \partial \mathcal{V}^+$ and $x^- \in \partial \mathcal{V}^-$. With this notation at hand, the periodic deformation condition (95)-a can be recast into the compact form

$$\llbracket \boldsymbol{u} \rrbracket (\boldsymbol{x}, t) = \bar{\boldsymbol{\varepsilon}}(t) \llbracket \boldsymbol{x} \rrbracket \quad \text{at} \quad \boldsymbol{x} \in \partial \mathcal{V} \tag{98}$$

which is in formal analogy to (94). Insertion of this result into (97) immediately shows that the averaging theorem is satisfied.

More details concerning the implementation of the microstructural boundary value problem and the accompanying boundary conditions in a discretized finite element setting for two- and three-dimensional continua can be found in [109]. For the case of thin shell structures and the specific manipulations that arouse from the plane stress conditions, the finite element implementation of the solution of the microstructural BVP will be described in detail in Chapter 4.

2.3 Micro-to-macro-transitions at finite deformations

2.3.1 Deformation of a microstructure at finite strains

The RVE deformation field in a point with the initial position vector $\boldsymbol{X}$ (in the reference domain V_0) and the actual position vector x (in the current domain) is described by the microstructural deformation gradient tensor $\boldsymbol{F}_m = (\nabla_{0m} \boldsymbol{x})^c$, where the gradient operator ∇_{0m} is taken with respect to the reference microstructural configuration

2.3.2 Microscale boundary value problem

We assume that the RVE deforms in a state of static equilibrium. This is expressed by the equilibrium equation in terms of the first Piola–Kirchhoff stress tensor $\boldsymbol{P}_m^c = \det(\boldsymbol{F}_m)\boldsymbol{\sigma}_m \cdot (\boldsymbol{F}_m^c)^{-1}$ as (in the absence of body forces) :

$$\nabla_{0m} \cdot \boldsymbol{P}_m^c = 0 \quad in \quad V_0 \tag{99}$$

where ∇_{0m} is the the gradient operator with respect to the current configuration of the microstructural cell.

The mechanical characterisations of the microstructural components are described by certain constitutive laws, specifying a time- and history-dependent stress–deformation relationship for every microstructural constituent.

$$\boldsymbol{P}_m^{(a)}(t) = \mathcal{F}_P^{(a)}\{\boldsymbol{P}_m^{(a)}(\tau), \tau \in [0, t]\} \tag{100}$$

where t denotes the current time; $\alpha = 1,\dots,N$ with N being the number of microstructural constituents to be distinguished (e.g. matrix, inclusion, etc.).

2.3.3 Averaging Equations

The actual coupling between the macroscopic and microscopic levels is based on averaging theorems. The integral averaging expressions have been initially proposed by Hill [110] for small deformations and later extended to a large deformation framework [111,112].

Firstly we focus on the averaging equations (Figure 3) concerning the micro–macro coupling of kinematic quantities. It is postulated that the macroscopic deformation gradient tensor $\boldsymbol{F_M}$ is the volume average of the microstructural deformation gradient tensor $\boldsymbol{F_m}$

$$\boldsymbol{F_M} = \frac{1}{V_0} \int_{V_0} \boldsymbol{F_m} \, dV_0 = \frac{1}{V_0} \int_{\Gamma_0} \boldsymbol{x} \boldsymbol{N} \, d\Gamma_0 \tag{101}$$

where the divergence theorem has been used to transform the integral over the undeformed volume V_0 of the RVE to a surface integral.

A similar averaging equation for the first Piola–Kirchhoff stress tensor can be expressed as

$$\boldsymbol{P_M} = \frac{1}{V_0} \int_{V_0} \boldsymbol{P_m} \, dV_0 \tag{102}$$

The first Piola–Kirchhoff stress tensor $\boldsymbol{P_M}$ can be expressed in terms of microstructural quantities defined on the RVE surface, by use of the following equation (with account for microscopic equilibrium $\nabla_{0m} \cdot \boldsymbol{P_m^c} = 0$ and the equality $\nabla_{0m} \boldsymbol{X} = \boldsymbol{I}$):

$$\boldsymbol{P_m} = (\nabla_{0m} \cdot \boldsymbol{P_m^c}) \boldsymbol{X} + \boldsymbol{P_m} \cdot (\nabla_{0m} \boldsymbol{X}) = \nabla_{0m} \cdot (\boldsymbol{P_m^c} \boldsymbol{X}) \tag{103}$$

Substitution of (103) into (102) application of the divergence theorem, and the definition of the first Piola–Kirchhoff stress vector $\boldsymbol{p} = \boldsymbol{N} \cdot \boldsymbol{P_m^c}$ give

$$\boldsymbol{P_M} = \frac{1}{V_0} \int_{V_0} \nabla_{0m} \cdot (\boldsymbol{P_m^c} \boldsymbol{X}) \, dV_0 = \frac{1}{V_0} \int_{\Gamma_0} \boldsymbol{N} \cdot \boldsymbol{P_m^c} \boldsymbol{X} \, d\Gamma_0 = \frac{1}{V_0} \int_{\Gamma_0} \boldsymbol{p} \boldsymbol{X} \, d\Gamma_0 \tag{104}$$

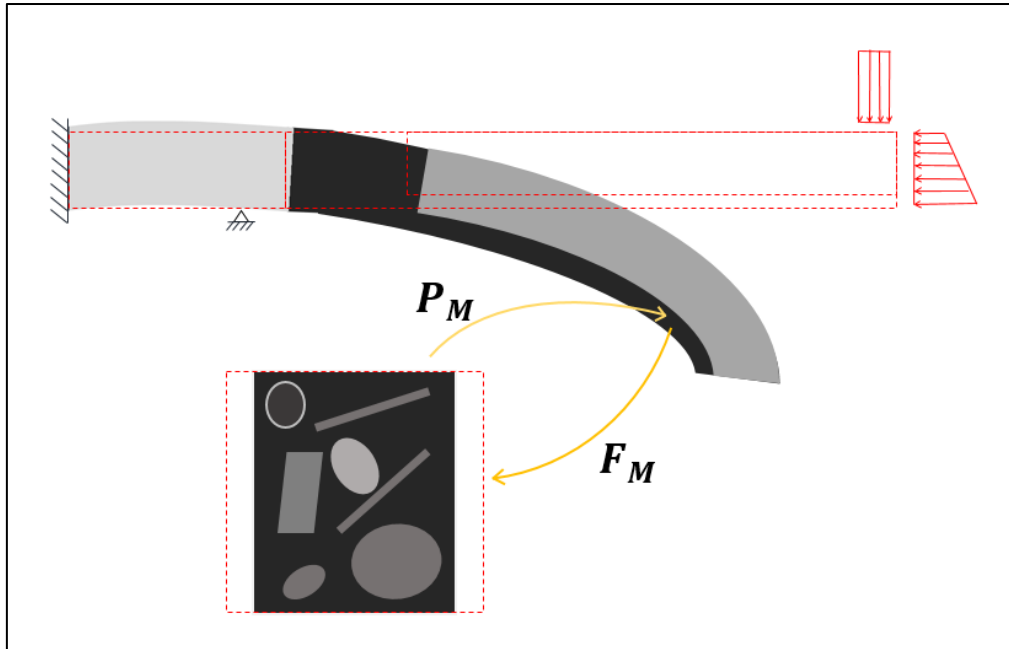**Figure 3 Scale transitions for large deformation multiscale problems. A dashed red line denotes the undeformed configuration of the structures**

2.3.4 Boundary Conditions for the microstructure

2.3.4.1   Prescribed Displacements

Deformation boundary constraints assume the following form for the position vector of a point on the RVE boundary in the deformed state:

$$x = F_M \cdot X \quad \text{with } X \text{ on } \Gamma_0 \tag{105}$$

where Γ_0 denotes the undeformed boundary of the RVE. This condition prescribes a linear mapping of the RVE boundary.

It can be verified that utilization of prescribed displacement boundary conditions (105) indeed leads to satisfaction of (101). Substitution of (105) into (101) and use of the divergence theorem with account for $\nabla_{0m} X = I$ give

$$
\tag{106}
$$
$$
F_M = \frac{1}{V_0} \int_{\Gamma_0} (F_M \cdot X) N \, d\Gamma_0 = \frac{1}{V_0} F_M \cdot \int_{\Gamma_0} XN \, d\Gamma_0
$$

$$
= \frac{1}{V_0} F_M \cdot \int_{\Gamma_0} (\nabla_{0m} X)^c \, d\Gamma_0 = F_M
$$

2.3.4.2   Periodic Conditions

A second possibility to a priori satisfy the averaging theorem (91) is to assume the periodicity conditions. These can be written in a general format for the microstructural RVE as

$$
\begin{aligned}
(x^+ - x^-) &= F_M(X^+ - X^-) &\quad \text{(a)} \\
p^+ &= -p^- &\quad \text{(b)}
\end{aligned}
\tag{107}
$$

representing periodic deformations (107)-a and antiperiodic tractions (107)-b on the boundary of the RVE. Here the (opposite) parts of the RVE boundary Γ_0^- and Γ_0^+ are defined such that $N^- = -N^+$ at correspondng points on Γ_0^- and Γ_0^+. The periodicity condition (107) being prescribed on an initially periodic RVE, preserves the periodicity of the RVE in the deformed state. Also it should be mentioned that, as has been observed by several authors [113,114] the periodic boundary conditions provide a better estimation of the overall properties than the prescribed displacement or prescribed traction boundary conditions.

The fact that use of periodic boundary conditions (107) indeed leads to satisfaction of (101), can be verified by direct substitution.

$$
\tag{108}
$$
$$
F_M = \frac{1}{V_0} \{ \int_{\Gamma_0^+} x^+ N^+ \, d\Gamma_0 + \int_{\Gamma_0^-} x^- N^- \, d\Gamma_0 \} = \frac{1}{V_0} \int_{\Gamma_0^+} (x^+ - x^-) N^+ \, d\Gamma_0
$$

$$
= \frac{1}{V_0} F_M \cdot \int_{\Gamma_0^+} (X^+ - X^-) N^+ \, d\Gamma_0 = \frac{1}{V_0} F_M \cdot \int_{\Gamma_0} XN \, d\Gamma_0 = F_M
$$

2.3.5 Hill's macro homogeneity condition

The averaging theorem, as formulated by Hill known also as macrohomogeneity condition [24,110] requires the macroscopic volume average of the variation of work performed on the RVE to be equal equal to the local variation of the work on the macroscale. Formulated in terms of a work conjugated set, i.e. the deformation gradient tensor and the first Piola–Kirchhoff stress tensor, the Hill–Mandel condition reads

(109)

$$\frac{1}{V_0} \int_{V_0} \boldsymbol{P_m} : \delta \boldsymbol{F_m^c} \, dV_0 = \boldsymbol{P_M} : \delta \boldsymbol{F_M^c} \quad \forall \delta \boldsymbol{x}$$

The averaged microstructural work in the left-hand side of (17) may be expressed in terms of RVE surface quantities

(110)

$$\delta W_{0M} = \frac{1}{V_0} \int_{V_0} \boldsymbol{P_m} : \delta \boldsymbol{F_m^c} \, dV_0 = \frac{1}{V_0} \int_{\Gamma_0} \boldsymbol{p} \cdot \delta \boldsymbol{x} \, d\Gamma_0$$

where the relation (with account for microstructural equilibrium)

$$\boldsymbol{P_m} : \nabla_{0m} \, \delta \boldsymbol{x} = \nabla_{0m} \cdot (\boldsymbol{P_m^c} \cdot \delta \boldsymbol{x}) - (\nabla_{0m} \cdot \boldsymbol{P_m^c}) \cdot \delta \boldsymbol{x} = \nabla_{0m} \cdot (\boldsymbol{P_m^c} \cdot \delta \boldsymbol{x}) \qquad \textbf{(111)}$$

and the divergence theorem have been used.

It can be easily shown that the previously introduced types of boundary conditions: prescribed displacements (105) or the periodicity conditions (107) all satisfy the Hill–Mandel condition a priori, if the averaging relations for the deformation gradient tensor (101) and for the first Piola–Kirchhoff stress tensor (102) are adopted. In the case of the prescribed displacements (105), substitution of the variation of the boundary position vectors $\delta \boldsymbol{x} = \delta \boldsymbol{F_M} \cdot \boldsymbol{X}$ into the expression for the averaged microwork (110) with incorporation of (104) gives

(112)

$$\delta W_{0M} = \frac{1}{V_0} \int_{\Gamma_0} \boldsymbol{p} \cdot (\delta \boldsymbol{F_M^c} \cdot \boldsymbol{X}) \, d\Gamma_0 = \frac{1}{V_0} \int_{\Gamma_0} \boldsymbol{p} \boldsymbol{X} \, d\Gamma_0 : \delta \boldsymbol{F_M^c} = \boldsymbol{P_M} : \delta \boldsymbol{F_M^c}$$

Similarly, substitution of the periodic condition (107) we get

$$\delta W_{0M} = \frac{1}{V_0} \left\{ \int_{\Gamma_0^+} \boldsymbol{p}^+ \delta \boldsymbol{x}^+ \, d\Gamma_0 + \int_{\Gamma_0^-} \boldsymbol{p}^- \delta \boldsymbol{x}^- \, d\Gamma_0 \right\} = \frac{1}{V_0} \int_{\Gamma_0^+} \boldsymbol{p}^+ (\delta \boldsymbol{x}^+ - \delta \boldsymbol{x}^-) \, d\Gamma_0$$

$$= \frac{1}{V_0} \int_{\Gamma_0} \boldsymbol{p}^+ (\boldsymbol{X}^+ - \boldsymbol{X}^-) \, d\Gamma_0 : \delta \boldsymbol{F_M^c} = \frac{1}{V_0} \int_{\Gamma_0} \boldsymbol{p} \boldsymbol{X} \, d\Gamma_0 : \delta \boldsymbol{F_M^c} = \boldsymbol{P_M} : \delta \boldsymbol{F_M^c}$$

(113)

More details concerning the implementation of the microstructural boundary value problem and the accompanying boundary conditions in a discretized finite element setting for two- and three-dimensional continua will not be discussed in this Chapter as they are given in detail in [57]. For large deformation multi-scale analysis of thin shell structures and the specific manipulations that arouse from the plane stress conditions, the finite element

implementation of the solution of the microstructural BVP will be described in detail in Chapter 5.

3 Non Linear Finite element modeling of thin shell structures

In this Chapter the incorporation of constitutive equations developed for three dimensional materials within the context of large deformation modelling of thin Kirchhoff Love shells is discussed. Two different approaches can be adopted: i) to use stress resultant material laws where the constitutive models are formulated entirely based on stress resultants ii) to define integration points in the thickness direction of the shell and to use stress-strain formulations of constitutive models. The second approach is presented, as it is the one to be utilized on the computational homogenisation of thin shells. The focus is on how the plane stress condition can be incorporated in the expression of existing constitutive laws and not on Kirchhoff Love kinematics that will be presented in detail in Chapters 4 and 5 for small and large deformation problems respectively. The Finite element solution of thin shell problems based on the Principle of Virtual Work is illustrated. Then the contribution of the constitutive law is outlined. Finally the implementation of the plane stress condition for several material models, such hyperelasticity[47,48] and elastoplasticity[39-46], is presented.

3.1 Principle of Virtual Work

The FE formulation is based on the Principle of Virtual Work. The internal and external virtual quantities for the KL shell take the following form:

$$\delta W_{int}^u = \int_{\Omega_0} \delta \boldsymbol{E} : \boldsymbol{S} \, dV = \int_{A_0} \delta \boldsymbol{\varepsilon} : \boldsymbol{N} + \delta \boldsymbol{\kappa} : \boldsymbol{M} \, dA \tag{114}$$

$$\delta W_{ext}^u = \int_{A_0} \delta \boldsymbol{u} \cdot \boldsymbol{f} \, dV \tag{115}$$

where $\boldsymbol{\varepsilon}$ and $\boldsymbol{\kappa}$ are the membrane and bending contributions of the in-plane Green Lagrange strain tensor $\boldsymbol{E} = E_{\alpha\beta}(\boldsymbol{G}^\alpha \otimes \boldsymbol{G}^\beta)$ such that

$$E_{\alpha\beta} = \varepsilon_{\alpha\beta} + \theta^3 \kappa_{\alpha\beta} \tag{116}$$
$$\varepsilon_{\alpha\beta} = \frac{1}{2}(\alpha_{\alpha\beta} - A_{\alpha\beta})$$
$$\kappa_{\alpha\beta} = B_{\alpha\beta} - b_{\alpha\beta}$$

where $\alpha_{\alpha\beta}$ and $\kappa_{\alpha\beta}$ are the covariant metric and curvature coefficients of the surface are defined by the first and second fundamental forms of surfaces, Ω_0 is the initial domain, A_0 denotes the undeformed midsurface, and $\boldsymbol{f}$ is the external load per unit area. $\boldsymbol{G}^i$ is the contravariant basis and $\boldsymbol{G}_i$ is the covariant basis at a point in the shell (Figure 4) Here the assumption that a differential volume element dV can be approximated by $dV \approx h dA$ applies.

Through thickness integration of the Second Piola Kirchhoff stress tensor $\boldsymbol{S} = S^{\alpha\beta}(\boldsymbol{G}_a \otimes \boldsymbol{G}_\beta)$ yields the membrane forces N and bending moments M

$$\boldsymbol{N} = \int_{-h/2}^{h/2} \boldsymbol{S} \, d\theta^3, \quad \boldsymbol{M} = \int_{-h/2}^{h/2} \boldsymbol{S} \theta^3 \, d\theta^3 \tag{117}$$

In the nonlinear FE solution, with residual vector $R^u = F^u_{ext} \text{-} F^u_{int}$, the vector of internal nodal forces $F^{u_r}_{int}$ is obtained by performing the variation of δW^u_{int} with respect to the discrete nodal displacement u_r. Its components read

$$F^{u_r}_{int} = \int \frac{\partial \boldsymbol{\varepsilon}}{\partial u_r} : \boldsymbol{N} + \frac{\partial \boldsymbol{\kappa}}{\partial u_r} : \boldsymbol{M} \, dA \tag{118}$$

$F^{u_r}_{ext}$ is the external load vector. The linearizaion of the residual vector yields the tangent stiffness matrix K^u, which, for displacement-independent loads, is obtained from the linearization of the internal force vector. Its components are

$$K^{internal}_{rs} = \int \left(\frac{\partial \boldsymbol{\varepsilon}}{\partial u_r} : \frac{\partial \boldsymbol{N}}{\partial u_s} + \frac{\partial^2 \boldsymbol{\varepsilon}}{\partial u_r \partial u_s} : \boldsymbol{N} + \frac{\partial \boldsymbol{\kappa}}{\partial u_r} : \frac{\partial \boldsymbol{M}}{\partial u_s} + \frac{\partial^2 \boldsymbol{\kappa}}{\partial u_r \partial u_s} : \boldsymbol{M} \right) dA \tag{119}$$

where $\widehat{\boldsymbol{C}}_A$, $\widehat{\boldsymbol{C}}_B$ and $\widehat{\boldsymbol{C}}_D$ are the thicknessintegrated material tensors

$$\widehat{\boldsymbol{C}}_A = \int_{-h/2}^{h/2} \widehat{\boldsymbol{C}} \, d\theta^3, \quad \widehat{\boldsymbol{C}}_B = \int_{-h/2}^{h/2} \widehat{\boldsymbol{C}} \theta^3 \, d\theta^3 \text{ and}, \quad \widehat{\boldsymbol{C}}_D = \int_{-h/2}^{h/2} \widehat{\boldsymbol{C}} (\theta^3)^2 \, d\theta^3 \tag{120}$$

and the components $\hat{C}^{\alpha\beta\gamma\delta}$ of the in-plane elasticity tensor at a through thickness integration point is obtained through static condensation as

$$\hat{C}^{\alpha\beta\gamma\delta} = C^{\alpha\beta\gamma\delta} - \frac{C^{\alpha\beta33} C^{33\gamma\delta}}{C^{3333}} \tag{121}$$

such that

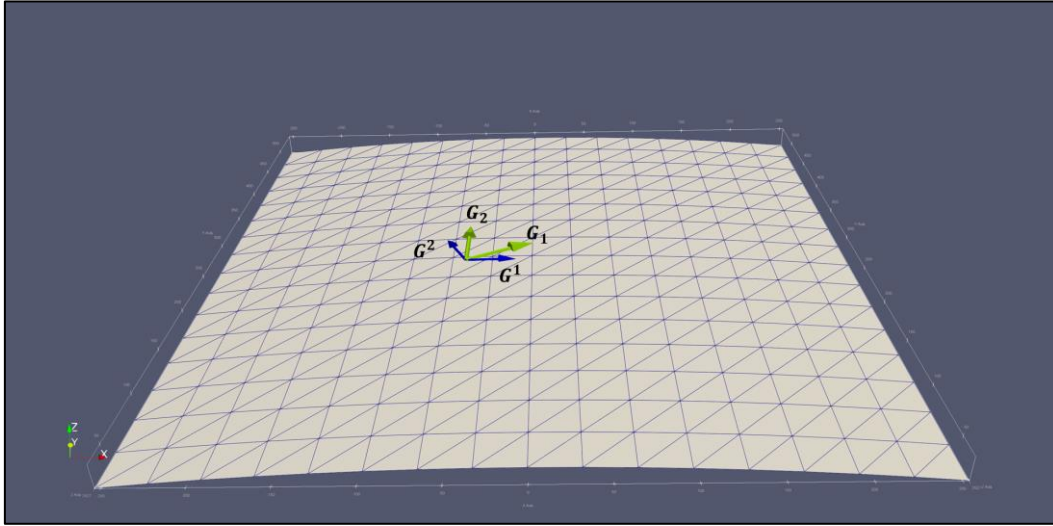$$dS^{\alpha\beta} = \hat{C}^{\alpha\beta\gamma\delta} E_{\gamma\delta} \tag{122}$$

Figure 4 : Vectors G_1, G_2 and G^1, G^2 of the covariant and contravariant bases respectively, in the undeformed configuration

3.2 Material Non linearity

The material response is reflected in the calculation of the stress and the corresponding elasticity tensor, given a certain strain value. The transverse normal deformation, that is originally undetermined in the kinematic description of the shell, is calculated such that the plane stress condition $S^{33}=0$ holds. Depending on the constitutive law expression, the plane

stress condition may yield the final value of the out of plane deformation in terms of the Green-Lagrange, the Cauchy-Green strain tensor or the out of plane stretch of the deformation gradient.

3.2.1 Hyperelasticity

3.2.1.1   Incompressible materials

To properly deal with incompressibility, the elastic strain energy function ψel(C) is classically augmented by a constraint term enforcing incompressibility ($J = 1$) via a Lagrange multiplier p, which can be identified as the hydrostatic pressure

$$\psi = \psi_{el}(\mathbf{C}) - p(J - 1) \tag{123}$$

For the shell model, the additional unknown p can be determined and statically condensed using the plane stress condition as shown in the following. First, the 3D tensors S^{ij} and C^{ijkl} are formally derived according to the following equations (124), considering also p as a function of C_{ij}

$$S^{ij} = \frac{\partial \psi}{\partial E_{ij}} = 2\frac{\partial \psi}{\partial C_{ij}} \quad \text{and} \quad C^{ijkl} = \frac{\partial S^{ij}}{\partial E_{kl}} = \frac{\partial^2 \psi}{\partial E_{ij}\partial E_{kl}} = 4\frac{\partial^2 \psi}{\partial C_{ij}\partial C_{kl}} \tag{124}$$

that yield

$$S^{ij} = 2\frac{\partial \psi_{el}}{\partial C_{ij}} - 2\frac{\partial p}{\partial C_{ij}}(J-1) - 2p\frac{\partial J}{\partial C_{ij}} \tag{125}$$

$$C^{ijkl} = 4\frac{\partial^2 \psi_{el}}{\partial C_{ij}\partial C_{kl}} - 4\frac{\partial^2 p}{\partial C_{ij}\partial C_{kl}}(J-1) - 4\frac{\partial p}{\partial C_{ij}}\frac{\partial J}{\partial C_{kl}} - 4\frac{\partial J}{\partial C_{ij}}\frac{\partial p}{\partial C_{kl}} - 4p\frac{\partial^2 J}{\partial C_{ij}\partial C_{kl}}$$

where the derivatives of the Jacobian determinant are obtained as

$$\frac{\partial J}{\partial C_{ij}} = \frac{1}{2}J\bar{C}^{ij}, \quad \frac{\partial^2 J}{\partial C_{ij}\partial C_{kl}} = \frac{1}{4}J(\bar{C}^{ij}\bar{C}^{kl} - \bar{C}^{ik}\bar{C}^{jl} - \bar{C}^{il}\bar{C}^{jk}), \quad C^{-1} = \bar{C}^{ij}\boldsymbol{G_i} \otimes \boldsymbol{G_j} \tag{126}$$

Substituting (126) into (124)

$$S^{33} = 2\frac{\partial \psi_{el}}{\partial C_{33}} - p\bar{C}^{33} = 0 \tag{127}$$

which can be solved for

$$p = 2\frac{\partial \psi_{el}}{\partial C_{33}}C^{33} = 0 \tag{128}$$

Accordingly the derivative of p is obtained as

$$\frac{\partial p}{\partial C_{ij}} = 2(\frac{\partial^2 \psi_{el}}{\partial C_{33}\partial C_{ij}}C_{33} + \frac{\partial \psi_{el}}{\partial C_{33}}\delta^{i3}\delta^{j3}) \tag{129}$$

Substituting Eqs. (128), (129) together with Eqs. (126) and $J = 1$ into Eqs. (125)we obtain:

$$S^{ij} = 2\frac{\partial \psi_{el}}{\partial C_{ij}} - 2\frac{\partial \psi_{el}}{\partial C_{33}}C_{33}\bar{C}^{ij} \tag{130}$$

$$C^{ijkl} = 4\frac{\partial^2 \psi_{el}}{\partial C_{ij}\partial C_{kl}} - 2\frac{\partial \psi_{el}}{\partial C_{33}}C_{33}(\bar{C}^{ij}\bar{C}^{kl} - \bar{C}^{ik}\bar{C}^{jl} - \bar{C}^{il}\bar{C}^{jk}) - 4\left(\frac{\partial^2 \psi_{el}}{\partial C_{33}\partial C_{ij}}C_{33} + \right. \tag{131}$$

$$\left. \frac{\partial \psi_{el}}{\partial C_{33}}\delta^{i3}\delta^{j3}\right)\bar{C}^{kl} - 4\bar{C}^{ij}(\frac{\partial^2 \psi_{el}}{\partial C_{33}\partial C_{kl}}C_{33} + \frac{\partial \psi_{el}}{\partial C_{33}}\delta^{k3}\delta^{l3})$$

Eqs. (130),(131) represent the 3D stress and material tensor for a general incompressible material with $J = 1$ and $S^{33} = 0$ incorporated and p eliminated.

For the shell model, only the in-plane components $S^{\alpha\beta}$ and $C^{\alpha\beta\gamma\delta}$ are considered, where $\bar{C}^{\alpha\beta} = g^{\alpha\beta}$ is used and $C_{33} = J_0^{-2}$ is obtained by $J = J_0 \sqrt{C_{33}}$ for $J = 1$. In the incompressible case, the static condensation of E_{33} can also be performed analytically. Eventually, the stress tensor and the statically condensed material tensor for the shell with incompressible materials are obtained as follows:

$$S^{\alpha\beta} = 2\frac{\partial\psi_{el}}{\partial C_{\alpha\beta}} - 2\frac{\partial\psi_{el}}{\partial C_{33}}J_0^{-2}g^{\alpha\beta} \tag{132}$$

$$\hat{C}^{\alpha\beta\gamma\delta} = 4\frac{\partial^2\psi_{el}}{\partial C_{\alpha\beta}\partial C_{\gamma\delta}} + 4\frac{\partial^2\psi_{el}}{\partial C_{33}^2}J_0^{-4}g^{\alpha\beta}g^{\gamma\delta} - 4\frac{\partial^2\psi_{el}}{\partial C_{33}\partial C_{\alpha\beta}}J_0^{-2}g^{\gamma\delta} \tag{133}$$

$$- 4\frac{\partial^2\psi_{el}}{\partial C_{33}\partial C_{\gamma\delta}}J_0^{-2}g^{\alpha\beta} + 2\frac{\partial\psi_{el}}{\partial C_{33}}J_0^{-2}(2g^{\alpha\beta}g^{\gamma\delta} + g^{\alpha\gamma}g^{\beta\delta}$$

$$+ g^{\alpha\delta}g^{\beta\gamma})$$

With Eqs. (132)(133), 3D solid material libraries providing $\frac{\partial\psi_{el}}{\partial C_{ij}}$ and $\frac{\partial^2\psi_{el}}{\partial C_{ij}\partial C_{kl}}$ can be directly used for the shell formulation.

3.2.1.2 Compressible material

For compressible materials, the plane stress condition $S^{33} = 0$ is satisfied by iteratively solving for C_{33}, using a Newton linearization of the plane stress condition similar to what was presented in [115,116]

$$S^{33} + \frac{\partial S^{33}}{\partial C_{33}}\Delta C_{33} = S^{33} + \frac{1}{2}C^{3333}\Delta C_{33} = 0 \tag{134}$$

From Eq (134) we obtain the incremental update

$$\Delta C_{33}^{(1)} = -2\frac{S_{(1)}^{33}}{C_{(1)}^{3333}}, \quad C_{33}^{(I+1)} = C_{33}^{(I)} + \Delta C_{33}^{(1)} \tag{135}$$

where I indicates the iteration step. With the updated $\mathbf{C}$, we compute the updates of $S(\mathbf{C})$ and $C(\mathbf{C})$. As an example, let us consider the following compressible neo-Hookean strain energy function

$$\psi = \frac{1}{2}\mu\left(J^{-2/3}tr(C) - 3\right) + \frac{1}{4}K(J^2 - 1 - \ln(J)) \tag{136}$$

with μ, K s the shear and bulk moduli. The 3D stress and material tensors are obtained, according to Eqs. (124) as

$$S^{ij} = \mu J^{-2/3}\left(G^{ij} - \frac{1}{3}tr(C)\bar{C}^{ij}\right) + \frac{1}{2}K(J^2 - 1)\bar{C}^{ij} \tag{137}$$

$$C^{ijkl} = \frac{1}{9}\mu J^{-2/3}\left(tr(C)\left(2\bar{C}^{ij}\bar{C}^{kl} + 3\bar{C}^{ik}\bar{C}^{jl} + 3\bar{C}^{il}\bar{C}^{jk}\right) - 6(G^{ij}\bar{C}^{kl} + \bar{C}^{ij}G^{kl})\right)$$

$$+ K(J^2\bar{C}^{ij}\bar{C}^{kl} - \frac{1}{2}(J^2 - 1)(\bar{C}^{ik}\bar{C}^{jl} + \bar{C}^{il}\bar{C}^{jk}))$$

As initial condition we use $C_{ij}^{(0)} = g_{ij}$

$$C_{ij}^{(0)} = \begin{bmatrix} g_{11} & g_{12} & 0 \\ g_{21} & g_{22} & 0 \\ 0 & 0 & 1 \end{bmatrix} \tag{138}$$

where the in-plane components remain invariant throughout the iteration, $C_{\alpha\beta} \equiv g_{\alpha\beta}$, and only $C_{33}^{(I)}$ is updated. With $C_{33}^{(I+1)}$ obtained according to Eqs. (135) $\text{tr}(C)^{(I+1)}$ and $J^{(I+1)}$ are updated, and the new values of $S_{(I+1)}^{ij}$, $C_{(I+1)}^{ijkl}$ are computed. This procedure is repeated until the plane stress condition is satisfied within a defined tolerance. Finally, the statically condensed material tensor $\hat{C}$ is computed according to (121), and only the in-plane components $S_{(I+1)}^{\alpha\beta}$ and $\hat{C}^{\alpha\beta\gamma\delta}$ are used for the shell model. As in the incompressible case, arbitrary 3D material models can be used for the shell formulation with this approach.

3.2.2 Elastoplasticity

The case of a three-dimensional isochoric von-Mises (J2) rate-independent plasticity theory in combination with isotropic hardening is examined, and we adopt the framework based on the multiplicative decomposition of the deformation gradient in elastic and plastic parts and on maximum plastic dissipation developed by Simo [117], see also Simo and Hughes [118]. With the chosen approach, the deformation gradient, F = dx/dX (dx, dX being infinitesimal line elements in the deformed and reference configurations), is decomposed in the product

$$F = F^e F^p \tag{139}$$

where F^e and F^p are, respectively, the elastic and plastic deformation gradients. This decomposition may be interpreted as a plastic deformation to a stress-free intermediate configuration, followed by a purely elastic deformation.

Based on the decomposition in Eq. (139), the total and plastic right Cauchy–Green deformation tensors are given by

$$\mathbf{C} = F^T F \quad \text{and} \quad \mathbf{C}^p = F^{pT} F^p \tag{140}$$

and the elastic left Cauchy–Green deformation tensor is given by

$$\mathbf{b}^e = F^e F^{eT} \tag{141}$$

A useful relation between elastic and plastic deformation playing an important role for the elasto-plasticity theory employed is

$$\mathbf{b}^e = F\mathbf{C}^{p-1}F^T \tag{142}$$

with its Lie derivative

$$\mathcal{L}\{\mathbf{b}^e\} = F\dot{\mathbf{C}}^{p-1}F^T \tag{143}$$

The total (free) energy functional is expressed as the sum of elastic and plastic energy contributions as follows

$$\tag{144}$$

$$\Phi(\mathbf{b}^e, J^e, a) = \int_{\Omega_0} (\Psi^e(\mathbf{b}^e, J^e) + |\Psi^p(a)) \, dV$$

where Ψ^e is the elastic strain energy density, $J^e = \det[\boldsymbol{F}^e]$, Ψ^p is the plastic energy density assuming isotropic hardening and α is the internal hardening variable.

For the purpose of describing the elastic response of the material, a neo-Hookean constitutive law of decoupled type is used, which will prove to be convenient for the subsequently introduced plasticity model. The elastic strain energy density Ψ^e is decomposed into a deviatoric (volume preserving) and volumetric (shape preserving) part

$$\Psi^e = \Psi^e_{vol} + \Psi^e_{dev} \tag{145}$$

with

$$\Psi^e_{vol} = \frac{k_0}{2}\left(\frac{J^{e2}-1}{2} - \ln J^e\right), \quad \Psi^e_{dev} = \frac{\mu}{2}(\bar{I}^e_b - 3) \tag{146}$$

where $\bar{\boldsymbol{b}}^e = J^{e^{-2/3}}\boldsymbol{b}^e$, $\bar{I}^e_b = \mathrm{tr}(\bar{\boldsymbol{b}}^e)$. Moreover, μ and κ_0 are the shear and the bulk modulus of the material, respectively. The Cauchy stress $\boldsymbol{\sigma}$ follows from the elastic strain energy density through the well-known relation

$$\boldsymbol{\sigma} = \frac{2}{J}\boldsymbol{b}^e\left(\frac{\partial \Psi^e}{\partial \boldsymbol{b}^e}\right) = \frac{2}{J}\boldsymbol{b}^e\left(\frac{\partial \Psi^e_{vol}}{\partial \boldsymbol{b}^e} + \frac{\partial \Psi^e_{dev}}{\partial \boldsymbol{b}^e}\right) = \frac{1}{J}\left(\frac{k_0}{2}(J^2 - 1)\mathbf{I} + \mu\,\mathrm{dev}\{\bar{\boldsymbol{b}}^e\}\right) \tag{147}$$

$$= \frac{1}{J}\{\boldsymbol{\tau}_{vol} + \boldsymbol{\tau}_{dev}\}$$

with $\boldsymbol{\tau}_{vol}$ and $\boldsymbol{\tau}_{dev}$ dev as the volumetric and deviatoric parts of the Kirchhoff stress tensor $\boldsymbol{\tau}$ and $dev(\cdot) = (\cdot) - 1/3\,tr(\cdot)\boldsymbol{I}$. Taking into account that plastic deformation is stress-free and isochoric, the superscript e has been omitted in $\boldsymbol{\sigma}$ and J.

The von-Mises yield function is given by

$$f(\boldsymbol{\tau}_{dev}, \boldsymbol{a}) = \|\boldsymbol{\tau}_{dev}\| - \sqrt{\frac{2}{3}}R(a) \leq 0 \tag{148}$$

where $R(a)$ is the hardening function that depends on the considered material. The associative flow rule stemming from the principle of maximum plastic dissipation can be shown to be [116]

$$\dot{\mathbf{C}}^{p-1} = \frac{2}{3}\dot{\lambda}\bar{I}^e_b \boldsymbol{F}^{-1}\boldsymbol{n}\boldsymbol{F}^{-T}, \quad \mathcal{L}\{\mathbf{b}^e\} = \frac{2}{3}\dot{\lambda}I^e_b\boldsymbol{n} \tag{149}$$

with $I^e_b = \mathrm{tr}[\mathbf{b}^e]$, $\boldsymbol{n} = \boldsymbol{\tau}_{dev}/\|\boldsymbol{\tau}_{dev}\|$ and $\dot{\lambda}$ as the plastic consistency factor. The evolution equation for the hardening variable is given by

$$\dot{\alpha} = \sqrt{\frac{2}{3}}\dot{\lambda} \tag{150}$$

Loading and unloading conditions are governed by the Kuhn–Tucker relations

$$\dot{\lambda} \geq 0, \, f \leq 0 \quad \text{and} \quad \dot{\lambda}f = 0 \tag{151}$$

Solution of the elasto-plastic constitutive equations requires a time integration scheme. A backward Euler integration scheme for the evolution equations is described in [40] (a consistent material tangent C is also provided therein). By use of this integration scheme calculation of the plastic factor λ, the hardening variables α and the Cauchy stress $\boldsymbol{\sigma}$ is achieved for the case of evolving plastic deformations. Then we express stresses by the second Piola–Kirchhoff stress tensor, which is obtained by the pull-back operation

$$S = JF^{-1}\sigma F^{-T} \tag{152}$$

and the plane stress condition $S^{33} = 0$ is achieved through a Newton Raphson by use of the linearization eq. (134). By use of eq. (135) C_{33} is iteratively updated and the update of the thickness stretch can be computed as

$$\lambda_3^{(I+1)} = \sqrt{C_{33}^{(I+1)}} \tag{153}$$

which is finally used to compute the updated deformation gradient coefficients of the deformation gradient

$$F_{i\beta}^{(I+1)} = F_{i\beta}^{(I)} \tag{154}$$
$$F_{i3}^{(I+1)} = \lambda_3^{(I+1)} \boldsymbol{G_i} \cdot \boldsymbol{a_3}$$

With the updated $\boldsymbol{F}$, the stress and material tangent tensors $\boldsymbol{S}$, and $\boldsymbol{C}$ are recomputed according to the procedure given in this section and in [40]. This iterative procedure outlined by equations (134)-(135),(153) and (154), along with the subsequent calculations of $\boldsymbol{S}$, and $\boldsymbol{C}$ is repeated until the plane stress condition is satisfied within a specified tolerance.

4 Multiscale modelling of thin Kirchhoff-Love shells at small deformations

In this Chapter an integrated theory for multi-scale analysis of thin shells is presented. It is based on the first order homogenization theory and it allows for modelling, in a FE^2 method's context of, of thin Kirchhoff Love shells. The shells can undergo small deformations and they exhibit a heterogeneous micro-structure consisting of nonlinear materials and cohesive interfaces. Emanating from Hill's averaging theorem, which is satisfied by appropriate averaging relations for thin shells, the macroscopic and microscopic boundary value problems are formulated with account for the specific assumptions of Kirchhoff Love theory in a small deformation and strains analysis context.

Main assumption of the proposed formulation is the out of plane periodicity of the microstructure, i.e. the thickness of the RVE is sufficiently smaller than that of the shell layer or the total shell section such that the scale separation hypothesis holds for the third dimension of the shell as well. This assumption is implemented by use of a multitude of RVEs that are assigned on each trough thickness integration point and are subjected to a different deformation state according to the macroscopic membrane and curvature strain that are extracted in Section 4.1 based on Kirchhoff Love theory.

A typical nested finite element solution scheme is represented in **Figure 5**. The consideration of a multilayered shell allows for the possibility of varying the RVE configuration in the thickness direction. For each mid-surface integration position (point A0 in **Figure 5**b), a multitude of through thickness integration points (points Ai in **Figure 5**c) are considered, each one corresponding to the material zone of a subsection in which plane stress conditions are assumed.
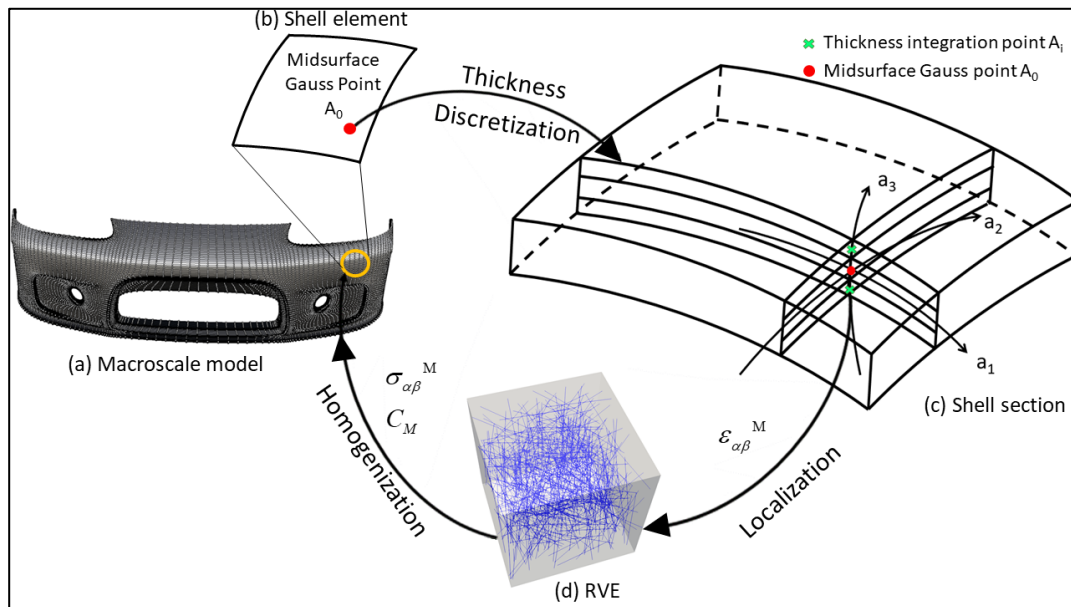

Figure 5: Schematic representation of the nested FE^2 flow for the analysis of Kirchhoff-Love shells (a) IGA discretization (b) Shell element (c)Through-thickness discretization at midsurface point A$_0$ of a shell element (d) Random RVE of local microstructural material topology at thickness integration point A$_i$

The mechanical response of the microscopically heterogeneous microstructure is extracted,

through appropriate averaging relations, for each macroscopic material point Ai, from a 3D RVE describing the local microstructural topology of the material. On the one hand the total macroscopic in-plane strains at a distance ζ of the mid-surface, are assigned to the corresponding through thickness integration material point (i.e point Ai in **Figure 5**c) represented by a 3D RVE of the composite material (localization step of **Figure 5**). The in-plane strains are enforced as equivalent displacements to the 3D RVE (Section 4.2). For the imposed displacements a microscale boundary value problem is formulated and solved (Section 4.4). On the other hand, another set of averaging equations is exploited for the calculation of averaged equivalent material properties, namely the stress and the corresponding plane stress constitutive matrix that are subsequently returned back to the macroscale Gauss Point A0. Through thickness integration of these quantities yields stress resultants at the mid-surface point A0 of the macroscopic model as well as their sensitivities. A detailed description of this step is provided in Section 4.4.

4.1 Small Deformation Kirchhoff-Love shell kinematics

Kirchhoff-Love shell formulation is an extension of the Euler-Bernoulli beam theory, where the shell kinematics can be described by the position of its mid-surface [119]. The main assumption of this theory is that lines that are normal to the surface, remain normal and straight after deformation, while the shell thickness remains unaltered.

The basic geometric quantities of the Kirchhoff-Love shell are depicted in **Figure 6**. Given a material point $\mathbf{x}$ on the mid-surface of the shell, the tangent vectors are obtained by $\mathbf{a}_\alpha = \mathbf{x},_\alpha$. Any point $\mathbf{x}_\theta$ that lies ζ distance from the mid-surface can be described by

$$\mathbf{x}_\theta = \mathbf{x}_{mid} + \zeta \mathbf{a}_3, \quad -t/2 \leq \zeta \leq t/2 \tag{155}$$

The unit normal vector is considered constant througout the thickness and is calculated by

$$\mathbf{a}_3 = \frac{\mathbf{a}_1 \times \mathbf{a}_2}{|\mathbf{a}_1 \times \mathbf{a}_2|} \tag{156}$$

The metric and curvature coefficients of the middle surface are defined as follows:

$$\alpha_{\alpha\beta} = \mathbf{a}_\alpha \cdot \mathbf{a}_\beta \tag{157}$$

$$b_{\alpha\beta} = -\alpha_\alpha \cdot \alpha_{3,\beta} = -\alpha_\beta \cdot \alpha_{3,\alpha} = \alpha_{\alpha,\beta} \cdot \alpha_\alpha \tag{158}$$

Similar to the base vectors of the mid-surface, the base vectors of all points can be defined accordingly:

$$\mathbf{g}_\alpha = \mathbf{a}_\alpha + \zeta \mathbf{a}_{3,\alpha} \tag{159}$$

$$\mathbf{g}_3 = \mathbf{a}_3$$

Throughout eqs (157)-(159), the Greek letters α,β take the values 1,2. The contravariant basis vectors are computed from $\mathbf{g}^i \cdot \mathbf{g}_j = \delta_j^i$, where δ_j^i is the Kronecker delta. Finally, the displacement of a mid-surface material point is obtained as the difference between the current and the reference configuration.

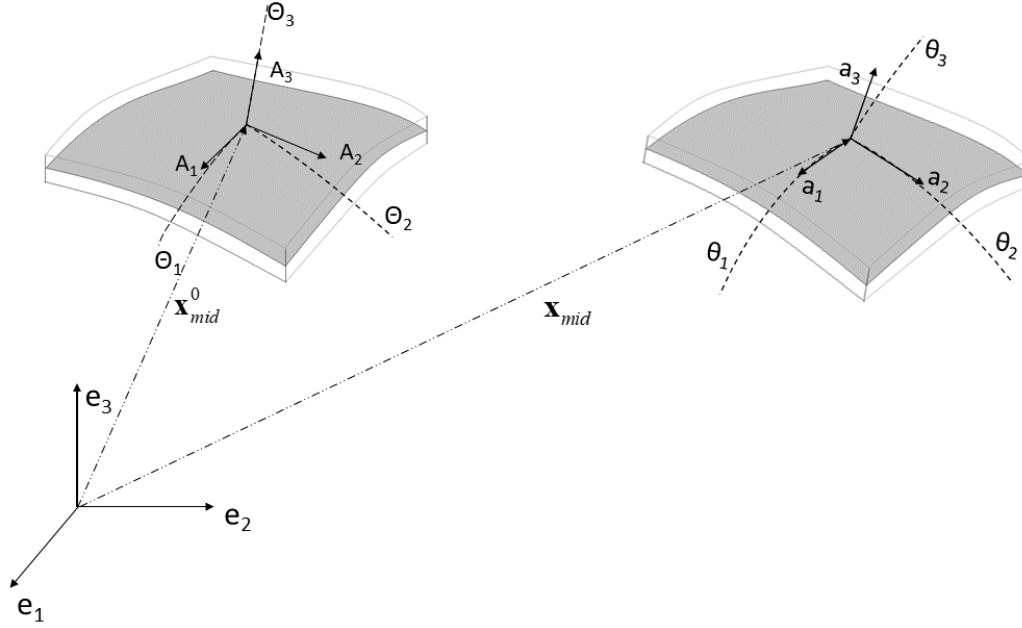$$\mathbf{u} = \mathbf{x}_{mid} - \mathbf{x}_{mid}^0 \tag{160}$$

Figure 6: Reference and deformed configuration of the shell represented by the mid-surface

Kinematic variables are described in terms of the quantities described in the previous section. The linear membrane and bending strains are calculated based on eqs. (157) and (158) by neglecting the quadratic terms in the derivatives of the displacements:

$$\varepsilon_{\alpha\beta} = \frac{1}{2}\left(a_\alpha^0 \cdot u_{,\beta} + a_\beta^0 \cdot u_{,\alpha}\right) \tag{161}$$

and

$$\kappa_{\alpha\beta} = \frac{1}{2}\left(a_\alpha^0 \cdot \Delta a_{3,\beta} + a_\beta^0 \cdot \Delta a_{3,\alpha} + u_{,\alpha} \cdot a_{3,\beta}^0 + u_{,\beta} \cdot a_{3,\alpha}^0\right) \tag{162}$$

where a_α^0 denotes the shell tangent vector at the reference configuration, while the derivatives of the normal vector in the reference configuration are calculated using the Jacobian j^0 as

$$a_{3,\alpha}^0 = \left(j^0\right)^{-1}\left(a_{1,\alpha}^0 \times a_2^0 + a_1^0 \times a_{2,a}^0\right) \tag{163}$$

$$\Delta a_{3,\alpha} = \left(j^0\right)^{-1}\left(u_{,1a} \times a_2^0 + u_{,1}^0 \times a_{2,a}^0 + a_{1,a}^0 \times u_{,2} + a_1^0 \times u_{,2a}\right) \tag{164}$$

The total macroscopic in-plane strains at a point of coordinate ζ from the mid-surface are given by:

$$\varepsilon_{\alpha\beta}^{M} = \varepsilon_{\alpha\beta} + \zeta \kappa_{\alpha\beta} \tag{165}$$

4.2 Microscale boundary value problem and Averaging Equations

Neglecting inertia forces, we assume that the RVE deforms in a state of static equilibrium [33] :

$$\nabla \cdot \sigma = 0 \quad \text{in} \quad \Omega_{RVE} \tag{166}$$

One of the basic assumptions of the proposed formulation is that the total strain of the macro-continuum equals the volume average of the microscopic strain:

$$\boldsymbol{\varepsilon}_M = \frac{1}{V_{RVE}} \int_{\Omega_{RVE}} \boldsymbol{\varepsilon}_m dV \qquad \text{(167)}$$

For the case of thin shells, this classic strain averaging condition is translated to an in-plane constraint only. Accordingly, in the following equation, a circumflex denotes restriction of the strain tensor to its in-plane coefficients only that are given by equation (165) and they refer to the covariant basis of the undeformed configuration.

$$\hat{\boldsymbol{\varepsilon}}_M = \frac{1}{V_{RVE}} \int_{\Omega_{RVE}} \hat{\boldsymbol{\varepsilon}}_m dV \qquad \text{(168)}$$

This condition is met by imposition of appropriate constraints in the 3D RVE boundary value problem. Specifically, a virtual plane stress element (element ABCD in **Figure 7**) is embedded at the mid-surface of the RVE as shown in **Figure 7**. Then, in-plane displacements equal to

$$\hat{u}_m = \hat{\boldsymbol{\varepsilon}}_M \hat{X}_m \qquad \text{(169)}$$

are prescribed to all perimeter nodes of the virtual element ABCD, while all peripheral mesh nodes of the 3D RVE are subjected to the same displacements as their projection nodes on the perimeter of the virtual element. More specifically, with reference to **Figure 7**, an edge nodal point L_{in} of the RVE with coordinates X_1, X_2, X_3 is prescribed with the same u_1 and u_2 displacement values, as dictated by eq. (22), with those of the corresponding vertex node Vi of the virtual element, i.e. with the node having the same X_1, X_2 coordinates:

$$u_1^{edge}\left(X_1, X_2, X_3\right) = \hat{u}_1^{vertex}\left(X_1, X_2\right) \qquad \text{(170)}$$
$$u_2^{edge}\left(X_1, X_2, X_3\right) = \hat{u}_2^{vertex}\left(X_1, X_2\right)$$

This way, the in-plane enforced displacements of the virtual element ABCD, make the 3D RVE to deform in a pattern that is consistent to plane stress conditions. The basic 3D deformation modes consistent to plane stress $\varepsilon_{11}^M, \varepsilon_{22}^M, \varepsilon_{12}^M$ are shown in **Figure 7**b. As for the out-of-plane strain coefficients ε_{33}^M, there is no need of imposing it as a constraint, since its value results indirectly from the out-of-plane deformation of the 3D RVE. As a result, out-of-plane shear strains $\varepsilon_{3\alpha}^M$ are automatically set to zero. Special care is taken to constraint out-of-plane rigid body motions. This is attained by constraining the displacements of three nodes of the bottom face, that are parallel to axis 3. Specifically, with reference to **Figure 7** 4, vertical displacements of nodes 3, 4 and 8 of the RVE are constrained. This boundary condition allows the RVE to deform freely in the in-plane directions, while at the same time eliminating possible out-of-plane rigid body motions.
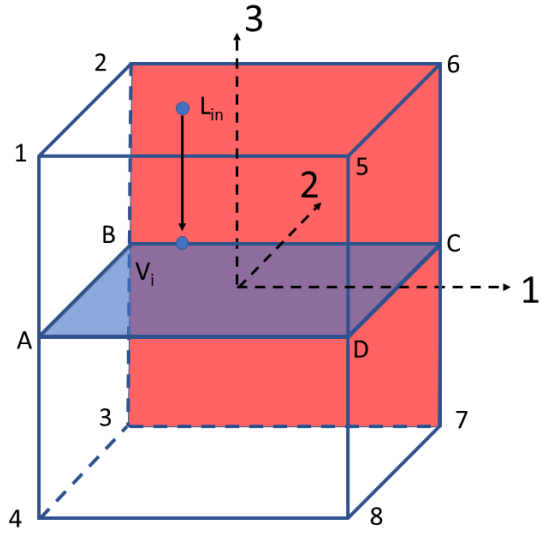
(a) Boundary conditions applied to the microstructure boundary value problem
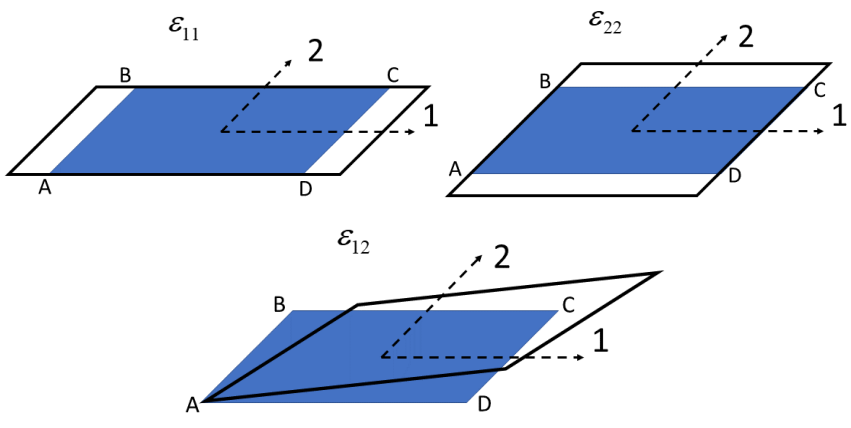
(b) Virtual element deformation modes
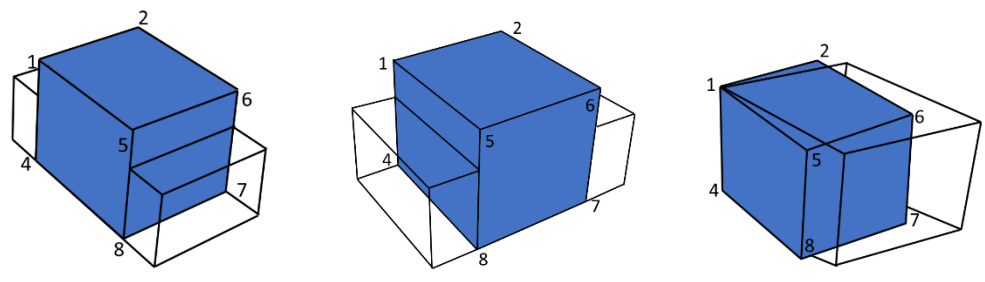
(c) Corresponding RVE deformation modes

Figure 7: Microstructure boundary value problem on a 3D RVE

The following averaging relation concerning the stress holds [33]:

$$\widehat{\boldsymbol{\sigma}}_M = \frac{1}{V_{RVE}} \int_{\Omega_{RVE}} \widehat{\boldsymbol{\sigma}}_m \ dV = \frac{1}{V_{RVE}} \int_{\partial\Omega_{RVE}} sym[\hat{t} \otimes x] \ dA \qquad (171)$$

where the divergence theorem has been applied and $\hat{t} = \sigma \cdot n$ is the field of the developed tractions on the boundary of the RVE. Out of plane tractions t are identically equal to zero, as no constraint is enforced in the direction 1 and the plane stress condition $\sigma_{33}^M = 0$ holds. By combination of eqs. (167) and (171) and taking into account eq.(169), the 3D macroscopic stress power equals to the volume average of the microscopic stress power.

$$\boldsymbol{\sigma}_M : \dot{\boldsymbol{\varepsilon}} = \frac{1}{V_{RVE}} \int_{\Omega_{RVE}} \boldsymbol{\sigma}_m : \dot{\boldsymbol{\varepsilon}}_m dV \tag{172}$$

This relation satisfies the Hill-Mandel principle of macro-homogeneity [54]. This way, the macroscopic energetic conjugate strain and stress measures can be replaced by their averaged microscopic counterparts in the expression of the principle of virtual work at the macroscale level.

4.3 Finite element solution of the microscale boundary value problem

A standard finite element solution scheme is employed for the boundary value problem of **Figure 7**, expressed at the micro-level in eq.(166). Upon discretization of the displacement field u_m and after constraining the rigid body modes of the 3D RVE model, the remaining degrees of freedom are partitioned into two categories, the constrained ones enforced by eq. (169) and the internal nodes that are totally free. The constrained nodes, denoted as e, include the in-plane displacement degrees of freedom of the peripheral nodes of the RVE and the internal, denoted as p, are the remainder internal nodes, combined with the out-of-plane degrees of freedom of the peripheral nodes.

$$u = \begin{bmatrix} u_e \\ u_p \end{bmatrix} \tag{173}$$

The same partitioning applies to the internal nodal forces P and the stiffness matrix K as well:

$$f = \begin{bmatrix} f_e \\ f_p \end{bmatrix} \qquad K = \begin{bmatrix} K_{ee} & K_{ep} \\ K_{pe} & K_{pp} \end{bmatrix} \tag{174}$$

For a peripheral node q of the RVE, the in-plane displacement vector u_q is derived from the corresponding projection of the RVE on ABCD and is given as:

$$u_q = \begin{bmatrix} u_1 & u_2 \end{bmatrix}^T = D_q^T \hat{\varepsilon} \tag{175}$$

where D_q and $\hat{\varepsilon}$ are given as:

$$D_q := \frac{1}{2} \begin{bmatrix} 2x_1 & 0 \\ 0 & 2x_2 \\ x_2 & x_1 \end{bmatrix}, \hat{\varepsilon}^T := [\varepsilon_{11}^M \quad \varepsilon_{22}^M \quad 2\varepsilon_{12}^M] \tag{176}$$

Assembling a global matrix D associated with all peripheral nodes P, the discretized form of the constraint eq. (169) is given as:

$$u_e = D^T \hat{\varepsilon}, \qquad D = \begin{bmatrix} D_1, D_2, ..., D_p \end{bmatrix} \tag{177}$$

Regarding the reaction forces acting on the internal degrees of freedom "e", an appropriate Lagrange multiplier δ is applied to enforce the constraint eq.(177). Then the discretized boundary value problem takes the form of the following algebraic equations:

$$f_e = \delta \tag{178}$$

$$f_p = 0$$

$$u_e - D^T \hat{\varepsilon} = 0$$

Upon solution of the micro-level boundary value problem of Figure 7, the macroscopic stress tensor can be calculated from eq.(171) that takes the discretized form:

$$\hat{\sigma} := \frac{1}{|V|} D\delta \tag{179}$$

For an equilibrium state of the microstructure and for an infinitesimal macroscopic strain increment $\Delta\hat{\varepsilon}$, the corresponding increments of the displacements $\Delta u_e, \Delta u_p$, Lagrange multipliers $\Delta\delta$ and total macroscopic strain $\Delta\hat{\sigma}$, is given as follows:

$$\Delta u_e = D^T \Delta\hat{\varepsilon} \tag{180}$$

$$\Delta u_p = -K_{pp}^{-1} K_{pe} \Delta u_e$$

$$\Delta d = \tilde{K}_{ee} D^T \Delta\hat{\varepsilon}$$

$$\Delta\hat{\sigma} = \frac{1}{V} D\Delta\delta$$

where $\tilde{K}_{ee} = K_{ee} - K_{ep} K_{pp}^{-1} K_{pe}$. Hence the macroscopic moduli are given as:

$$C = \frac{1}{|V|} D\tilde{K}_{ee} D^T \tag{181}$$

4.4   Principle of Virtual Work and Linearization of Internal Nodal Forces

The macroscopic shell stiffness matrix is derived from the principle of virtual work which can be written as

$$W = \int_V \boldsymbol{\sigma}_{\mathrm{M}} : \delta\boldsymbol{\varepsilon}_{\mathrm{M}} dV = \int_V f \cdot \delta u_M dV \tag{182}$$

where the virtual displacement δu_{M} is in the macroscopic level. The expression of internal virtual work at the left-hand side is further elaborated as:

$$\int_V \boldsymbol{\sigma}_{\mathrm{M}} : \delta\boldsymbol{\varepsilon}_{\mathrm{M}} = \int_A \left(\mathbf{n} : \delta\boldsymbol{\varepsilon}_{\mathrm{M}} + \mathbf{m} : \delta\boldsymbol{\kappa}_{\mathrm{M}} \right) dA \tag{183}$$

where through thickness integration delivers the macroscopic stress resultants as

$$n^{\alpha\beta} = \int_{-h/2}^{h/2} \sigma_{\mathrm{M}}^{\alpha\beta} d\zeta \tag{184}$$

$$m^{\alpha\beta} = \int_{-h/2}^{h/2} \sigma_{\mathrm{M}}^{\alpha\beta} \zeta d\zeta$$

where α, β take the values 1,2. Similar expressions are used for "thickness integrated" material matrices [47]. The moduli at each thickness integration point are obtained directly from eq.(181) as :

$$C_A = \int_{-h/2}^{h/2} C d\zeta, \qquad C_{\mathrm{B}} = \int_{-h/2}^{h/2} C\zeta d\zeta, \qquad C_D = \int_{-h/2}^{h/2} C\zeta^2 d\zeta \tag{185}$$

The differentials of membrane forces and bending moments are computed from:

$$dn^{\alpha\beta} = C_{M_A}^{\alpha\beta\gamma\delta} d\varepsilon_{\gamma\delta} + C_{M_B}^{\alpha\beta\gamma\delta} d\kappa_{\gamma\delta} \tag{186}$$

$$dm^{\alpha\beta} = C_{M_B}^{\alpha\beta\gamma\delta} d\varepsilon_{\gamma\delta} + C_{M_D}^{\alpha\beta\gamma\delta} d\kappa_{\gamma\delta}$$

Since equilibrium must be met for any variation of the displacement matrices δu_r it can be written that

$$\delta W = \frac{\partial W}{\partial u_r} \delta u_r = 0 \tag{187}$$

This leads to the following internal and external nodal forces:

$$F_r^{internal} = \int \boldsymbol{n} : \frac{\partial \boldsymbol{\varepsilon}_M}{\partial u_r} + \boldsymbol{m} : \frac{\partial \boldsymbol{k}_M}{\partial u_r} dA \tag{188}$$

$$F_r^{ext} = \int f \cdot \frac{\partial u}{\partial u_r} dA$$

Subsequently, the stiffness matrix is obtained as:

$$K_{rs}^{internal} = \int \frac{\partial \boldsymbol{n}}{\partial u_s} : \frac{\partial \boldsymbol{\varepsilon}_M}{\partial u_r} + \frac{\partial \boldsymbol{m}}{\partial u_s} : \frac{\partial \boldsymbol{k}_M}{\partial u_r} dA \tag{189}$$

Substitution of eq. (186) in eq. (189) yields the final expression for the shell's macroscopic stiffness matrix:

$$K_{rs}^{internal} = \int \left(C_{M_A} : \frac{\partial \boldsymbol{\varepsilon}_M}{\partial u_s} + C_{M_B} : \frac{\partial \boldsymbol{k}_M}{\partial u_s} \right) : \frac{\partial \boldsymbol{\varepsilon}_M}{\partial u_r} + \left(C_{M_B} : \frac{\partial \boldsymbol{\varepsilon}_M}{\partial u_s} + C_{M_D} : \frac{\partial \boldsymbol{k}_M}{\partial u_s} \right) : \frac{\partial \boldsymbol{k}_M}{\partial u_r} dA \tag{190}$$

4.5 Macroscale discretization

The displacement field that describes the deformation of the discretized shell in eq. (160) is interpolated as

$$u = \sum_{i=1}^{m} N_i u_i \tag{191}$$

where N_i are the shape function of multitude m used for the discretization and   are the nodal displacement quantities. Since quantities $\varepsilon_{\alpha\beta}^M, \kappa_{\alpha\beta}^M$ and $\Delta\alpha_{3,\alpha}$ in Section 4.1 are products of the displacements, they are obtained by partial differentiation of the shape functions. For the approximation of the displacement field of eq. and the resulting kinematic variables, a minimum C^1 continuity is required, due to the second derivatives of the displacements appearing in the curvature terms of eq. (162). This continuity requirements can be met with by use of appropriate discretization techniques such as subdivision surfaces or IGA.

4.5.1 Subdivision Sutfaces

The use of subdivision surfaces for thin shell element analysis was initially introduced and also used for finite deformation analysis by Cirak [120-121]. Main characteristic of the subdivision surfaces based interpolation scheme is that, contrary to conventional finite element interpolations, the displacement field within an element depends not only on the displacements of the nodes attached to the element but also on the adjacent elements.

Subdivision schemes construct smooth surfaces through a limiting procedure of repeated refinement starting from an initial mesh. This initial mesh can be referred to as the control mesh of the surface. The mesh is refined, e.g., all faces are quadrisected followed by the computation of new nodal positions. These positions are simple, linear functions of the

nodal positions of the coarser mesh. For the schemes of interest these computations are local, i.e. they involve only nodal positions of the coarser mesh within a small, finite topological neighborhood, leading to very efficient implementations. Using a suitable choice of weights, such subdivision schemes can be designed to produce a smooth surface in the limit. Subdivision methods which result in limit surfaces whose curvature tensor is square integrable are especially appealing for geometrical modelling applications and for the purpose of thin-shell analysis.

In this thesis use of Loop's subdivision scheme was made. It is an 'approximating' scheme, which means that according to it, we evaluate new nodal positions for the newly created vertices, as well as for the vertices inherited from the coarser mesh. This scheme produces limit surfaces which are globally C2 except at a number of isolated points where they are only C1.

Refinement process

In Loop's subdivision scheme, the control mesh and all refined meshes consist of triangles only. These are refined by quadrisection (Figure 8). After the refinement step, the nodal positions of the refined mesh are computed as weighted averages of the nodal positions of the unrefined mesh.
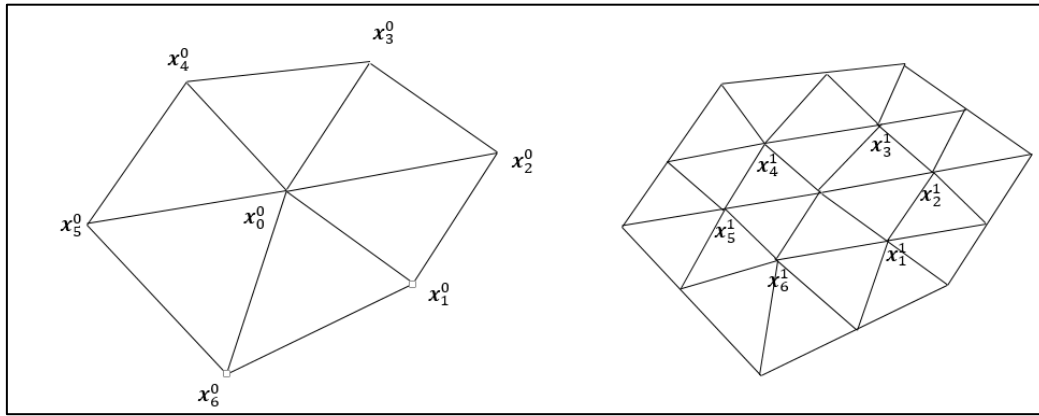

Figure 8 Refinement of triangular mesh by quadrisection

We distinguish two cases: new vertices associated with the edges of the coarser mesh, and old vertices of the coarse mesh. The coordinates of the newly generated nodes x_1^1, x_2^1 and x_3^1 on the edges of the previous are computed as

$$x_I^{k+1} = \frac{3x_0^k + x_{I-1}^k + 3x_I^k + x_{I+1}^k}{8}, \ \ I=1,\dots,N \tag{192}$$

whereby index I is to be understood in modulo arithmetic. The old vertices get new nodal positions according to

$$x_0^{k+1} = (1 - Nw)x_0^k + wx_I^k \dots + wx_N^k \tag{193}$$

where x^k are the nodal positions of the mesh at level k and x^{k+1} are the respective positions for the mesh $k + 1$. The valence of the vertex, i.e. the number of edges incident on it, is denoted by N. Note that all newly generated vertices have valence 6 while only the vertices of the original mesh may have valence other than 6. We will refer to the former case (valence = 6) as regular and to the latter case as irregular. Equations (192) and (193) are
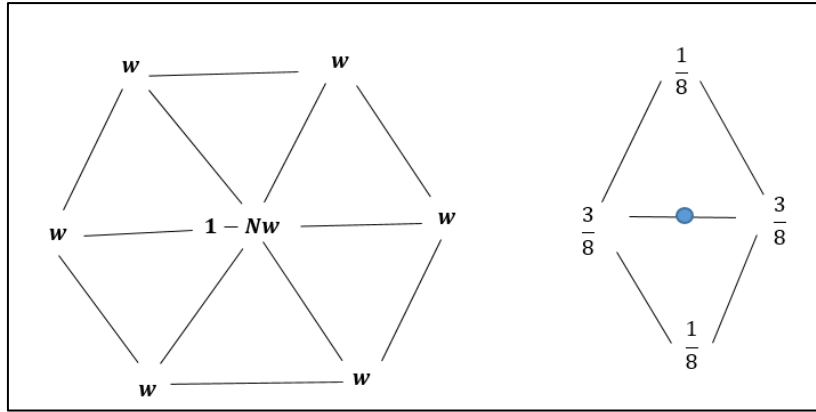
Figure 9 Refinement mask for Loop's Subdivision scheme

visualized in symbolic form in Figure 9 with the so-called subdivision mask. It is not obvious how to choose the parameter w to get C1 continuous surfaces. In the original scheme, Loop [122] proposed

$$w = \frac{1}{N}\left[\frac{5}{8} - \left(\frac{3}{8} + \frac{1}{4}\cos(\frac{2\pi}{N})\right)^2\right]$$

(194)

As it turns out other values for w also give smooth surfaces. For example, Warren's [123] choice for w is simpler to evaluate than that of Equation (194):

$$w = \frac{3}{8N} \ for \ N > 3 \quad and \quad w = \frac{3}{16} \ for \ N = 3$$
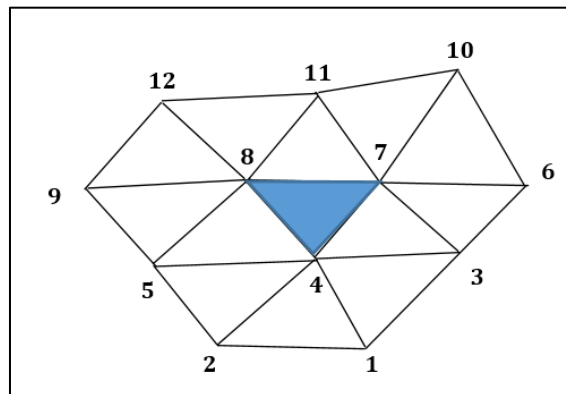
(195)

Figure 10 A regular box-spline patch with 12 control points

Limit surface

A convergence study followed in [120] shows that a limit position of the subdivision surface can easily be evaluated. For the interior of a triangular subsection, at a gauss point for example, the position and tangents of the limit surface can be calculated by use of quartic box splines, since Loop's scheme actually generalizes them. If the valencies of the vertices of a given triangle are all equal to 6, the resulting piece of limit surface is exactly described by a single quartic box-spline patch, for which very efficient evaluation schemes exist at arbitrary parameter locations. We call such a patch '*regular*' (Figure 10). Regular patches are controlled by the following 12 basis functions since only their support overlaps the given patch. A local triangular parametrization of the element is given as v=ξ, w=η and u=1-ξ-η.

68

$$N_1 = a(u^4 + 2\,u^3 v), \qquad\qquad (a=1/12) \tag{196}$$
$$N_2 = a(u^4 + 2\,u^3 w)$$
$$N_3 = a(u^4 + 2\,u^3 w + 6\,u^3 v + 6\,u^2 vw + 12u^2 v^2 + 6uv^2 w + 6uv^3 + 2v^3 w + v^4)$$
$$N_4 = a(6u^4 + 24u^3 w + 24u^2 w^2 + 8uw^3 + w^4 + 24u^3 v + 60u^2 vw + 36uvw^2$$
$$+ 6vw^3 + 24u^2 v^2 + 36uv^2 w + 12v^2 w^2 + 8uv^3 + 6v^3 w + v^4)$$
$$N_5 = a(u^4 + 6u^3 w + 12u^2 w^2 + 6uw^3 + w^4 + 2u^3 v + 6u^2 vw + 6uvw^2 + 2vw^3)$$
$$N_6 = a(2uv^3 + v^4)$$
$$N_7 = a(u^4 + 6u^3 w + 12u^2 w^2 + 6uw^3 + w^4 + 8u^3 v + 36u^2 vw + 36uvw^2 + 8vw^3$$
$$+ 24u^2 v^2 + 60uv^2 w + 24v^2 w^2 + 24uv^3 + 24v^3 w + 6v^4)$$
$$N_8 = a(u^4 + 8u^3 w + 24u^2 w^2 + 24uw^3 + 6w^4 + 6u^3 v + 36u^2 vw + 60uvw^2 +$$
$$24vw^3$$
$$+ 12u^2 v^2 + 36uv^2 w + 24v^2 w^2 + 6uv^3 + 8v^3 w + v^4)$$
$$N_9 = a(2uw^3 + w^4)$$
$$N_{10} = a(2v^3 w + v^4)$$
$$N_{11} = a(2uw^3 + w^4 + 6uvw^2 + 6vw^3 + 6uv^2 w + 12v^2 w^2 + 2uv^3 + 6v^3 w + v^4)$$
$$N_{12} = a(2vw^3 + w^4)$$

If a triangle is irregular, i.e. one of its vertices has valence other than 6 the resulting patch is not a quartic box spline. Figure 11 shows an irregular patch (center) with a single vertex of valence 7. After one level of subdivision this patch is divided into four patches, three of which are regular. If the desired parameter value lies within those patches we may immediately evaluate the surface by using the canonical regular-patch evaluation routine. If our desired parameter location lies within the fourth sub-patch, we must repeatedly subdivide until it falls within a regular patch. This can be achieved for any parameter value away from the irregular vertex. As shown in Figure 11, after one subdivision step the triangles marked one, two, and three are regular patches. The action of the subdivision operator for this entire neighbourhood can again be described by a matrix

$$\mathbf{X}^1 = A\mathbf{X}^0 \tag{197}$$

In the following applications simple geometries consisting of regular patches are considered. More details for the derivation of matrix $\mathbf{A}$ are given in [120].
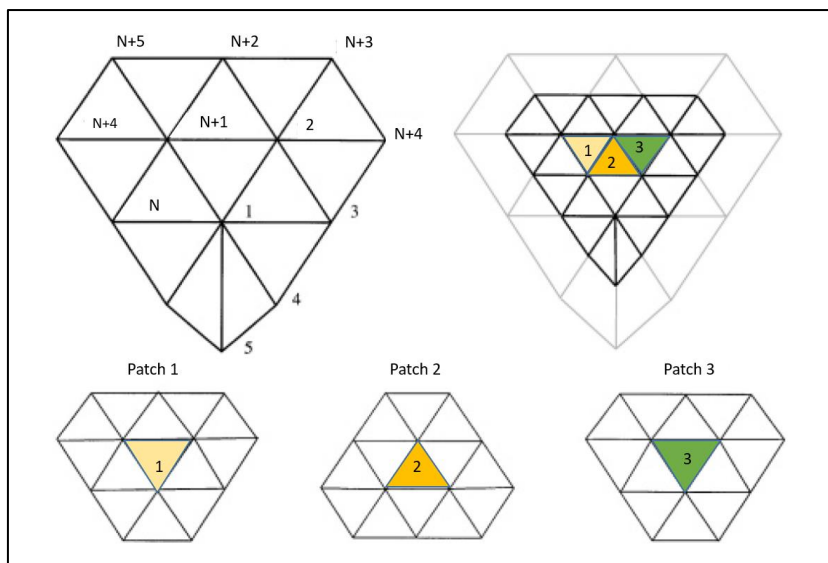

Figure 11 Refinement near an extraordinary vertex

4.5.2 T-Splines

T-spline shape functions [124] are also utilized for the discretization of the macroscale models. The formulation proposed in [125] is adopted, in which higher continuity T-splines are transformed with the aid of a T-spline plugin, to an equivalent C^0 finite element representation utilizing Bézier shape functions [126]. This process enables the use of complex T-spline geometries, which cannot be represented with NURBS without laborious preprocessing. In addition, the resulting C^0 Bézier elements [127] permits a straightforward integration of isogeometric analysis into the existing in-house FEM code MSolve [128]

T-splines were introduced as a generalization of NURBS in order to alleviate their drawbacks, the most profound among which is that they achieve only C^0 continuity across patch boundaries. In addition, in case two NURBS patches do not share a common boundary curve, even the aforementioned C^0 continuity is not attainable, thus making the coupling laborious, as several knot insertions are required, that propagate throughout the domain. This procedure introduces a multitude of Control Points thus adding a significant burden to the geometrical modelling procedure. T-splines alleviate all the aforementioned deficits by abolishing the tensor product structure of NURBS, thus being the first CAD technology that enables actual local refinement. More specifically, using T-spline technology enables the control grid to include T- junctions which are mesh vertices with three converging edges. The new control grid structure is referred to as T-mesh. In contrast to NURBS, where isogeometric elements are generated by the tensor product segmentation of a parametric domain from global knot vectors, the T-splines elements are rectangular tiles of the parametric domain. Figure 12a depicts an example of a simple T-mesh configuration where it can be seen that the tensor product structure of NURBS is no longer present. Despite the fact that no global knot vector exists, local knot vectors can be calculated for each one of the control points using the T-mesh structure, in order to define the support of the shape functions. As illustrated in **Figure 12**b, anchors denoted by the square dots represent the parametric positions of control points. Depending on even or odd polynomial degrees, these anchors lie at the center of the elements or at the edges of the faces (**Figure 12**a). By picking p+2 values, including the anchor position in odd degree cases, local knot vectors are generated for each parametric direction. Thus, given a local knot vector $\Xi_\alpha = \left\{\xi_1, \xi_2, \ldots, \xi_{p+1}, \xi_{p+2}\right\}$ and the polynomial degree p, the T-Spline basis functions can be computed using the Cox-de-Boor recursive formula [129]. For the purposes of numerical examples given in Section 4.7, the computation of the T-Spline basis functions is not performed via the aforementioned local knot value vector procedure, rather with the aid of the Bézier extraction process that enables the representation of highly continuous advanced Splines into multiple C^0 Bézier pieces. For a detailed description the reader is referred to [124,130,131], that provide an extensive study of the T-Splines technology. The Bézier extraction [132,133] utilized in the numerical examples will be now described.

Specifically, given the univariate local knot vector $\Xi_\alpha = \left\{\xi_1, \xi_2, \ldots, \xi_{p+1}, \xi_{p+2}\right\}$ of a T-Spline, the extended local knot value vector is generated by transforming the arbitrary type into an open one. This is achieved by repeating initial and final values of the local knot vector, until their multiplicity is p+1. Then, the extraction procedure is performed at the extended knot value vector. The process of computing the Bézier extraction operator **C**, is based on isogeometric h-refinement. By repeating all internal knot values until their multitude is p, p being the polynomial degree a refinement operator is produced, which coincides with the

extraction operator. In detail, for every Knot Value ξ_κ inserted in the local knot value vector, the initial Control Points net P_A is augmented and thus the new Control Points $\bar{P}_A$ are computed by

$$\bar{P}_A = \begin{cases} P_1, & A=1 \\ a_A P_A + (1-a_A)P_{A-1}, & 1<A<m \\ P_n, & A=m \end{cases} \tag{198}$$

where m is the initial multitude of Control Points and n the final one. The coefficients a_A are computed by

$$a_A = \begin{cases} 1, & 1 \le A \le k\text{-}p \\ \dfrac{\xi_\kappa - \xi_A}{\xi_{A+p} - \xi_A}, & k\text{-}p\text{+}1 \le A \le k \\ 0, & A \ge k\text{+}1 \end{cases} \tag{199}$$

In case of multiple simultaneous insertions, eq.(198) is transformed to

$$\bar{P}^{j+1} = \left(C^j\right)^T P^j \tag{200}$$

The product of these insertion operators yields the expected extraction operator. Note that in case of T-Spline basis functions, the univariate extraction operator is generated in a row-by-row basis from the shape functions that affect the element. For the bivariate case, the equivalent extraction operator is produced as a Kronecker product of the univariate extraction operators per parametric direction as follows

$$C^e = C^\xi \otimes C^\eta \tag{201}$$

The detailed process of Bézier extraction is described in detail in [127,133]. Since the process of [125] is employed, the Bézier extraction operation is utilized for the mapping of the T-Spline domain to the Bézier elements domain:

$$\mathbf{N}^e(\xi,\eta) = \mathbf{C}^e \mathbf{B}(\xi,\eta) \tag{202}$$

where C^e is the elemental extraction operator and $\mathbf{B}(\xi,\eta)$ the bivariate Bernstein polynomials that serve as basis for the Bézier geometries:

$$\mathbf{B}(\xi,\eta) = B_i^n(\xi) B_j^m(\eta) \tag{203}$$

where

$$B_i^n(u) = D(i,n) u^i (1-u)^{n-i} \tag{204}$$

the univariate Bernstein polynomials and $D(n,i)$ the binomial coefficients.

$$D(n,i) = \frac{n!}{i!(n-i)!} \tag{205}$$

Rational T-spline shape functions are then calculated using the following formula:

$$R^e(\xi) = \frac{W^e N^e(\xi)}{\left(w^e\right)^T N^e(\xi)} \tag{206}$$

where $R^e(\xi)$ are the elemental rational T-Spline shape functions, w^e and W^e the element weight vector and diagonal weight matrix, respectively. By combining eqs. (202) and (205) we obtain:

$$R^e(\xi) = \frac{W^e C^e B(\xi)}{(w^e)^T C^e B(\xi)} \tag{207}$$

Consequently, having computed the rational T-spline functions at any given control point grid P_{ij}, the T-spline surface is generated by:

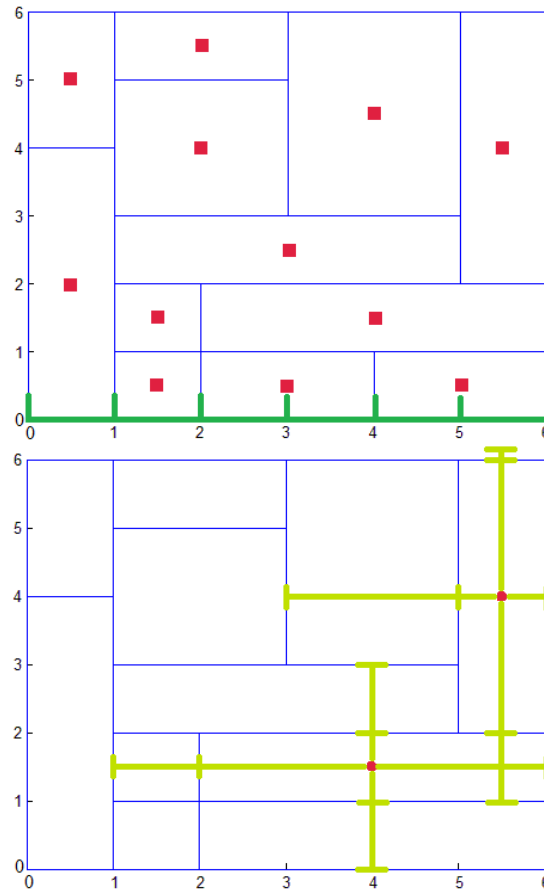$$S(\xi,\eta) = \sum_i \sum_j P_{ij} R_i^e(\xi) R_j^e(\eta) \tag{208}$$

Figure 12: a) T-mesh with rectangular isogeometric elements. Green line indicates the parametric axis ξ segmentation in case of a full tensor product NURBS shape functions that would result in the knot value vector $\Xi=\{0,0,0,1,2,3,4,5,6,6,6\}$. b) Local knot-vectors

4.6 Stochastic properties of the microstucture

As mentioned above, a stochastic RVE generator is developed to account for material heterogeneities at the mesoscale level of RVEs. The generator is based on two uncertainty types, namely the inclusion dispersion and orientation inside the matrix as well as their spatial variability inside the RVE described with a variable volume fraction parameter [134].

4.6.1 RVE with embedded inclusions

Given the RVE dimensions, i.e. length L_{matrix}, width W_{matrix} and height H_{matrix} and the type of inclusions, the RVE generator distributes the inclusions in the matrix either uniformly in a unidirectional pattern (**Figure 14**), or with random orientations (**Figure 21**). The coordinates of an insertion point (Point A in **Figure 13**) of an inclusion are randomly generated inside the matrix assuming a uniform distribution described by the uncorrelated random variables X_A, uniformly distributed in the range $[0, L_{matrix}]$, Y_A uniformly distributed in the range $[0, W_{matrix}]$ and Z_A, uniformly distributed in the range $[0, H_{matrix}]$.

To define the orientation of the inclusions, an additional point is inserted (Point B in **Figure 13**) defining an additional orientation random variable, namely the Euler angle φ, which is also assumed uniformly distributed in $[0, 2\pi]$. This angle, together with a fixed length parameter completely define the coordinates of insertion point B.

The spatial variability of the volume fraction (VF) is taken into account by assigning a different RVE at each integration point of the domain. Specifically, a multitude of RVEs with varying VFs are constructed and randomly distributed throughout the macroscopic domain. The spatial variability of the VF used for the construction of the RVEs at different domain locations is modeled using random fields and simulated via series expansion of the Karhunen-Loève method [135]:

$$w(\mathbf{x}, \theta) = \sum_{n=0}^{\infty} \sqrt{\lambda_n} \xi_n(\theta) f_n(\mathbf{x}) \tag{209}$$

where $\xi_n(\theta)$ is a set of uncorrelated Gaussian random variables and λ_n and $f_n(\mathbf{x})$ are the eigenvalues and eigenvectors of the autocorrelation function, respectively.

Both the matrix and the inclusions are discretized independently, i.e. without common nodes. For the purposes of the numerical examples of Section 4.7, continuum finite elements are used for the discretization of the RVE matrix, while inclusions in the form of carbon nanotubes are discretized with two-noded structural beam elements. The contribution of each inclusion to the stiffness of the RVE is calculated via the embedded element technique (**Figure 13**a), in which the discretized inclusion degrees of freedom are kinematically constrained to the degrees of freedom of the surrounding matrix. This kinematic relationship between the matrix and the inclusion degrees of freedom, is analyzed in the three-dimensional case, by utilizing a single spatial beam element, representing a CNT, embedded in an n-noded continuum finite element. The degrees of freedom of the CNT element are given by

$$U_{beam} = \left\{ u_1^b, u_2^b, u_3^b, ..., u_{12}^b \right\} \tag{210}$$

And the equivalent degrees of freedom of the continuum finite element by:

$$U_{continuum} = \left\{ u_1^c, u_2^c, u_3^c, ..., u_{3n}^c \right\} \tag{211}$$

The kinematic relation between the inclusion degrees of freedom and those of the continuum finite element is given by:

$$U_{beam} = \left[T_{embedded} \right] U_{continuum} \tag{212}$$

where T is a compatibility matrix that contains the shape function values at the coordinates of each of the inclusion nodes. This translates to

$$\left[T_{embedded} \right] = \begin{bmatrix} \mathbf{T}_A^{(1)} & \mathbf{T}_A^{(2)} & \cdots & \mathbf{T}_A^{(n)} \\ \mathbf{T}_B^{(1)} & \mathbf{T}_B^{(2)} & \cdots & \mathbf{T}_B^{(n)} \end{bmatrix} \tag{213}$$

where A, B denote the initial and final node of the beam element according to **Figure 13**a. And $\mathbf{T}_K^{(j)}$ is a matrix that transforms the translational and rotational degrees of freedom of a beam element to only the translation degrees of freedom of the matrix as follows

$$\mathbf{T}_K^{(j)} = \begin{bmatrix} N_j\left(\xi_K,\eta_K,\zeta_K\right) & 0 & 0 \\ 0 & N_j\left(\xi_K,\eta_K,\zeta_K\right) & 0 \\ 0 & 0 & N_j\left(\xi_K,\eta_K,\zeta_K\right) \\ 0 & -\dfrac{1}{2}\dfrac{\partial N_j\left(\xi_K,\eta_K,\zeta_K\right)}{\partial z} & -\dfrac{1}{2}\dfrac{\partial N_j\left(\xi_K,\eta_K,\zeta_K\right)}{\partial y} \\ -\dfrac{1}{2}\dfrac{\partial N_j\left(\xi_K,\eta_K,\zeta_K\right)}{\partial z} & 0 & -\dfrac{1}{2}\dfrac{\partial N_j\left(\xi_K,\eta_K,\zeta_K\right)}{\partial x} \\ -\dfrac{1}{2}\dfrac{\partial N_j\left(\xi_K,\eta_K,\zeta_K\right)}{\partial y} & -\dfrac{1}{2}\dfrac{\partial N_j\left(\xi_K,\eta_K,\zeta_K\right)}{\partial x} & 0 \end{bmatrix} \tag{214}$$

The terms $\dfrac{\partial N_j}{\partial x}, \dfrac{\partial N_j}{\partial y}, \dfrac{\partial N_j}{\partial z}$ represent the shape function derivatives, evaluated at the coordinates ξ_K, η_K, ζ_K beam node at the local coordinate system of the continuum element. As a result, the stiffness contribution of the inclusion to the matrix is given as follows

$$K_{embedded} = T_{embedded}^T \cdot K_{beam} \cdot T_{embedded} \tag{215}$$

The final stiffness matrix of the RVE is calculated as the sum of the contributions of the continuum finite elements and the equivalent contributions of the structural beam elements transformed to the nodal degrees of freedom of their host elements with the aid of eq. (215). The use of the embedded FEM technique [136] allows for the use of relatively coarse and simple meshes, with respect to a standard FEM discretization. A standard FEM discretization would require fully conforming meshes in the matrix-inclusion interphases that would lead to complicated and laborious preprocessing of the RVE FEM models. This can be avoided by use of the embedded FEM technique. As a result, the proposed discretization procedure significantly reduces the computational cost for the solution of the RVE.

4.6.2 Metamaterial RVEs

Another typical material microstructure used in advanced composites is the metamaterial illustrated **Figure 13**b. A metamaterial is created as a combination of a matrix material with volumetric inclusions of different material properties or cavities. The volumetric nature of these inclusions does not allow their modelling as beam or shell elements. As a result, both the matrix and the inclusion are discretized with 3D continuum finite elements, ensuring that the mesh at the boundary between them is conforming. This might lead to increased RVE mesh size compared to the embedded inclusions presented in Section 4.6.1, yet it is inevitable in case of complex inclusion geometries. Since these materials do not exist in nature and are manufactured, they are commonly placed in a periodic lattice as **Figure 13**b illustrates. A single periodic portion of the lattice is extracted (**Figure 13**b) and serves as the RVE geometry to be used throughout the model. The stochasticity for this RVE case is introduced as the

variability of the material properties of the matrix or the incorporated inclusions. Similar to the embedded inclusions case, the spatial variability of the material properties is dictated by the Karhunen-Loève method as provided in eq. (209).

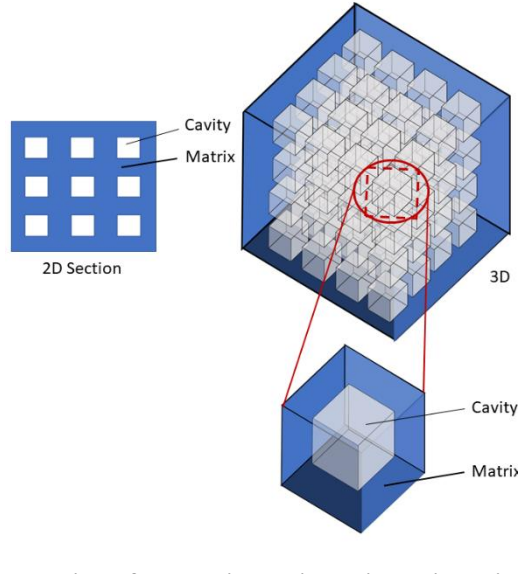
<p align="center">(a)　　　　　　　　　　　　　　　　　　　　　　　　　　(b)</p>

Figure 13: (a) Schematic representation of the arbitrary inclusions discretized with beam elements, embedded in a 3D matrix, discretized with solid continuum finite elements. (b) Schematic representation of metamaterial microstructure in 2D and 3D and its decomposition into 3D RVEs.

4.7 Numerical results

This section provides benchmark examples that demonstrate the merits of the proposed computational methodology. The first example verifies the accuracy of the imposed plane stress conditions as described in Section 4.3, followed by two real-scale examples that demonstrate the applicability of the proposed approach of integrating isogeometric T-splines discretization of Kirchhoff-Love shells with stochastic multiscale analysis of composite materials. The second benchmark example illustrates the performance of the proposed methodology applied to a cylindrical shell composed of a metamaterial, while the third example deals with the analysis of a real-scale car bumper made of a polymer reinforced with stochastically distributed carbon nanotube (CNT) inclusions.

All modules of isogeometric analysis, multiscale analysis and stochastic analysis were developed and integrated in the open-source computational mechanics software platform MSolve [128] with HPC capabilities.

4.7.1 Verification of homogenization procedure for plane stress conditions

This benchmark test is used as a proof of concept of the proposed computational procedure described in Section 4.3 for extracting the plane stress constitutive law from the analysis of a three-dimensional microstructure. For a Young's modulus E=4 GPa and Poisson's ratio ν=0.4, the theoretic isotropic plane stress elasticity matrix is calculated as:

$$\mathbf{C} = \frac{E}{1-v^2}\begin{bmatrix} 1 & v & 0 \\ v & 1 & 0 \\ 0 & 0 & 1-v \end{bmatrix} = \begin{bmatrix} 4.762 & 1.905 & 0 \\ 1.905 & 4.762 & 0 \\ 0 & 0 & 1.429 \end{bmatrix} \tag{216}$$

The same material properties are used for the computation of the constitutive matrix **C'** via the homogenization procedure implementing the plane stress extraction described in Section 4.3. To this purpose, a cubic RVE of 100 nm edge is considered, and discretized with a mesh of 10x10x10 hexahedral finite elements. The difference **ΔC** between this calculation and the theoretic constitutive matrix of eq. (189) is computed at:

$$\Delta \mathbf{C} = \mathbf{C} - \mathbf{C'} = \begin{bmatrix} 0.0 & \text{-9.992E-15} & -9.60E-16 \\ \text{-9.992E-15} & 0.0 & -2.20E-16 \\ -7.08E-16 & -3.37E-16 & 0.0 \end{bmatrix} \tag{217}$$

The comparison of the constitutive matrix components in eq. (217) illustrates the accuracy of the proposed plane stress constraint procedure. It can be seen that the nonzero values of both matrices coincide, while the zero terms of the isotropic plane stress elasticity matrix are computed close to zero within the computer accuracy. This indicates that the extraction of the constitutive matrix from the homogenization procedure described in Section 4.3 provides accurate results compared to the analytical formula of plane stress constitutive matrix.

To test the performance of the proposed procedure for an anisotropic material, two composite RVE cases are examined with a matrix of the same material as before reinforced with CNTs of different volume fractions. The CNTs are modelled as embedded beam elements assuming fully bonded interfacial conditions [137], with properties listed in Table 1. The finite element model is created using the random RVE generator described in Section 4.6.1 for 200 and 800 embedded CNTs respectively. A unidirectional orientation of CNTs is considered with the principal direction being the axis X, as illustrated in **Figure 14**. The length of the CNTs is considered to be 100 nm while its position in the YZ plane is given by two uncorrelated uniform variables for coordinates Y_A and Z_A, as described in Section 4.6.1.
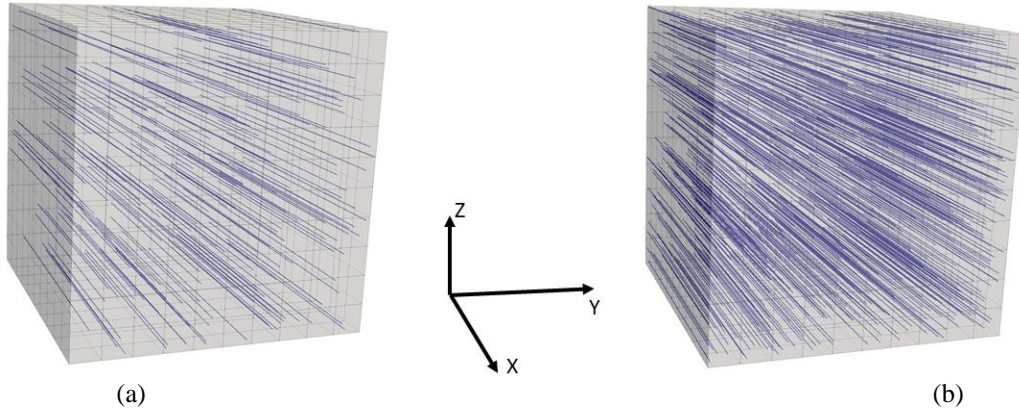

(a)   (b)

Figure 14: Representative volume element with embedded CNTs a) 2.5% embedded CNTs volume fraction a) 10% embedded CNTs volume fraction

EBE properties for CNT(8,8)	
CNT diameter	1.06 nm
CNT thickness	0.34 nm
Bending inertia X,Y	100.18 nm^4
Torsional constant	68.77 nm^4
Young's Modulus	4 GPa
Poisson's ratio	0.4

Table 1: CNT Properties

$$\mathbf{C}_{RVEa} = \begin{bmatrix} 18.328 & 1.905 & -9.09\text{E-}18 \\ 1.905 & 4.762 & 5.80\text{E-}16 \\ 4.57\text{E-}16 & -5.01\text{E-}16 & 1.429 \end{bmatrix} \qquad \textbf{(218)}$$

$$\mathbf{C}_{RVEb} = \begin{bmatrix} 58.554 & 1.905 & 6.47\text{E-}16 \\ 1.905 & 4.762 & -3.18\text{E-}17 \\ 9.68\text{E-}17 & 1.15\text{E-}15 & 1.429 \end{bmatrix}$$

The computed constitutive matrices for the two RVE cases are presented in eq. (218). In comparison with the isotropic constitutive matrix of eq. (189), the reinforced RVE matrices provide a notable increase of stiffness in the X direction. Specifically, the principal component of axis X for the RVE reinforced with 2.5% volume fraction of CNTs, is increased by 385% compared to the isotropic case, while for the 10% volume fraction case an increase of 1230% is observed, thus making apparent the contribution of the reinforcing material in its mechanical performance. In both cases, the zero terms of the isotropic elasticity matrix are close to zero within computer accuracy and thus the extracted constitutive matrices are in agreement with the plane stress matrix.

4.7.2 Cylindrical shell

The second example is the benchmark example of the cylindrical shell shown in **Figure 15**a. Its cross-section is a circular arc of 25 meters radius with its angle being 40°. The thickness of the shell is 0.25 m and the total length of the structure is 50 m. The shell is subjected to a gravitational load of magnitude $f_0=90$ N/m^2 per unit surface [138,139]. The boundary conditions of the structure are the following: translational degrees of freedom per axis X and Z are constrained in edge AB and CD.

The material considered in this example is the metamaterial of **Figure 15**b with periodic voids. A unit cell of 100x100x100 nm with a void of 50x50x50nm (see **Figure 15**) is used to construct the 3D RVE for this case. The modulus of elasticity of the RVE material is considered to be a random variable assumed to follow the lognormal distribution with mean value E=4 GPa and standard deviation 0.5 GPa. Two spatial correlation cases were considered. In the first, all spatial through thickness integrations points are assumed to have the same modulus of elasticity (random variable case). In the second case, a through thickness variation of the modulus of elasticity was considered in addition to the surface variability. The modulus of elasticity in this case is described as a white noise random field, according to eq. (209).
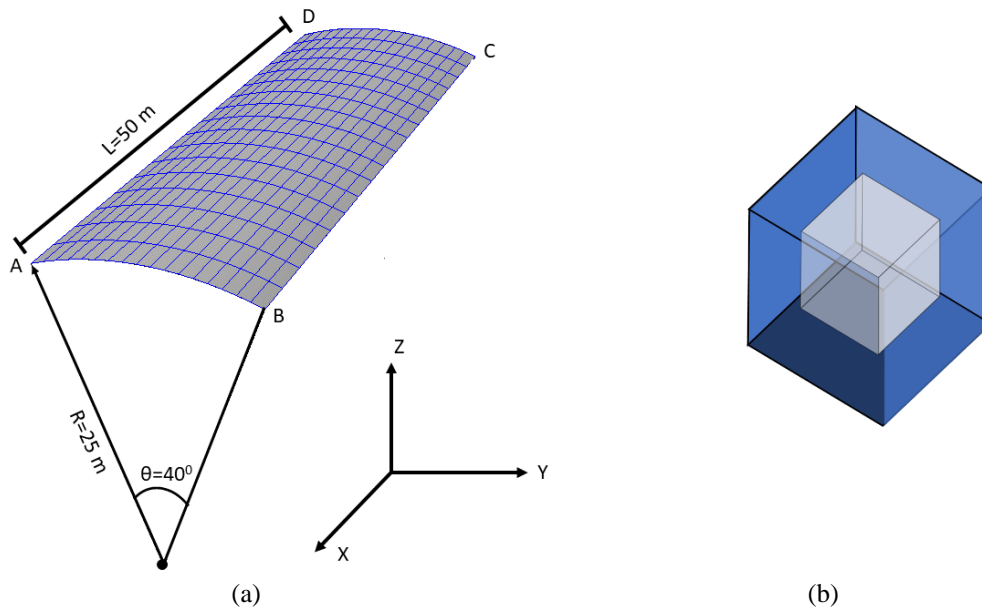
Figure 15: a) Geometry of the cylindrical shell example. b) Geometry of representative volume element defined at each thickness integration point

20.000 Monte Carlo simulations of the stochastic cylindrical shell are performed for each spatial variability case. **Figure 16**a, displays the histogram of the vertical displacements of monitor node in the middle of the edge BC for the first spatial variability case. As can be seen, the results follow a near-to normal distribution, with a mean value of -0.038762m and a standard deviation of 1.3428-04m. In the white noise spatial variability case, the histogram of displacements versus probability is displayed in **Figure 16**b, where the mean value of the results is -0.0791m and their standard deviation 0.0233m

Inspection of these results immediately indicates the importance of the multiscale modelling proposed in this study. Considering a constant material for the whole macroscale model, gives a standard deviation of the displacements equivalent to 30%, i.e. COV=0.3 of the resulting mean value, while in white-noise case the COV reduces to 0.18. In addition, the shapes of the distributions differ significantly with the first (**Figure 16**a) being near to Gaussian and the second being near to lognormal, thus in alignment to the input random variables.
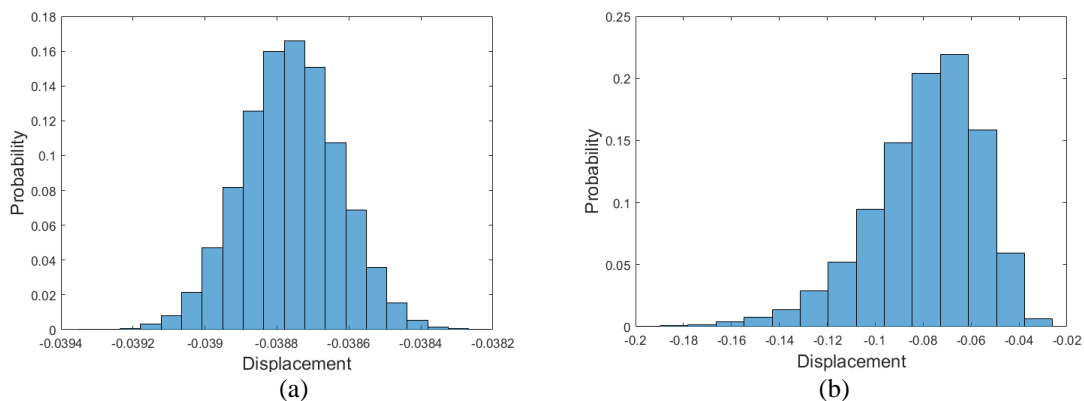

Figure 16: Histograms for the vertical displacements of monitor Control Point C

4.7.3 Car composite bumper example

The next example is a real-scale model of a car bumper illustrated in **Figure 17**. The model is retrieved from [140]. Utilizing T-Spline plugin for Rhino [126], the CAD surface is

transformed to T-splines surface. By extracting a Bezier mesh, an analysis of the bumper model is performed in MSolve platform [128]. Details of the bumper boundary conditions and IGA discretization parameters are given in **Figure 17**a and Table 3, respectively. A front view of the bumper is given in **Figure 17**. The right edge of the bumper is considered clamped, while loading of 100KN is applied at the control points of the left edge. The deformed bumper configuration is given in **Figure 17**b for an isotropic material with E=4GPa modulus of elasticity and Poisson's ratio ν=0,4.

a)   Boundary conditions

b)   Deformed bumper configuration
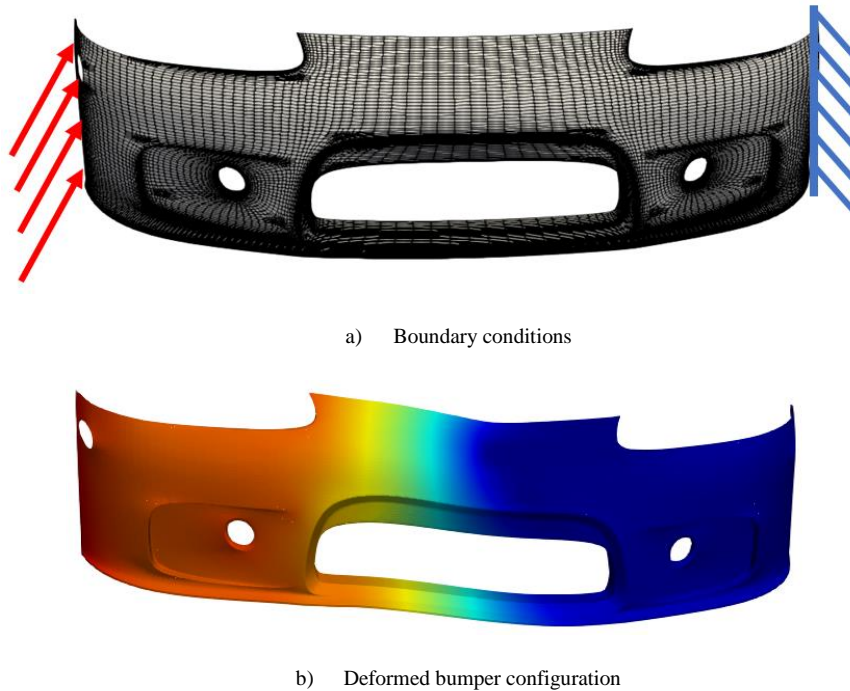
Figure 17: Boundary conditions of the bumper model and deformed configuration

Assuming that the bumper is made of a polymer matrix reinforced with CNTs, the proposed methodology presented in this Chapter is applied. In this context, a cubic RVE with dimensions of 100x100x100nm is constructed using the RVE generator of Section 4.6.1. The RVE is comprised of a poly-ether-ether-ketone matrix (PEEK) [141] matrix with Young's modulus E=4 GPa and Poisson's ratio ν=0.4. The matrix is reinforced with (8,8) armchair CNTs that are modeled as beam elements [137] (**Figure 18**) embedded in the surrounding matrix assuming fully bonded interfacial conditions, as described in Section 4.6.1.
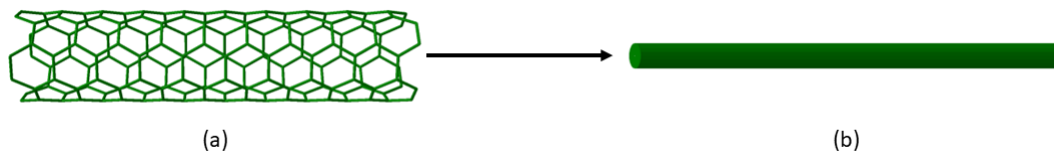

(a)   (b)

Figure 18: Schematic CNT representation (a) MSM model of the CNT (b) Beam element with equivalent properties to the detailed CNT model

Both matrix and CNTs are considered linear elastic. The matrix is discretized with 1000 hexahedral elements, while the CNTs are modelled utilizing equivalent beam elements (EBEs). The EBEs are extracted from detailed Molecular Structural Mechanics models (MSM) of the CNTs [137]. As shown in **Figure 18**, a CNT portion is modelled as a space frame lattice according to the MSM formulation and then projected to an equivalent surrogate beam element model with much lower degrees of freedom. The full CNT is then modelled as a series of EBE elements. **Table 2** presents the mechanical properties of the EBEs that are

extracted with the MSM approach for a CNT (8,8). A detailed description of this surrogate modeling procedure can be found in [137,80].

EBE properties for CNT(8,8)	
CNT diameter	1.06 nm
CNT thickness	0.34 nm
Bending inertia X,Y	100.18 nm^4
Torsional constant	
Young's Modulus	68.77 nm^4
Poisson's Ratio	4 GPa
	0.4

Table 2:Properties of the EBE extracted from the MSM analysis of a CNT (8,8).

Since nanotubes are in theory indefinitely long cylinders organized in hexagonal lattice, the notation (m,n) serves to define the atoms positioning on the circumference of the nanotube. In literature, the term (m,m) refers to armchair type nanotubes, whose paths are defined by two consecutive 60° left turns, followed by two 60° right turns repeated every four steps. **Figure 19** provides an example of a graphene sheet that will serve as the. The vector c_1, c_2 illustrated are considered the unit vectors based on a unit cell hexagon of the lattice. By combining **m** unit cells along c_1 direction and **n** along c_2 direction an (m,n) type nanotube is generated.
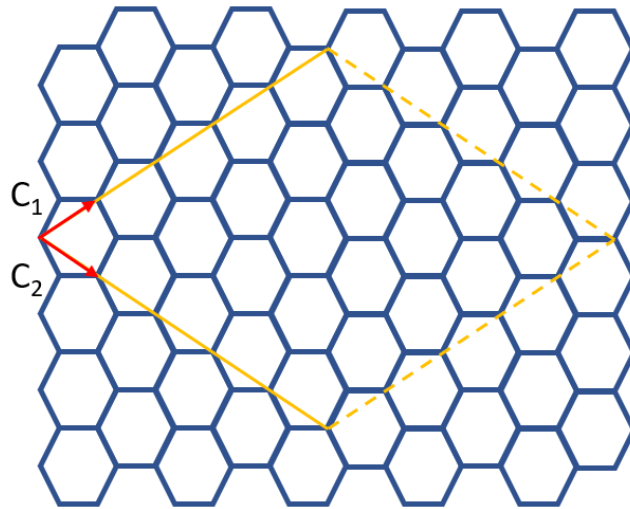

Figure 19: Graphene sheet honeycomb structure.

A sensitivity analysis is initially performed to determine the sensitivity of the bumpers response to the CNTs volume fraction (VFs). To this purpose, 10 RVEs are constructed with varying VFs in the range between 2.5-10%. The RVE matrix geometry is considered constant throughout the structure, while the CNTs are placed unidirectionally parallel to the X axis of the mesoscale model (see **Figure 14**) in the first subcase and randomly oriented in the second subcase (see **Figure 21**). The longitudinal direction coincides with a_1 local element axis as shown in **Figure 5**. Their position in the YZ plane is determined by the random RVE generator as described in Section 4.6.1, with the coordinates Y_A and Z_A modeled with two uniformly distributed and uncorrelated random variables as

$$Y_A \sim U(0,100nm), \ Z_A \sim U(0,100nm) \tag{219}$$

Figure 20, presents the results of the aforementioned sensitivity analysis. The horizontal axis represents the VF of the inclusions, while the vertical provides a measure of the stiffness increase of the structure expressed as a normalized displacement. This displacement is defined as the ratio of the maximum bumper displacement of the CNT reinforced bumper to the maximum displacement for the unreinforced bumper, at the same monitoring degree of freedom

$$U(\%) = \frac{U_{CNT_{max}}}{U_{Matrix_{max}}}$$

(220)

As observed in **Figure 20**, the minimum volume fraction of 2.5% results in a maximum displacement U~0.55, that is approximately 55% of the corresponding displacement of the bumper with neat PEEK material. This reduction can reach a maximum of U=30% in the case of 10% CNT volume fraction randomly dispersed in the matrix, revealing a 70% stiffness increase of the bumper. In addition, it can be observed that the variation of U as a function of the weight fraction is nonlinear reaching towards a plateau beyond which the increase of stiffness for weight fractions larger than 10% becomes negligible. Inspection of the curves for longitudinal and randomly oriented CNTs presented in **Figure 20**, immediately emphasizes the importance of the proposed material microstructure modelling in revealing the sensitivity of the macroscale response to microstructural parameters. A significant stiffness increase is observed for the case of longitudinal CNTs. For example, for a stiffness increase of ~50% with respect to the unreinforced material illustrated with a dashed line in **Figure 20**, a 3% VF of longitudinal CNTs is required, while the same increase is achieved with 7% VF of randomly oriented CNTs. This indicates that the CNT inclusions of a polymer matrix can be reduced up to ~57% while meeting the desired stiffness requirements. In a similar fashion, for a given a CNT VF of 4.3%, a 58% stiffness increase is observed for the case of longitudinal CNTs compared to 40% in case of the random oriented CNTs, as indicated by the dotted lines of **Figure 20**. This translates to a 31% deviation between the two cases, showcasing the importance of the detailed microstructure modelling. As a result, it observed that the proposed nested IGA-FEM scheme, can quantitatively assess the influence of the material microstructure to the final structural response, while at the same time providing crucial insight for the design of advanced composite materials.

Model	
Control Points	23312
Bezier Elements	24664
Degrees of freedom	69936

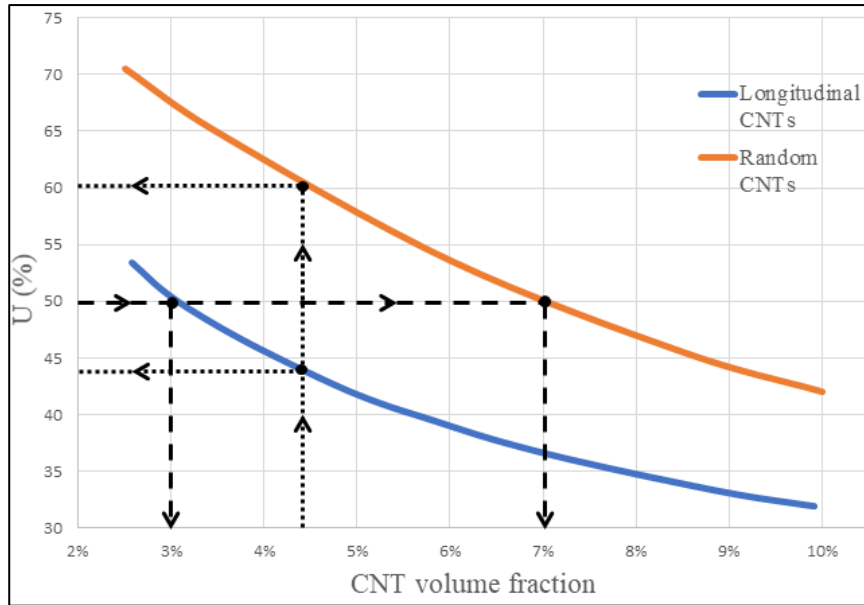**Table 3: Details of the T-Spline model discretization.**

Figure 20: Impact of CNT volume fraction to the maximum deflection of the car bumper

The random RVE generator is utilized next to introduce spatial and through thickness variability to the RVEs. Four cases for the reinforcement of the bumper are examined. In the first two cases, unidirectional CNTs are assumed parallel to the axis X of the mesoscale model (**Figure 14**), uniformly distributed inside the matrix according to eq(219). For the latter two cases, the embedded CNTs have random orientations (**Figure 21**) given by eq. (209) . In both cases a Gaussian band limited white noise is assumed for the generation of a 3D random field, with two VF subcases of 3.5% and 6% respectively and a coefficient of variation of 1%. **Table 4** , contains the results generated by 2.500 Monte Carlo simulations for each of the cases described above, while **Figure 22** presents their respective histograms. Comparing unidirectional and randomly oriented CNTs for their two equivalent volume fraction cases, it can be observed that the random orientation of the CNTs has more impact on the performance of the bumper as indicated by the maximum displacement ratio which is significantly lower for the case of randomly oriented CNTs. Specifically, for the 3.5% volume fraction the mean ratio of ~50% stiffness augmentation for the aligned CNTs is reduced to ~35% for the randomly oriented and similarly for the 6% volume fraction case, the 60% stiffness increase is reduced to 46%. In both cases the impact of random orientation gives a compelling 25-30% reduced stiffness compared to the corresponding unidirectional positioning of the inclusions. From **Figure 20** it can be seen that the stiffness of the nanocomposites exhibits a significant increase for CNT volume fractions ranging between 2,5-9%. In addition, the rate of the stiffness increase is slowing down for higher CNT volume fraction exhibiting a plateau behavior in which the stiffness increase becomes insignificant.

As in the previous example, inspection of the results immediately indicates the importance of the detailed multiscale modelling proposed in this study. As indicated in the examples considered, the modelling of the micromechanics can severely affect the constitutive response of the material, therefore the accurate description of the materials microstructure, as addressed by the proposed approach, becomes crucial. The inclusion's volume fraction effect on the final material performance follows a non-linear law (Figure 20), while the randomness of the inclusion directionality can reduce the overall material performance up to ~30%. The sensitivity of material and structural performance to the parameters assumed for the micromechanics modelling emphasizes the necessity of utilizing approaches like the proposed methodology, for the accurate modeling of shell composites.

% Reduction	Longitudinal CNTs 3.5% VF	Longitudinal CNTs 6% VF	Random orientation CNTs 3.5% VF	Random orientation CNTs 6% VF
Mean Value	50.9828%	60.53195%	35.1657%	46.4423%
Standard Deviation	7.36139%	3.55056%	7.57816%	7.03846%

Table 4: Results for two volume fraction cases, for longitudinal and randomly oriented CNTs.
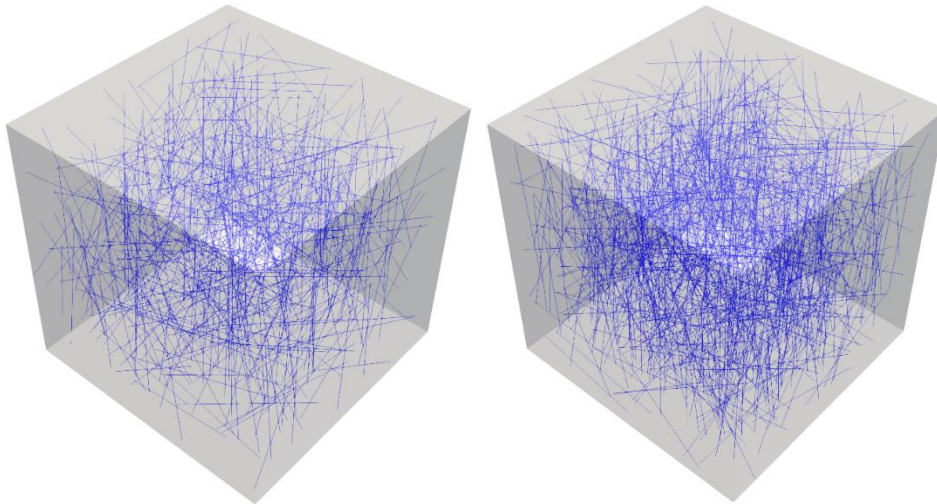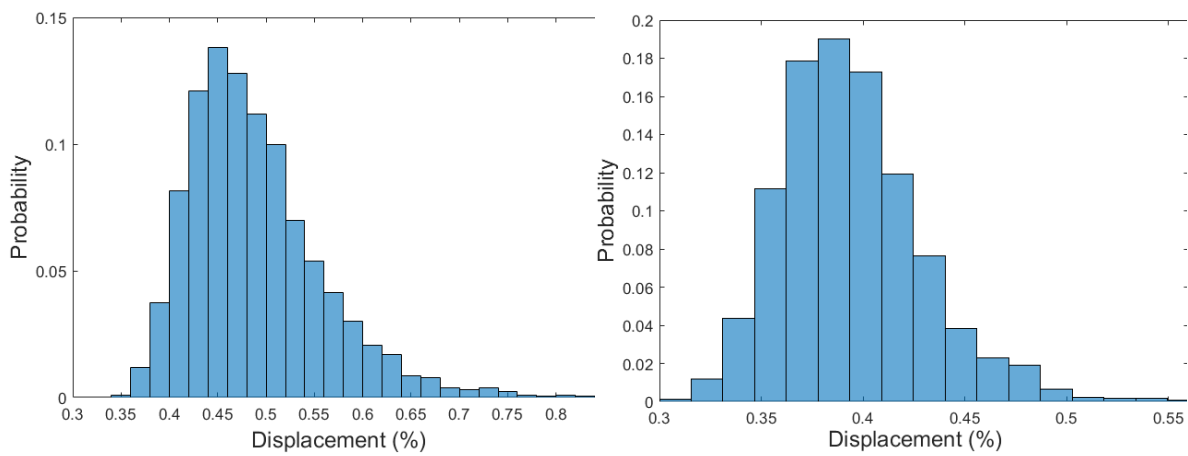

Figure 21: Randomly distributed CNTs a) Volume fraction 3.5% b) Volume fraction 6%.

(a)   Unidirectional CNTs with 3.5% mean volume fraction.
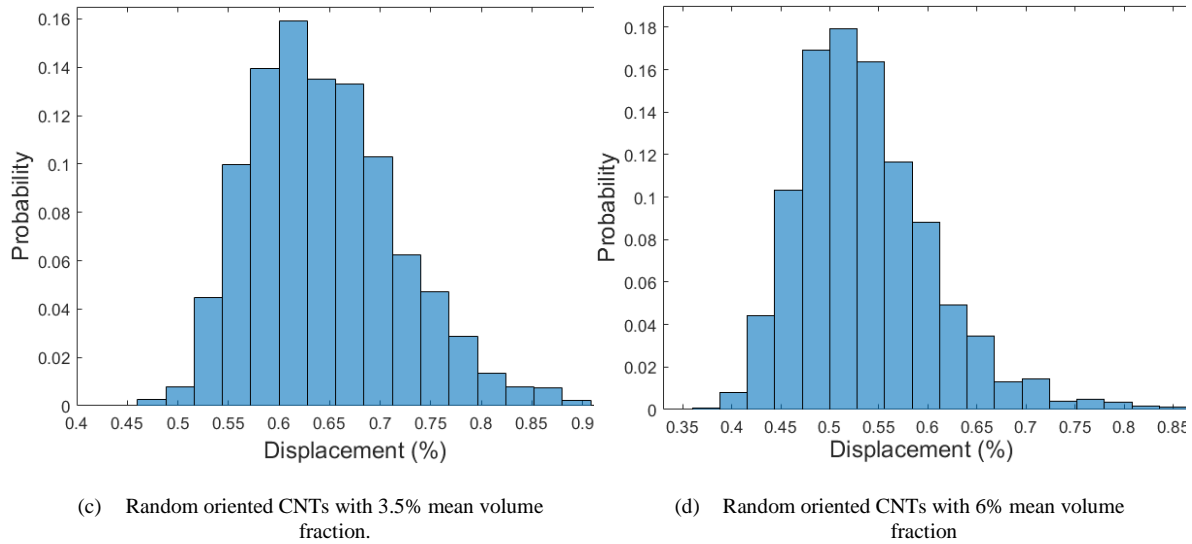
(b)   Unidirectional CNTs with 6% mean volume fraction.

(c) Random oriented CNTs with 3.5% mean volume fraction.

(d) Random oriented CNTs with 6% mean volume fraction

Figure 22: Histogram for the displacement reduction vs its probability of occurrence

4.7.4 Parallel computer implementation

Since both the nested FE^2 multiscale analysis and the Monte Carlo simulations require extensive computational workload, the developed code is parallelized with the aid the HPC oriented platform MSolve which implements the Task Parallel Library (TPL) [142] and MPI.NET [143] which are the equivalents to the OpenMP [144] and MPI [145] frameworks for the C# programming language. The parallelization procedure is illustrated schematically in **Figure 23** and is performed in two phases. Phase 1 includes the generation of the random RVE geometries, of multitude n for each macroscale model and the off-line computation of their equivalent properties. In this phase each computing node of the MPI environment is assigned to a number of RVE geometries. This number is equal to the independent integration points of the macroscale model. Then, finite element analyses are performed independently for each RVE utilizing the cores of the computing node in a shared memory computing environment. As a result, a collection of constitutive responses, linked to a specific RVE is created in each MPI node.

Following the generation of the required multitude of RVEs, a second parallelization phase (Phase 2) is implemented for the Monte Carlo simulations of m macroscale models. In this Phase a different mesoscale RVE model is assigned to each of the thickness integration points for each macroscale model generated by MCS and the corresponding constitutive matrix is retrieved from the formerly generated collection without additional calculation. The FEM analyses of the macroscale models are also independent and are performed in an embarrassingly parallel way as well. Specifically, each MPI computing node is assigned to macroscale models in which their corresponding RVEs are already computed in the node. As a result, there is no need for communication between the nodes to retrieve RVE data, thus maximizing the parallelization performance.
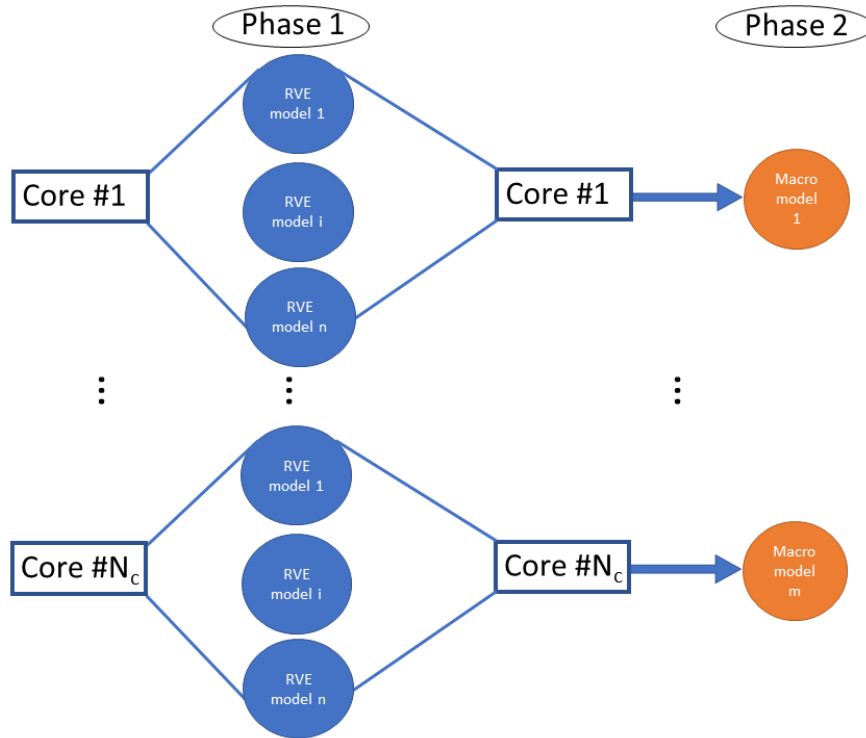
84

Figure 23: Schematic representation of parallelization strategy

Table 5, shows the discretized degrees of freedom of the macroscale level shell models, the number of Monte Carlo simulations and the corresponding computing times required for examples 2 and 3 in both sequential and parallel computing implementations. The CPU used in in the single CPU case is an i7-980x with 6 cores. Specifically, the sequential time of 363 minutes is reduced to 96 minutes resulting in a speedup of 5.67 times, in the case of 20.000 Monte Carlo simulations of the cylindrical shell. Similarly, for 2.500 simulations of the CNT reinforced bumper, the sequential time is 6.325 minutes is reduced in the parallel implementation to 2.027 minutes resulting in a 4.68 times speedup. It is observed that for the bumper model the speedup is reduced compared to the linear speed up of the cylindrical shell example. This is attributed to the increased memory requirements of the bumper model, that do not allow for the full utilization of the CPU cores. In order to study the scalability of the proposed parallel implementation, both examples are computed on a cluster consisting of 6 computing nodes, containing a 6 core i7-980x processor each. For the cylindrical shell test case, the sequential time of 363 minutes is further reduced to 11 minutes thus achieving a 33 times faster execution. Similarly, for the car bumper case, the sequential time of 6.325 minutes is reduced to 226 minutes achieving a 28 times faster execution of the MCS simulations. It is observed that in both the single node and multi-node cases the parallelization scheme yields a close to linear speedup and thus significantly reduces the required execution time to tractable computational timeframes.

Analysis time	Degrees of freedom	Monte Carlo simulations	Sequential time	Parallel (6 cores) time	Parallel (36 cores) time
Cylindrical shell	1.083	20.000	363 min	64 min	11 min
Bumper	69.936	2.500	6.325 min	1.351 min	226 min

Table 5: Comparison of sequential and parallel stochastic analysis times.

4.8 Conclusions

In this Chapter a formulation for the multi-scale analysis of Kirchhoff Love shells is presented. A random mesoscale model generator is introduced in order to account for the intrinsic inclusion randomness, and for the spatial variability of the RVE throughout the structure. The focus is on the implementation of metamaterial models, as well as composite materials described by RVEs with arbitrary inclusions. The numerical tests performed confirm the accuracy of extracting plane stress conditions via a 3D homogenization scheme in the framework of nested FE^2 multiscale analysis. Furthermore, benchmark and real-scale applications demonstrated the applicability of the proposed formulation, while providing useful insights to the performance enhancements that reinforced polymer materials can achieve in case of industrial applications. The detailed modelling of the material microstructure via a detailed 3D RVE, allows for the accurate representation of the micromechanics parameters, such as inclusion directionality and volume fraction, which, as the numerical results indicate have significant impact on the final structural performance of the shell. The proposed approach is easily parallelizable and can accurately handle realistic stochastic multiscale analysis problems accompanied with realistic representations of the material microstructures at the RVE level, at reasonable and affordable computational timeframes.

5   Nonlinear multiscale modeling of thin Kirchhoff Love shells at finite deflections

The theoretical framework of multi-scale modeling in continuum mechanics, presented in Chapter 2 is well established and ranges from small strain and displacement theories [32, 33] to finite strain [34] and higher order models [146]. It is even possible to include inertia effects or thermal conduction phenomena in multi-scale simulations [35, 36]. An theoretical framework for computational homogenization in electro-elasticity and magneto-mechanics was introduced in [37] and [38] respectively. The benefits from such models, apart from their accuracy and fidelity, concern the reduction of cost of experimental testing of material or entire structures for existing entities or in the design of new applications. The main drawback that in general characterises multi-scale FE^2 models, i.e. their high computational cost, can now been alleviated, by use of HPC methods [27] and advances in surrogate modeling. Specifically in [28] interpolation schemes were used, in [29] radial basis functions were adopted and [30,31] neural networks were utilized.

However, the aforementioned benefits of multi-scale analysis have yet to be exploited in non-linear thin shell formulations. In this field, the focus is on large deflection shell formulations appropriately reworded for the incorporation of nonlinear material phenomenological laws such as hyperelasticity [47,48], elasto-plasticity [39-46] or arbitrary three-dimensional material laws [115] as it was presented in detail in Chapter 3. Although non linear shell finite element formulations have great applicability in various fields of science, ranging from aerospace engineering [147] and structural modeling [148-152] to the mechanical modeling of thin biological membranes natural or artificial [153-158]   the development of more accurate multi-scale formulations for thin shell structures is still limited. To this direction a seven parameter shell formulation, introduced in [49], is appropriate for finite deformation analysis but it is limited to non-concurrent multiscale simulations as it employs a pre-integrated constitutive relationship. A coupled atomistic continuum approach was given in [50] for modeling of fracture of solid shells. The thermo-mechanical performance of shell structures with orthogonal periodic configurations was studied in [51] with regard in a setting of a second-order two-scale SOTS numerical algorithm. In [52,53] a second gradient based multiscale scheme is employed and shell stress resultants are exracted from a representative volume element (RVE) that describes the entire shell section, limiting though their applicability to shell structures of specific thickness configurations. Finally a multiscale formulation was introduced in [159] for thin shells undergoing small deflections and srains.

In this Chapter we extend the methodology presented in Chapter 5 to the finite deformation range. For the shell structures it is assumed that through thickness periodicity holds as well, and the macroscopic constitutive response at each shell section, is obtained from multiple Representative volume elements RVEs each one at a different deformation state depending on the height from the mid-surface of the shell. In a deformation gradient based expression of the Principle of Virtual Work, governing equilibrium on the macroscopic level, the strain state to be enforced on the micro-structure and its through thickness variations, are obtained directly by the expression of the Kirchhoff Love hypotheses, depending on the curvature of the structure and its membrane deflections Intermediate calculations of the curvature tensor and stress resultants are avoided. Their calculation is only

useful on the post processing phase of the obtained solution. The effect of the change in the orientation of the midsurface of the shell, due to large deflections, on the direction of the constraints to be enforced in the RVE, is neutralized by expressing the averaging equations in appropriate attached coordinate bases, leading to the formulation of a classical boundary value problem at the micros-scale level.

This Chapter is organized as follows. In section 2 basic kinematics of the Kirchhoff-Love shell theory and necessary transformations of the utilized strain measures are presented. In section 3 basic stress and strain averaging equations for thin shells, undergoing finite straining, are formulated and the fulfilment of the Hill-Mandel macro-homogeneity condition is proven. Section 4 focuses on an analytical derivation of macroscopic tangent stiffness matrix. In section 5 the formulation is verified against benchmark problems and its potential uses are demonstrated.

The following notation is used: bold letters indicate vectors or second order tensors, plain characters are used for matrix vector manipulations or the coefficients of second order tensors in specified bases, Latin indices take on the values {1,2,3} and Greek indices take on the values {1,2}.

5.1 Large Displacements Kirchhoff Love Shell kinematics

The midsurface of the shell is given as a mapping $\psi(\xi)$ of a parametric space $\xi=[\xi,\eta]$ onto the three dimensional Euclidean space $\psi: \xi \rightarrow R^3$. In a discretized setting, the parametrization of a position vector along this surfaces ensues as a linear combination of shape functions and nodal values.

$$X_m = \Psi(\xi,\eta) = \sum N^i(\xi,\eta)X^i \tag{221}$$

By use of a third coordinate in the direction of the thickness the volume of the shell is fully defined and the position of a particle in the undeformed configuration is given as

$$X = X_m + \zeta A_3 \tag{222}$$

Based on the Kirchhoff Love hypothesis which assumes that the cross sections that are originallly normal to the midsurface remain normal to the midsurface in the deformed configuration, the current position of a particle is given as

$$x = x_m + \zeta a_3 \tag{223}$$

where again a_3 is the director, the unit vector normal to the midsurface of the shell.

The covariant basis vector g_i of a point in the shell continuum at the deformed configuration is obtained as

$$g_\alpha = a_\alpha + \zeta a_{3,\alpha} \tag{224}$$

$$g_3 = a_3$$

where $a_1 = x_{m,\xi}$, $a_2 = x_{m,\eta}$ are those of the midsurface and the unit normal vector a_3 is given as

$$a_3 = \frac{a_1 \times a_2}{|a_1 \times a_2|} \tag{225}$$

Similarilly, the covariant basis in the undeformed configuration is

$$G_1 = X_{m,\xi} + \zeta A_{3,\xi}$$
$$G_2 = X_{m,\eta} + \zeta A_{3,\eta}$$
$$G_3 = A_3$$

(226)

and the corresponding metric coefficients follow from the relation $G_{ij} = G_i \cdot G_j$ as $G_{\alpha\beta} = G_\alpha \cdot G_\beta$, $G_{\alpha 3} = G_{3\alpha} = 0$ and $G_{33} = 1$. The contravariant basis vectors are defined by the Kronecker delta property $G^i \cdot G_j = \delta^i{}_j$. They can be calculated in terms of contravariant metric coefficients $G^{\alpha\beta}$ as $G^\alpha = G^{\alpha\beta} G_\beta$, and $G^3 = G_3$ where $[G^{\alpha\beta}] = [G_{\alpha\beta}]^{-1}$ are given by a matrix inversion.

An auxilarry local cartesian basis is introduced for the undeformed configuration as

$$E_1 = \frac{G_1}{|G_1|} \qquad E_2 = \frac{G_1 - (G_2 \cdot E_1)E_1}{|G_1 - (G_2 \cdot E_1)E_1|} \qquad E_3 = A_3$$

(227)

and it is stationary. Another local cartesian basis is used for the deformed configuration, it is given as:

$$e_1 = \frac{g_1}{|g_1|} \qquad e_2 = \frac{g_1 - (g_2 \cdot e_1)e_1}{|g_1 - (g_2 \cdot e_1)e_1|} \qquad e_3 = a_3$$

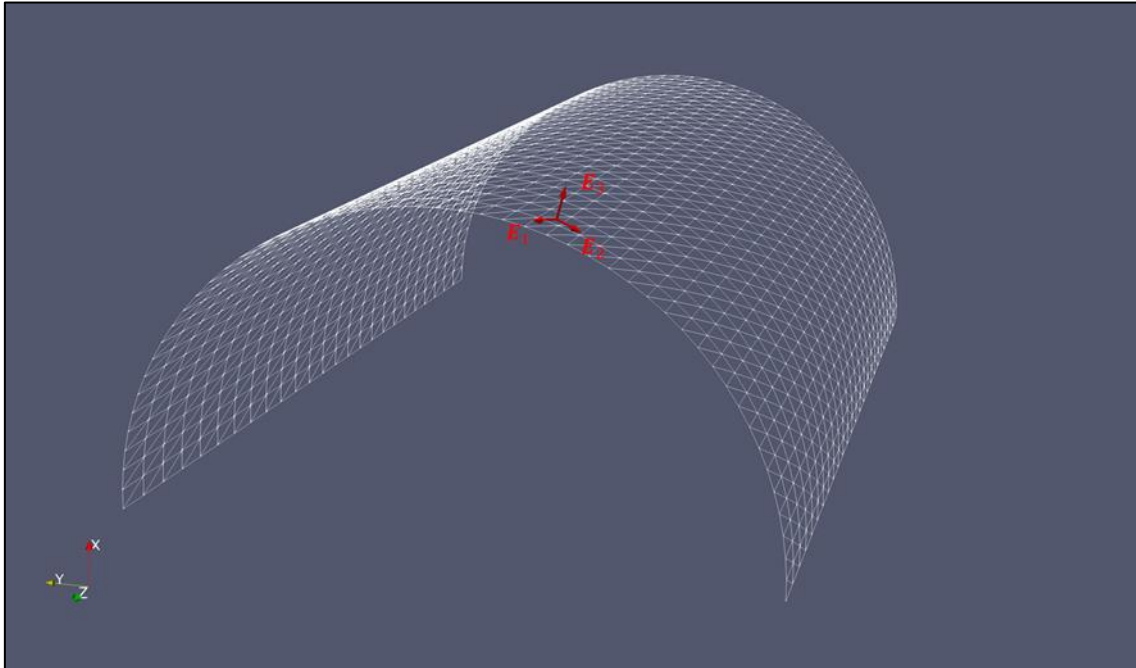(228)

and it is attached to the midsurface of the shell.

Figure 24 Auxiliary cartesian basis Eᵢ is stationary in the undeformed configuration.
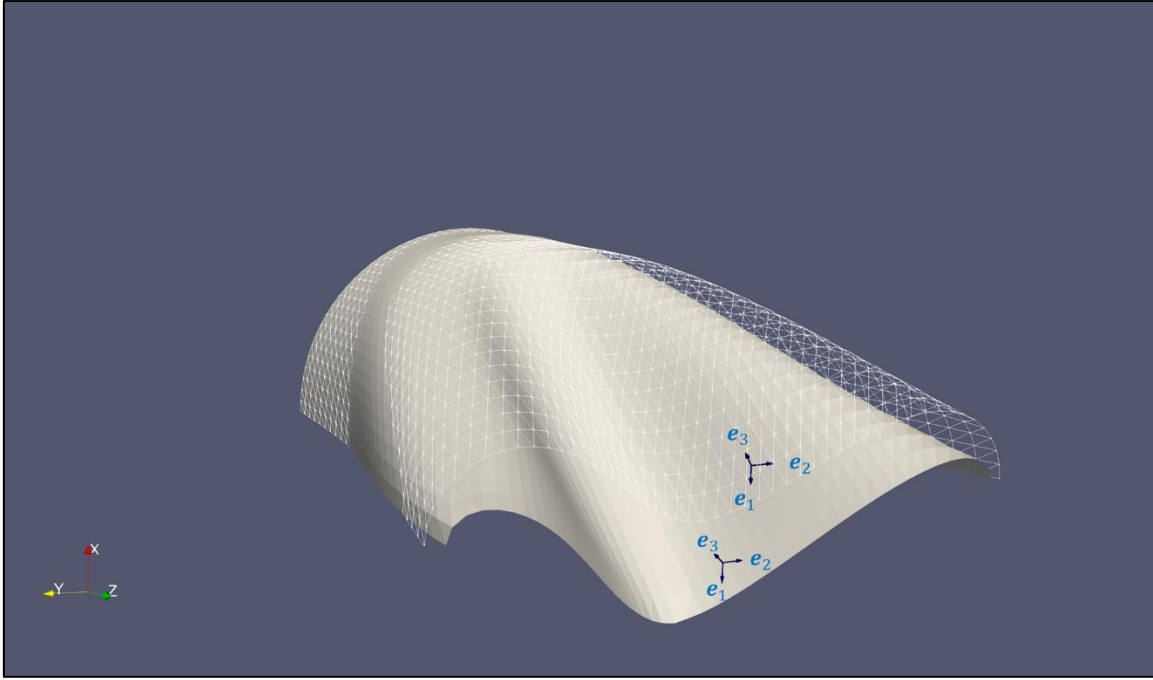
Figure 25 An attached auxiliary cartesian basis e$_i$ follows the deformation of the shell. A white wireframe configuration denotes an intermediate deformation state of the shell structure.

The deformation gradient is defined as

$$\boldsymbol{F_N} = \boldsymbol{g}_i \otimes \boldsymbol{G}^i \tag{229}$$

and it can be decomposed into a membrane and a normal contribution

$$\boldsymbol{F} = \boldsymbol{F_S} + \boldsymbol{F_N} \tag{230}$$

where $\boldsymbol{F_S} = \boldsymbol{g}_a \otimes \boldsymbol{G}^a$ and $\boldsymbol{F_N} = \boldsymbol{g}_3 \otimes \boldsymbol{G}^3$. It is a two point tensor and it can be expressed by use of the auxilliary bases as

$$\boldsymbol{F} = F^{ij}\boldsymbol{e}_i \otimes \boldsymbol{E}_j \tag{231}$$

This representation is chosen as it collects the contribution of the membrane part in a 2 by 2 matrix $[F^{\alpha\beta}]$ and as it easily can be seen by subtitution of (226)(227) and (228), $F^{\alpha 3} = F^{3a} = 0$. Finally the out of plane contribution $F^{33} = 1$, as we have temporarilly ignored the out of plane strech λ_N, the actual value of which results from the material response.

5.2 Averaging Relations and the Macrohomogeneity condition for thin shell structures

Neglecing acceleration forces, based on the scale separation hypothesis [34], we assume that the RVE deforms in a state of static equilibrium [57]:

$$\nabla \cdot \boldsymbol{P_m} = 0 \tag{232}$$

Its deformation is coupled to the macroscopic deformation through a strain averaging relation:

$$F = F_M := \frac{1}{V_{RVE}} \int_{V_{RVE}} F_m \, dV$$

where subscript m refers to microstructural values and M denotes averaged quantities. This assumption is translated to a constraint for all of the coefficients of the deformation gradient tensor except F^{33}. For this coefficient, it is rather exploited for the calculation of its value, upon solution of the microscale boundary value problem.

To meet with these constraints appropriate boundary conditions are enforced on the RVE. Specifically, in a prescribed displacements setting, to ensure that $F^{\alpha\beta} = F_M^{\alpha\beta}$ it is demanded for the peripheral boundary nodes of the RVE that

$$\widehat{x}_m = \widehat{F} \cdot \widehat{X}_m \tag{234}$$

where $\widehat{F} = F^{\alpha\beta} e_a \otimes E_\beta$ is the in plane part of deformation gradient tensor and $\widehat{x}_m = x_1 e_1 + x_2 e_2$ and $\widehat{X}_m = X_1 E_1 + X_2 E_2$ are the position vectors that are tangent to the midsurface of the shell, in the deformed and the reference configuration, respectively.

Alternatively periodic boundary conditions might be employed as $\widehat{x}_m^+ - \widehat{x}_m^- = \widehat{F}(\widehat{X}_m^+ - \widehat{X}_m^-)$ and applied as relative in plane displacement of opposing faces of the rve.

For the out of plane shear deformation contributions $F_M^{3\alpha}$, it suffices to constrain the out of plane displacement of each node on a peripheral face of the rve to equal to the displacement of its corresponding node in the opposing face

$$\widetilde{x}^+ - \widetilde{x}^- = 0 \tag{235}$$

Similar boundary conditions are enforced for the realization of the constraint $F_M^{\alpha3} = 0$. Direct substitution of these conditions (235) and (234) in (233) verify that it holds.

The second averaging relation concerns the First Piola Kirchhoff stress tensor [58, 160]:

$$P = P_M := \frac{1}{V_{RVE}} \int_{V_{RVE}} P_m \, dV = \frac{1}{V_{RVE}} \int_{\Gamma_{RVE}} p \otimes X_m \, d\Gamma \tag{236}$$

where $p = N \cdot P_m$ the nominal traction vector. For the last part of equation (236), we have made use of the divergence theorem, (232) and the fact that $\nabla \cdot X_m = I$. This averaging relation is exploited as a micro to macro scale transition in the homogenisation step. The homogeneous constraint (235) results in antiperiodic tractions p in the opposing faces of the RVE where it is enforced [52,57]. The contributions of those tractions p in (236) cancel out and collectively result to a zero contribution on the averaged microscopic word for the terms $P^{\alpha3}$ and P^{3a}.

Due to plane stress conditions of the Kirchoff Love theory, the resulting P_M^{33} stress is zero since no kinematic constrains have been imposed on the RVE in the out of plane didirection. More details on the calculation of the in Plane part of the macroscopic First Piola Kirchhoff stress $P^{\alpha\beta}$ are given in the next section of a finite element implementation setting.

By substitution of the averaging relations and taking into account the adopted boundary conditions it can be seen that the Hill Mandel condition is indeed satisfied, i.e. the local variation of strain energy on the macroscale equals the volume average of the variation of work performed on the RVE [34,54,57]

$$\frac{1}{V_{RVE}} \int_{V_{RVE}} \boldsymbol{P}_m : \delta \boldsymbol{F}_m^T \, dV_0 = \boldsymbol{P}_M : \delta \boldsymbol{F}_M^T \quad \forall \delta \boldsymbol{x} \tag{237}$$

Hence the macroscopic energetic conjugate strain and stress measures can be replaced by their averaged microscopic counterparts in the expression of the principle of virtual work at the microscal level.

5.3 Finite element solution of the microscale boundary value problem

In order to implement the constraints described in the previous section in a discretized setting, we can proceed by partitioning the degrees of freedom of the finite element mesh to those that are totally free denoted "a", those that are involved in a non-homogenous constraint expressed in terms of a macroscopic in plane strain value Fab of the deformation gradient denoted "b" and finally those that participate in a homogenous equality constraint symbolized "c". This partitioning concerns the remainder of the degrees of freedom after rigid body motions of the RVE are fully constrained. Employing the Lagrange multiplier method, for the imposition of the constraints, the finite element solution of the boundary value problem **(232)** choosing linear deformations [32] for the imposition of non-homogenous constraints consists of the following nonlinear algebraic equations

$$
\begin{aligned}
f_a(x) &= 0 & \text{(a)} \\
f_b(x) &= \delta & \text{(b)} \\
x_b - D^T F &= 0 & \text{(c)} \\
f_c(x) - P^T \pi &= 0 & \text{(d)} \\
P x_c &= 0 & \text{(e)}
\end{aligned}
\tag{238}
$$

Where **(238)**-c is a discretized form of equation **(234)** and the matrix D is a combination of matrices D_p for each node by the relation

$$[x_b] = \begin{bmatrix} x_1 \\ x_2 \end{bmatrix} = [D_p^T][F] = \begin{bmatrix} X_1 & 0 & X_2 & 0 \\ 0 & X_2 & 0 & X_1 \end{bmatrix} \begin{bmatrix} F^{11} \\ F^{22} \\ F^{12} \\ F^{21} \end{bmatrix} \tag{239}$$

Where the coordinates x_1, x_2 and X_1, X_2 refer to the local cartesian coordinate system of the RVE that coincides with the attached to the midsurface of the shell. For simplicity in the undeformed configuration the origin of this local basis is placed at the geometric center of the RVE. B is assembled by node pair wise operators B_p

$$B_b = \begin{bmatrix} 0 & \cdots & 1 & \cdots & 0 & | & 0 & \cdots & -1 & \cdots & 0 \end{bmatrix} \tag{240}$$

corresponding to equation **(235)**. B_p takes a non zero value for the dofs involved in each constraint and appropriately signed. The first dimension of B equals the number of the constraints. For simplicity we order first, in K_{cc}, all of the positively signed dofs involved in the constraints.

In a Newton Raphson iterative solution scheme, around a equilibrium state, where equations **(238)** hold, any increment ΔF in macroscopic strain results in an increment in x_b denoted Δx_b and subsequently in an iterative update of the values of x_a, x_c, δ and π, until equations **(238)** hold, and equilibrium is achieved. This is expressed with the following linearization scheme which is solved progressively in the frame of the iterative solution:

$$f_a(x) + K_{aa}\Delta x_a + K_{ab}\Delta x_b + K_{ac}\Delta x_c = 0 \quad \text{(a)} \quad \textbf{(241)}$$
$$f_b(x) - \delta + K_{ba}\Delta x_a + K_{bb}\Delta x_b + K_{bc}\Delta x_c - \Delta\delta = 0 \quad \text{(b)}$$
$$x_b - D^T F + \Delta x_b - D^T \Delta F = 0 \quad \text{(c)}$$
$$f_c(x) - P^T \pi + K_{ca}\Delta x_a + K_{cb}\Delta x_b + K_{cc}\Delta x_c - P^T \Delta\pi = 0 \quad \text{(d)}$$
$$P x_c + P \Delta x_c = 0 \quad \text{(e)}$$

For simplicity we introduce a basis transformation [161,162] operating on each constrained dof pair of dofs "c"

$$[\hat{u}_c] = \begin{bmatrix} \hat{u}_{c1}^p \\ \hat{u}_{c2}^p \end{bmatrix} = [T_p^T] \begin{bmatrix} u_c^+ \\ u_c^- \end{bmatrix} \quad \text{(a)} \quad \textbf{(242)}$$

$$[T_p^T] = \begin{bmatrix} T_1^p \\ T_2^p \end{bmatrix} = \begin{bmatrix} \dfrac{\sqrt{2}}{2} & -\dfrac{\sqrt{2}}{2} \\ \dfrac{\sqrt{2}}{2} & \dfrac{\sqrt{2}}{2} \end{bmatrix} \quad \text{(b)}$$

Each constraint of (241)-e can equivalently be applied by setting u_c^+ equal to zero and thus eliminating it from the total equations. The second line of the transformation matrix (242)-b results from a Gram-Schmidt orthogonalization process. It should also be noted that

$$T_1^p B_p^T \neq 0 \quad \textbf{(243)}$$
$$T_2^p B_p^T = 0$$

Equations (242) and (243) are expressed, in a global setting as:

$$[\hat{u}_c] = \begin{bmatrix} \hat{u}_{c1} \\ \hat{u}_{c2} \end{bmatrix} = \begin{bmatrix} T_1 \\ T_2 \end{bmatrix} [u_c] = [T^T][u_c] \quad \text{(a)} \quad \textbf{(244)}$$

$$T^T B^T = \begin{bmatrix} T_1 \\ T_2 \end{bmatrix} [B^T] = \begin{bmatrix} B'^T \\ 0 \end{bmatrix} \quad \text{(b)}$$

Accordingly, using (244)-b, (241)-d transforms to

$$T_1(f_c(x) + K_{ca}\Delta x_a + K_{cb}\Delta x_b) - T_1 K_{cc}\left(T_1^T \hat{u}_{c1} + T_2^T \hat{u}_{c2}\right) - T_1 B^T(\lambda + \Delta\lambda) = 0 \quad \text{(a) (245)}$$
$$T_2(f_c(x) + K_{ca}\Delta x_a + K_{cb}\Delta x_b) - T_2 K_{cc}\left(T_1^T \hat{u}_{c1} + T_2^T \hat{u}_{c2}\right) = 0 \quad \text{(b)}$$

Equation (241)-e is now replaced by $\hat{u}_{c1} = 0$ that is then directly substituted in the transformed form of equations (241)-a,b and in (a) (245)-b to yield the final form of the linearized equations, as below:

$$f_a(x) + K_{aa}\Delta x_a + K_{ab}\Delta x_b + K_{ac}T_2^T \hat{u}_{c2} = 0 \quad \text{(a)} \quad \textbf{(246)}$$
$$f_b(x) - \delta + K_{ba}\Delta x_a + K_{bb}\Delta x_b + K_{bc}T_2^T \hat{u}_{c2} - \Delta\delta = 0 \quad \text{(b)}$$
$$T_2(f_c(x) + K_{ca}\Delta x_a + K_{cb}\Delta x_b) - T_2 K_{cc}T_2^T \hat{u}_{c2} = 0 \quad \text{(c)}$$

For a given increment in the macroscopic strain ΔF resulting in an increment Δx_b by use of equation, x_a, and u_c are iteratively corrected utilizing equations (246)-a and (246)-c until $|\{f_a^T | (T_2 f_2)^T\}| < tol$. At this point the discretized form of equation (236) can be used, which is expressed as

$$[P] = \begin{bmatrix} P^{11} \\ P^{22} \\ P^{12} \\ P^{21} \end{bmatrix} = \frac{1}{V_{RVE}} D\delta = \frac{1}{V_{RVE}} D f_b \quad \textbf{(247)}$$

Finally, for an infinitesimal increment ΔF around a reached equilibrium state, where (54)a-e hold, using once again (241)-c after statically condensating equations (246)-a and (246)-c in (246)-b we obtain

93

$$\Delta\delta = K'_{bb} D^T \Delta F \tag{248}$$

and subsequently **(247)** gives

$$\Delta P = \frac{1}{V_{RVE}} D K'_{bb} D^T \Delta F \tag{249}$$

Hence the elasticity tensor coefficients are given in a matrix form as

$$\mathcal{A} = \frac{1}{V_{RVE}} D K'_{bb} D^T \Delta F \tag{250}$$

It is important to notice for the forthcoming derivations that the infinitesimal increments ΔP and ΔF that appear in the linearization process, refer to the coefficients of the tensors $\boldsymbol{P}$ and $\boldsymbol{F}$ in bases specified previously, and hence **(250)** doesn't imply a general relation between the total expression of the two tensors.

5.4 Principle of Virtual Work and consistent Linearization of internal nodal forces

Equilibrium on the macroscale level is expressed in the form of the Principle of Virtual Work that is expressed, by exploiting macrohomogeneity condition **(237)** as

$$\delta W = \delta W_{int} - \delta W_{ext} \qquad\text{(a)} \tag{251}$$
$$\delta W_{int} = \int_{V_0} \delta \boldsymbol{F}^T : \boldsymbol{P_M}\, dV_0 \qquad\text{(b)}$$

This variational formulation must hold for a variation in any discrete displacement u_r and this yields the equilibrium of external and internal nodal forces as follows

$$R = F_{int} - F_{ext} \qquad\text{(a)} \tag{252}$$
$$F_{int}^{u_r} = \int_{V_0} \frac{\partial \boldsymbol{F}^T}{\partial u_r} : \boldsymbol{P_M}\, d\Omega_0 \qquad\text{(b)}$$

A finite element solution approach requires C^1 continuity of the shape functions [59] In order to use, in the actual implementation entities that have been derived in previous sections, equation **(252)** is rewritten as

$$F_{int}^{u_r} = \int_{V_0} (\boldsymbol{G}^i \otimes \boldsymbol{g}_{i,u_r}) : (P^{jk} \boldsymbol{E}_j \otimes \boldsymbol{e}_k)\, d\Omega_0 \tag{253}$$

where $\quad \delta \boldsymbol{F} = (\boldsymbol{g}_{i,u_r} \otimes \boldsymbol{G}^i)\delta u_r$.

Equation **(252)**-a represents a nonlinear system that is subsequently linearized to be solved in a Newton Raphson iterative procedure. The tangential stiffness matrix of the internal forces is obtained as

$$K_{rs}^{int} = \int_{V_0} \frac{\partial^2 \boldsymbol{F}^T}{\partial u_r \partial u_s} : \boldsymbol{P_M} + \frac{\partial \boldsymbol{F}^T}{\partial u_r} : \frac{\partial \boldsymbol{P_M}}{\partial u_s}\, d\Omega_0 = \int_{V_0} (\boldsymbol{G}^i \otimes \boldsymbol{g}_{i,rs}) : \boldsymbol{P_M} + (\boldsymbol{G}^i \otimes \boldsymbol{g}_{i,r}) : \boldsymbol{P_{M,s}}\, d\Omega_0 \tag{254}$$

Once again to account for the derivations of previous section, in the second term of the integral of **(254)** it can be used that

$$(P^{ij} \boldsymbol{E}_i \otimes \boldsymbol{e}_j)_{,s} = P_{,s}^{ij} \boldsymbol{E}_i \otimes \boldsymbol{e}_j + P^{ij} (\boldsymbol{E}_i \otimes \boldsymbol{e}_j)_{,s} = A_{ijkl}(F_{,s}^{kl}) \boldsymbol{E}_i \otimes \boldsymbol{e}_j + P^{ij} (\boldsymbol{E}_i \otimes \boldsymbol{e}_{j,s}) \tag{255}$$

94

where the components A_{ijkl} are given by (250). The fact, that only variations of stationary bases' vectors are equal to zero, was taken into account for this derivation. More details concerning the calculation of the $\boldsymbol{g}_{i,r}$, $\boldsymbol{g}_{i,rs}$, $F_{,s}^{kl}$ and $\boldsymbol{e}_{j,s}$ will be given in Appendix. Finally taking into account the dependence of the external forces F^{ext} on the displacements of the structure, the total tangential stiffness matrix is given by

$$K = K_{int} - K_{ext} \tag{256}$$

and a residual in the total force vector R in (252)-a yields an iterative correction

$$K\Delta u = -R \tag{257}$$

of the total displacement vector.

5.5 Applications

5.5.1 Hemispherical Shell Subjected to alternating radial forces

The first application is based on a popular benchmark problem [163] for large deflection analysis of shells, namely hemispherical shell of Figure 26 with a 18°pole cut-out at is pole, subjected to four radial point Loads, of magnitude of P=400kN and of alternating sign at 90°integrals. The structure is considered to be heterogeneous at the microscale level, with its characteristic microstructure to be consisting of two different phases of Elastic material, i.e. the matrix material and two layers of perpendicularly stacked cylindrical inclusions.

The macroscopic geometry is discretized with subdivision surfaces [120,121] to achieve the necessary C1 continuity. The Representative volume element is discretized with hexahedral elements by use of Gmsh [164]. The total FE^2 solution scheme for the analysis in multiple scales of the studied thin shells under large deflections is implemented in Msolve [128]

A total of three FE2 simulations is performed. At first we assign to both phases of the RVE the same parameters for the Young's modulus E= 6.825 107 and Poisson's ratio ν= 0.3 coinciding with the benchmark problem's suggested values. This results in a homogeneous material configuration and the performed analysis intends in the verification of the proposed formulation.
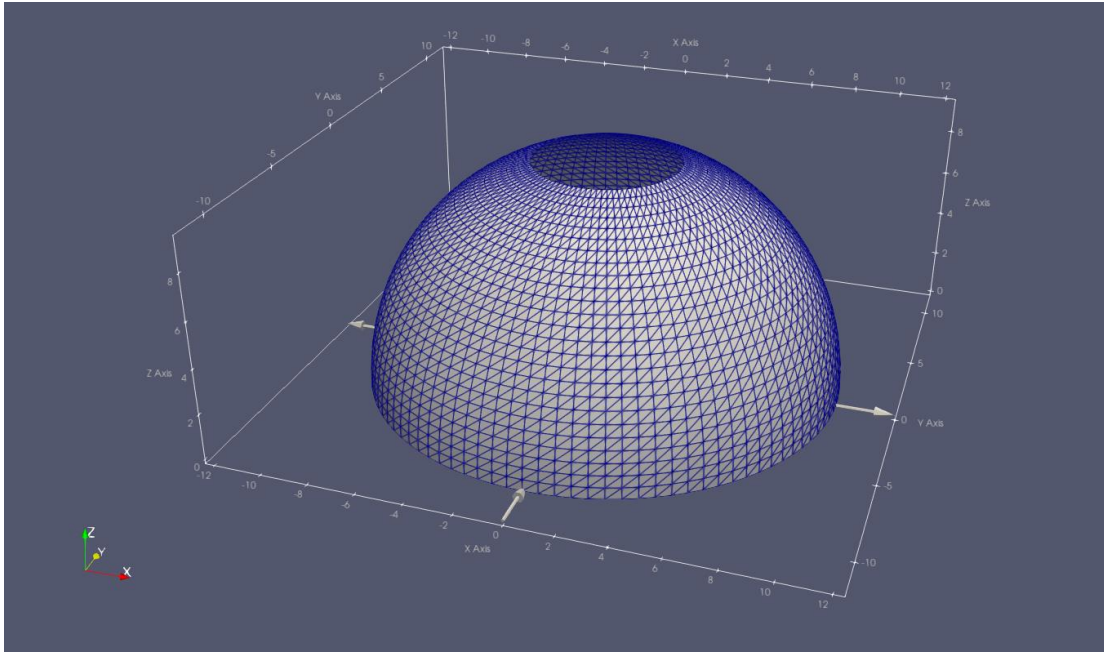
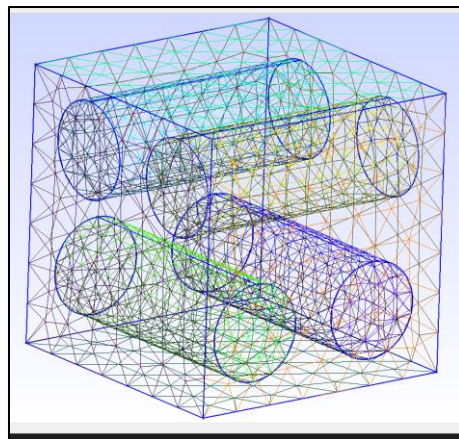**Figure 26 Hemispherical Shell with an 18deg pole cut-out**

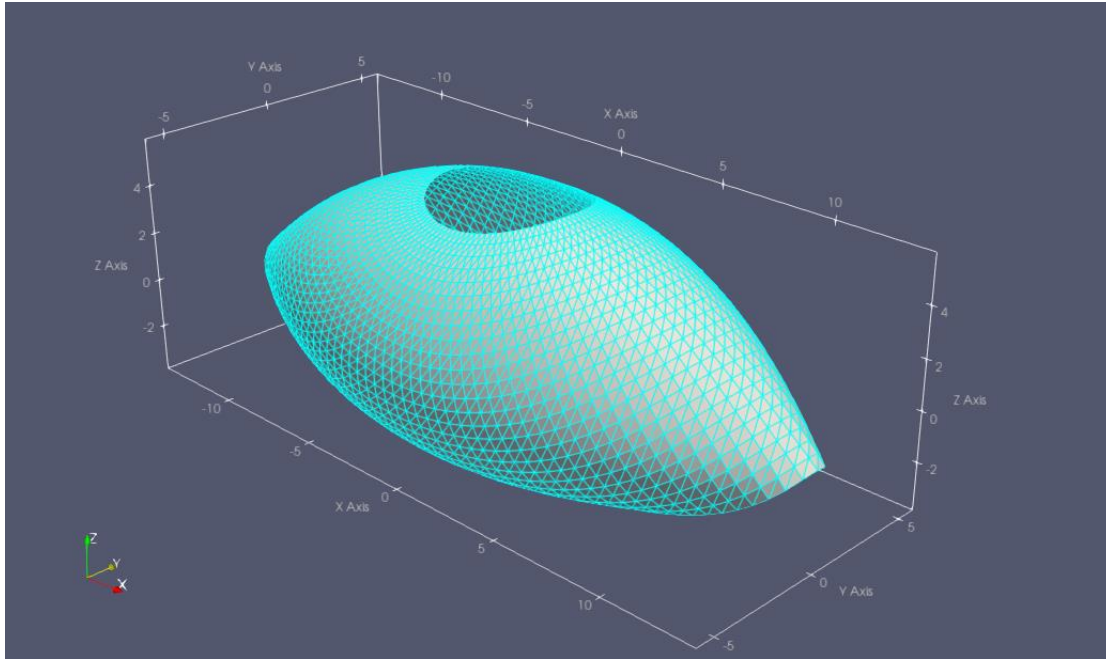**Figure 27 Cubic RVE with cylindrical inclusions**

Figure 28 Deformed configuration of the spherical shell for maximum imposed loading value

As it can be seen in Figure 11 and Figure 12 the obtained load displacement curves for the two monitored nodes of interest, are in perfect agreement with the expected values given in [163].

For the two following FE^2 analyses the focus is on an actual two phase material configurations, obtained by a 15% decrease in the Young's modulus values of the matrix and the inclusions separately.

These runs are a simple demonstration of the potential of the proposed formulation in the simulation of microscopically heterogeneous shell structures. The obtained results can also be verified by observing that the resulting load Deflection curves fall within the limits defined by the benchmark curve and a complementary run of our implementation of the formulations [121,165], for the configuration of the benchmark and only a 15% decrease in the value of Young's modulus.
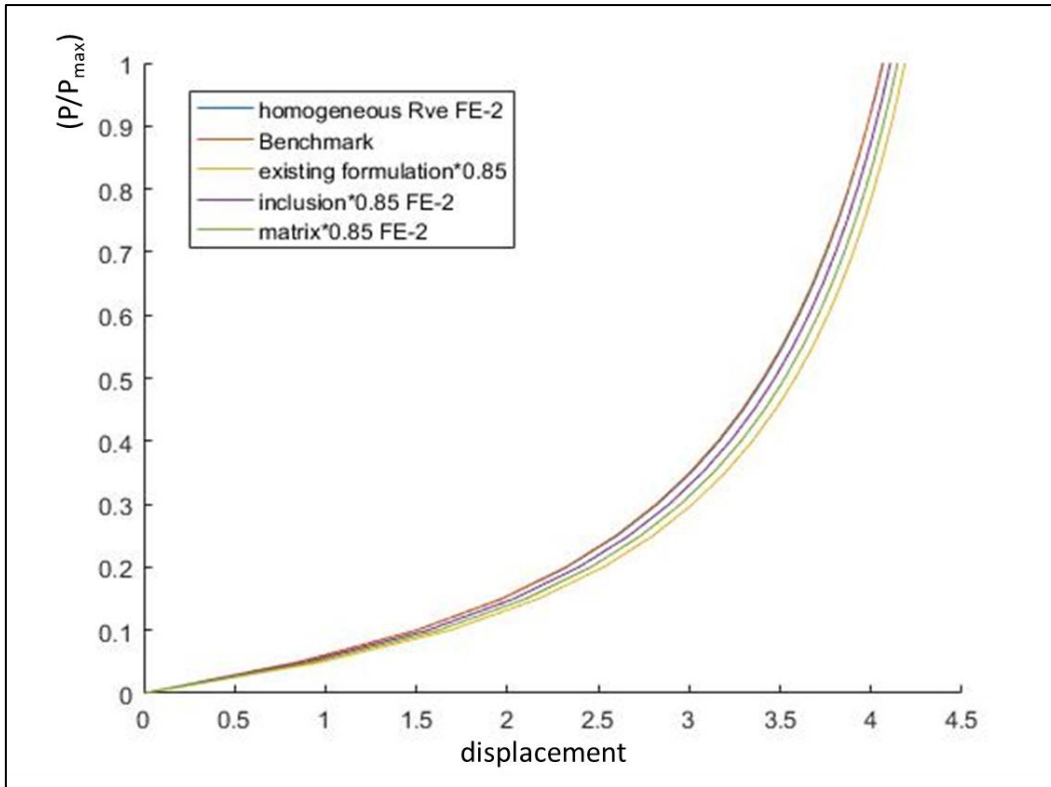
Figure 11 Positively loaded node 'A': benchmark load displacement curve and complementary analysis' results
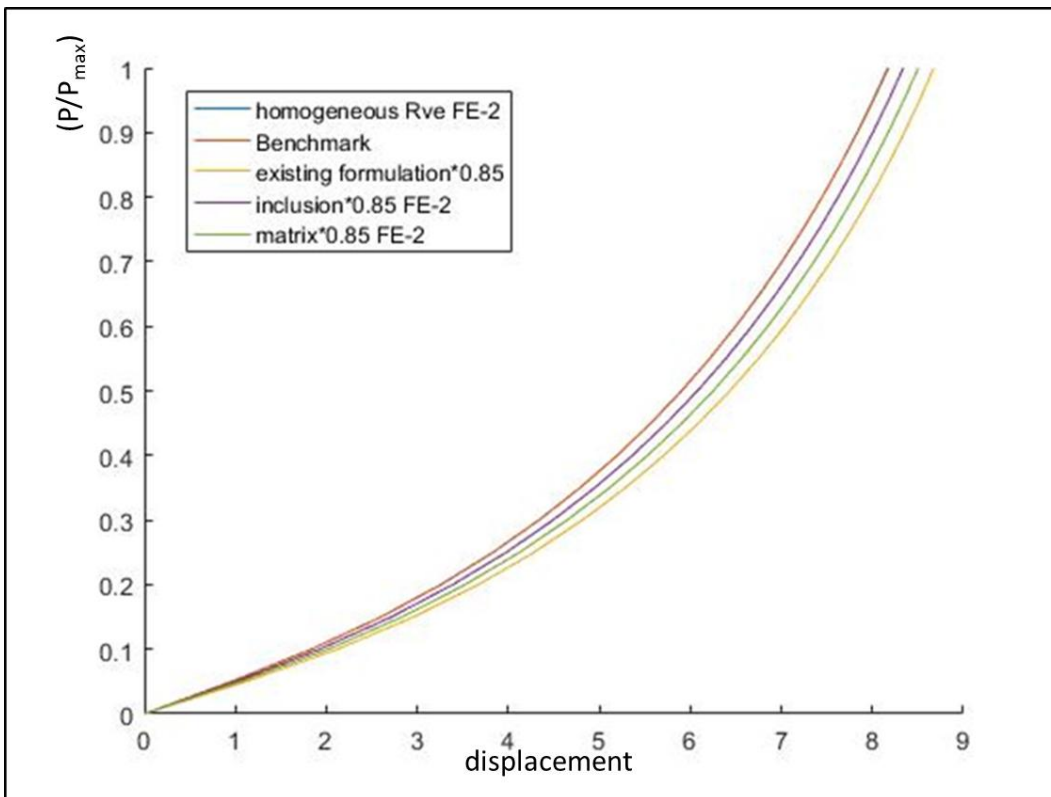

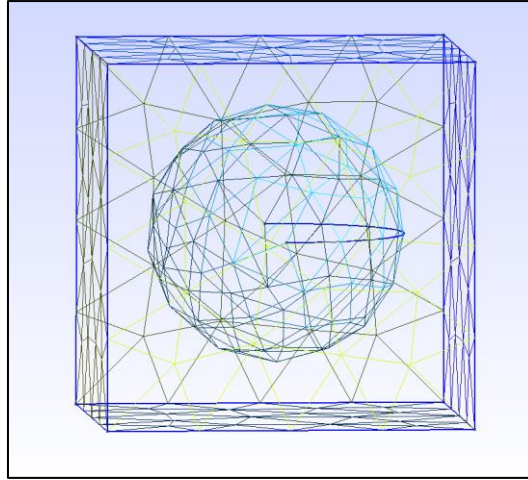**Figure 12 Negatively loaded node 'B': benchmark load displacement curve, FE² and complementary analysis' results**
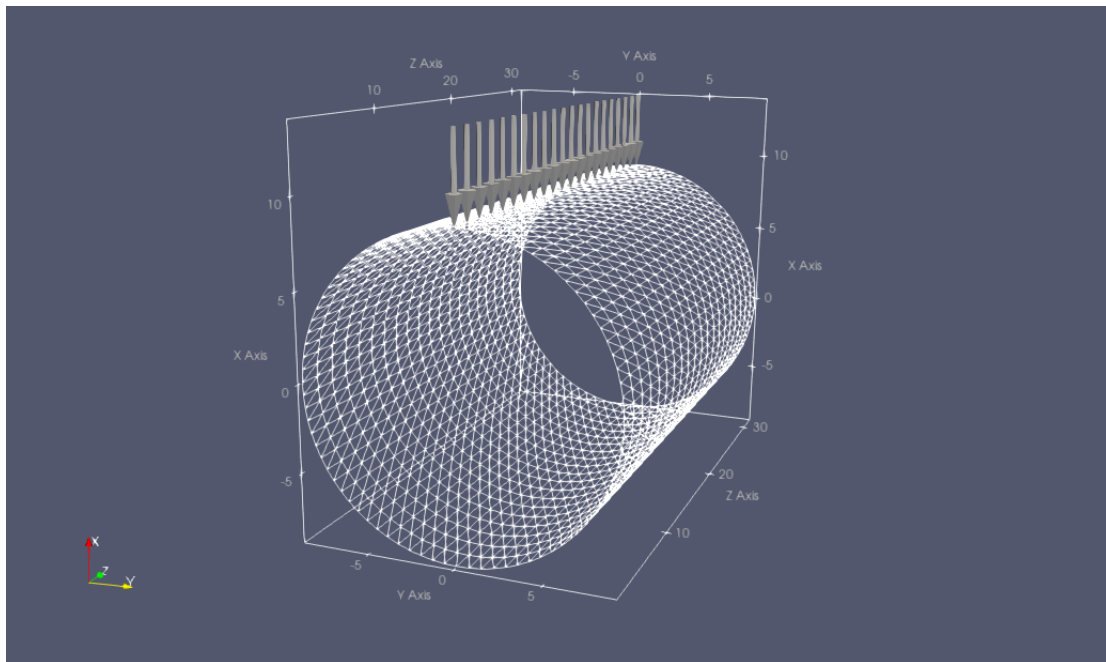
Figure 29 Cubic RVE with a spherical inclusion

Figure 30 Cylindrical shell, supported at the bottom with a distributed line load

5.5.2 Cylinder under line load

The next application is also based on a popular benchmark in the field of shell element technology which is a bending dominated problem originally introduced in [166] subsequently studied in [167-169] and [47]. A cylinder of length L=30 cm, radius R=9 cm and thickness h_0=0.2cm is considered supported at the bottom and subjected to a line load p as shown in Figure 30. The material RVE consists of a matrix material and one spherical inclusion Figure 29. For both phases a compressible Neo-Hookean material is used, defined by the following strain energy function

$$\psi = \frac{\mu}{2}(tr(\boldsymbol{C}) - 3) - \mu ln(\sqrt{det(\boldsymbol{C})}) + \frac{\lambda}{4}(det(\boldsymbol{C}) - 1 - 2ln(\sqrt{det(\boldsymbol{C})})) \tag{258}$$
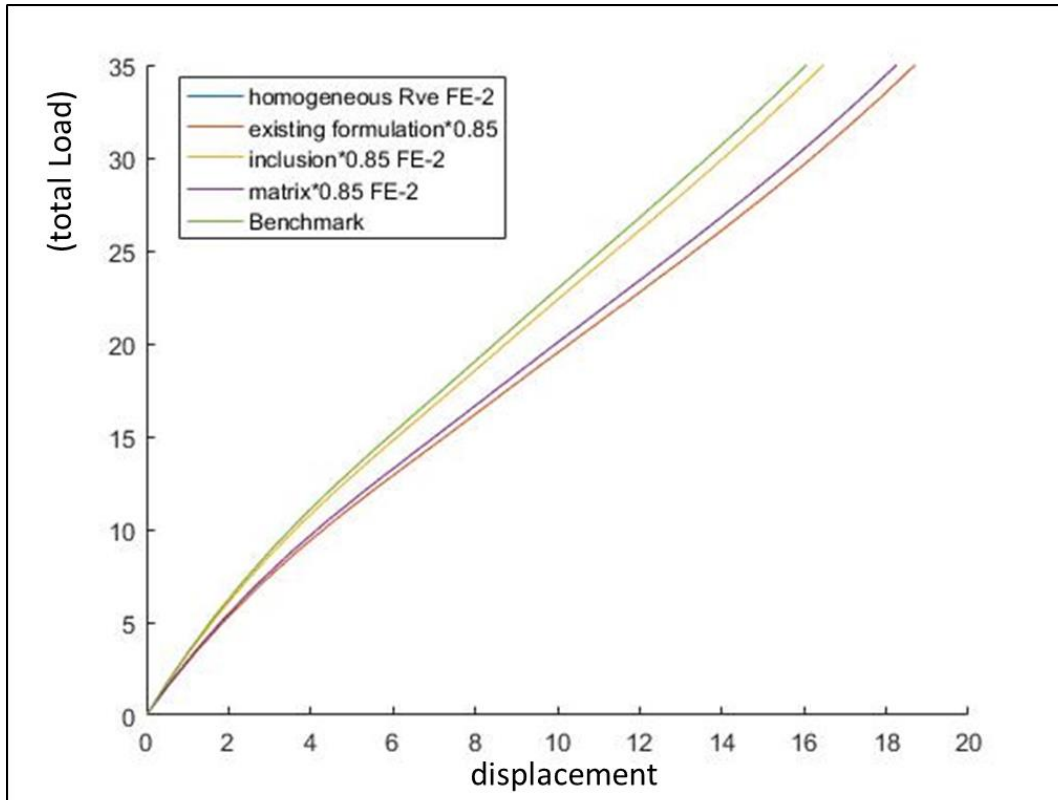
Figure 31 Monitored Node 'A': FE^2 and complementary analyses's results
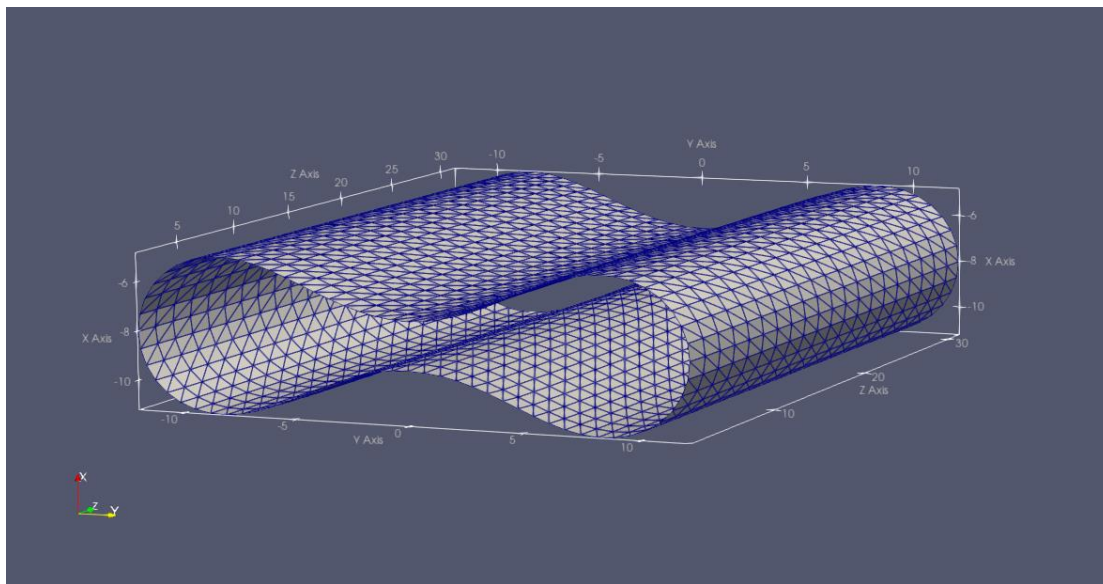

Figure 32 Deformed configuration of cylindrical shell at maximum deflection

Again, the macroscopic geometry is discretized with subdivision surfaces and supports are imposed by the Lagrange multiplier method [170]. Following the same verification strategy as in the first application, we perform once again three kinds of FE^2 analyses. At the first one we assign to the Lame constants the values used in the benchmark example, i.e. $\mu = 6000\text{kN/cm}^2$ and $\lambda = 24000$ kN/cm^2. We apply a total load of 35kN. The analysis yields a maximum displacement value of -16.06190 cm for the monitored node A. It is in a good

agreement with results obtained from [168,169] and the results reported in these works from referenced articles that range from -15.86 cm to 16.21 cm for various finite element formulations.

Subsequently two FE^2 simulations were preformed, accounting for a 15% decrease in the values of the Lame constants, fisrtly for the matrix material and secondly for the spherical inclusion. In order to define bound curves for the expected behaviour of the two microscopically heterogeneous cylinders we perform two complementary runs by use of our implementation of [121] combined with the methodology described in [165] and Section 3.2.1.2 for the incorporation of a hyperelastic phenomenological law in a thin shell formulation. Once again, the values assigned to the material model are those used in the original benchmark for the upper bounding curve and decreased by 15% for the analysis corresponding to the lower bounding curve.

As it can be seen from Figure 31 the load displacement curve of the FE^2 simulation of the practically homogeneous structure coincides with the first complementary analysis, and the behaviour exhibited the FE^2 modeling of the composite structures is well along the bounding lines determined by the complementary analyses.

5.6   Conclusions

In this Chapter, a formulation for multiscale modeling of thin shell structures at finite deformations has been proposed. The developed averaging relations, that are appropriate for thin Kirchhoff Love shells and meet the Hill Mandel condition, lead to a classical wording of the microscale boundary value problem avoiding the implementation of a change of direction of the releases of the constraints related to the plane stress condition. The accuracy of the introduced scale transition relations and the overall formulation of the problem is verified through benchmarking based on popular problems. The resulting methodology allows for a straight forward incorporation of the large displacement thin shell case in existing FE^2 codes. The simulation possibilities originating from this formulation are countless and are related to the wide applicability of the Kirchhoff Love theory in many fields of engineering.

6 Stochastic Multiscale modeling of Graphene reinforced composites

Graphene is an emerging material that has attracted tremendous scientific interest due to its extraordinary mechanical and electrical properties. An allotrope of carbon, graphene forms a hexagonal honeycomb lattice which can be one atom thick, known as single layer graphene sheet (SLGS) synthesized via various methods [60-62]. Graphene has been found to be the strongest material ever tested [63, 64] with a Young's Modulus of 1 TPa and Tensile Strength of 130 GPa, making it a very promising material for structural applications. Graphene sheets (GS) and its derivative products the carbon nanotubes (CNT), have been successfully used as filler materials in nanostructured composites [65, 66], greatly enhancing the mechanical properties of the matrix. Successful applications include both metal matrix [67, 68] and polymer matrix [69, 70] nanocomposites. In this Chapter an effective way for the modeling of the mechanical behavior and properties of graphene nanocomposites in multiple scales is presented in detail. Two distinct points in the modeling process of graphene nanocomposites are presented in detail, first the method of simulation of graphene and second the load transferring mechanism between the matrix and the filler.

The modeling methods currently available for the simulation of the mechanical behavior of graphene, take into account the interatomic interactions between the carbon atoms in the hexagonal lattice. Computational methods widely used, can be generally classified into two categories: i) the atomistic modeling [71, 72] with major techniques including molecular mechanics and ab-initio calculations and ii) continuum mechanics approaches [73, 75] including the analysis with finite element methods. Each of the above methods, comes with different performance along multiple time and size scales. Ab-initio and molecular mechanics techniques generally provide high accuracy at the smallest scales, but due to the high computational effort required, they are suitable for small size models and short time spans [75, 76]. On the other hand, continuum mechanics techniques aim to provide accurate and computationally efficient models at larger size and time scales.

The main principle behind continuum mechanics approaches, usually referred as Molecular Structural Mechanics (MSM) methods, is the simulation of the covalent bonds between the carbon atoms, with equivalent structural finite elements [76]. The physical properties of the equivalent finite elements can be analytically calculated by making use of equivalent strain energy criteria, with reference to the force field that defines the interatomic interactions. Currently, the dominant method is replacing the carbon covalent bonds with beam finite elements, which can capture both stretching and rotation between atoms. While this approach is computationally effective and accurate compared to the atomistic simulations [76-79], the computational effort increases dramatically while shifting time and size scales. For this reason the beam finite element model is replaced with equivalent coarser finite element mesh, aiming to provide a model with significantly fewer degrees of freedom (dofs) but with the reasonably close degree of accuracy. The finite element types that are used as alternatives to the detailed model depend on the geometry of the nanoparticle. For example, for the simulation of the mechanical behavior of beam-like CNTs, the initial MSM frame model is projected to equivalent beam element (EBE) series [80-82]. A lower element to volume ratio is then achieved, lowering the computational effort required and enabling more time or size demanding results to be achieved.

An equivalent continuum model is develop in this Chapter that can be used as a surrogate to the detailed beam element MSM model of GSs. GSs are found to have shell like behavior in relatively large models, compared to the beam like behavior of CNTs. The problem of finding an equivalent shell element (ESE) that can be used as an effective surrogate to the corresponding detailed molecular mechanics models of the graphene is addressed. The ESE should be able to accurately represent both the membrane and the plate behavior of the GS. If this requirement is satisfied then this ESE can be embedded into a 3D solid representation of a polymer matrix, for the study of the mechanical behavior of the nanocomposite. A representative volume element (RVE) is chosen for such simulations. The load transferring mechanism between the matrix and the filler has been found to play a crucial role in the mechanical properties of nanocomposites. Numerical simulations indicate that the interfacial stiffness and strength, define the limits of mechanical enhancement of the nanocomposite by the filler and the occurring slippage when failure arises [80, 83]. Functionalization techniques have been proposed for enhanced cohesion between the matrix and the filler [84, 85]. A load transferring mechanism via a friction model has been previously applied with success in modeling CNT nanocomposites [80, 86]. In the present study, the interfacial load transferring mechanism is being modeled with a definition of cohesive zone between the ESE and the three dimensional matrix. The cohesive behavior is defined through a traction-separation law between the two surfaces and can also follow a predefined damage model. Cohesive finite elements have been successfully applied for capturing delamination and debonding phenomena of composite or nanocomposite materials [87] and reinforced steel [88], with good agreement with the experimental data and hence are selected in this study for the modeling of this intermediate interface zone.

Numerical results which present extensive parametric investigations of the finite element simulations of graphene nanocomposites are provided and it is demonstrated that the representation of the hexagonal carbon lattice of GSs with ESE and the load transferring mechanism with a cohesive behavior, is an accurate and effective modeling technique.

6.1 Finite Element Modeling of Graphene

6.1.1 The Molecular Structural Mechanics model

Molecular Structural Mechanics (MSM) finite element models have been found to be effective ways for the modeling of graphene and carbon nanotubes (CNTs). Graphene sheets (GS) can be regarded as large molecules consisting of carbon atoms in a hexagonal honeycomb lattice. From the molecular mechanics point of view, atomic nuclei have their motions regulated by electron-nucleus and nucleus-nucleus interactions [89]. A representation of a GS hexagonal lattice is shown in Figure 1. The force field that defines the interatomic interactions depends only on the relative positions of the nuclei, and the molecular potential energy presents direct similarity with the beam element strain energy.
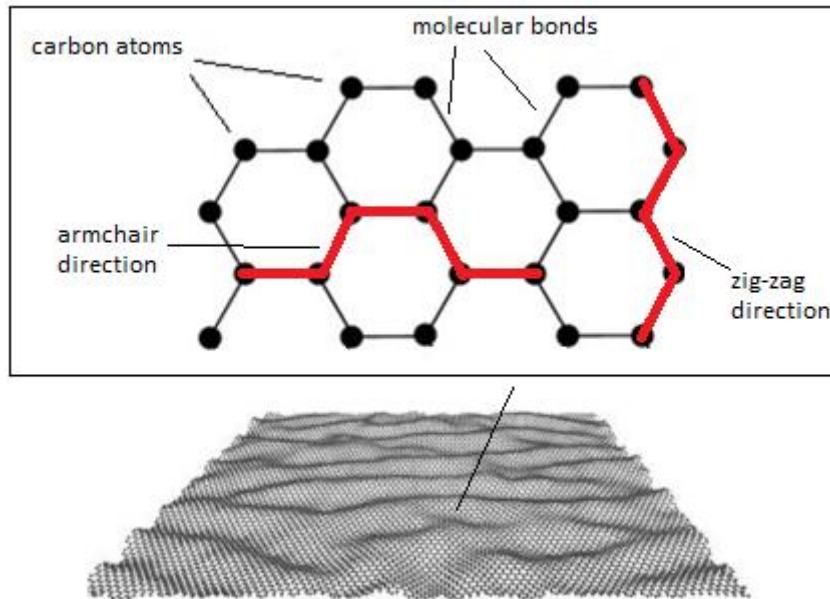
Figure 1: Representation of a GS hexagonal lattice

A detailed description of the MSM approach can be found in work of Li and Chou [76] who originally proposed the model, assuming a beam of circular cross-section. However, the circular beam section assumption of the classical MSM, which implies that the in-plane and out-of-plane bending rigidities of the beam are equal, is found to be accurate only for the in-plane modeling of the GSs. Lu and Hu [78] proposed an elliptical cross-section for the beam, since out of plane bending rigidity is largely overestimated in the MSM approach, a fact supported by atomistic simulations as well. Therefore, a modified version of the MSM was considered in which the out of plane bending rigidity of the beam elements was related to the weak inversion energy of the covalent bond. A detailed description of this so-called modified MSM (mMSM) approach can be found in the work of Chen [90] who proposed a rectangular cross section for the beam modeling of the covalent bonds.

Among common validation tests for mMSM graphene models is a tension test for the verification of GS mechanical properties. Such test was implemented for a GS of 22.1676x21.1676 nm, loaded in the zig-zag direction, as shown in Figure 2. For an interlayer distance of t=0.34nm, the Young's Modulus and the Poisson's ratio, referring to the in-plane Poisson's effect, of the sheet was computed at E=1.04TPa and v=0.0607, respectively. Practically the same results were obtained for the armchair direction, which verifies that GS can be regarded as having an isotropic membrane behavior [74]. Even though the calculated Young's Modulus of the GS is consistent with other studies, Poisson's ratio values reported in [71, 74, 76, 91, 92] are scattered in a wide range from 0.06 to 0.45. As stated in [91], there is lack of consistent experimental results that would allow for a proper validation of the models with respect to some reliable experimental values.
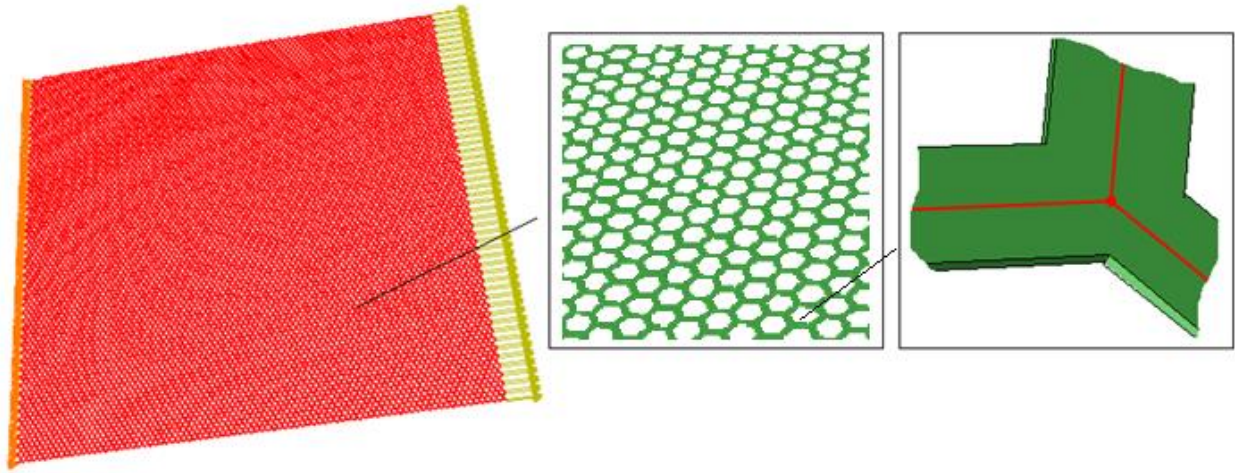
Figure 2: Tension test for a 22.1676x21.1676 nm GS in the zig-zag direction, with the mMSM approach

6.1.2 The Equivalent Shell Element of a Single Layer Graphene Sheet

Despite the fact that mMSM simulation is computationally effective compared to atomistic simulations [76-79], the cost of analysis is still high when relatively large GS models are simulated. For example an mMSM model of a single layer graphene sheet (SLGS) of 88.76x84.66 nm consists of approximately 10^6 dofs, making even simple static loading cases very computationally intensive. It is therefore evident that simulations in the scales of micrometers with current mMSM models are very inefficient. The restrictions of size and time analysis of the mMSM method are usually dealt with further substitution of MSM frame models, with equivalent continuum elements. This concept has already been implemented in the modeling of CNTs where series of coarser equivalent beam elements (EBE) were successfully used as surrogates to the complete CNT MSM models [80-82]. The much lower element to volume ratio achieved via the EBE, makes possible the simulation of larger scale models and longer time spans. Along with the low computational cost, great accuracy is also provided with the EBE [80].

An equivalent shell element (ESE) is proposed as surrogate to the mMSM model of a SLGS, similar to the EBE-CNT element in [80]. While CNTs behave like beams, SLGS are expected to have a plate-like behavior when subjected to out of plane loads and a membrane-type behavior when subjected to in-plane loads. Limited studies are currently available about modeling the plate behavior of a SLGS with equivalent plate elements [93, 94], but no information is available about combined plate and membrane behavior in a single approach. The difficulty arises when searching for the equivalent shell due to the fact that an ESE would have to validate both the membrane and the plate behavior of the SLGS simultaneously. Bending tests indicate that the correct bending rigidity for a plate SLGS is much less than the rigidity obtained when using the membrane behavior mechanical constants E=1TPa and v=0.0607. A simple approach is proposed here to address this issue in terms of a membrane behavior uncoupled to a plate behavior of a thin shell formulation according to:

$$K = \begin{bmatrix} K_m & \\ & K_b \end{bmatrix}$$

where *Km* is the stiffness sub-matrix that corresponds to the membrane behavior of the shell and *Kb* the stiffness sub-matrix that corresponds to the plate behavior of the shell. The use of a surrogate model with an uncoupled membrane and plate behavior, gives us the opportunity to determine different par6 ameters for the *Km* and *Kb* submatrices and choose the bending rigidity that fits best with the mMSM model behavior. Therefore, two equivalent continuum models are necessary for the determination of ESE according to eq. (259) : an equivalent membrane element (EME) and an equivalent plate element (EPE). A representation of the degrees of freedom that correspond to membrane and plate finite elements of a 4-noded ESE quadrilateral is shown in Figure 3.
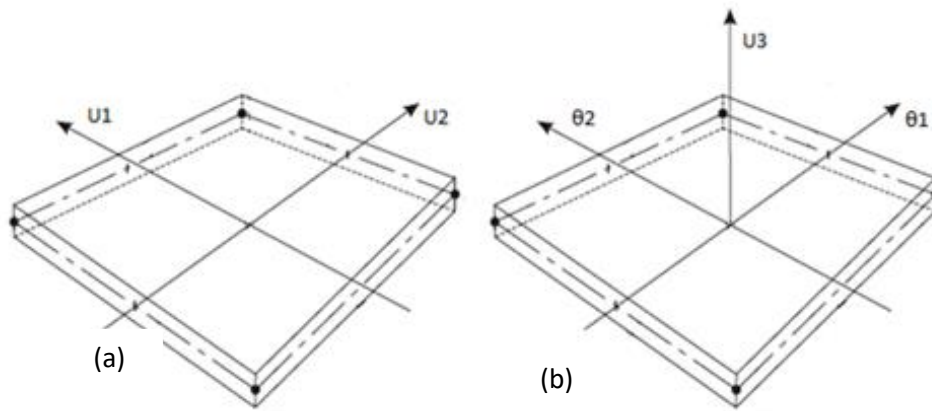

Figure 3: Degrees of freedom of a 4-noded quadrilateral membrane EME (a) and plate EPE (b)

As mentioned earlier, the EME physical properties are already derived from the tension test, that is described in section 2.1, as E=1TPa, v=0.0607 and thickness=0.34 nm, thus the *Km* submatrix of eq. (259) can be directly formulated. For the EPE to have consistency with the bending behavior of the mMSM model, a numerical procedure is required that guarantees that certain constraints must be satisfied, such as equal strain energy and displacements when the same loading and boundary conditions are applied. This procedure is described in the following section 6.1.3.

6.1.3 The Equivalent Plate Behavior of Graphene

Considering the mMSM solution as the exact SLGS plate response, an optimization algorithm is applied in order to reach a solution that minimizes the error between the EPE and the mMSM model. For this purpose, both models should be subjected to the same loading and boundary conditions. All of the edges of the plate and of the mMSM frame are clamped and a concentrated load is applied in the center of both models as shown in Figure 4. The objective function to be minimized in the proposed optimization formulation is the difference between the total strain energy of the mMSM and the EPE models, subjected to the constraint

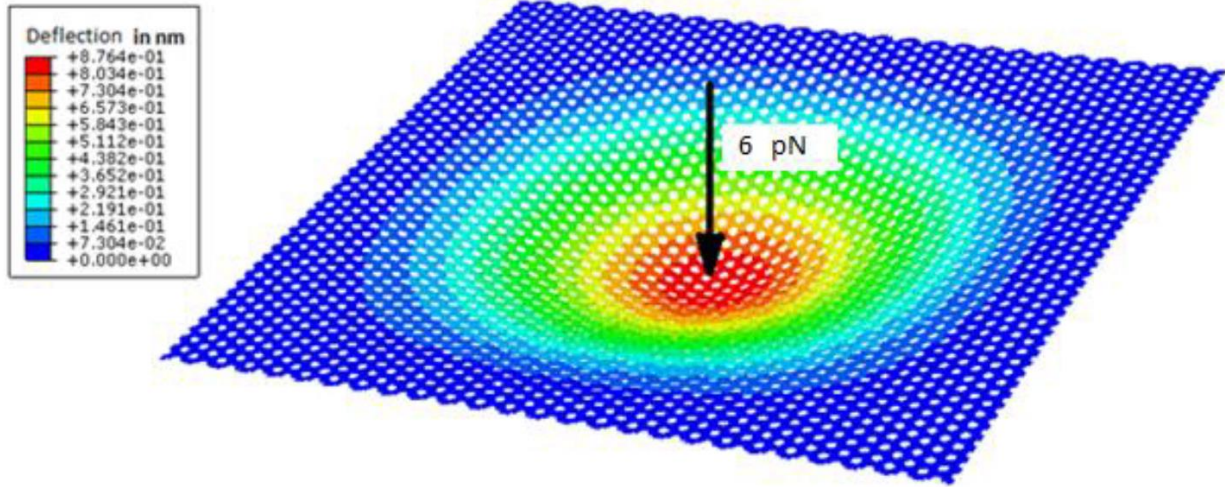that the maximum displacement of the two models should be almost identical.

Figure 4: A rectangular 11.08x10.58 nm SLGS with all edges clamped, subjected to an out of plane 6 pN load

The steps of the optimization procedure are as follows:
Minimize the objective function

$$f(X) = |Vfr - Vpl(X)| \tag{260}$$

Where *Vfr* is the strain energy of the mMSM frame model and *Vpl(X)* is the strain energy of the EPE model, which is a function of the parameters $X = [E \; \nu \; t]^T$, i.e. the Young's Modulus, the Poisson's ratio and the thickness of the EPE, respectively, subjected to the following maximum displacement constraint :

$$|\max Ufr - \max Upl(X)| \leq tol \tag{261}$$

where $\max Ufr$ is the maximum displacement of the mMSM model and $\max Upl$ is the maximum displacement of the EPE model.

The bending behavior of an isotropic plate is fully determined from its rigidity D_e given in Eq. (262):

$$D_e = \frac{Et^3}{12(1 - \nu^2)} \tag{262}$$

As we can see in eq. (262) the same rigidity D_e, and thus the same strain energy *Vpl(X)*, can be obtained for different values of the parameter vector *X*, i.e. for various combinations of parameters *E, t* and *ν*. Thus in order to simplify the optimization problem in eq. (260) we choose to arbitrarily set the values of *ν*=0.0607, which is the same value used for the membrane description, and some assumed thickness *t* and let the optimizer search only for the Young's Modulus *E* of the EPE. For consistency with the values of EME, the equivalent thickness can afterwards be altered to *t*=0.34nm, and then recalculate *E* from the plate rigidity equation (262). This simplification doesn't affect the success of the minimization problem,

for which we obtained a solution with maximum displacement error less than 0.3 % and less than 0.8 % for the objective function, as it is shown in Figure 7.

In the procedure described above, no assumptions were made regarding the SLG size and shape. Therefore, the derived EPE can substitute the plate behavior of the mMSM model of a SLG, regardless of lattice shape and dimension. The number of plate finite elements required for a reliable estimation of the equivalent modulus is determined by means of a convergence study. Figures 5 and 6 illustrate the sensitivity of the proposed method to the finite element mesh density and the size of the mMSM model. In Figure 5, the graph of E versus the number of plate elements is depicted for an 11.08x10.58 nm SLGS. A finite element mesh of 40x40 plate elements is adequately fine and converges to a solution of E=5.341e10 MPa. The effect of the SLGS model size is depicted in Figure 6 in which the computed homogenized E is plotted as a function of SLGS size. For these calculations, the converged EPE model of 40x40 plate finite elements was used. From this figure it can be seen that the SLGS of 11722 (105x111 nm), is homogenous enough to converge to the value of E=5.316e10 MPa. It is interesting to note that the size of the mMSM model seems to slightly affect the results, with a maximum of 0.37% difference in E between the smallest and largest size models.
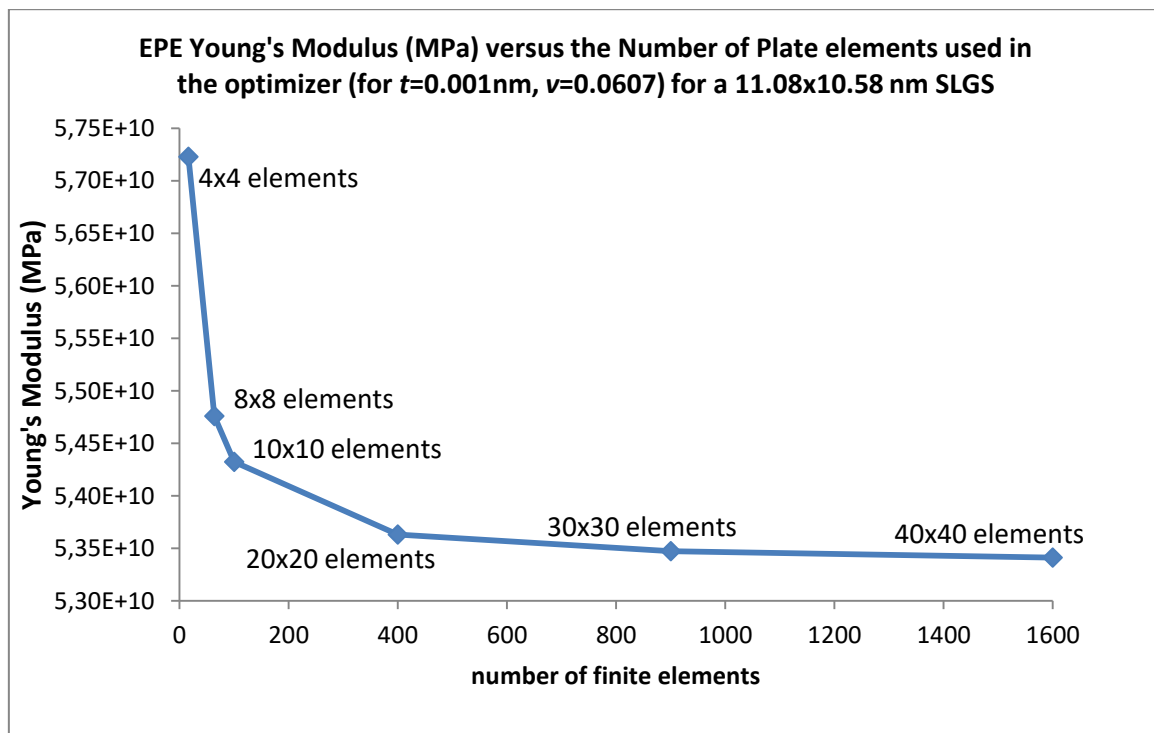

Figure 5: Dependence of the EPE Young's Modulus on the finite element mesh density

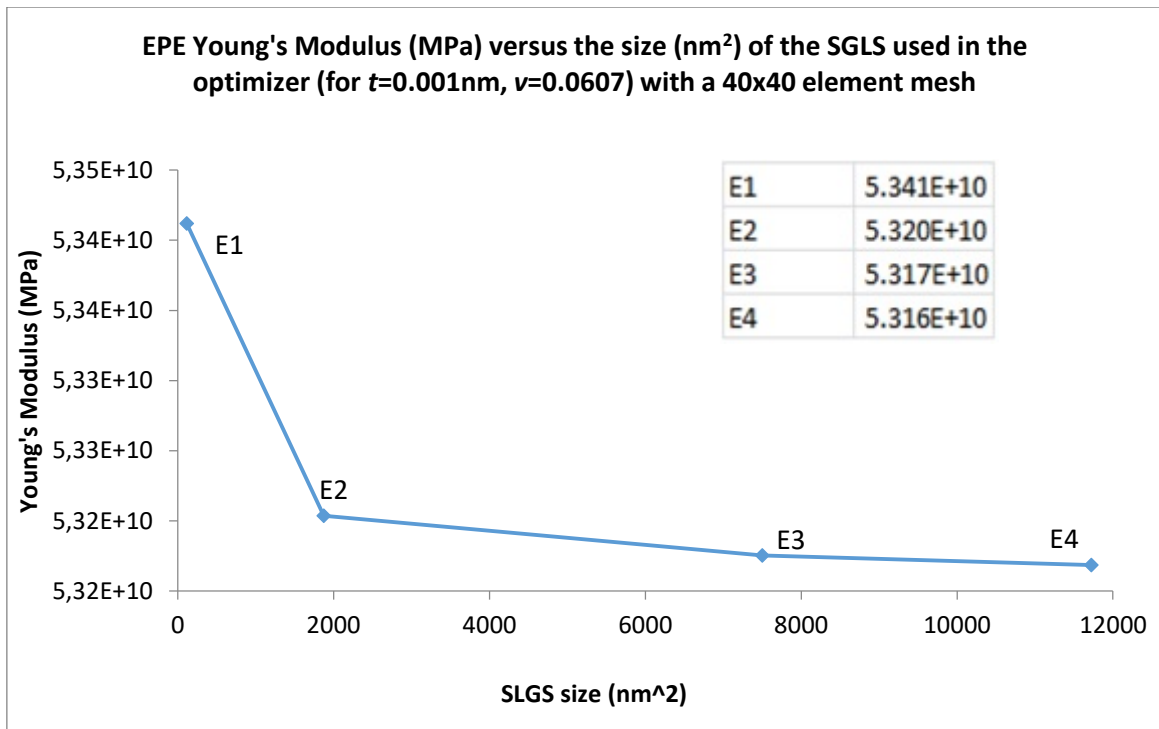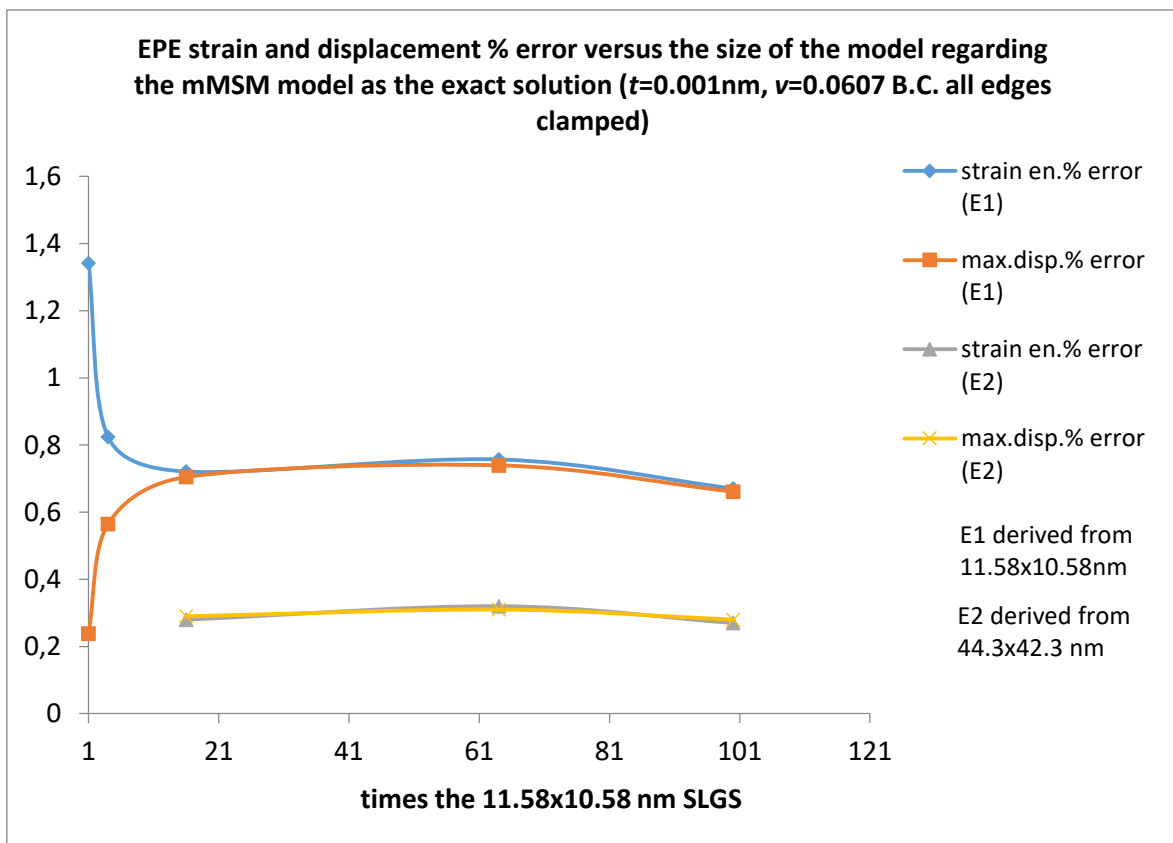**Figure 6: Dependence of the EPE Young's Modulus on the mMSM model size**

Figure 7: Strain and displacement % errors for EPE versus the size of the model

Figure 7, depicts the error in displacements and strain energy, versus the model, for an EPE Young's Modulus derived from the 11.08x10.58 nm SLGS. This error is computed with the mMSM solution as the reference "exact" one. The small error in displacements and strain

energy reveals the great accuracy of the EPE, while the model shifts sizes, and confirms that the converged value for the Young's Modulus, depicted in Figures 5 and 6 is correct. The strain energy and displacement error converge at a minimum value at the point that model becomes 20 times (in terms of surface) the 11.58x10.58 nm mode, which corresponds to a 44.3x42.3 nm SLGS surface. This error behavior is attributed to the higher homogeneity of the mMSM model as the size increases, behaving more like a plate. However, high accuracy is observed in all model sizes, with a bounded error growth, which is almost zero up to a 44.3x42.3 nm SLGS.

A plate is uniquely defined by its stiffness parameter D_e and once this parameter is obtained it can be used in problems with different boundary and loading conditions. Similar bending tests with different boundary and loading conditions, such as the asymmetric loading shown in Figure 8, indicate errors of similar magnitude, below 1% in strain energy and displacements for all model sizes.
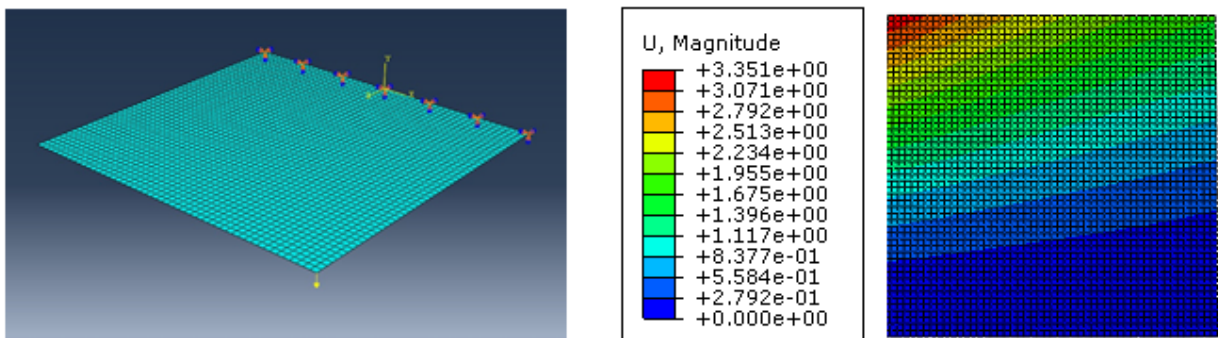

Figure 8: An asymmetric bending test with a concentrated force and one edge clamped for the EPE of a 44.3x42.3nm SLGS, modeled with 50x50 plate elements
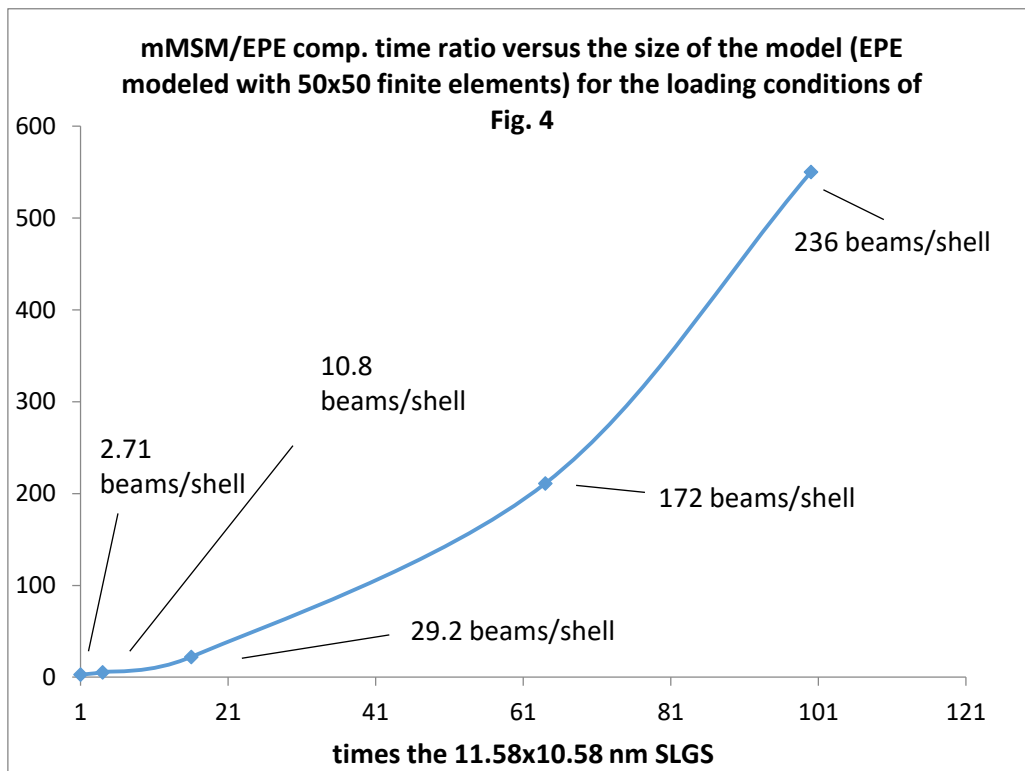

Figure 9: Computational time ratios achieved with the EPE for the problem of Fig. 4

110

Regarding the computational efficiency of the EPE, the graph of Figure 9 illustrates the effectiveness of the EPE as the size of the SLGS increases. The EPE approach is found to be over 600 times faster than the original mMSM model for a SLGS larger than 100x100 nm, while the accuracy in terms of strain energy and displacements is kept over 99%. Therefore, the EPE approach makes possible accurate finite element simulations of SLGS in large size and longer time scales. For the remaining applications the value of the Young's Modulus E has been chosen as the converged value E4 regarding the model size (Figure 6), and afterwards recalculated for t=0.34 nm using eq. (262). Thus the resulting value of E=1.352 GPa can be used for a SLGS in the scales of micrometers with over 99% accuracy. The ESE of a SLGS can afterwards be formulated as a combination of the derived EME and EPE using eq. (259).

6.2   The Finite Element Model of Graphene Reinforced Nanocomposites

6.2.1 The Interfacial Load Transferring Mechanism

The Interfacial Load Transferring Mechanism (ILTM) between the matrix and the filler has attracted a lot of scientific interest, due to its importance on the mechanical behavior and properties of nanocomposites. In a polymer matrix nanocomposite, while the carbon atoms in graphene interact through strong covalent bonds, graphene or CNTs interact with the matrix through weak Van der Waals forces [86, 95]. Techniques known as functionalization [84,85] have been applied, in order to covalently bond carbon atoms with the polymer, greatly enhancing the ILTM stiffness and strength. Experimental studies in CNT reinforced composites (CNT-RC) [93] reveal a non-linear pull-out force-displacement relation when the interfacial strength (IS) values are exceeded. Therefore, the correct modeling of a CNT-RC or a GS-RC has to take into account the effect of the ILTM.

Three main approaches have been proposed for the modeling of filler-matrix interactions: i) a friction or shear lag model [80, 86, 94], ii) a non-linear spring model [93, 95] and iii) a cohesive zone simulation [87,172]. In the proposed approach, a friction model cannot be directly applied due to the absence of shear stresses in the skin of ESE. In addition, a non-linear spring model requires the simulation of the GS with beams, as the filler-matrix atom interactions are modeled directly with spring elements that represent Lenard-Jones potentials. On the other hand, a cohesive zone simulation defines a traction-separation law between surfaces and can be used between the ESE and the matrix. Analytical expressions for a cohesive law in a GS-RC have been proposed based on a Lenard-Jones potential [96]. Also, pull-out molecular dynamics simulations [97] in a GS-RC reveal a similar behavior, suggesting [98] a cohesive zone for a multiscale finite element simulation. Therefore, the definition of a cohesive zone that follows a traction-separation law is applied in the developed methodology for the modeling of the ILTM.

A commonly used traction-separation law typically defines the traction vector t that is developed between two surfaces, as a function of their separation distances δ. In its simplest version this law is decoupled to the normal n, shear1 s and shear2 t directions of the contact surface, which also corresponds to the ESE u_3, u_2 and u_1 local axis (see figure3):

$$t = \begin{bmatrix} Kn & & \\ & Km & \\ & & Kt \end{bmatrix} \begin{bmatrix} \delta n \\ \delta s \\ \delta t \end{bmatrix} \tag{263}$$

fn, *Ks* and *Kt* are coefficients of the interfacial stiffness to the corresponding directions. Following an initial linear elastic cohesive behavior, damage initiation criteria are applied based on maximum traction. Therefore the maximum nominal stress criterion of damage initiation can be written as:

$$\max\left\{\frac{tn}{ISn} \quad \frac{ts}{ISs} \quad \frac{tt}{ISt}\right\}=1 \tag{264}$$

where *IS* is the interfacial shear strength at the corresponding directions. Once damage is initiated, the cohesive stiffness is degraded according to a damage evolution law. A damage variable *D* is introduced, representing the overall damage, with the value of *D*=0 for no damage and *D*=1 for maximum damage where no traction occurs. The contact stress components are calculated as functions of the damage variable D according to:

$$tn=(1-D)\overline{tn}, \quad ts=(1-D)\overline{ts}, \quad tt=(1-D)\overline{tt} \tag{265}$$

where $\overline{tn}$, $\overline{ts}$ and $\overline{tt}$ are the tractions calculated by the undamaged elastic traction-separation response. The values of *D* depend on the chosen damage evolution model. Typically the damage evolution can be based either on the fracture energy or the effective displacement and have a linear or exponential softening law. Modeling of failure depended on mix-mode condition laws can also be simulated. This general approach to the damage evolution could be used in every type of ILTM in a GS-RC, covalently bonded or not. It is assumed that the damage evolution in the GS-RC is based on effective displacements, is not depended on a mix-mode law and the stiffness degrades linearly. The effective displacement *δm* is expressed as a combination of the separations in each direction as:

$$\delta m=\sqrt{\delta n^2+\delta s^2+\delta t^2} \tag{266}$$

As shown in Figure 10, the damage variable *D* degrades linearly following the expression:

$$D=\frac{\delta_m^f (\delta_m^{max} - \delta_m^0)}{\delta_m^{max}(\delta_m^f - \delta_m^0)} \tag{267}$$

Where δ_m^f, δ_m^0 and δ_m^{max} are the separations at complete failure, damage initiation and loading history maximum respectively.
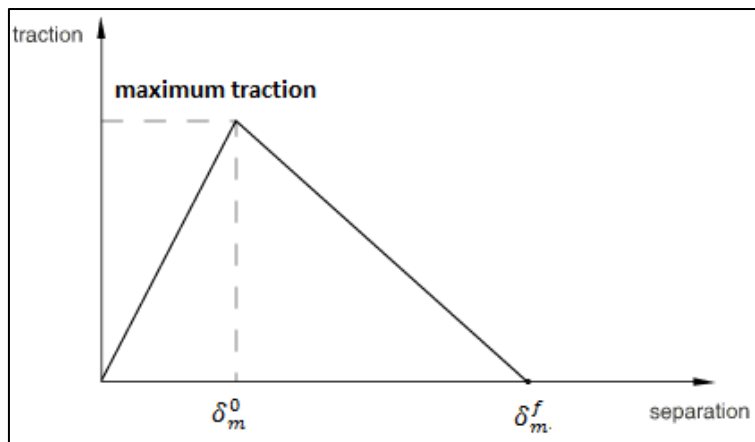

Figure 10: A Linear traction-separation response and damage evolution

An approximation of the values of the necessary input parameters for a bilinear traction separation law in the normal and in the shear direction can be derived from molecular dynamics calculations. Indicative maximum stress values, observed in such simulations, between the graphene and a polymer, are presented in Figure 11:

Reported by	Loading conditions	Maximum Shear Traction observed	Maximum Normal Traction observed
Zhang [98]	Normal separation of Flat SLGS from polyethylene		503.4 MPa
	damage zone located in polymer		217.3MPa
Liu [99]	Pull-out of Flat SLGS in polyethylene	112 MPa	
Awasthi [100]	Normal and Shear Mode separation of SLGS in polyethylene	108.3 MPa	170.6 MPa

Figure 11: Traction values observed in various molecular dynamics simulations of GS-RC with Vdw matrix filler interactions.

As reported in [100] various model parameters such as the model size and the imposed boundary conditions may affect the accuracy of the simulations and the obtained traction separation data. From this table it can be seen that the interfacial strength values calculated in the aforementioned simulations vary and more importantly differ significantly from those derived from experiments. The maximum values of the shear stress obtained experimentally in [101-104] are 2.3MPa, 0.46-0.69MPa, 0.5MPa, and 0.5 MPa respectively, while the value of the work of separation obtained in [100] dissents from the experimentally measured values in [102, 104] as well.

Another crucial factor that may affect the values of these parameters is the so called functionalization which is a chemical surface treatment that enhances the interfacial bond properties. As it is shown in [105] and [106] the interfacial shear strength can be improved through functionalization, and reach values that exceed 350 MPa and correspond to a full bonding situation. In [105] it is demonstrated that the interfacial strength in the normal separation mode decreases as the grafting density of functionalization increases, but the original value calculated for pristine graphene 727.9 MPa is very high. From these works it is concluded that parameters such as model size, grafting density, polymer molecular chain length and graphene sheet length affect the observed interfacial strength value.

All aforementioned data indicate that the uncertainty in measuring ILTM parameters is substantial, leading to large variations of the measured parameters. This leads us to the necessity to perform a sensitivity analysis with respect to the range of possible values that ILTM parameters may attain, and evaluate their relative effect of the macroscopic equivalent material properties. Results of this approach are presented in the numerical examples section 4. It is demonstrated that the proposed surrogate model can successfully incorporate the effect of the matrix inclusion interfacial properties on the overall behavior of the nanocomposite.

6.2.2 The Representative Volume Element of Graphene Reinforced Nanocomposites

Computational homogenization using RVEs is a versatile approach for multiscale modeling of composites and nanocomposites. For CNT-RCs various RVE geometries [107] have been used to calculate equivalent material properties. Along these lines, a rectangular RVE is constructed, where the SLGS is embedded in a polymer matrix. 3D solid elements are used for the matrix polymer, while thin shell elements are used for the ESE. If the ILTM is not to be considered, meaning a perfect bonding, embedded element constraints can be applied directly between the ESE and the matrix. Information about the embedded element techniques can be found in [80, 86]. This technique is generally simple and avoids complicated discretization, while it can be used both for straight and wrinkled SLGS. A typical representation of an embedded SLGS in a nanocomposite matrix is shown in Figure 12.

matrix with linear 3D elements

Interface Cohesive elements

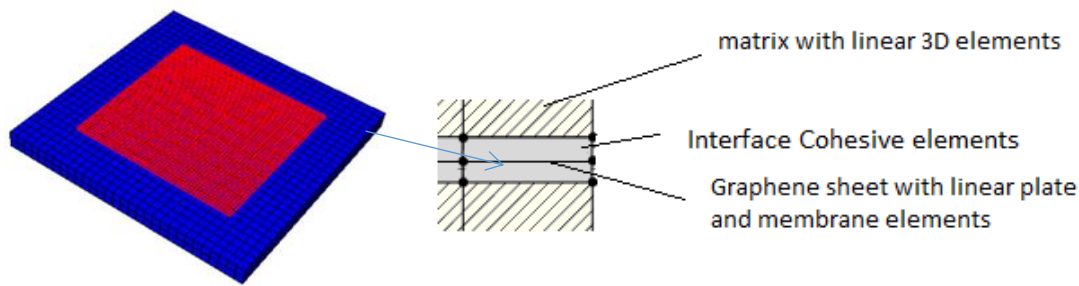Graphene sheet with linear plate and membrane elements

Figure 12: Finite element discretization of the symmetric part of an RVE of a SLGS-RC showing the embedded ESEs and the interface modeling using cohesive elements

For the representation of the ILTM by a cohesive zone, as described in section 3.1 cohesive elements were used that implement the damage model of Figure 10 [173]. This type of finite elements can be regarded as special purpose elements that can have almost zero thickness, with a constitutive response defined in terms of traction versus separation law. In particular, expressing the displacement jumps (slip degrees of freedom) Δ as the difference between top and bottom interfaces, as

$$\Delta = \begin{bmatrix} u \\ v \\ w \end{bmatrix}_{top} - \begin{bmatrix} u \\ v \\ w \end{bmatrix}_{bot} = BD_{coh} \tag{268}$$

where u, v, w are the nodal displacements of the cohesive elements at top and bottom ends, B is the strain matrix and D_{coh} are the nodal degrees of freedom of the cohesive elements. The virtual work equation can be written as

$$\delta D_{coh}^T \int_A B^T (I - D) C \, B dA = \delta D_{coh}^T \int_A B^T \sigma \, dA \tag{269}$$

where D_{coh} is a diagonal matrix composed of the damage states at the interface according to eq. (267), I represents the identity matrix, and C is the undamaged constitutive matrix whose diagonal is composed of the stiffness parameters K in eq. (263), and σ is the stress tensor. The stiffness matrix K_{coh} of can then be computed as

$$K_{coh} = \int_A B^T (I - D) C \, B dA \tag{270}$$

6.2.3 Stochastic modeling of wrinkled SLGS

Wrinkled SLGS can be seen as SLGS with random geometric imperfections, i.e random out-of-plane deviations from an ideal perfectly-planar configuration. A rational description of these random defects was performed in this study using stochastic process theory. To this purpose, a 2D univariate zero mean random field was introduced for the modelling of the random imperfections. Samples of such field are generated with the spectral representation simulation method [108]. According to this approach, samples of such imperfect geometries can be simulated that are compatible to a power spectral density function (SDF). The following SDF of exponential type was used in the present study

$$S_{f_0 f_0} = \frac{\sigma_f^2}{4\pi} b_1 b_2 \exp\left[-\frac{1}{4}\left(b_1^2 \kappa_1^2 + b_2^2 \kappa_2^2 \right) \right] \qquad \textbf{(271)}$$

where σ_f denotes the standard deviation of the stochastic field and b_1 and b_2 denote correlation length parameters that influence the shape of the spectrum. Figure 13 shows sample functions of such randomly generated wavy SLGS.
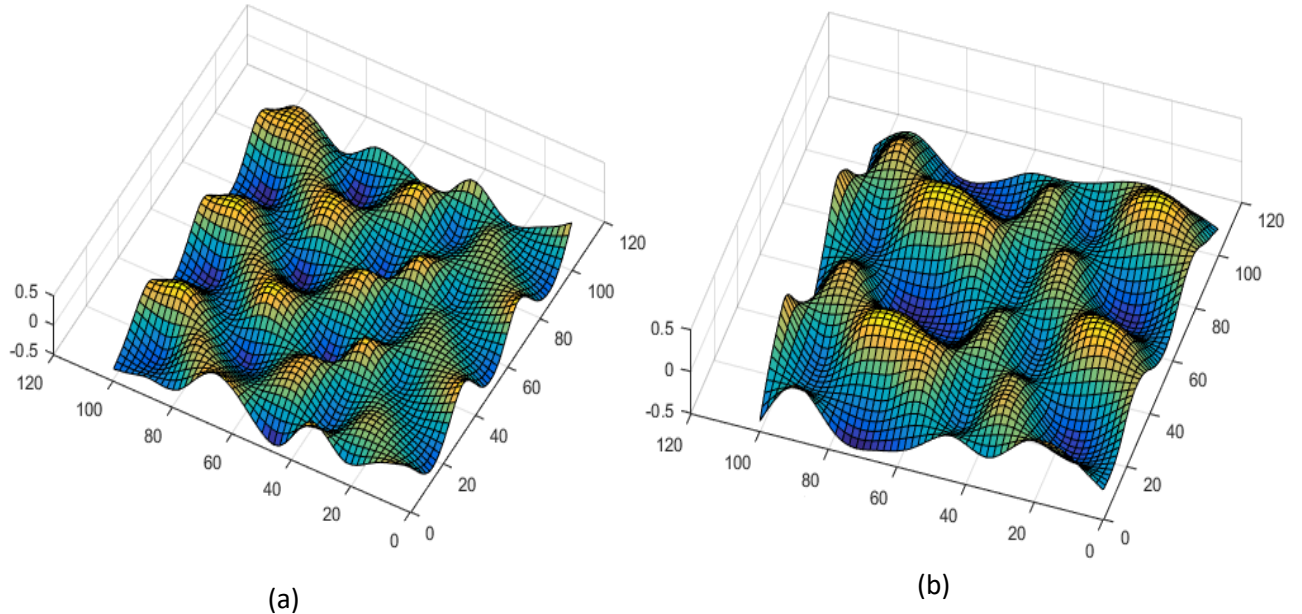

(a)

(b)

Figure 13: Randomly generated wavy 100x100nm SLGS, a) a relatively high frequency wave (b_1=b_2=1), b) low frequency waviness (b_1=b_2=20)

6.3   Numerical Results and Discussion

In this Section, the effect of the ILTM and wrinkles on the mechanical behavior of the SLGS-RC is assessed on the basis of a sensitivity analysis using the previously described multiscale modeling strategy. The test RVE used in the examples is of rectangular shape with dimensions of 150x150x20nm and consists of a 0.75%vol SLGS-RC. The matrix is assumed to be linear elastic with a Young's Modulus of 2GPa and the 100x100nm SLGS is placed in the center of the RVE and horizontally oriented. A sensitivity analysis is carried out for the various parameters that define the cohesive zone and embedded element constraints (perfect bonding) are applied for the study of the effect of random wrinkles.

6.3.1 Effect of ILTM

The effect of the interfacial cohesive stiffness *CS* (*Kss* and *Ktt* in eq. (263)) on the Young's Modulus of the nanocomposite is first investigated. Figure 14 presents the stress-strain relationship for various stiffness values *Kss* and *Ktt* of the cohesive zone for perfect bonding between matrix and filler. From this figure it is evident that the homogenized Young's Modulus of the composite increases with increasing cohesive zone stiffness, as expected. It is evident that *CS* stiffness values over 1000 MPa/nm do not contribute significantly to the overall stiffness enhancement of the composite.
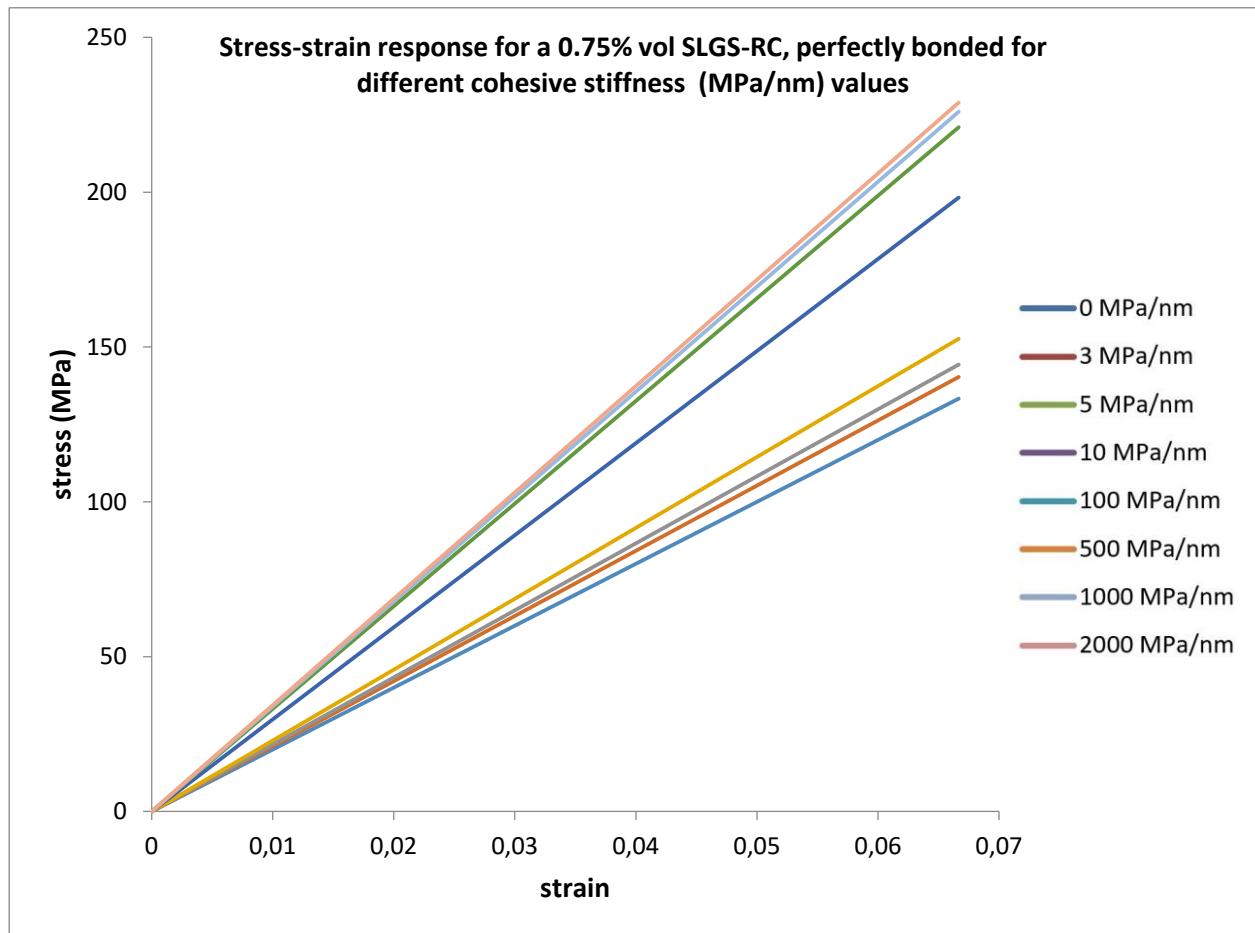

Figure 14: The effect of the interfacial cohesive stiffness on the Young's Modulus of the SLGS-RC with perfect bonding assumed

As a next step, the effect of the ILTM damage evolution stress-strain response of the SLGS is investigated. As shown in Figure 10, the damage evolution parameter *D* is defined relative to a maximum plastic displacement *mpd* which corresponds to δ_m^f in eq. (267), assuming a linear degradation branch. Figure 15 displays the force-displacement curves evaluated for a constant interfacial shear strength value of *IS*=70MPa and cohesive zone stiffness *Ks*=*Kt*=1000MPa, for various cut-off separations *mpd* considered. A stress-strain response for the nanocomposite is depicted in Figures 16.
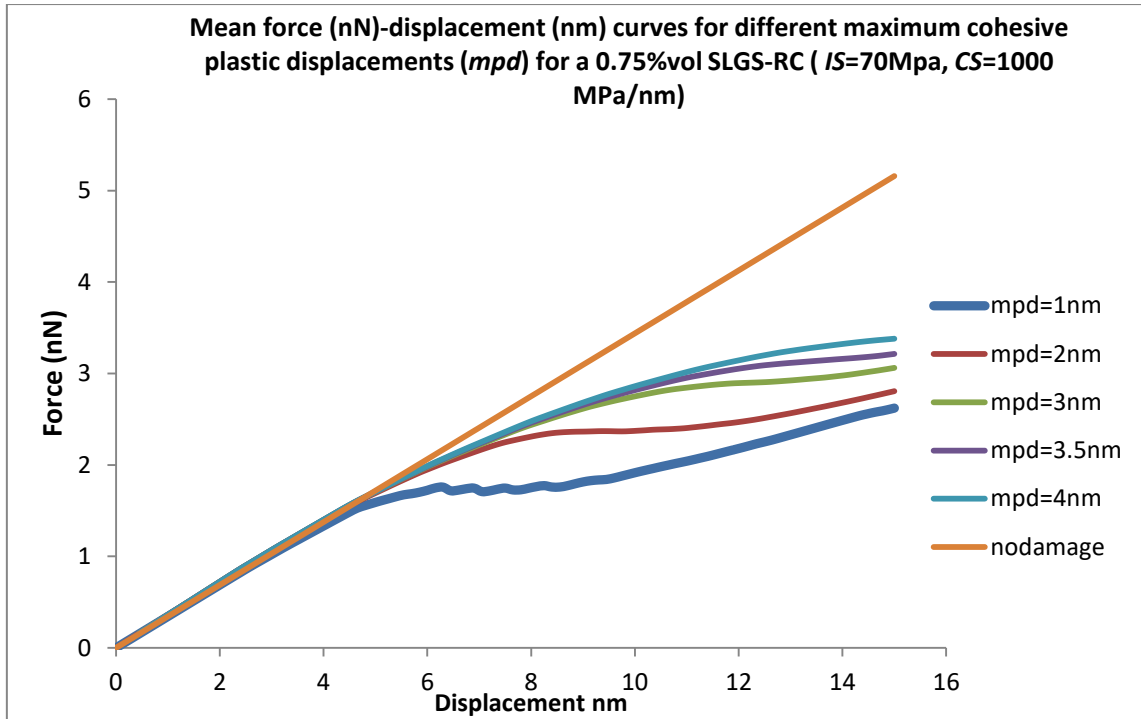
Figure 15: The effect of the ILTM maximum cohesive plastic displacement on a mean tensile force-displacement response
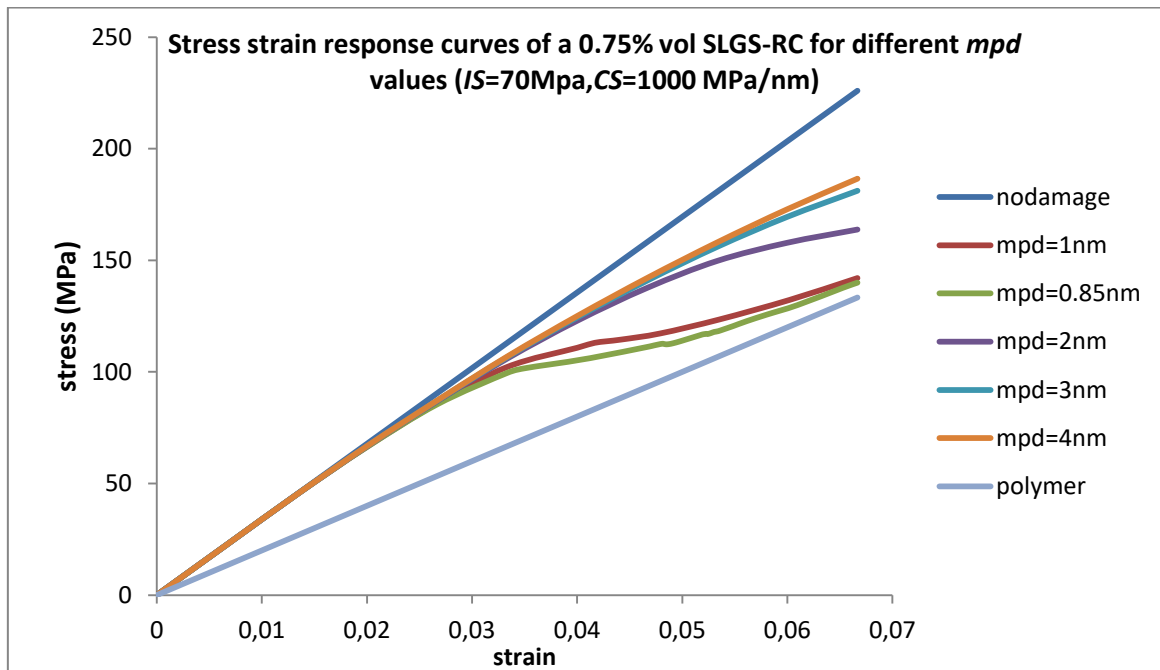

Figure 16: Stress-strain response of a SLGS-RC with ILTM damage simulation

Figure 17: Snapshots of the Mises stress distribution on the SLGS of nanocomposite corresponding to the force-displacement curve of Figure 15 for *mpd* = 0.85nm.

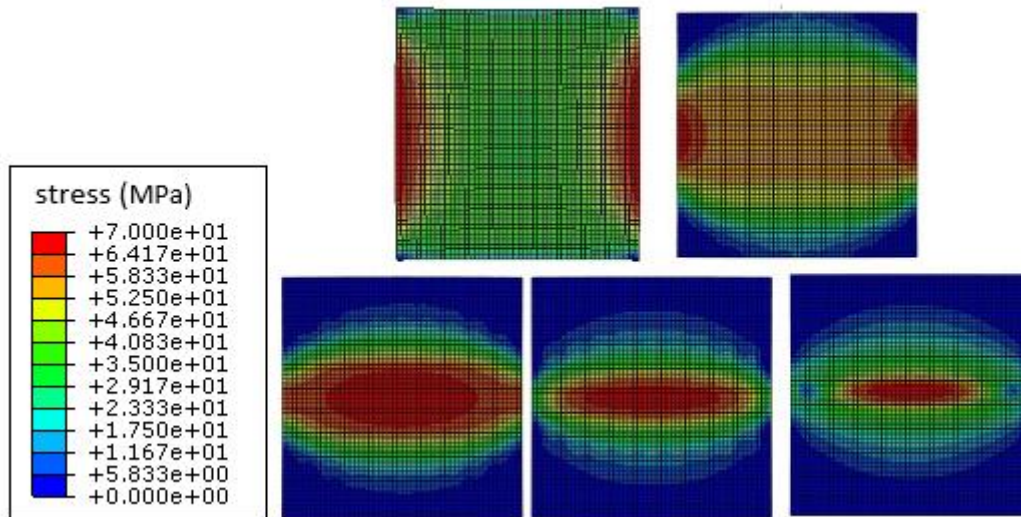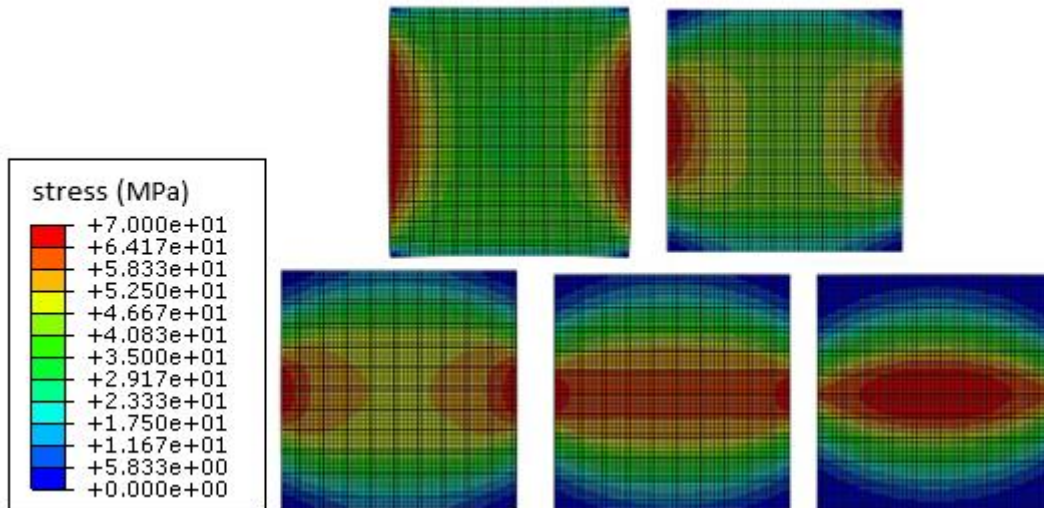**Figure 18: Snapshots of the Mises stress distribution on the SLGS of nanocomposite corresponding to the force-displacement curve of Figure 15 for *mpd*= 4nm.**

Figures 17 and 18 present snapshots of the nanocomposite as the delamination evolves, for the *mpd* values of 0.85nm and 4nm, respectively. As can be seen in Figures 16 and 18, for the largest allowed plastic displacement (4 nm) almost no delamination occurs, with a resultant stress close to that of the full-bonded condition. For intermediate plastic displacement values, the stress strain relationship is non-linear until the lowest allowed plastic displacement (0.85 nm), where delamination of almost the total area is observed (see Figure 17), with a behavior very close to that of the neat polymer. It is worth mentioning that the non-linear spring GS-RC model in [95] as well as the CNT-RC in [171], exhibit a similar response.

Assuming now that damaged bonds can be recreated in reverse loading, the cyclic stress-strain response of the SLGS-RC RVE is presented in Figure 19. Hysteresis loops that are similar to those of Figure 19, have been reported for CNT-RCs in [80, 86].
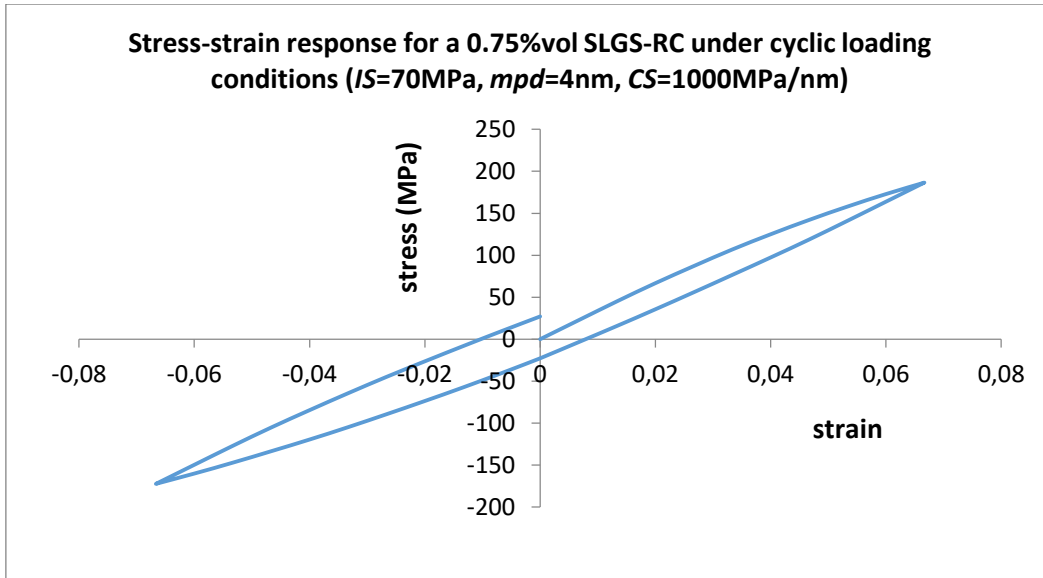
Figure 19: Stress-strain response of the SLGS-RC under cyclic loading conditions

The effect of the interfacial strength on the mechanical behavior is next evaluated. Figure 20 depicts the homogenized stress-strain behavior of the composite material for a constant CS=1000Mpa/nm and mpd=2nm and various IS parameter values in eq. (264) for all directions. From this figure it is obvious that higher stiffness of the RC is achieved for greater interfacial strength values, as expected.
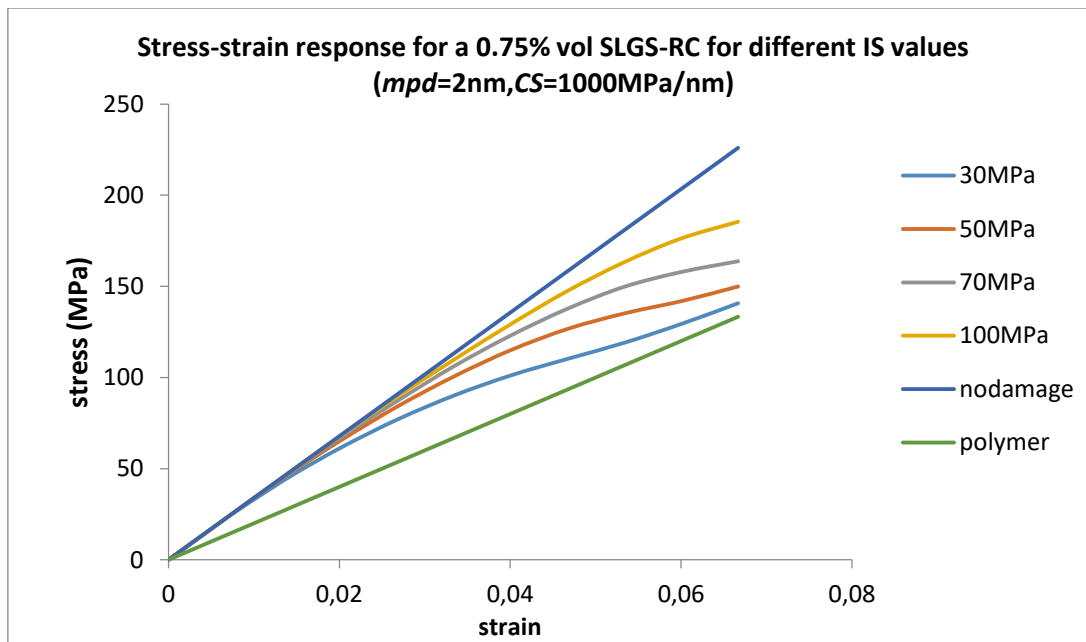
Figure 20: The effect of the interfacial strength on the stress-strain response of the SLGS-RC

Assuming now a more ''brittle'' bond with mpd=1.5 nm, the effect of IS on the damping behavior can be identified on the hysteretic loops of Figure 21. In this figure only half of the stress-strain cycle is depicted for visualization purposes. From this figure it can be seen that increasing the IS, leads to larger dissipated energy area and also to higher maximum stress, as expected. However, very high values of IS, over 90 MPa initiate a reduction in dissipation area due to fewer bonds failing in the interface.
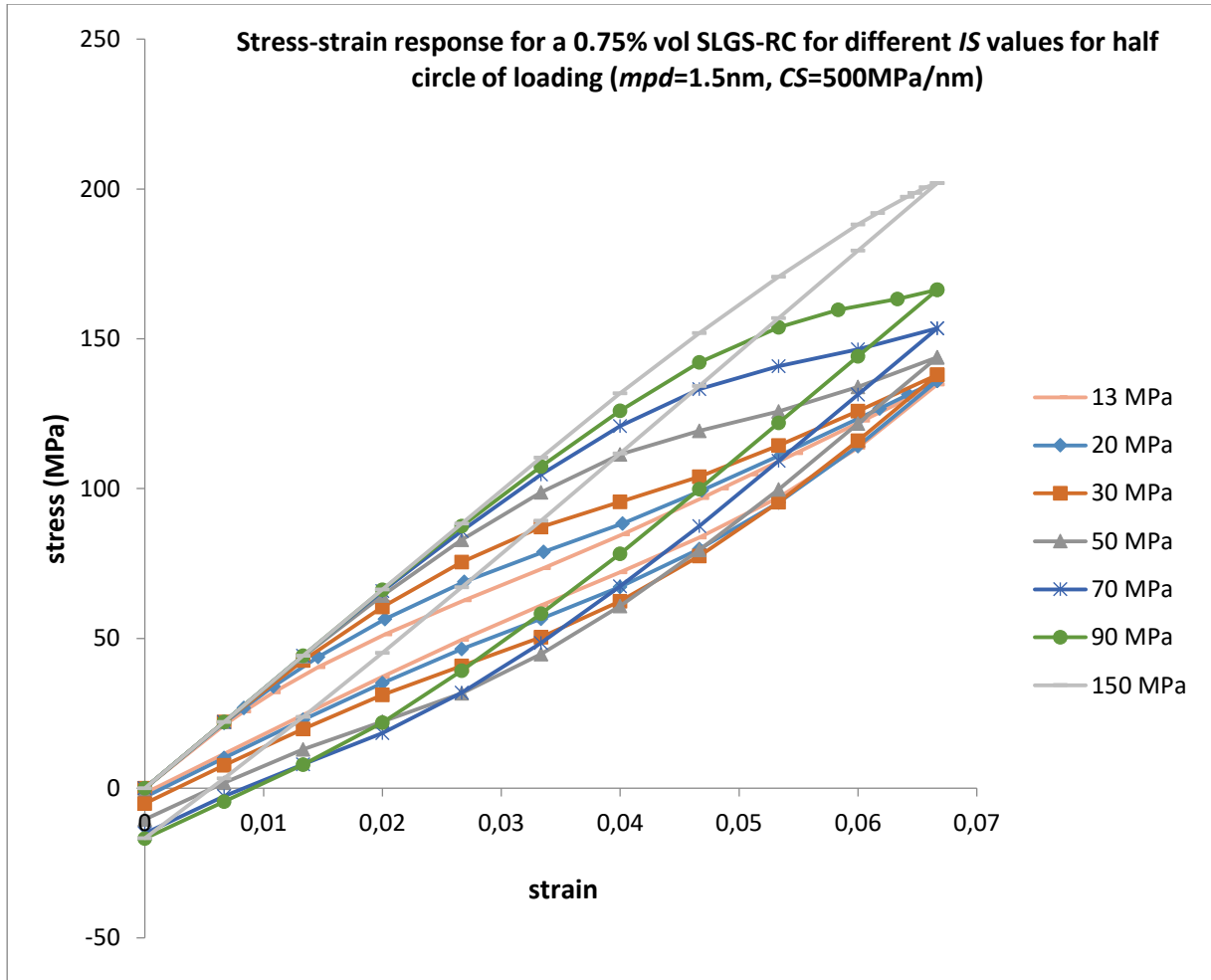
Figure 21: Stress-strain response for half cycle of loading with respect to different *IS* values

The loss factor η for hysterical damping in one circle of loading can be calculated as:

$$\eta = \frac{D_e}{\pi U} \tag{272}$$

where D_e is the dissipated energy area and U the energy stored during loading. Figure 22 plots the loss factor for different *IS* values for a full loading circle. As can be seen from this figure, the loss factor and the energy dissipation starts at a zero value in the near zero *IS*, which corresponds to the neat polymer behavior, increases as *IS* value increases and reaches a maximum plateau. Beyond this maximum plateau, the *IS* values are high enough that damage is difficult to occur. Thus the loss factor drops gradually, for increasing *IS*, towards zero which corresponds to the full-bonded condition. A similar dependence of the loss factor on the *IS* values is reported in CNT-RC studies [80, 86].
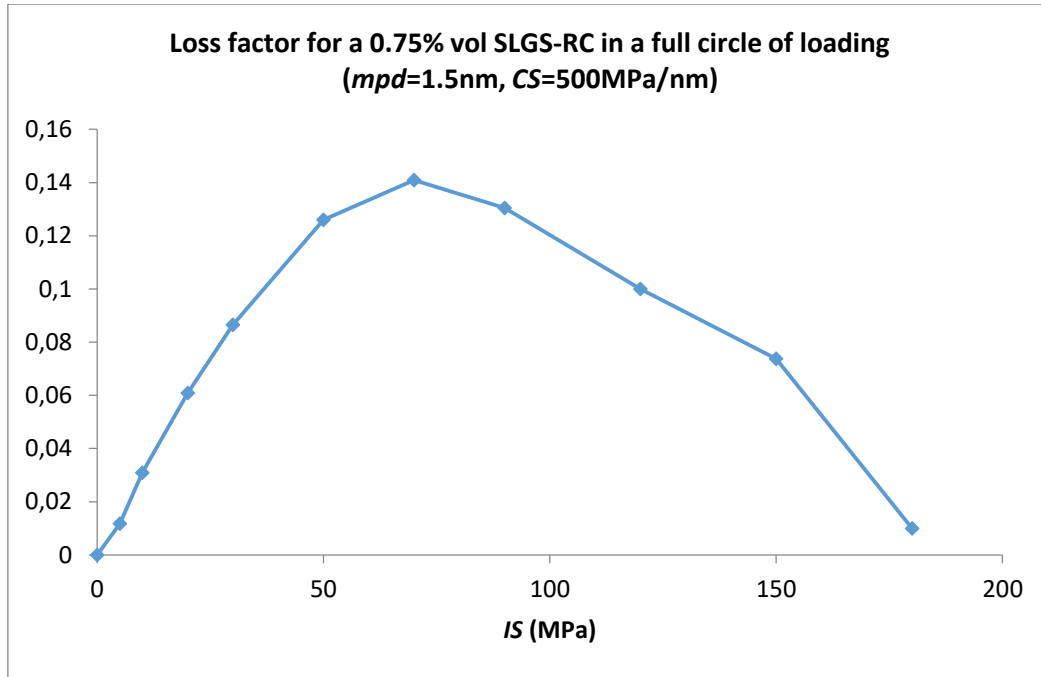
Figure 22: Loss factor of the SLGS-RC in cyclic loading conditions with respect to different *IS* values

6.3.2 The Effect of random Wrinkles

Randomly wrinkled SLGS have been finally considered in the present study. All of the wrinkled SLGS have been generated on a 100x100nm SLGS specimen using the spectral representation simulation and various values of the standard deviation parameter σ_f of the power spectral density in eq. (270). The value of σ_f parameter is directly related to the amplitudes of the imperfections field.

Samples of the randomly generated imperfection patterns are depicted in Figure 23, for different values of σ_f. Note the scale difference in the axis of vertical deflection as σ_f increases.
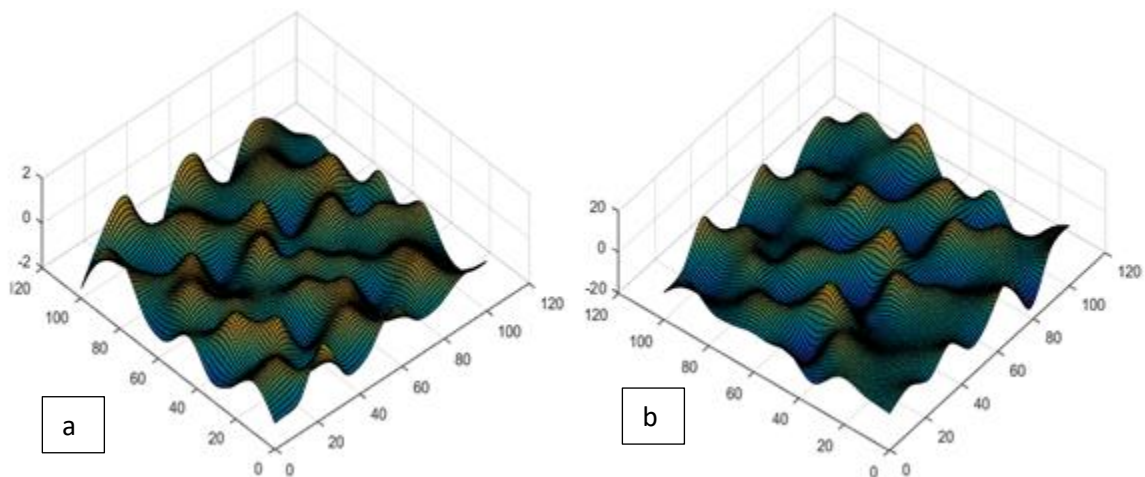
Figure 23: Randomly generated wavy SLGS for different σ_f amplitude parameters: a) σ_f =5, b) σ_f =55

121

For each value of the amplitude parameter σ_f a Monte Carlo simulation was carried out and the corresponding average Young's Modulus enhancement for the wavy SLGS-RC is depicted in Figure 24. The correlation length parameters' values used in the analysis are $b_1=1$ and $b_2=1$. It can be observed that slight waviness leads to negligible changes, however as the amplitude magnification increases, reduction in stiffness is observed. Again, similar mechanical behavior has been observed in wavy CNT-RCs [80, 86]. It is noted that no damage has been incorporated in the present simulation.
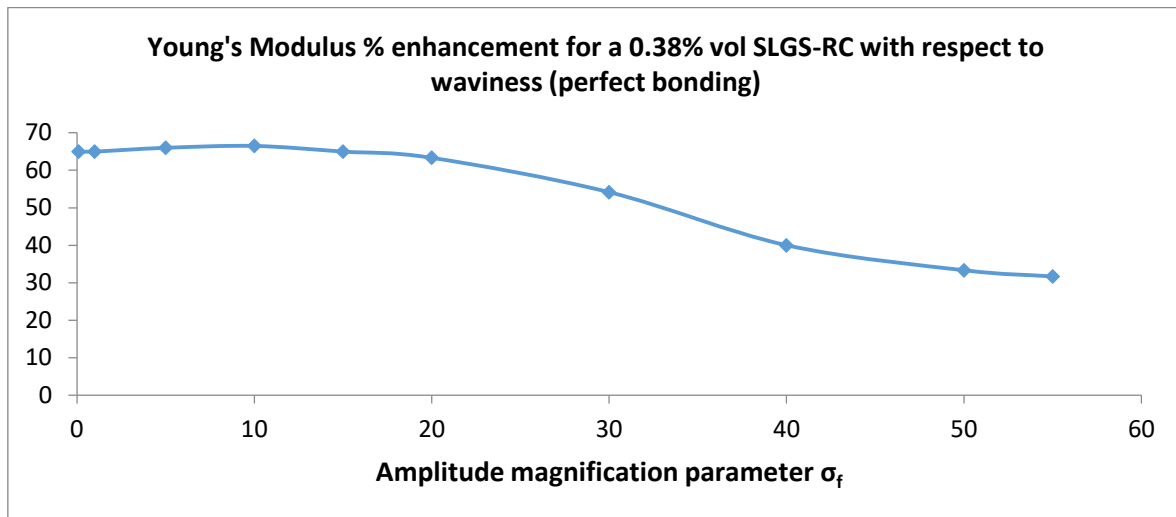
Figure 24: Young's Modulus enhancement of the nanocomposite for different random wave amplitude parameters

The observed reduction in stiffness could be attributed to the smaller effective membrane area due to the sheet orientation. Figure 25 shows the stress distribution on (a) a wrinkled and (b) a straight SLGS inside the RVE of the RC. As the plate behavior has smaller stiffness compared to the membrane, wavy areas with a more dominant plate bending behavior have a lower contribution to the RC stiffness.
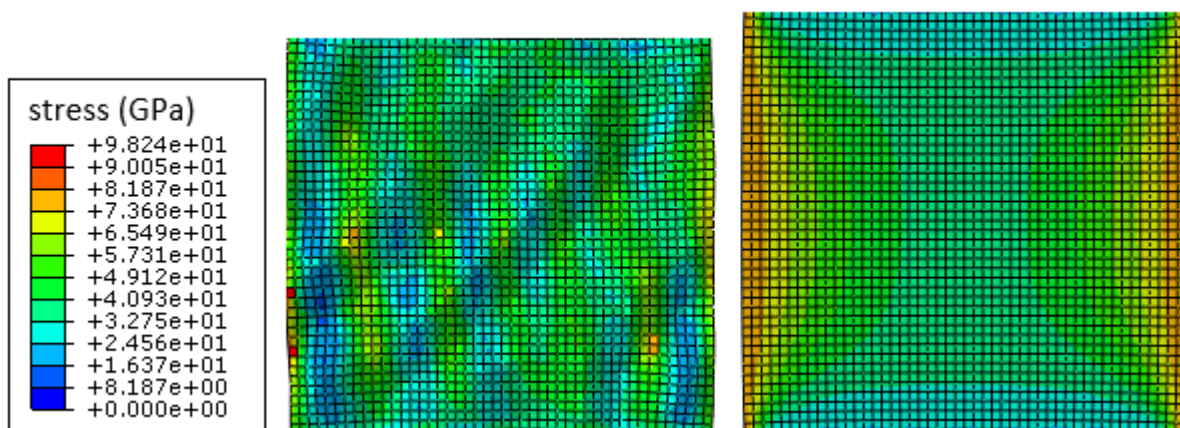
Figure 25: Tensile stress distributions on a SLGS, a) wrinkled, b) straight.

6.4 Conclusions

In the Chapter, a multiscale finite element framework is proposed for the study of the mechanical behavior of graphene reinforced nanocomposites. Equivalent continuum mechanics methods were applied for modeling interatomic interactions, providing a linkage between the small atomic scales and larger sizes with computational efficiency. The interactions between carbon atoms in a SLGS lead to a continuum shell behavior, which can be represented with the ESE. The interactions between the matrix and graphene, which define the ILTM, are modeled with a continuum cohesive zone. It is shown that cohesive damage leads to a non-linear stress-strain response due to failed bonds. Debonding phenomena in the SLGS-RC result in the same behavior as delamination in conventional composites. The values of the cohesive strength have a direct impact on the mechanical behavior, with stronger bonds leading to better enhancement of the nanocomposite, and bonds that can be regenerated leading to hysteresis loops in cyclic loadings. Damping occurring from hysteresis, has been found to depend on the interfacial strength and maximized in a limited range of strength values. Wrinkles on graphene lead to reduced stiffness of the nanocomposite, which depends on the waviness amplitude of the sheets. The ESE approach with a cohesive zone between matrix and filler can capture all of these phenomena with a low computational cost. The derivation of the cohesive damage initiation and propagation parameters for specific bond types from molecular dynamics or experimental data designed for this purpose, together with the investigation of more realistic RVEs with a number of SLGS with random orientations, are subjects of future work.

7 Conclusions - Innovation of thesis

7.1 Conclusions Summary

For the multiscale analysis of Kirchhoff Love thin shells, the first order homogenisation theory is employed along with its accompanying assumptions. Firstly the scale transition equations are appropriately formulated to incorporate the assumptions of Kirchhoff Love theory. These assumptions result in modifications of the typical expression of the boundary value problem of the microstructure. Although a three-dimensional model of microstructure (RVE) is considered, the constraints arising from the averaging relations apply only to in plane deformations tangent to the mid-surface of the shell, as the RVE deforms in plane stress conditions and the out of plane normal stress should be equal to zero. Direct substitution of the considered averaging relations in the expression of Hill's macro-homogeneity condition for small strains verify that it holds. As a result these averaging relations can be used on the expression of the Principle of the Virtual Work to yield its final form and subsequently the macroscopic equations of equilibrium.

In order to extend the above methodology to large deformation modelling of thin shells, certain work conjugate stress and strain measures are to be used in the expression of the Principle of the Virtual Work. Additionally the chosen measures should also be appropriate to be used in averaging equations according to already established homogenization theories for three dimensional continua. Once again the averaging relations are adapted to include the assumptions of Kirchhoff Love theory. Upon enforcing the plane stress condition on the RVE, the out of plane releases in the constraints of the boundary degrees of freedom constantly change direction, depending on the accumulated rotation of the plane that is tangent to the mid-surface of the shell, macroscopic material point corresponding to the RVE. Appropriate use of an attached coordinate system for the transformation of the utilized strain measures enables the neutralization of the moderately large rotations' effect on the implementation of constraints at the RVE level, simplifying this way the boundary value problem to be solved at the micro-structural level. Upon verification of satisfaction of the macro-homogeneity condition, the utilized averaging relations are substituted into the macroscopic formulation of the Principle of Virtual Work and in its linearized expression for the detailed calculation of macroscopic stiffness matrix which is necessary for the convergence of the Newton Raphson algorithm and the overall implemented FE^2 analysis. The verification of the accuracy of the proposed methodology is performed by considering the RVE of a practically homogeneous material and for microscopically heterogeneous structures consisting of a two-phase material with properties that are expected to be in-between specific upper and lower limits. The verification processes is carried out at the RVE level or for full scale models of thin shell problems with a specific expected Load-Displacement curve under the assumption of large deformations.

Finally, a two-step computational homogenization technique is used to simulate nanocomposites with graphene inclusions. On the one hand, a hierarchical homogenization approach is followed to determine the properties of shell finite elements that exhibit a mechanical behaviour equivalent to those of graphene sheets. On the other hand, a first order computational homogenization scheme is employed for the concurrent multiscale modelling of the whole nanocomposite material that includes graphene sheets together with the polymeric matrix and the considered traction separation law. In order to determine the

properties of the equivalent shell elements that can be used as surrogate to the detailed Molecular Structural Mechanics model of graphene, loading tests of the models for the two forms of deformation (flexural and membrane) are performed. In the final model those two modes are considered decoupled. The final values of the required parameters result from a minimization problem for the declination between the deformation energy of the two systems for the considered loading tests under a maximum error constraint for the developed displacements. A convergence study is performed for the obtained values of the surrogate model parameters, with respect to the size of the graphene sheet for which a homogenous mechanical behaviour is exhibited and with respect to the mesh discretization of the finite element model. The final values obtained for these parameters are verified via examples with different boundary and loading conditions for the graphene sheets. To simulate the bond at the polymer to graphene interface a cohesive zone model is employed. It is implemented by use of finite elements and it allows for the incorporation in the analysis of various constitutive law descriptions. The considered traction separation law results from molecular dynamics simulations and experimental data found in literature. Due to the wide range of proposed values for the various parameters of the considered cohesive law, a parametric study was performed for each one of them. The influence of the geometrical imperfections of the graphene sheets, on the overall mechanical behaviour of the nanocomposite material, was investigated in the context of a stochastic analysis.

7.2 Innovative Aspects of this Thesis

The innovative aspects of the present thesis, can be summarized to the following:

1. The development of an integrated formulation for multiscale finite element modelling of microscopically heterogeneous thin Kirchhoff Love shells for small deformation problems.
2. The extension of the aforementioned methodology to large deformation analysis. Both contributions assume non-linear material response of the constituents of the microstructure.
3. The development of a methodology for the nonlinear multiscale modelling of graphene reinforced polymer nanocomposite. The detailed modelling of the microstructure of the nanocomposite material includes an accurate description of the mechanical response of graphene sheets, an effective modelling strategy for the interfacial load transferring mechanism and a stochastic description of the imperfections of the graphene sheets.

Appendix

Linearization of strain variables

In this section, we provide useful formulas regarding derivations utilized in the formulation presented in Chapter 5.

The variation of the position vector of point in the midsurface of the shell is

$$\boldsymbol{x}_{m,r} = N^a \boldsymbol{c}_i \tag{273}$$

where r denotes the global degree of freedom number corresponding to the i-th displacement component (i=1,2,3 referring x,y,z) of node a, N^a is the corresponding shape function, and $\boldsymbol{c}_i$ the global cartesian base vector.

The variation of the base vectors is obtained as

$$\boldsymbol{a}_{\alpha,r} = N^a_{,\alpha} \boldsymbol{c}_i \tag{274}$$

$$\boldsymbol{a}_{\alpha,rs} = 0$$

and the variations of their derivatives as

$$\boldsymbol{a}_{\alpha\beta,r} = N^a_{,\alpha\beta} \boldsymbol{c}_i \tag{275}$$

$$\boldsymbol{a}_{\alpha\beta,rs} = 0$$

Subsequently it is derived

$$\boldsymbol{g}_{\alpha,r} = \boldsymbol{a}_{\alpha,r} + \zeta \boldsymbol{a}_{3\alpha,r} \tag{276}$$

$$\boldsymbol{g}_{\alpha,rs} = \zeta \boldsymbol{a}_{3\alpha,rs}$$

where the calculation of the variation of the derivative of the unit normal vector $\boldsymbol{a}_3$ with respect to the natural coordinates requires some intermediate calculations.

Defining the auxiliary variables $\tilde{\boldsymbol{a}}_3$ and $\bar{a}_3$ as

$$\tilde{\boldsymbol{a}}_3 = \boldsymbol{a}_1 \times \boldsymbol{a}_2 \tag{277}$$

$$\bar{a}_3 = |\boldsymbol{a}_1 \times \boldsymbol{a}_2|$$

the unit normal vector $\boldsymbol{a}_3$ can be rewritten as

$$\boldsymbol{a}_3 = \frac{\tilde{\boldsymbol{a}}_3}{\bar{a}_3} \tag{278}$$

Then the variation of the unit normal vector $\boldsymbol{a}_3$ and its derivative with respect to the natural coordinates are given as

$$\boldsymbol{a}_{3,a} = \frac{\tilde{\boldsymbol{a}}_{3,a}\bar{a}_3 - \tilde{\boldsymbol{a}}_3\bar{a}_{3,a}}{\bar{a}_3^2} \tag{279}$$

$$\boldsymbol{a}_{3,r} = \frac{\tilde{\boldsymbol{a}}_{3,r}\bar{a}_3 - \tilde{\boldsymbol{a}}_3\bar{a}_{3,r}}{\bar{a}_3^2}$$

where it can be used that

$$\tilde{\boldsymbol{a}}_{3,a} = \boldsymbol{a}_{1,a} \times \boldsymbol{a}_2 + \boldsymbol{a}_1 \times \boldsymbol{a}_{2,a} \tag{280}$$

$$\tilde{\boldsymbol{a}}_{3,r} = \boldsymbol{a}_{1,r} \times \boldsymbol{a}_2 + \boldsymbol{a}_1 \times \boldsymbol{a}_{2,r}$$

For the higher order derivatives and variations we get successively for the normal vector $\tilde{\boldsymbol{a}}_3$, its norm $\bar{a}_3$ and the unit normal vector

$$\tilde{\boldsymbol{a}}_{3,a,s} = \boldsymbol{a}_{1a,s} \times \boldsymbol{a}_2 + \boldsymbol{a}_{1,a} \times \boldsymbol{a}_{2,s} + \boldsymbol{a}_{1,s} \times \boldsymbol{a}_{2,a} + \boldsymbol{a}_1 \times \boldsymbol{a}_{2a,s} \tag{281}$$
$$\tilde{\boldsymbol{a}}_{3,rs} = \boldsymbol{a}_{1,r} \times \boldsymbol{a}_{2,s} + \boldsymbol{a}_{1,s} \times \boldsymbol{a}_{2,r}$$

$$\bar{a}_{3,rs} = \frac{\tilde{\boldsymbol{a}}_{3,rs}\tilde{\boldsymbol{a}}_3 + \tilde{\boldsymbol{a}}_{3,r}\tilde{\boldsymbol{a}}_{3,s}}{\bar{a}_3} - \frac{(\tilde{\boldsymbol{a}}_{3,r}\tilde{\boldsymbol{a}}_3)(\tilde{\boldsymbol{a}}_{3,s}\tilde{\boldsymbol{a}}_3)}{\bar{a}_3^3} \tag{282}$$

$$\bar{a}_{3,a,s} = \frac{\tilde{\boldsymbol{a}}_{3,a,s}\tilde{\boldsymbol{a}}_3 + \tilde{\boldsymbol{a}}_{3,a}\tilde{\boldsymbol{a}}_{3,s}}{\bar{a}_3} - \frac{(\tilde{\boldsymbol{a}}_{3,a}\tilde{\boldsymbol{a}}_3)(\tilde{\boldsymbol{a}}_{3,s}\tilde{\boldsymbol{a}}_3)}{\bar{a}_3^3}$$

$$\boldsymbol{a}_{3,rs} = \frac{\tilde{\boldsymbol{a}}_{3,rs}}{\bar{a}_3} - \frac{\tilde{\boldsymbol{a}}_{3,r}\bar{a}_{3,s}}{\bar{a}_3^2} - \frac{\tilde{\boldsymbol{a}}_{3,s}\bar{a}_{3,r}}{\bar{a}_3^2} - \frac{\tilde{\boldsymbol{a}}_3\bar{a}_{3,rs}}{\bar{a}_3^2} + \frac{\tilde{\boldsymbol{a}}_3 2\bar{a}_{3,r}\bar{a}_{3,s}}{\bar{a}_3^3} \tag{283}$$

$$\boldsymbol{a}_{3,a,s} = \frac{\tilde{\boldsymbol{a}}_{3,a,s}}{\bar{a}_3} - \frac{\tilde{\boldsymbol{a}}_{3,a}\bar{a}_{3,s}}{\bar{a}_3^2} - \frac{\tilde{\boldsymbol{a}}_{3,s}\bar{a}_{3,a}}{\bar{a}_3^2} - \frac{\tilde{\boldsymbol{a}}_3\bar{a}_{3,a,s}}{\bar{a}_3^2} + \frac{\tilde{\boldsymbol{a}}_3 2\bar{a}_{3,a}\bar{a}_{3,s}}{\bar{a}_3^3}$$

Finally, the variation of the derivative of the unit normal vector $\boldsymbol{a}_3$ with respect to the natural coordinates is given as

$$\boldsymbol{a}_{3,a,rs} = \frac{\tilde{\boldsymbol{a}}_{3,a,rs}}{\tilde{a}_3} - \frac{\tilde{\boldsymbol{a}}_{3,a,r}\bar{a}_{3,s}}{\tilde{a}_3^2} - \frac{\tilde{\boldsymbol{a}}_{3,a,s}\bar{a}_{3,r}}{\tilde{a}_3^2} + \frac{2\tilde{\boldsymbol{a}}_{3,a}\bar{a}_{3,r}\bar{a}_{3,s}}{\tilde{a}_3^3} - \frac{\tilde{\boldsymbol{a}}_{3,a}\bar{a}_{3,rs}}{\tilde{a}_3^2} - \frac{\tilde{\boldsymbol{a}}_{3,rs}\bar{a}_{3,a}}{\tilde{a}_3^2} + \frac{2\tilde{\boldsymbol{a}}_{3,r}\bar{a}_{3,a}\bar{a}_{3,s}}{\tilde{a}_3^3} - \frac{\tilde{\boldsymbol{a}}_{3,r}\bar{a}_{3,a,s}}{\tilde{a}_3^2}$$
$$+ \frac{2\tilde{\boldsymbol{a}}_{3,S}\bar{a}_{3,a}\bar{a}_{3,r}}{\tilde{a}_3^3} - \frac{6\tilde{\boldsymbol{a}}_3\bar{a}_{3,a}\bar{a}_{3,r}\bar{a}_{3,s}}{\tilde{a}_3^4} + \frac{2\tilde{\boldsymbol{a}}_3\bar{a}_{3,a,s}\bar{a}_{3,r}}{\tilde{a}_3^3} + \frac{2\tilde{\boldsymbol{a}}_3\bar{a}_{3,a}\bar{a}_{3,rs}}{\tilde{a}_3^3} - \frac{\tilde{\boldsymbol{a}}_{3,s}\bar{a}_{3,a,r}}{\tilde{a}_3^2} + \frac{2\tilde{\boldsymbol{a}}_3\bar{a}_{3,a,r}\bar{a}_{3,s}}{\tilde{a}_3^3} - \frac{\tilde{\boldsymbol{a}}_3\bar{a}_{3,a,rs}}{\tilde{a}_3^2}$$

$$\tag{284}$$

where the following intermediate calculations can be used concerning the normal vector $\boldsymbol{a}_3$

$$\tilde{\boldsymbol{a}}_{3,a,rs} = \boldsymbol{a}_{1a,rs} \times \boldsymbol{a}_2 + \boldsymbol{a}_{1a,r} \times \boldsymbol{a}_{2,s} + \boldsymbol{a}_{1a,s} \times \boldsymbol{a}_{2,r} + \boldsymbol{a}_{1a} \times \boldsymbol{a}_{2,rs} + \boldsymbol{a}_{1,rs} \times \boldsymbol{a}_{2,a} + \boldsymbol{a}_{1,r} \times \boldsymbol{a}_{2,a,s} + \boldsymbol{a}_{1,s} \times \boldsymbol{a}_{2,a,r} + \boldsymbol{a}_1 \times \boldsymbol{a}_{2,a,rs} \tag{285}$$

and the norm $\bar{a}_3$ of the normal vector

$$\bar{a}_{3,a,rs} = \left(\frac{1}{\bar{a}_3}\right)\{\tilde{\boldsymbol{a}}_{3,a,rs}\tilde{\boldsymbol{a}}_3 + \tilde{\boldsymbol{a}}_{3,a,r}\tilde{\boldsymbol{a}}_{3,s} + \tilde{\boldsymbol{a}}_{3,a,s}\tilde{\boldsymbol{a}}_{3,r} + \tilde{\boldsymbol{a}}_{3,a}\tilde{\boldsymbol{a}}_{3,rs}\} - \left(\frac{\bar{a}_{3,s}}{\bar{a}_3^2}\right)\{\tilde{\boldsymbol{a}}_{3,a,r}\tilde{\boldsymbol{a}}_3 + \tilde{\boldsymbol{a}}_{3,a}\tilde{\boldsymbol{a}}_{3,r}\}$$
$$-\left(\frac{1}{\bar{a}_3^3}\right)\{(\tilde{\boldsymbol{a}}_{3,a,s}\tilde{\boldsymbol{a}}_3 + \tilde{\boldsymbol{a}}_{3,a}\tilde{\boldsymbol{a}}_{3,s})(\tilde{\boldsymbol{a}}_{3,r}\tilde{\boldsymbol{a}}_3) + (\tilde{\boldsymbol{a}}_{3,a}\tilde{\boldsymbol{a}}_3)(\tilde{\boldsymbol{a}}_{3,r,s}\tilde{\boldsymbol{a}}_3 + \tilde{\boldsymbol{a}}_{3,r}\tilde{\boldsymbol{a}}_{3,s})\} + \left(\frac{3\bar{a}_{3,s}}{\bar{a}_3^4}\right)\{(\tilde{\boldsymbol{a}}_{3,a}\tilde{\boldsymbol{a}}_3)(\tilde{\boldsymbol{a}}_{3,r}\tilde{\boldsymbol{a}}_3)\}$$

$$\tag{286}$$

Next the variation of in plane membrane coefficients of the deformation gradient tensor, in the specified bases (231) are given as

$$F_{,s}^{\alpha\beta} = (\boldsymbol{g}_i \boldsymbol{e}_\alpha)_{,s}(\boldsymbol{G}^i \boldsymbol{E}_\beta) = (\boldsymbol{g}_{i,s}\boldsymbol{e}_\alpha + \boldsymbol{g}_i \boldsymbol{e}_{\alpha,s})(\boldsymbol{G}^i \boldsymbol{E}_\beta) \tag{287}$$

and the variation of the basis vectors of the attached basis $\boldsymbol{e}_\alpha$ is performed similarly to equation (279) via a chain rule.

References

[1] Eshelby JD (1957) The determination of the field of an ellipsoidal inclusion and related problems, *Proc. Royal Soc. London* A241: 376-396

[2] Hashin Z. (1962) The elastic moduli of heterogeneous materials. *J. Appl. Mech.* 29: 143-150

[3] Hashin Z., Shtrikman S. (1963) A variational approach to the theory of the elastic behavior of multiphase materials. *J. Mech. Phys. Solids* 11: 127-140

[4] Budiansky B. (1965) On the elastic moduli of some heterogeneous materials, *J. Mech. Phys. Solids* 13: 223-227

[5] Hill R. (1965) A self-consistent mechanics of composite materials *J. Mech. Phys. Solids* 13: 213-222

[6] Christensen R.M., Lo K.H. (1979) Solutions for effective shear properties in three phase sphere and cylinder models. *J. Mech. Phys. Solids* 27: 315-330

[7] A. Bensoussan, J.-L. Lionis and G. Papanicolaou, Asymptotic Analysis for Periodic Structures (North-Holland, Amsterdam, 1978).

[8] E. Sanchez-Palencia, Non-homogeneous Media and Vibration Theory, *Lecture Notes in Physics*, Vol. 127 (Springer-Verlag, Berlin, 1980).

[9] A. Tolenado and H. Murakami, A high-order mixture model for periodic particulate composites, *Int. J. Solids Struct.* 23, 989–1002 (1987).

[10] F. Devries, H. Dumontet, G. Duvaut and F. Lene, Homogenization and damage for composite structures, *Int. J. Numer. Meth. Eng.* 27, 285–298 (1989).

[11] J. M. Guedes and N. Kikuchi, Preprocessing and postprocessing for materials based on the homogenization method with adaptive finite element methods, *Comput. Meth. Appl. Mech. Eng.* 83, 143–198 (1990).

[12] S. J. Hollister and N. Kikuchi, A comparison of homogenization and standard mechanics analysis for periodic porous composites, *Comput. Mech.* 10, 73–95 (1992).

[13]. J. Fish, Q. Yu and K. Shek, Computational damage mechanics for composite materials based on mathematical homogenisation, *Int. J. Numer. Meth. Eng.* 45, 1657–1679 (1999).

[14] S. Nemat-Nasser and M. Hori, Micromechanics: Overall Properties of Heterogeneous Materials (Elsevier, Amsterdam, 1993).

[15] T. Christman, A. Needleman and S. Suresh, An experimental and numerical study of deformation in metal-ceramic composites, *Acta Metall.* 37, 3029– 3050 (1989).

[16] V. Tvergaard, Analysis of tensile properties for wisker-reinforced metalmatrix composites, *Acta Metall. Mater.* 38, 185–194 (1990).

[17] G. Bao, J. W. Hutchinson and R. M. McMeeking, Plastic reinforcement of ductile materials against plastic flow and creep, *Acta Metall. Mater.* 39, 1871–1882 (1991).

[18] J. R. Brockenbrough, S. Suresh and H. A. Wienecke, Deformation of metal-matrix composites with continuous fibers: Geometrical effect of fiber distribution and shape, *Acta Metall. Mater.* 39, 735–752 (1991).

[19] T. Nakamura and S. Suresh, Effect of thermal residual stress and fiber packing on deformation of metal-matrix composites, *Acta Metall. Mater.* 41, 1665– 1681 (1993).

[20] P. E. McHugh, R. J. Asaro and C. F. Shin, Computational modeling of metal matrix composite materials — II. Isothermal stress–strain behaviour, *Acta Metall. Mater.* 41, 1477–1488 (1993).

[21] O. van der Sluis, P. J. G. Schreurs and H. E. H. Meijer, Effective properties of a viscoplastic constitutive model obtained by homogenisation, *Mech. Mater.* 31, 743–759 (1999).

[22] O. van der Sluis, Homogenisation of structured elastoviscoplastic solids, PhD thesis, Eindhoven University of Technology, Eindhoven, The Netherlands (2001).

[23] S. Suresh, A. Mortensen and A. Needleman (eds.), Fundamentals of Metal- Matrix Composites (Butterworth-Heinemann, Boston, 1993).

[24] P. M. Suquet, Local and global aspects in the mathematical theory of plasticity, in Plasticity Today: Modelling, Methods and Applications, eds. A. Sawczuk and G. Bianchi (Elsevier Applied Science Publishers, London, 1985), pp. 279–310

[25] F. Feyel and J.-L. Chaboche, FE2 multiscale approach for modelling the elastoviscoplastic behaviour of long fiber SiC/Ti composite materials, *Comput. Meth. Appl. Mech. Eng*. 183, 309–330 (2000).

[26] V. Kouznetsova, Computational homogenization for the multi-scale analysis of multi-phase materials, PhD thesis, Eindhoven University of Technology, Eindhoven, The Netherlands (2002).

[27] A. Klawonn, S. Köhler, M. Lanser, O. Rheinbach, Computational homogenization with million-way parallelism using domain decomposition methods, *Computational Mechanics* 65 (1) (2020). doi:10.1007/s00466-019-01749-5.

[28] J. Yvonnet, D. Gonzalez, Q.-C. He, Numerically explicit potentials for the homogenization of nonlinear elastic heterogeneous materials, *Computer Methods in Applied Mechanics and Engineering* 198 (33) (2009) 2723 - 2737.

[29] F. Fritzen, O. Kunc, Two-stage data-driven homogenization for nonlinear solids using a reduced order model, *European Journal of Mechanics* - A/Solids 69 (2018) 201 - 220.

[30] L. Ba Anh, J. Yvonnet, Q. He, Computational homogenization of nonlinear elastic materials using neural networks: Neural networks-based computational homogenization, *International Journal for Numerical Methods in Engineering* 104 (05 2015).

[31] X. Lu, D. Giovanis, J. Yvonnet, V. Papadopoulos, F. Detrez, J. Bai, A data-driven computational homogenization method based on neural networks for the nonlinear anisotropic electrical response of graphene/polymer nanocomposites, *Computational Mechanics* (10 2018).

[32] C. Miehe, A. Koch, Computational micro-to-macro transitions of discretized microstructures undergoing small strains, Archive of Applied Mechanics 72 (2002) 300-317.

[33] V. Kouznetsova, W. Brekelmans, F. Baaijens, Approach to micro-macro modeling of heterogeneous materials, *Computational Mechanics* 27 (1) (2001) 37-48. doi:10.1007/s004660000212

[34] C. Miehe, Computational micro-to-macro transitions for discretized micro-structures of heterogeneous materials at finite strains based on the minimization of averaged incremental energy, *Computer Methods in Applied Mechanics and Engineering* 192 (5) (2003) 559-591.

[35] E. Tikarrouchine, G. Chatzigeorgiou, Y. Chemisky, F. Meraghni, Fully coupled thermo-viscoplastic analysis of composite structures by means of multi-scale three-dimensional finite element computations, *International Journal of Solids and Structures* 164 (2019) 120-140. doi:10.1016/j.ijsolstr.2019.01.018.

[36] E. Tikarrouchine, G. Chatzigeorgiou, F. Praud, B. Piotrowski, Y. Chemisky, F. Meraghni, Three-dimensional fe2 method for the simulation of non-linear, rate-dependent response of composite structures, *Composite Structures* 193 (2018) 165-179. doi:10.1016/j.compstruct.2018.03.072.

[37] M.-A. Keip, P. Steinmann, J. Schröder, Two-scale computational homogenization of electro-elasticity at finite strains, *Computer Methods in Applied Mechanics and Engineering* 278 (2014) 62-79. doi:https://doi.org/10.1016/j.cma.575 2014.04.020.

[38] A. Javili, G. Chatzigeorgiou, P. Steinmann, Computational homogenization in magneto-mechanics, *International Journal of Solids and Structures* 50 (25-26) (2013) 4197-4216. doi:10.1016/j.ijsolstr.2013.08.024.

[39] G. Huynh, X. Zhuang, H. Bui, G. Meschke, H. Nguyen-Xuan, Elasto-plastic large deformation analysis of multi-patch thin shells by isogeometric approach, *Finite Elements in Analysis and Design* 173, cited By 2 (2020). doi:10.1016/j. finel.2020.103389.

[40] M. Ambati, J. Kiendl, L. De Lorenzis, Isogeometric Kirchhoff love shell formulation for elasto-plasticity, *Computer Methods in Applied Mechanics and Engineering* 340 (2018) 320-339, cited By 20. doi:10.1016/j.cma.2018.05.023.

[41] J. Simo, J. Kennedy, On a stress resultant geometrically exact shell model. part v. nonlinear plasticity: formulation and integration algorithms, *Computer Methods in Applied Mechanics and Engineering* 96 (2) (1992) 133-171, doi:10.1016/0045-7825(92)90129-8.

[42] B. Skallerud, L. Myklebust, B. Haugen, Nonlinear response of shell structures: Effects of plasticity modelling and large rotations, *Thin-Walled Structures* 39 (6) (2001) 463-482, doi:10.1016/S0263-8231(01)00014-3.

[43] Q. Zeng, A. Combescure, F. Arnaudeau, An e-cient plasticity algorithm for shell elements application to metal forming simulation, *Computers and Structures* 79 (16) (2001) 1525-1540. doi:10.1016/S0045-7949(01)00032-3.

[44] J. Dujc, B. Brank, Stress resultant plasticity for shells revisited, *Computer Methods in Applied Mechanics and Engineering* 247-248 (2012) 146-165 doi:10.1016/j.cma.2012.07.012.

[45] K. Kim, G. Lomboy, A co-rotational quasi-conforming 4-node resultant shell element for large deformation elasto-plastic analysis, *Computer Methods in Applied Mechanics and Engineering* 195 (44-47) (2006) 6502-6522. doi:10.1016/j.cma.2006.02.004.

[46] N. Cortivo, C. Felippa, H. Bavestrello, W. Silva, Plastic buckling and collapse of thin shell structures, using layered plastic modeling and co-rotational andes finite elements, *Computer Methods in Applied Mechanics and Engineering* 198 (5-8) (2009) 785-798. doi:10.1016/j.cma.2008.10.013.

[47] J. Kiendl, M.-C. Hsu, M. Wu, A. Reali, Isogeometric kirchhoff-love shell formulations for general hyperelastic materials, *Computer Methods in Applied Mechanics and Engineering* 291 (2015) 280-303, doi:10.1016/j.cma.2015.03.010.

[48] Y. Basar, Y. Ding, Finite-element analysis of hyperelastic thin shells with large strains, *Computational Mechanics* 18 (3) (1996) 200-214. doi:10.1007/BF00369938.

[49] Y. Cong, S. Nezamabadi, H. Zahrouni, J. Yvonnet, Multiscale computational homogenization of heterogeneous shells at small strains with extensions to finite displacements and buckling, *International Journal for Numerical Methods in Engineering* 104 (4) (2015) 235-259. doi:10.1002/nme.4927.

[50] P. Budarapu, J. Reinoso, M. Paggi, Concurrently coupled solid shell-based adaptive multiscale method for fracture, *Computer Methods in Applied Mechanics and Engineering* 319 (2017) 338-365. doi:10.1016/j.cma.2017.02.023.

[51] H. Dong, X. Zheng, J. Cui, Y. Nie, Z. Yang, Q. Ma, Multi-scale computational method for dynamic thermo-mechanical performance of heterogeneous shell structures with orthogonal periodic configurations, *Computer Methods in Applied Mechanics and Engineering* 354 (2019) 143-180. doi:10.1016/j.cma.2019.05.022.

[52] E. W. C. Coenen, V. G. Kouznetsova, M. G. D. Geers, Computational homogenization for heterogeneous thin sheets, *International Journal for Numerical Methods in Engineering* 83 (8-9) (2010) 1180-1205

[53] W. Wagner, F. Gruttmann, An adaptive strategy for the multi-scale analysis of plate and shell structures with elastoplastic material behaviour, *Technische Mechanik* 36 (1-2) (2016) 142-154.

[54] R. Hill, On constitutive macro-variables for heterogeneous solids at finite strain, *Proc. R. Soc. Lond.* 326 (1565) (1972) 131-147. doi:10.1098/rspa.1972.0001.

[55] V. Kouznetsova, W.A.M. Brekelmans, F.P.T. Baaijens, Approach to micro-macro modeling of heterogeneous materials, *Comput. Mech.* (2001). https://doi.org/10.1007/s004660000212

[56] A.E.H. Love, On the Small Free Vibrations and Deformations of Thin Elastic Shells, Phil. Trans. Roy. Soc. (1888).

[57] V. G. Kouznetsova, M. Geers, W. Brekelmans, Computational homogenisation for non-linear heterogeneous solids, 2010.

[58] V. Kouznetsova, M. G. D. Geers, W. A. M. Brekelmans, Multi-scale constitutive modelling of heterogeneous materials with a gradient-enhanced computational homogenization scheme, *International Journal for Numerical Methods in Engineering*
625 54 (8) (2002) 1235-1260

[59] D. Braess, Finite Elements: Theory, Fast Solvers, and Applications in Solid Mechanics, Cambridge University Press,

[60] A. Srivastava, C. Galande, Lijie Ci, L. Song, C. Rai, D. Jariwala, Kevin F. Kelly, and P.M. Ajayan, Novel Liquid Precursor-Based Facile Synthesis of Large-Area Continuous, Single, and Few-Layer Graphene Films, *Chemistry of Materials*, 22 (11), 3457–3461 2010

[61] A. Dato, V. Radmilovic, Z. Lee, J. Phillips, and M. Frenklach, Substrate-Free Gas-Phase Synthesis of Graphene Sheets, *Nano Letters*, 8(7), 2012–2016, 2008.

[62] A. Reina, X. Jia, J. Ho, D. Nezich, H. S., Vladimir B., M.S. Dresselhaus, and J. Kong, Large Area, Few-Layer Graphene Films on Arbitrary Substrates by Chemical Vapor Deposition, *Nano Letters*, 9 (1), 30-35, 2009.

[63] I.A.Ovid'ko, Mechanical properties of graphene, Rev.Adv. Mater. Sci. 34, 1-11, 2013.

[64] C. Lee, X. Wei, J. W. Kysar, J. Hone, Measurement of the Elastic Properties and Intrinsic Strength of Monolayer Graphene, *Science* 321-385, 2008.

[65] M.A. Rafiee, J. Rafiee, Z. Wang, H.e Song, Z. Yu, and N. Koratkar, Enhanced Mechanical Properties of Nanocomposites at Low Graphene Content, *ACS NANO*, 3, 12, 2009

[66] K. Lau, D. Hui, The revolutionary creation of new advanced materials –carbon nanotubes composites, *Composites Part B*, 33, 263-277, 2002.

[67] [8] J. Hwang , T. Yoon , S.H. Jin , J. Lee , T. Kim ,S.H. Hong and S. Jeon, *Adv. Mater.* 25, 6724–6729, 2013.

[68] S.F. Bartoluccia, J. Parasa, M. A. Rafieeb, J. Rafieec, S. Leea, D. Kapoora, N. Koratkarc, Graphene–aluminum nanocomposites, *Materials Science and Engineering Part A* 528, 7933– 7937, 2011.

[69] J.N. Coleman, U. Khan, W.J. Blau, Y.K. Gun'ko, Small but strong: A review of the mechanical properties of carbon nanotube–polymer composites, *Carbon* 44, 1624–1652, 2006.

[70] F. Wang, Y. Zhang, B.B. Zhang, R.Y. Hong, M.R. Kumar, C.R. Xie, Enhanced electrical conductivity and mechanical properties of ABS/EPDM composites filled with graphene, *Composites Part B*, 83, 66-74, 2015.

[71] G. Cao, Atomistic Studies of Mechanical Properties of Graphene, *Polymers*, 6, 2404-2432, 2014.

[72] G.V. Lier, C.V. Alsenoy, V.V. Doren, P. Geerlings, Ab initio study of the elastic properties of single-walled carbon nanotubes and graphene, *Chemical Physics Letters* 326, 181–185, 2000.

[73] P. Zhao and G. Shi, Study of Poisson's Ratios of Graphene and Single-Walled Carbon Nanotubes Based on an Improved Molecular Structural Mechanics Model, *SL*, vol.5, no.1, pp.49-58, 2011.

[74] M.M. Shokrieh, R.Rafiee, Prediction of Young's Modulus of graphene sheets and carbon nanotubes using nanoscale continuum mechanics approach, Materials and Design 31, 790–795, 2010.

[75] K.I.Tserpes, P.Papanikos, Finite element modeling of single-walled carbon nanotubes, *Composites: Part B*, 36, 468–477, 2005.

[76] C. Li, T.W. Chou, A structural mechanics approach for the analysis of carbon nanotubes, *International Journal of Solids and Structures* 40, 2487–2499, 2003.

[77] M, Meo, M. Rossi, Prediction of Young's Modulus of single wall carbon nanotubes by molecular-mechanics based finite element modeling, *Composites Science and Technology*, 66, 1597–1605, 2006.

[78] X. Lu, Z. Hu, Mechanical property evaluation of single-walled carbon nanotubes by finite element modeling, *Composites: Part B*, 43, 1902–1913, 2012.

[79] H.C. Cheng, Y.L. Liu, C.H. Wu, W.H. Chen, On radial breathing vibration of carbon nanotubes, *Comput. Methods Appl. Mech. Eng*. 199, 2820–2827, 2010.

[80] D.N. Savvas , V. Papadopoulos, M. Papadrakakis, The effect of interfacial shear strength on damping behavior of carbon nanotube reinforced composites, *International Journal of Solids and Structures*, 49, 3823–3837, 2012.

[81] P. Papanikos, D.D. Nikolopoulos, K.I. Tserpes b, Equivalent beams for carbon nanotubes, *Computational Materials Science*, 43, 345–352, 2008

[82] R. Górski, Elastic properties of composites reirforced by wavy carbon nanotubes, *Mechanics and Control* 30(4), 203-212, 2011.

[83] G. Dai, L. Mishnaevsky Jr, Graphene reinforced nanocomposites: 3D simulation of damage and fracture, *Computational Materials Science*, 95, 684–692, 2014.

[84] X. Huang, XQi, F.Y.C. Boey, H. Zhang, Graphene-Based Composites. *Chemical Society Reviews*, 41, 666-686, 2012.

[85] B. Shen, W. Zhai, M. Tao, D. Lu, W. Zheng, Chemical functionalization of graphene oxide toward the tailoring of the interface in polymer composites, *Composites Science and Technology*, 77, 87–94, 2013.

[86] D. Savvas, V. Papadopoulos, Nonlinear multiscale homogenization of carbon nanotube reinforced composites with interfacial slippage, *Journal for Multiscale Computational Engineering*, 12 (4), 271–289, 2014.

[87] M. Kulkarni, D. Carnahan, K. Kulkarni, D. Qian, J. L. Abot, Elastic response of a carbon nanotube fiber reinforced polymeric composite: A numerical and experimental study, *Composites: Part B*, 41, 414–421, 2010.

[88] M. Ramezani, J. Vilches and T. Neitzert, Pull-out behavior of galvanized steel strip in foam Concrete, *International Journal of Advanced Structural Engineering*, 5-24, 2013.

[89] K. Machida, Principles of Molecular Mechanics, Tokyo: Kodansha and John Wiley & Sons Co-publication, 1999.

[90] W.H. Chen, H.C. Cheng, Y.L. Liu, Radial mechanical properties of single-walled carbon nanotubes using modified molecular structure mechanics, *Computational Materials Science*, 47, 985–993, 2010.

[91] C. Baykasoglu, A. Mugan, Dynamic analysis of single-layer graphene sheets, *Computational Materials Science*, 55,228–236, 2012.

[92] R. Faccio, L. Fernández-Werner, H. Pardo, C. Goyenola, P.A. Denis and Á.W. Mombrú, Mechanical and Electronic Properties of Graphene Nanostructures, Physics and Applications of Graphene - Theory, Dr. Sergey Mikhailov (Ed.), ISBN: 978-953-307-152-7, 2011.

[93] Y. Chandra, F. Scarpa, R. Chowdhury, S. Adhikari, J. Sienz, Multiscale hybrid atomistic-FE approach for the nonlinear tensile behavior of graphene nanocomposites, *Composites: Part A*, 46, 147–153, 2013.

[94] Y. Ganesan, C. Peng, Y. Lu, P. E. Loya, P. Moloney, E, Barrera, B. I. Yakobson, J. M. Tour, R. Ballarini and J. Lou, Interface Toughness of Carbon Nanotube Reinforced Epoxy Composites, *ACS Appl. Mater. Interfaces*, 3, 129–134, 2011.

[96] M. Safaei, A. Sheidaei, M. Baniassadi, S. Ahzi , M. Mosavi Mashhadi, F. Pourboghrat, An interfacial debonding-induced damage model for graphite nanoplatelet polymer composites, *Computational Materials Science, Part A*, 96, 191-199, 2015.

[97] L.Y.Jiang, Y.Huang, H.Jiang, G.Ravichandran, H.Gao, K.C Hwang, B. Liu, A cohesive law for carbon nanotube/polymer interfaces based on the van der Waals force, *Journal of the Mechanics and Physics of Solids*, 54, 2436–2452, 2006.

[98] Y. Zhang, X. Zhuang, J. Muthu, T. Mabrouki, M. Fontaine, Y. Gong, T. Rabczuk, Load transfer of graphene/carbon nanotube/polyethylene hybrid nanocomposite by molecular dynamics simulation, *Composites: Part B*, 63, 27–33, 2014.

[99] F. Liu, N. Hu, H. Ning, Y. Liu, Y. Li, L. Wu, Molecular dynamics simulation on interfacial mechanical properties of polymer nanocomposites with wrinkled graphene, *Computational Materials Science*, 108, 160–167, 2015.

[100] A. Awasthi, D. Lagoudas and D. Hammerand, Modeling of graphene–polymer interfacial mechanical behavior using molecular dynamics, *Modelling Simul. Mater. Sci. Eng*. 17 015002, 2009.

[101] Gong L., Kinloch I. A., Young R. J., Riaz I., Jalil R., and Novoselov K. S., Interfacial Stress Transfer in a Graphene Monolayer Nanocomposite, *Advanced Materials*, 22 (24), 2694–2697, 2010.

[102] T. Jiang, R. Huang, Y. Zhu, "Interfacial Sliding and Buckling of Monolayer Graphene on a Stretchable Substrate", *Advanced Functional Materials* 24, 396-402, 2014.

[103] G. Anagnostopoulos, Ch. Androulidakis, E. Koukaras, G. Tsoukleri, I. Polyzos, J. Parthenios, K. Papagelis, and C. Galiotis, Stress Transfer Mechanisms at the Submicron Level for Graphene/ Polymer Systems, *ACS Applied Materials & Interfaces* 7 (7), 4216-4223, 2015.

[104] G. Guo, Y. Zhu, Cohesive-Shear-Lag Modeling of Interfacial Stress Transfer Between a Monolayer Graphene and a Polymer Substrate, *Journal of Applied Mechanics* 82 (3), 031005, 2015.

[105] F. Liu, N. Hu, J. Zhang, S. Atobe, S. Weng, H. Ning, et al., The interfacial mechanical properties of functionalized graphene epolymer nanocomposites, RSC Adv. 6 (71), 66658-66664, 2016.

[106] M.C. Wang, Z.B. Lai, D. Galpaya, C. Yan, N. Hu, L.M. Zhou, Atomistic simulation of surface functionalization on the interfacial properties of graphene-polymer nanocomposites, *J. Appl. Phys*. 115 (12), 123520, 2014.

[107] Y.J. Liu , X.L. Chen, Evaluations of the effective material properties of carbon nanotube-based composites using a nanoscale representative volume element, *Mechanics of Materials*, 35, 69–81, 2003.

[108] M. Shinozuka, G. Deodatis, Simulation of stochastic processes by spectral representation, *Appl. Mech. Rev*, 44(4), 191-204, 1991.

[109] C. Miehe, A. Koch, Computational micro-to-macro transitions of discretized microstructures undergoing small strains, *Arch. Appl. Mech*. (2002). https://doi.org/10.1007/s00419-002-0212-2.

[110] R. Hill, Elastic properties of reinforced solids: Some theoretical principles, *J. Mech. Phys. Solids*. 11, 357–372 (1963).

[111]. R. Hill, On macroscopic effects of heterogeneity in elastoplastic media at finite strain, *Math. Proc. Cam. Phil. Soc*. 95, 481–494 (1984).

[112]. S. Nemat-Nasser, Averaging theorems in finite deformation plasticity, *Mech. Mater*. 31, 493–523 (1999).

[113]. O. van der Sluis, P. J. G. Schreurs,W. A. M. Brekelmans and H. E. H. Meijer, Overall behaviour of heterogeneous elastoviscoplastic materials: Effect of microstructural modelling, *Mech. Mater.* 32, 449–462 (2000).

[114]. K. Terada, M. Hori, T. Kyoya and N. Kikuchi, Simulation of the multi-scale convergence in computational homogenization approach, *Int. J. Solids Struct.* 37, 2285–2311 (2000).

[115] S. Klinkel, S. Govindjee, Using finite strain 3d-material models in beam and shell elements, *Engineering Computations* 685 (Swansea, Wales) 19 (3-4) (2002) 254-271. doi:10.1108/02644400210423918

[116] Y. Bazilevs, M.-C. Hsu, D.J. Benson, S. Sankaran, A.L. Marsden, Computational fluid–structure interaction: methods and application to a total cavopulmonary connection, *Comput. Mech.* 45 (2009) 77–89.

[117] J.C. Simo, A framework for finite strain elastoplasticity based on maximum plastic dissipation and the multiplicative decomposition Part I: continuum formulation, *Comput. Methods Appl. Mech. Eng.* 66 (1998) 199–219.

[118] J.C. Simo, T.J.R. Hughes, Computational Inelasticity, Springer-Verlag, New York, 1998.

[119] A.E.H. Love, On the Small Free Vibrations and Deformations of Thin Elastic Shells, Phil. Trans. Roy. Soc. (1888).

[120] F. Cirak, M. Ortiz, P. Schröder, Subdivision surfaces: A new paradigm for thin-shell finite-element analysis, *International Journal for Numerical Methods in Engineering* 47 (12) (2000) 20392072. doi:10.1002/(SICI)1097-0207(20000430)47:
12<2039::AID-NME872>3.0.CO;2-1

[121] F. Cirak, M. Ortiz, Fully c1-conforming subdivision elements for finite deformation thin-shell analysis, *International Journal for Numerical Methods in Engineering* 51 (7) (2001) 813-833. doi:10.1002/nme.182.abs.

[122] Loop C. Smooth subdivision surfaces based on triangles. Master's Thesis, University of Utah, Department of Mathematics, 1987

[123] Warren J. Subdivision methods for geometric design. Unpublished manuscript, Department of Computer Science, Rice University, November 1995.

[124] T.W. Sederberg, J. Zheng, A. Bakenov, A. Nasri, T-splines and T-NURCCs, in: ACM SIGGRAPH 2003 Pap. SIGGRAPH '03, 2003. https://doi.org/10.1145/1201775.882295

[125] M. Scott, T. Hughes, T. Sederberg, M. Sederberg, An integrated approach to engineering design and analysis using the Autodesk T-spline plugin for Rhino3d, *Adv. Eng.* (2013)

[126] Autodesk, T-Spline plugin for Rhino, (2019). https://knowledge.autodesk.com/search-result/caas/sfdcarticles/sfdcarticles/Autodesk-T-Splines-plug-in-for-Rhino-licensing.html.

[127] M.A. Scott, M.J. Borden, C. V. Verhoosel, T.W. Sederberg, T.J.R. Hughes, Isogeometric finite element data structures based on Bézier extraction of T-splines, *Int. J. Numer. Methods Eng.* (2011). https://doi.org/10.1002/nme.3167.

[128] MSolve, (n.d.). https://github.com/mgroupntua/.

[129] The NURBS book, Choice Rev. Online. (1997). https://doi.org/10.5860/choice.35-0952

[130] T.W. Sederberg, D.L. Cardon, J. Zheng, T. Lyche, T-spline simplification and local refinement, in: ACM SIGGRAPH 2004 Pap. SIGGRAPH 2004, 2004. https://doi.org/10.1145/1186562.1015715.

[131] Y. Bazilevs, V.M. Calo, J.A. Cottrell, J.A. Evans, T.J.R. Hughes, S. Lipton, M.A. Scott, T.W. Sederberg, Isogeometric analysis using T-splines, *Comput. Methods Appl. Mech. Eng.* (2010). https://doi.org/10.1016/j.cma.2009.02.036.

[132] M.A. Scott, M.J. Borden, C. V. Verhoosel, T.W. Sederberg, T.J.R. Hughes, Isogeometric finite element data structures based on Bézier extraction of T-splines, *Int. J. Numer. Methods Eng.* (2011). https://doi.org/10.1002/nme.3167.

[133] M.J. Borden, M.A. Scott, J.A. Evans, T.J.R. Hughes, Isogeometric finite element data structures based on Bézier extraction of NURBS, *Int. J. Numer. Methods Eng.* (2011). https://doi.org/10.1002/nme.2968

[134] B. Arash, H.S. Park, T. Rabczuk, Tensile fracture behavior of short carbon nanotube reinforced polymer composites: A coarse-grained model, *Compos. Struct.* (2015). https://doi.org/10.1016/j.compstruct.2015.09.001.

[135] R.G. Ghanem, P.D. Spanos, Stochastic Finite Elements: A Spectral Approach, 1991. https://doi.org/10.1007/978-1-4612-3094-6.

[136] G. Markou, M. Papadrakakis, An efficient generation method of embedded reinforcement in hexahedral elements for reinforced concrete simulations, *Adv. Eng. Softw.* (2012). https://doi.org/10.1016/j.advengsoft.2011.09.025.

[137] V. Papadopoulos, G. Soimiris, D.G. Giovanis, M. Papadrakakis, A neural network-based surrogate model for carbon nanotubes with geometric nonlinearities, *Comput. Methods Appl. Mech. Eng.* (2018). https://doi.org/10.1016/j.cma.2017.09.010.

[138] R.H. Macneal, R.L. Harder, A proposed standard set of problems to test finite element accuracy, *Finite Elem. Anal. Des.* (1985). https://doi.org/10.1016/0168-874X(85)90003-4.

[139] Computer Analysis of Cylindrical Shells, *ACI J. Proc.* (1964). https://doi.org/10.14359/7796.

[140] Turbosquid, Front Bump. (2015). https://www.turbosquid.com/FullPreview/Index.cfm/ID/987828 (accessed September 6, 2019).

[141] S. Kurtz, PEEK Biomaterials Handbook, 2012. https://doi.org/10.1016/C2010-0-66334-6.

[142] D. Leijen, W. Schulte, S. Burckhardt, The design of a task parallel library, in: ACM SIGPLAN Not., 2009.

[143] B.M. Douglas Gregor, Andrew Lumsdaine, MPI.NET: High-performance C# Library for Message Passing, (n.d.). https://github.com/mpidotnet/MPI.NET.

[144] J.J. Costa, T. Cortes, X. Martorell, E. Ayguade, J. Labarta, Running OpenMP applications efficiently on an everything-shared SDSM, *J. Parallel Distrib. Comput.* (2006). https://doi.org/10.1016/j.jpdc.2005.06.018

[145] R.E. White, R.E. White, Message Passing Interface, in: *Comput. Math.*, 2020. https://doi.org/10.1201/b19005-8

[146] V. Kouznetsova, M. Geers, W. Brekelmans, Multi-scale second-order computational homogenization of multi-phase materials: A nested nite element solution strategy, *Computer Methods in Applied Mechanics and Engineering* 193 (48-51) (2004) 5525-5550. doi:10.1016/j.cma.2003.12.073.

[147] H. Wagner, C. Hühne, S. Niemann, Buckling of launch-vehicle cylinders under axial compression: A comparison of experimental and numerical knockdown factors, *Thin-Walled Structures* 155 (2020) 106931.

[148] A. Zingoni, K. Mudenda, V. French, B. Mokhothu, Buckling strength of thin-shell concrete arch dams, *Thin-Walled Structures* 64 (2013) 94-102, cited By 3. doi:10.1016/j.tws.2012.12.001.

[149] S. Aghajari, K. Abedi, H. Showkati, Buckling and post-buckling behavior of thin-walled cylindrical steel shells with varying thickness subjected to uniform external pressure, *Thin-Walled Structures* 44 (8) (2006) 904-909. doi:10.1016/j.tws.2006.08.015.

[150] M. Zhang, X. Xie, X. Gao, Y. Pan, G. Parke, Study on failure criterion of thin-walled steel frame structures based on the esed parameter, *Thin-Walled Structures* 161 (2021). doi:10.1016/j.tws.2020.107357.

[151] S. Maleki, A. M. Mehretehran, 3d wind buckling analysis of steel silos with stepped walls, *Thin-Walled Structures* 142 (2019) 236-261.

[152] E. Verwimp, T. Tysmans, M. Mollaert, M. Wozniak, Prediction of the buckling behaviour of thin cement composite shells: Parameter study, *Thin-Walled Structures* 108 (2016) 20-29. doi:https://doi.org/10.1016/j.tws.2016.07.011.

[153] A. Tepole, H. Kabaria, K.-U. Bletzinger, E. Kuhl, Isogeometric Kirchhoff-Love shell formulations for biological membranes, *Computer Methods in Applied Mechanics and Engineering* 293 (2015) 328-347. doi:10.1016/j.cma.2015.05.006.

[154] H. Kim, K. Chandran, M. Sacks, J. Lu, An experimentally derived stress resultant shell model for heart valve dynamic simulations, *Annals of Biomedical Engineering* 35 (1) (2007) 30-44. doi:10.1007/s10439-006-9203-8.

[155] A. Gilmanov, H. Stolarski, F. Sotiropoulos, Non-linear rotation-free shell finite-element models for aortic heart valves, *Journal of Biomechanics* 50 (2017) 56-62. doi:10.1016/j.jbiomech.2016.11.031.

[156] M.-C. Hsu, D. Kamensky, Y. Bazilevs, M. Sacks, T. Hughes, Fluid-structure interaction analysis of bioprosthetic heart valves: significance of arterial wall deformation, *Computational Mechanics* 54 (4) (2014) 1055-1071. doi:10.1007/s00466-014-1059-4.

[157] A. Hasan, K. Ragaert, W. Swieszkowski, T. Selimovi¢, A. Paul, G. Camci-Unal, M. Mofrad, A. Khademhosseini, Biomechanical properties of native and tissue engineered heart valve constructs, *Journal of Biomechanics* 47 (9) (2014) 1949-1963, cited By 131. doi:10.1016/j.jbiomech.2013.09.023.

[158] A. Gilmanov, H. Stolarski, F. Sotiropoulos, Flow-structure interaction simulations of the aortic heart valve at physiologic conditions: The role of tissue constitutive model, *Journal of Biomechanical Engineering* 140 (4) (2018). doi:10.1115/1.4038885.

[159] D. Tsapetis, G. Sotiropoulos, G. Stavroulakis, V. Papadopoulos, M. Papadrakakis, A stochastic multiscale formulation for isogeometric composite Kirchhoff Love shells, *Computer Methods in Applied Mechanics and Engineering* 373 (2021).
755 doi:10.1016/j.cma.2020.113541.

[160] V. Kouznetsova, Computational homogenization for the multi-scale analysis of multi-phase materials, Ph.D. thesis, Department of Mechanical Engineering (2002). doi:10.6100/IR560009.

[161] M. Jarosová, A. Klawonn, O. Rheinbach, Projector preconditioning and transformation of basis in feti-dp algorithms for contact problems, Mathematics and Computers in Simulation 82 (10) (2012) 1894-1907, "*The Fourth IMACS Conference: Mathematical Modelling and Computational Methods in Applied Sciences and Engineering*" Devoted to Owe Axelsson in ocassion of his 75th birthday.

[162] A. Klawonn, O. Rheinbach, A parallel implementation of dual-primal feti methods for three-dimensional linear elasticity using a transformation of basis, *SIAM Journal on Scientific Computing* 28 (5) (2006) 1886-1906. doi:10.1137/050624364.

[163] K. Sze, X. Liu, S. Lo, Popular benchmark problems for geometric nonlinear analysis of shells, *Finite Elements in Analysis and Design* 40 (11) (2004) 1551-1569. doi:10.1016/j.finel.2003.11.001.

[164] C. Geuzaine, J.-F. Remacle, Gmsh: A 3-d finite element mesh generator with built-in pre- and post-processing facilities, *International Journal for Numerical Methods in Engineering* 79 (11) (2009) 1309-1331. doi:10.1002/nme.2579.

[165] J. Kiendl, K.-U. Bletzinger, J. Linhard, R. Wüchner, Isogeometric shell analysis with Kirchhoff-Love elements, *Computer Methods in Applied Mechanics and Engineering* 198 (49-52) (2009) 3902-3914. doi:10.1016/j.cma.2009.08.013.

[166] N. Buchter, E. Ramm, D. Roehl, Three dimensional extension of non-linear shell formulation based on the enhanced assumed strain concept, *International Journal for Numerical Methods in Engineering* 37 (15) (1994) 2551-2568, doi:10.1002/nme.1620371504.

[167] S. Reese, P. Wriggers, B. Reddy, New locking-free brick element technique for large deformation problems in elasticity, *Computers and Structures* 75 (3) (2000) 291-304, cited By 119. doi:10.1016/S0045-7949(99)00137-6.

[168] B. Brank, J. Korelc, A. Ibrahimbegovic, Nonlinear shell problem formulation accounting for through-the-thickness stretching and its finite element implementation, *Computers and Structures* 80 (9-10) (2002) 699-717. doi:10.1016/
S0045-7949(02)00042-1.

[169] M. Schwarze, S. Reese, A reduced integration solid-shell finite element based on the eas and the ans concept-large deformation problems, *International Journal for Numerical Methods in Engineering* 85 (3) (2011) 289-329, cited By 99. doi:10.1002/nme.2966.

[170] S. Green, G. Turkiyyah, Second-order accurate constraint formulation for subdivision finite element simulation of thin shells, *International Journal for Numerical Methods in Engineering* 61 (3) (2004) 380-405. doi:10.1002/nme.1070.

[171] K.I.Tserpes, P.Papanikos, G.Labeas, S.Pantelakis, Multi-scale modeling of tensile behavior of carbon nanotube-reinforced composites, *Theoretical and Applied Fracture Mechanics* 49, 51–60, 2008.

[172] M. M. Shokrieh, R. Rafiee, On the tensile behavior of an embedded carbon nanotube in polymer matrix with non-bonded interphase region, *Composite Structures* 92, 647–652, 2010.

[173] R. Krueger, M.K. Cvitkovich, T.K. O'Brien, and P.J. Minguet, Testing and Analysis of Composite skin/stinger debonding under multiaxial loading, *J. of Composite Materials*, 15, 1263-1300, 2000